From Hybrid to Actively-Controlled Gas Lubricated Bearings – Theory and Experiment

Morosi, Stefano; Santos, Ilmar

Publication date:
2011

Document Version
Publisher's PDF, also known as Version of record

Citation (APA):
Morosi, S., & Santos, I. (2011). From Hybrid to Actively-Controlled Gas Lubricated Bearings – Theory and Experiment. DTU Mechanical Engineering. (DCAMM Special Report; No. S137).

From Hybrid to Actively-Controlled Gas Lubricated Bearings – Theory and Experiment

PhD Thesis

$$(EIv'')'' = q - \rho A\ddot{v}$$

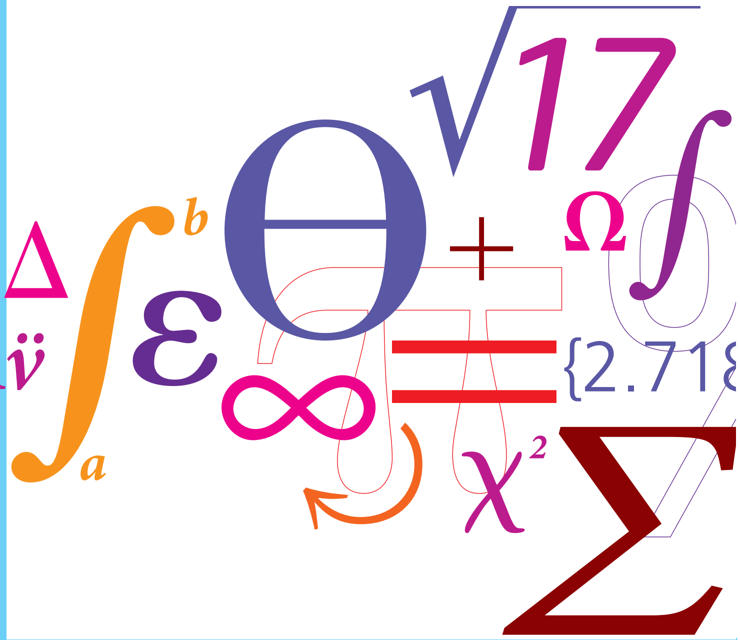

Stefano Morosi
DCAMM Special Report No. S137
September 2011

DTU Mechanical Engineering
Department of Mechanical Engineering

From Hybrid to Actively-Controlled Gas Lubricated Bearings – Theory and Experiment

Stefano Morosi

DTU Mekanik - Department of Mechanical Engineering

Danmarks Tekniske Universitet

A thesis submitted as partial fulfillment for the degree of

PhilosophiæDoctor (PhD)

2008-2011

Project Advisor: Ass. Prof. Ilmar F. Santos

Examiners and Reviewers: Prof. Chong-Won Lee, Prof. Karsten Stahl, Prof. Peder Klit.
Chairman: Ass. Prof. Niels L. Pedersen

Day of the defense: 30 January 2012

Signature from head of PhD committee:

Abstract

From a rotordynamic point of view there are two phenomena that limit the widespread of traditional gas lubrication: 1) low damping makes operation across critical speed dangerous, as even low level of unbalance can generate large vibration responses; 2) an upper bound to supercritical operation is determined by the appearance of subsynchronous whirl instability. In fact, postponing the onset speed of instability poses one of the greatest challenges in high-speed gas bearing design. A great deal of research is devoted to attack such issues, where most propose passive designs such as compliant foil bearings, tilting pad and flexure pivot gas bearings. These solutions proved to be effective in improving static and dynamic properties of the bearings, however issues related to the manufacturing and accuracy of predictions has so far limited their applications. Another drawback is that passive bearings offer a low degree of robustness, meaning that an accurate optimization is necessary for each application.

Another way of improving gas bearings operation performance is by using active control systems, transforming conventional gas bearings in an electro-mechanical machine component. In this framework the main focus of this thesis is the theoretical modeling, numerical simulation and experimental rotordynamic testing of a flexible rotor supported by hybrid aerostatic-aerodynamic gas journal bearing equipped with an electronic radial air injection system.

Experimental results on a specially designed test-rig are backed by a comprehensive mathematical model that couples a finite element model of a flexible rotor, a thermohydrodynamic model based on a modified form of the Reynold's equation for hybrid aerostatic-aerodynamic lubrication of compressible fluid, a piezoelectric injection system and a proportional-derivative controller. It is shown that synchronous vibrations can be effectively addressed ensuring safe operation across the critical speeds; whirling instability is suppressed; intervening on the software, rather than the hardware can modify the response of the system. Optimum tuning of the

control loop is addressed experimentally, showing dependency on the supply pressure and, less prominently, the rotational velocity.

Moreover, additional research is carried out in order to perform a feasibility study on a new kind of hybrid permanent magnetic – aerodynamic gas bearing. This new kind of machine is intended to exploit the benefits of the two technologies while minimizing their drawbacks. The idea is to improve the poor start-up and low speed operation performance of the gas bearing by using magnetic forces to lift the rotor. At high speeds the dynamic characteristics of the gas bearing can also be modified by using the same magnetic forces.

Resumé

Fra et rotordynamisk synspunkt er der to fænomener der begrænser udbredelsen af den traditionelle gas smøring: 1) lav dæmpning gør drift på tværs af kritiske hastigheder usikker, da selv et lavt niveau af ubalance kan generere store vibrationsamplituder, 2) den øvre grænse for superkritisk drift bestemmes af forekomsten af sub-synkrone hvirvel ustabiliteter. Forøgelsen af den hastighed hvorved ustabilitet indtræder er en af ?de største udfordringer ved design af højhastigheds gaslejer. Meget forskning adresserer de ovennævnte problematikker; med et udtalt fokus på passive designs så som eftergivende folielejer, vippe-sko og fleksible pivot gaslejer. Nævnte løsninger har vist sig at være effektive til at øge de statiske og dynamiske egenskaber af lejerne, men de lider under fremstillingsrelaterede komplikationer og problemer i forbindelse med nøjagtig matematisk forudsigelse af lejernes præstationer har hidtil begrænset deres udbredelse. En yderlig ulempe er, at passive lejer kun i ringe grad tilbyder robusthed, hvilket betyder at lejerne skal optimeres til vær enkelt applikation.

En anden måde at forbedre gas lejers drift er, gennem indførelse af aktive kontrolsystemer, at omdanne konventionelle gas lejer til elektro-mekaniske maskinkomponent. Inden for disse rammer er det primære fokus i denne afhandling den teoretiske modellering, numeriske simulering og eksperimentelle validering af en fleksibel rotor understøttet af aerostatiske-aerodynamiske hybrid gasleje, udstyret med et aktivt elektronisk radialt luftindblæsning system.

Eksperimentelle resultater optaget på en til formålet specielt designet testopstilling, understøttes af en omfattende matematisk model, som kombinerer en finite element model af en fleksibel rotor, en termohydrodynamisk model baseret på en modificeret version af Reynolds ligning for hybrid aerostatic-aerodynamisk smøring af komprimerbare væsker, et piezoelektrisk indsprøjtningssystem og en proportional-afledte controller. Det bliver vist at synkrone vibrationer kan adresseres effektivt og derigennem sikre stabil drift på tværs af kritiske hastigheder, rotorhvirvlen kan

undertrykkes ved modificering af systemresponset igennem software i stedet for hardware. Optimal tuning af kontrolsystemet er udført eksperimentelt, og viser afhængighed af tryk og, i mindre grad, rotores rotationshastighed.

Hertil kommer, at yderligere forskning er gennemført for at udføre en forundersøgelse omhandlende en ny type hybrid permanent magnet - aerodynamisk gas leje. Denne nye type maskine skal udnytte fordelende ved de to teknologier og samtidig minimere deres ulemper. Ideen er at forbedre de relativt dårlige opstart og lav hastighedsdriftsegenskaber af gas lejer ved at gøre brug af de magnetiske kræfter fra de permanente magnetlejer til at løfte rotoren. Ligeledes kan de dynamiske egenskaber af gaslejet ved høje driftsegenskaber modificeres ved hjælp af magnetiske kræfter.

Acknowledgements

This thesis is submitted as partial fullfillment of the requirements for awarding the Danish Ph.D. degree. The work has been carried out from April 2008 to September 2011 at the Section of Solid Mechanics (FAM), Department of Mechanical Engineering (MEK), Technical University of Denmark (DTU). The project was supervised by Associate Professor, Dr.-Ing, Dr.-Tech. Ilmar Ferreira Santos, whom I would like to gratefully acknowledge for being a constant source of inspiration, guidance and assistance. It is also thanks to his dedication and support -both in technical and human matters- that this project could come to an end.

Part of the research was also carried out in a visit to the Catholic University of Rio de Janeiro (January 2010), where I was a visiting PhD student in Professor Hans Ingo Weber team. I thank everybody there for the warm welcome.

In another external visit (September-October 2010) I joined Professor Minel J. Braun's research team at the University of Akron, OH. I would like to particularly express my gratitude to Professor Braun, whose profound knowledge of fluid mechanics and thermodynamics I deeply admire and consider as great source of motivation. Also, I would like to thank Frank E. Horvat in Akron's PhD team, for the practical help and proficient discussions. I hope to continue our collaboration.

Thank you to my closest PhD student colleagues at DTU, Edgar Estupinan, Alejandro Cerda, Emil Bureau, Said Lahriri for sharing many hours at the office, exchanging opinions and suggestions, developing challenging talks and stimulating ideas. Also at DTU, I would like to thank Bo Terp Paulsen for working together in the thermodynamic part, Charbel Trad for finalizing the design and following the manufacturing of the gas bearing, Christian Simonsen for upgrading the magnetic bearings and Asger Hansen and Tomasz Boguta for the exceptional dedication in setting up and carrying out experiments and implementing the measurement set up. Their exceptional work made the closing of this project some order of magnitude smoother.

I would also like express my gratitude to the Lloyd's Register ODS team, who provided substantial financial backing to project, and allowed me to finish writing the manuscript while welcoming me in the company. Too many would deserve a mention here, but paraphrasing Fermat's words, this page is too narrow to contain.

On the personal side, I would like to say a big "tak", "grazie", "obrigado" and "merci" to my best friends in Denmark, which always made and make me feel at home and for sharing countless laughs.

But most of all, I specially want to thank my dear Marie, for...everything really, especially for bringing out the best out of me. She gets the shortest acknowledgement here, but the biggest in my heart.

I dedicate this work to my family in Italy, papa' Luciano, mamma Laura and little sister Gaia, because they always encouraged me to go and get what I want and for understanding my decision to leave home and settle a bit far. I have never been too good to express my gratitude to them, but I hope to make amendment here.

Technical University of Denmark
Kgs. Lyngby, September 2011

Stefano Morosi

Contents

List of Figures

List of Tables

Nomenclature

Latin symbols

A : Transversal area [m^2]
$\mathbf{A}$: System matrix
$\mathbf{B}$: Magnetic flux density [T]
c : Heat capacity coefficient [J/mol·K]
c_D : Coefficient of discharge
c_{piezo} : Piezoelectric coupling coefficient [C/N]
C : Nominal journal clearance [m]
$\mathbf{D}$: Damping matrix [N·s/m]
d_{mech} : Piezoactuator equivalent damping [N·s/m]
d_o : Orifice diameter [m]
e : Journal eccentricity [m]
e_u : Unbalance eccentricity [m]
E : Elasticity modulus [Pa]
$\mathbf{F}$: Fluid film or magnetic forces [N]
$\mathbf{G}$: Gyroscopic matrix [kg·m]
G^d : Derivative gain [V·/m]
G^k : Proportional gain [V/m]
h : Fluid film thickness [m]
i, j : complex number
k : Thermal conductivity coefficient [W/m·K]
$\mathbf{K}$: Stiffness matrix [N/m]
k_{mech} : Belleville spring stiffness [N/m]
k_{piezo} : Piezoelectric element stiffness [N/m]
L : Bearing length [m]
l_o : Orifice length [m]
m : Mass [kg]
m_u : Unbalance mass [kg]
m_{pin} : Piezoactuator pin mass [kg]
M : Magnetization constant [A/m]

$\mathbf{M}$	:	Mass matrix [kg]
$\mathbf{n}_{\pm}$	:	Unitary vector normal to the surface
N_{stack}	:	Number of piezoelectric elements in the stack
p	:	Fluid film pressure [Pa]
p_{atm}	:	Atmospheric pressure [Pa]
P_{inj}	:	Injection pressure [Pa]
q	:	Heat flux [W]
$\mathbf{q}$	:	Generic coordinate vector for the rotor bearing FE model
$\dot{Q}$	:	Fluid volumetric flow [m^3/s]
R	:	Universal gas constant [J/mol·K]
R_a	:	Roughness [m]
R_b	:	Bearing sleeve nominal radius [m]
R_j	:	Journal nominal radius [m]
$\mathbf{S}_F$	:	Surface current density [A/m]
t	:	Time [s]
T	:	Temperature [K]
T_{inj}	:	Fluid injection temperature [K]
U	:	Journal peripheral linear velocity [m/s]
V_{inj}	:	Fluid injection velocity [m/s]
x	:	Fluid film bearing radial coordinate [m]
y	:	Fluid film bearing circumferential coordinate [m]
z	:	Fluid film bearing axial coordinate [m]
$\mathbf{z}$	:	State space vector
(r_m, α_m, z_m)	:	cylindrical coordinate system for the magnetic ring
(x_m, y_m, z_m)	:	cartesian coordinate system attached to the outer magnetic ring
(u_m, v_m, w_m)	:	cartesian coordinate system attached to the inner magnetic ring

Greek symbols

α	:	Coefficient of thermal expansion
Δt	:	Time step [s]
λ_k	:	Eignevalues
μ	:	Fluid viscosity [Pa·s]
μ_0	:	Vacuum permeability [T·m/A]
ν	:	Poisson's ratio
ρ	:	Fluid density [kg/m^3]
φ_k	:	Eignevectors

Φ	:	Attitude angle [rad]
Θ	:	Absolute circumferential coordinate [rad]
ω	:	Excitation frequency [rad/s]
Ω	:	Rotational speed [rad/s]

1

Introduction

1.1 Motivation

Using air as a lubricant

Hydrodynamic lubrication (HD), or fluid film lubrication, is one exceptional mechanical process where a thin layer of fluid is used to support a rotating shaft inside a bearing, with no mutual contact between solid surfaces. Osborne Reynolds (1842-1912) was the first to investigate this phenomenon. Among his observations he noted that when a shaft rotates it conveys a wedge of lubricant fluid between itself and a bearing. If the shaft was rotating sufficiently fast the fluid film would develop a pressure gradient strong enough to produce a carrying load which would keep the two bodies separated. This ability is due to the viscosity of the fluid, which generates shear stresses that directly contribute to generate these loads. Viscous forces are also cause of friction in the bearing, although these are usually several magnitude orders lower than its carrying capacity. As it appears, viscosity is one of the fundamental variables in HD lubrication. The higher its value, the stronger is the ability of carrying loads, but also more friction is generated. This produces heat, which in turn decreases the viscosity. Although this is beneficial for friction matters, too low viscosity may cause, under some operating conditions, the fluid film pressure not to be strong enough to carry the load from the shaft, which could come in contact with the bearing. The relative distance between the two surfaces in fact decreases with higher applied loads and lower rotational speeds, other than decreased fluid viscosity.

Aerodynamic lubrication (AD) represent a more recent development of HD theory. Despite sharing the common base principle, for which a carrying load is developed as a result of viscous shear stress generation, the main difference is that compressibility effects need to be taken into consideration. Due to the fact that the lubricants, typically air, have a much lower viscosity than oil, gas bearings are characterized by lower carrying capacity, higher rotational speed and lower film thickness. This decreased clearance implies the need for a superior degree of surface finishing, to minimize the risk of contact between surfaces. Utilizing air as the lubricant does however have several advantages. The most evident is surely the fact that air is abundant, cheap and clean. Already after the end of the Second World War the scientific community acknowledged the potential of this type of bearing for vast scale industrial purposes. Emphasis was given on different aspects of this technology, such as:

- friction forces are very limited, almost null, even at high rotational speed. As a consequence, heat generation is also very low;
- gas lubricants are generally very stable with respects to the temperature, they can't boil, freeze or become flammable;
- contrary to oil lubricants, air viscosity increases with increasing temperatures, thus overheating provides additional carrying capacity;
- operation is possible at rotational speeds that exceed the maximum admissible for rolling or even HD bearings;
- gas lubricants do not contaminate the surfaces they come in contact with, making them suitable for applications where a clean environment is required;
- contact free lubrication has low acoustic noise;

Research on AD bearings was especially driven by expectations of employment in the fast growing aeronautic field, which was seeking new bearing solutions that could cope with faster rotational speeds of new engine developments. The technology had nevertheless potential to attract other applications, such as the new born computer industry. Small scale, high speed and clean operation environment made gas lubricated bearings the perfect candidate for the use in magnetic memory devices, where they are still in use to date. High speed operation and minimal heat generation are also perfect characteristic for the use in machine tools, such as lathes, drills and milling machines.

Thermal effects in aerodynamic bearings

Among the main advantages relative to more traditional oil lubrication is the ability of gas lubricated bearings to operate at rotational speeds that far exceed the limits imposed by traditional lubrication. This is mainly due to the fact that the lubricant, typically air, is characterized by much lower values of viscosity, thus - for equivalent operational conditions - viscous friction forces are largely reduced. Because of such considerations, thermal effects in gas lubrication literature have historically not been addressed. This choice has generally been justified by the fact that gas lubrication happens in near-isothermal regimes, as the viscous heat generation is small compared to the dissipation capacity of the bearing itself (Czolczynski [16], Powell [72]). For most practical situations, the flow will be nearly isothermal because of the relatively high conductivity of the bearing material and the assumptions are reasonable for typical operational ranges. However, the drive to meet modern day ever-growing need of extremely high rotational speeds and/or heavy loading makes the inclusion of a thermohydrodynamic analysis of relevant importance.

Active lubrication: answering the need for performance

Current research on rotating machinery is driven by an ever-growing demand for higher performance and greater availability. On one hand, modern industrial needs, for example the API 617 specification, push the performance boundaries to faster speed, lighter components, more efficiency. Increasing availability, on the other hand, means enhancing the flexibility of the machine to adapt to different operation conditions and environments, eliminate or minimize service intervals, extend their useful life. Such extreme needs demand not only very accurate design, optimization and manufacturing, but also continuous monitoring and control of vibration levels.

Along with traditional oil lubrication, increasing demand for high speed application has renewed attention to gas bearings technology. Passive aerostatic and aerodynamic gas lubrication has been widely used in a variety of applications, ranging from high speed spindles to micro and meso-scale turbomachinery. Aerodynamic bearings offer excellent high speed, limited friction, clean environment and low heat generation characteristic, but also a limited load carrying capacity and poor dynamic performance, particularly prone to the onset of whirling and whipping motions. Aerostatic bearings have the advantage of offering excellent stiffness and start-up performance, however they suffer from inherent tendency to onset instability, known as pneumatic hammer. Hybrid configurations aim at combining the advantages of either technologies, however they also inherit their instability related drawbacks. Whirling is a subsynchronous rotor precession which draws energy from the rotation of the rotor; when the whirling frequency approaches one of the system natural frequencies, the whip phenomenon occurs, where the motion is excited yielding dangerously large vibrations. It can be observed in both aerodynamic and aerostatic bearings. Similarly, pneumatic hammer can be described as a nonsynchronous precession of the rotor, which mechanism is however unrelated to rotation, but rather to the pressurized air delivery system. It is characterized by a typical ”hammering” sound (hence the name) which can be present also at zero rotational speed.

Recent years have seen an increasing number of researchers to explore innovative and non traditional solutions to address such needs and the relative arising issues. Passive solutions, such as squeeze film [80], [70] and seal dampers [100] have been investigated as well as active ones. The use of ”active” mechatronic elements, combining transducers, actuators and control systems, can serve multiple purposes, from calibration and self-diagnostic tasks, to the reduction of vibration levels, minimizing the effect of system unbalances and smoothening the operation during those critical operational phases, such as the crossing of critical speeds or when starting-up and coasting-down.

Another contactless solution: magnetic bearings

Magnetic bearing are suspension devices which enable operation in contact-free conditions. This is the key characteristic of such devices, as no mechanical contact results in frictionless operation, which allows for extreme levels of performance and efficiency at rotational speeds that exceed the maximum admissible for rolling or even oil lubricated journal bearings. No lubrication is required: the absence of contamination of the surfaces makes them suitable for applications in clean environments; furthermore, they do not suffer from wear and have low acoustic noise. However, there are also some drawbacks; one of the most relevant comes from their physical nature: as Earnshaw demonstrated [24], it is impossible for an object to be suspended in stable equilibrium purely by means of magnetic or electrostatic forces.

Typically, magnetic bearing are grouped in two categories, depending on whether an electronic control system is used: active (AMB) or passive (PMB) magnetic bearings.

The working principle of an active magnetic bearing is relatively simple: a strong electromagnetic stator is used to generate attracting reluctant forces acting on a ferromagnetic rotor. The hardware setup is completed by power amplifiers, necessary to supply current to the electromagnets, and gap sensors to provide position feedback of the rotor. Moreover an electronic controller is needed. AMBs offer the great advantage of having adjustable bearing characteristics such as stiffness and damping, and dynamic control, however in order to compensate loads that are either large in amplitude and/or characterized by fast dynamics require powerful and complex electronics. Hence, they typically offer a modest force to weight ratio, require expensive components and a back-up system in case of controller or power failures. As a consequence they have been often relegated to high performance applications, such as compressors, gas turbines, motors, flywheels, gyroscopes, fans and machine tool spindles.

Permanent magnetic bearings are a completely passive solution, where magnetic forces produced by the interaction between permanent magnets is exploited. Compared to their active counterparts, passive magnetic bearings are on the other hand simple, relatively cheap and lightweight. Their disadvantages are however a lower load capacity and poor dynamic properties. Their main applications are high speed systems such as turbo-molecular pumps, energy storage flywheels, high-speed machine tool spindles, ultra-centrifuges and they are used in watt-hour meters and other systems in which a very low friction is required [41], [28].

Combining aerodynamic and magnetic effects

Despite sharing many characteristics, the combination of gas lubrication and magnetic bearing has not been very popular among researchers; Lee and Gweon [50] used magnetic force for preloading and controlling motions of a planar stage, while Ro et al. [77] describe a linear air-bearing that uses active magnetic bearings to compensate for its motion errors. The performance of an hybrid foil-magnetic bearing is investigated by Heshmat et al [39].

However, the aforementioned solutions all involve a magnetic bearing in its active form, whereas permanent magnet based solution remain unexplored.

1.2 State of the art

1.2.1 Literature review on gas journal bearings with thermal aspects

Studies on gas/air lubrication saw a fast development in the fifties, when analytical approximations of the load carrying capacity of full journal bearings were presented by Katto and Soda [44]. They assumed an infinitely long bearing and used the isothermal hypotheses, following earlier experimental observations and studies dating back to the beginning of the century.

These results were compared with experimental findings by Ford, Harris and Pantall [30]. The general trend of their data indicated an underestimation by the theoretical predictions. To check the validity of the isothermal assumption, they compared the variation of load carrying capacity using gases with different specific heat ratios. They attributed the discrepancies to side leakages and not thermal effects. Ausman treated the film thickness as a small deviation from a uniform clearance and found analytical solutions of the side leakage problem of both the journal bearing [4] and stepped sector thrust bearing [5]. Potential significance of the thermal wedge effect, was first noted in the work of Hughes and Osterle [38]. They reasoned that the operating characteristics of gas bearings should fall somewhere between the isothermal and adiabatic limits, depending on the conductivity of the bearing material and degree of thermal insulation. They suggested that at very high speed operation the thermal wedge effect may augment the load supporting pressure in addition to geometrical wedge effects. Whitley and Betts [104] conducted experiments on a long bearing, and yielded results deviating up to 24% from the Katto-Soda theory. While keeping faith with the isothermal conditions of the film, they found that side leakage losses only accounted for up to half the discrepancies, leaving the remainder unexplained. While refining the infinitely long bearing theory, Elrod and Burgdorfer [26] showed analytically that in non-extreme conditions the internal temperature rise of the film can be neglected. Thus, as numerical studies of gas bearings became popular, e.g. Castelli and Pirvics [13], the isothermal hypothesis has been largely accepted.

In incompressible lubrication the thermal issue acquired an ever-growing prominence, yielding the thermohydrodynamic (THD) branch of fluid film lubrication theory. With THD analysis one formally refers to the solution of the Reynolds equation in which the viscosity field is updated by coupling the solution of the energy conservation equation and the use of a suitable formula for temperature-dependence of viscosity. In 1966 Dowson and March [22] presented the first comprehensive paper considering compatible solutions of the Reynolds, energy and heat conduction equations for two-dimensional conditions, as well as taking into account experimental observations presented earlier (Dowson et al. [23]). This milestone work opened the field to a prolific literature, with the most significant contributions being included in the work of Pinkus [71].

The subject of thermal aspects in gas lubrication remained rather unexplored until much recent years, in the context of research on compliant foil bearings; Salehi and Heshmat [78] were the first to include an analytical thermal analysis of foil bearings. Their model was based on the "Couette approximation", as proposed by Pinkus [71] in which heat dissipation is calculated without allowance for pressure gradients. This method substantially simplifies the numerics as it uncouples the energy and Reynolds equations. Good agreement with experimental data was found. The same model was utilized a year later by Salehi et al [79]; who published a more comprehensive study for steady state operation as well as start-up and coast-down regimes. They concluded that for speeds up to 30,000 rpm and 1.5 kN loads, the Couette approximation provided a reasonable tool for predicting temperatures, with over-prediction estimated at 8-19% compared to the experimental values. Radil and Zeszotek [75] published an experimental study showing both load and rotational speed to cause heat generation in foil bearings, the latter being responsible for a more significant role. A comprehensive THD analysis of applied foil bearing was presented by Peng and Khonsari [69], that treats a simplified 3D energy equation. Sim and Kim studied compliant flexure pivot tilting pad bearings [94], treating the Reynolds and 3D energy equations simultaneously with boundary conditions found internally through global energy balance. The work also shows the effect of thermal and centrifugal expansions on the hollow rotor, and the influence of heating on the linear dynamic coefficients of the tilting pad bearing. They conclude that the dynamic performance of the bearing improves at high temperature, due to reduced clearance and increased viscosity. Lee and Kim [51] further developed the model for foil gas bearings analysis; the heat balance involves top foil, bump foils, cooling air channels and bearing sleeve, allowing for thermal expansion of top/bump foils and bearing sleeve.They observe that the maximum growth of the rotor is about 20 times that of the foil structure. Their analysis also examines the influence of cooling flow rates on the temperatures of the system, identifying the influential parameters. Kim and San Andrés [85], [46] presented a comprehensive thermal energy transport model, that includes convection and conduction through the bearing surfaces. They quantify the effectiveness of foil cooling flows on the bearing temperatures; showing experimental data in remarkable agreement with theoretical predictions.

1.2.2 Literature review on gas journal bearings with focus on active control

Recent years have seen increasing interest from the research community on mechatronic applied on rotating machinery problems. Several active elements have been proposed, many characterized by unique solutions and working principles. Smart fluids have been successfully used in conjunction with dampers, like electro-rheological and magneto-rheological squeeze film dampers [42], [108] and disk-type dampers [101], [108]. However, active bearings in different forms and configurations have been by far the most investigated subject. On one hand, active magnetic bearings [91] can be nowadays considered as an established technology, finding industrial applications in electric power generation, petroleum refining, machine tool operation and natural gas pipelines. On the other, active control of fluid film bearings represent a more novel branch of research. Nevertheless, several authors have turned their attention to active hydrodynamic problems, from connecting active controlled hydraulic chambers [98], to variable impedance journal bearings [34]; using piezo and piezo-hydraulic actuators [68], [96].

The first hydrodynamic journal bearing equipped with controllable radial oil injection was proposed almost two decades ago [86]. This kind of bearing operates by acting directly on the fluid film by radially injecting lubricant through orifices distributed on the bearing surface. Servo-valves are used to modify the injection pressures, which in turn makes it possible to significantly influence the hydrodynamic forces [88].

In order to improve their performance, a number of solutions have been proposed. Among other, much research has been devoted to compliant foil bearings [1] [18], [45]. As they offer some improvements compared to conventional rigid sleeve bearings, with improved static and dynamic properties, they are objective of current research supported by many manufacturers. However, issues associated with high costs and lack of reliable analytical designing tools have for now limited their diffusion. Another solution is represented by tilting pad gas bearings. Their main advantage concerns the dynamic properties, as they lack of cross-coupling stiffness and damping coefficients which generally results in improved rotordynamic stability [14]. However, pivot wear and especially manufacturing tolerance stack-up are their drawback. A design improvement proposed to overcome such issues is represented by flexure pivot gas journal bearings [81], [93], but the small bearing clearance in tilting pad gas bearings is still a technical challenge to overcome for their wide applications [94].

The first active gas journal bearing was introduced by Horikawa and Shimokohbe, [37]. In their prototype four pads provide a contact free support to a rotating shaft. These pads are connected to the bearing housing through elastic hinges, in which space piezoelectric actuators are also fitted. Thus, measurements of the radial position of the shaft are sent to a control system which acts by sending a control signal to the actuators, which effectively work by modifying the fluid film thickness profile.

Mizumoto et al. [60] propose an active inherent restrictor design which can be retrofitted in conventional aerostatic bearings. The system is comprised of a set of piezoelectric actuators with through holes coupled to capacitance displacement sensors. The control system simply takes the measured input and a control feedback signal is calculated using a PI algorithm, which produces beneficial effects on static stiffness and vibration levels.

Qiu et al. [74] describe a tilting pad gas journal bearing, where each pad is supported by a pivot with an embedded piezoelectric actuator, which is used to adjust the radial clearance between shaft and pad. Experimental work is carried out to perform active control of the self-excited vibrations of a rotor-bearing system, making use of a PID controller. It is shown that - provided that the controller gains are accurately tuned - subsynchronous vibrations can be effectively suppressed, however synchronous vibrations could not be addressed.

A hybrid flexure pivot gas bearing with controllable supply pressure is investigated by San Andres and Ryu [84]. Stemming from previous work on flexure pivot bearings, in which they demonstrate how external pressurization induces an increase in stiffness and decrease of damping coefficients, they develop a regulated supply pressure system with the aim of minimizing a rotor-bearing system response while passing its critical speeds. Their strategy is to employ electro-pneumatic air regulators combined with open and closed loop control rules in order to modify the supply pressure level in relation with the rotational speed of the machine. Theoretical and experimental coast down tests are in good agreement, and so in most situation the effectiveness of suppressing vibration levels.

Mizumoto et al. [61] propose a high speed aerodynamic bearing where the wedge angle on the aerodynamic bearing surface is controlled by piezoelectric actuators in order to generate aerodynamic damping force. Experimental findings show how the spindle vibrations at high rotational speed are suppressed.

1.2.3 Literature review on permanent magnetic bearings

Early research on permanent magnetic bearing (PMB) technology dates back the 1930s, when Holmes investigated the feasibility of developing such components for high speed centrifuges operation. Recent progress in magnetic materials science, particularly with the introduction of rare earth magnets, has made feasible their application for passive magnetic bearing purposes [62] [105]. The basic configuration of a PMB consists of two concentric magnetic rings (stator and rotor) separated by a cylindrical air gap or of two rings of same dimensions separated by a plane air gap. Depending on the magnetization direction of the rings, the bearing can be configured to work either for radial or axial applications, as shown by Delamare et al. [17]

and Lemarquand [52]. Nevertheless, regardless of the configuration adopted, repulsive magnetic forces are exploited. More complex configurations involve the use of more magnetic rings, which can be stacked in opposite magnetization directions in order to enhance their stiffness characteristic [106] [48]. The focal point of PMBs theoretical investigation is to deduce formulas which enable the evaluation of stiffness and force characteristics. To do so, it is first necessary to obtain evaluations of the intensity of the magnetic field produced by the permanent magnets. Early methods to obtain analytical calculations and experimental validation of permanent magnetic journal bearing was Backers [9]. Expressions for the evaluation of the magnetic field created by permanent magnetic rings are detailed in the work of Yonnet [105] and more recently relatively simple formulations are detailed among others in [7] and [52]. Analytical methods for the definition of force expressions have also been been developed, for example in the works of Baatz and Hyrenbach [8] and Lang [49].

Simple ring magnets bearing need a contact bearing to operate (typically a ball bearing), due to the axial instability dictated by the Earnshaw theorem. However, more advanced solutions call for the use of specially shaped conical magnets, in which case the bearing can offer both axial and radial support capability. This concept was originally developed by Gilbert [33] and employed in flywheel bearings for gyroscopic stabilization of satellites. These ideas further evolved for use in molecular vacuum pumps, X-ray tubes, flywheel for energy storage and other industrial applications [10] [31] .

1.3 Aim and focus of the project

The main scientific aim of the project is the mathematical modeling, design and experimental analysis of a flexible rotor bearing system supported by an active gas bearing. Additionally, the feasibility of combining the effect of a permanent magnetic bearing and aerodynamic bearing shall be investigated. Such problems can be subdivided in the following main subjects:

- Analysis and characterization of a hybrid aerostatic/aerodynamic gas journal bearing with controllable radial injection.
- Coupling with the modeling of a piezoelectric injector system.
- Development of an analytical model for the characterization of a permanent magnetic ring bearing to enhance the performance of an aerodynamic journal bearing.
- Design, experimental validation and testing.

1.3.1 Original contribution

The main original contributions of the thesis can be summarized as follows:

1. A coupled thermohydrodynamic solution for hybrid aerodynamic-aerostatic bearing is proposed. Findings suggest the thermal effect to be negligible for the problem under consideration.
2. A theoretical and experimental investigation of active lubrication applied to gas bearings through controllable air injection is performed. Significant improvements in bearing performance are obtained.
3. Development and design of a passive hybrid aerodynamic magnetic gas bearing. Despite promising numerical findings, issues with the experimental setup prevent a formal validation of the idea.

The above points are detailed in the following paragraphs.
Moreover, during the PhD project a number of publications have been produced. Their content is hereby briefly described; journal papers are included in appendix.

Articles published in peer reviewed Journals:

- **J1**: Paulsen, B T, Morosi, S, Santos, I F (2011), Static, Dynamic, and Thermal Properties of Compressible Fluid Film Journal Bearings. Tribology Transactions, vol: 54(2), p. 282-299.

  The present contribution presents a detailed mathematical modeling for non-isothermal lubrication of a compressible fluid film journal bearing, in order to identify when this type of analysis should be of concern. Load capacity, stiffness and damping coefficients are determined by the solution of the standard Reynolds equation coupled to the energy equation. Numerical investigations show how bearing geometry, rotational speed and load influence the bearing performance. Comparisons between isothermal and thermohydrodynamic models and discrepancies are quantified for three different types of bearing geometries.

- **J2**: Morosi, S, Santos, I F (2011), On the modeling of hybrid aerostatic-gas journal bearings.Proc. IMechE Vol. 225 Part J: Journal of Engineering Tribology.

  The present study presents a detailed mathematical model for hybrid lubrication of a compressible fluid-film journal bearing. Additional forces are generated by injecting pressurized air into the bearing gap through orifices located on the bearing walls. A modified form of the compressible Reynolds equation for active lubrication is derived. By solving this equation, stiffness and damping coefficients can be determined. A multibody dynamics model of a global system comprised of rotor and hybrid journal bearing is built in order to study the lateral dynamics of the system. Campbell diagrams and stability maps are presented, showing the main advantages and drawbacks of this special kind of hybrid fluid-film bearing.

- **J3**: Morosi, S, Santos, I F (2011), Active Lubrication Applied to Radial Gas Journal Bearings. Part 1: Modeling. Tribology International, in press (Available online 19 August 2011).
  The present contribution aims at demonstrate the feasibility of applying active lubrication to gas journal bearings. The principle of operation is to generate active forces by regulating radial injection of lubricant through the means of piezoelectric actuators mounted on the back of the bearing sleeves. A feedback law is used to couple the dynamic of a simplifed rotor-bearing system with the pneumatic and dynamic characteristics of a piezoelectric actuated valve system. Selected examples show the considerable performance advantages of such new kind of bearing.

Articles published in conference proceedings:

- **C1**: Morosi, S, Santos, I F (2009), Modeling of Hybrid Permanent Magnetic-Gas Bearings. Proceedings of COBEM 2009 - 20th International Congress of Mechanical Engineering, ABCM,. Gramado -RS, Brazil.

- **C2**: Morosi, S, Santos, I F (2010) Stability Analysis of Flexible Rotors Supported by Hybrid Permanent Magnet – Gas Bearings. Proceedings of PACAM XI - 11th Pan-American Congress of Applied Mechanics. Foz do Iguaçu, PR - Brazil.

- **C3**: Morosi, S, Santos, I F (2010) On the stability analysis of flexible rotors supported by Hybrid Aerostatic - Gas Journal Bearings. Proceedings of International Joint Tribology Conference. San Francisco, USA.

- **C4**: Morosi, S, Santos, I F (2010) On The Modeling Of Hybrid Aerostatic - Gas Journal Bearings. Proceedings of Nordic Tribology Conference, NordTrib 2010 Storforsen, Sweden.

- **C5**: Morosi, S, Santos, I F (2010) On The Modeling Of Hybrid Aerostatic - Gas Journal Bearings. Proceedings of Society of Tribologists and Lubrication Engineers. Annual meeting. Las Vegas, Nevada.

All above articles were written under the supervision of Dr. Ing, Dr. Tech Ilmar F. Santos.

Scope of present work with respect to the thermal problem

The purpose of this work is to scrutinize the theoretical foundation of gas lubrication and assessing when the isothermal hypothesis may not be valid and what parameters may call for attention under these circumstances. The full energy equation will be brought in to formulate a modeling approach of compressible fluid film lubrication. Heat balance will include allowance of net heat conduction across the bearing walls. Performance parameters - eccentricity and attitude angle for a given steady state load, and dynamic perturbation coefficients - will be examined for significant departure from isothermal predictions.

Firstly a detailed analytical modeling of compressible fluid film journal bearing considering non-isothermal conditions. The static (steady-state) and dynamic performance parameters are found from a linear perturbation analysis (Lund [57], [58] , Faria and San Andres [27], Kim and San Andres [45]), where numerical results for the zeroth and first order fields are computed by a finite difference method. The thermodynamic analysis is based on the solution of the energy equation coupled to the Reynolds equation (Dowson [22]), upon the introduction of certain simplifications that are compatible with the condition of nearly-parallel flows and with due consideration of the thermal transport properties of gases.

Since the isothermal hypothesis has been established to be valid for common application environments, computation of the incipience of non-isothermal effects necessarily calls for an extraordinary demand for high numerical precision, including the baseline case of the isothermal solution.

Scope of present work with respect to active lubrication

The present contribution lays the theoretical and numerical background for the modeling of a compressible fluid journal bearing with active radial injection, as well as providing experimental validation. In principle, the injection of air can be used to actively modify the pressure profile over the bearing, which in turn changes the thickness of the fluid film, thus creating an active force on the rotor that can be used to suppress vibrations of the rotor-bearing system.

A modified form of the compressible Reynolds equation for hybrid gas journal bearings is proposed, coupled with the dynamic model of a piezoelectric injection system. A proportional-differential feedback law is established in order minimize the vibration response of the system.

Scope of present work with respect to hybrid magnetic-gas bearings

In the present project a hybrid permanent magnetic-gas bearing is developed. This new kind of machine is intended to exploit the benefits of the two technologies while minimizing their drawbacks. Two simple passive ring magnet journal bearings are designed to be mounted in parallel with a gas journal bearing, with the aim of improving its static and dynamic characteristics. Essentially the magnetic force is intended to give to an aerodynamic bearing a contribution similar to that of aerostatic nature. However, such force can be oriented differently with respect to the rotational speed:

- the lack of carrying capacity at low speeds of the gas bearing is provided by the magnetic one;
- at higher speed, when the aerodynamic lift suffices to carry the load, the magnetic bearing can be used to improve the dynamic characteristics by offsetting the stator ring magnet.

Analytical expressions for calculating the magnetic flux density and forces are derived for the characterization of a magnetic bearing consisting of two concentric, axially magnetized rings. The procedure for obtaining such parameters is based on that presented by Baatz and Hyrenbach [8]. Moreover, the effect of ferromagnetic shielding is evaluated as proposed by Mayer and Vesley, [59], with the aim of enhancing the bearing stiffness and load carrying capacity.

1.4 Structure of the Thesis

The thesis is composed of 6 Chapters, the core of description, modeling, numerical and experimental results is presented. The focus is on the development of a self containing dissertation regarding the main original contribution of the thesis. In addition, appendices provide source of auxiliary information, included for completeness; **Chapter 2** Gives a presentation of the developed experimental test rig. Each main machine element and its functioning principle is described, as well as a review of the measurement instrumentation.

Chapter 3 The fluid film problem is presented. The chapter opens presenting analytical expressions for the calculation of static and dynamic properties of a compressible fluid film journal bearing under the assumption of small, harmonic perturbations. Analytical expressions for the solution of the pressure-temperature problem are developed, coupling the energy and Reynold's equation. Moreover, an approach to the active lubrication problem is discussed, and a mathematical model consisting of fluid film, piezoelectric injection system and feedback control law are coupled. Numerical validation and selected examples are provided.

Chapter 4 Analytical expressions are used for the characterization of a permanent magnetic bearing. The main result of this analysis is the calculation of the characteristic curve (radial force vs. displacement) of the permanent magnetic bearing. Numerical and experimental validations are presented, where static and dynamic characteristics of the magnetic-gas bearing are evaluated. Moreover, the feasibility of combining magnetic and aerodynamic effects is presented and numerically evaluated.

Chapter 5 In this chapter all the models developed and discussed in the previous part of the thesis are combined and applied in order to perform a characterization of a flexible rotor-bearing system. Analytical results are first presented and discussed, successively compared and validated with experimental findings.

Chapter 6 The thesis closes with this final Chapter, where conclusions and future aspects of the research are outlined.

2

Description of Rotor Hybrid-Bearing Test Rig

This chapter presents a description of the test rig designed and developed in order to study the performance of the active magnetic-gas journal bearing. A global overview of the setup is given, followed by a more detailed description of its main components: overhung rotor (flexible shaft and discs), prototype bearing components (permanent magnets and controllable aerostatic/aerodynamic setups), support bearing (high precision ball bearing) and drive train (compressor-turbine).

2.1 Overview

The rotor-bearing system is driven by an air turbine (1), derived from a diesel engine turbocharger. Pressurized air at 60 bar is provided by a reciprocating compressor - pressure tank system. Connection between turbine shaft and rotor shaft is provided by flexible couplings (2). The shaft (4) is supported on the driven end by a ball bearing (3) and on the non driven end by the active magnetic-gas journal bearing: two passive magnetic bearings (5) and the active hybrid aerostatic/aerodynamic gas journal bearings (6). Up to four piezo actuators (7) can be assembled on the gas bearing in order to control radial air injection into the sleeve. A flywheel (rigid disc) is overhung (8) at the non driven extremity of the shaft, and additionally two inductive proximity sensors are fixed to the holder around the disc (9). These sensors are used to measure the lateral displacement of the shaft during operation. The angular velocity of the shaft is measured by a three channel incremental encoder (10) mounted at the end of the shaft just before the flexible coupling.

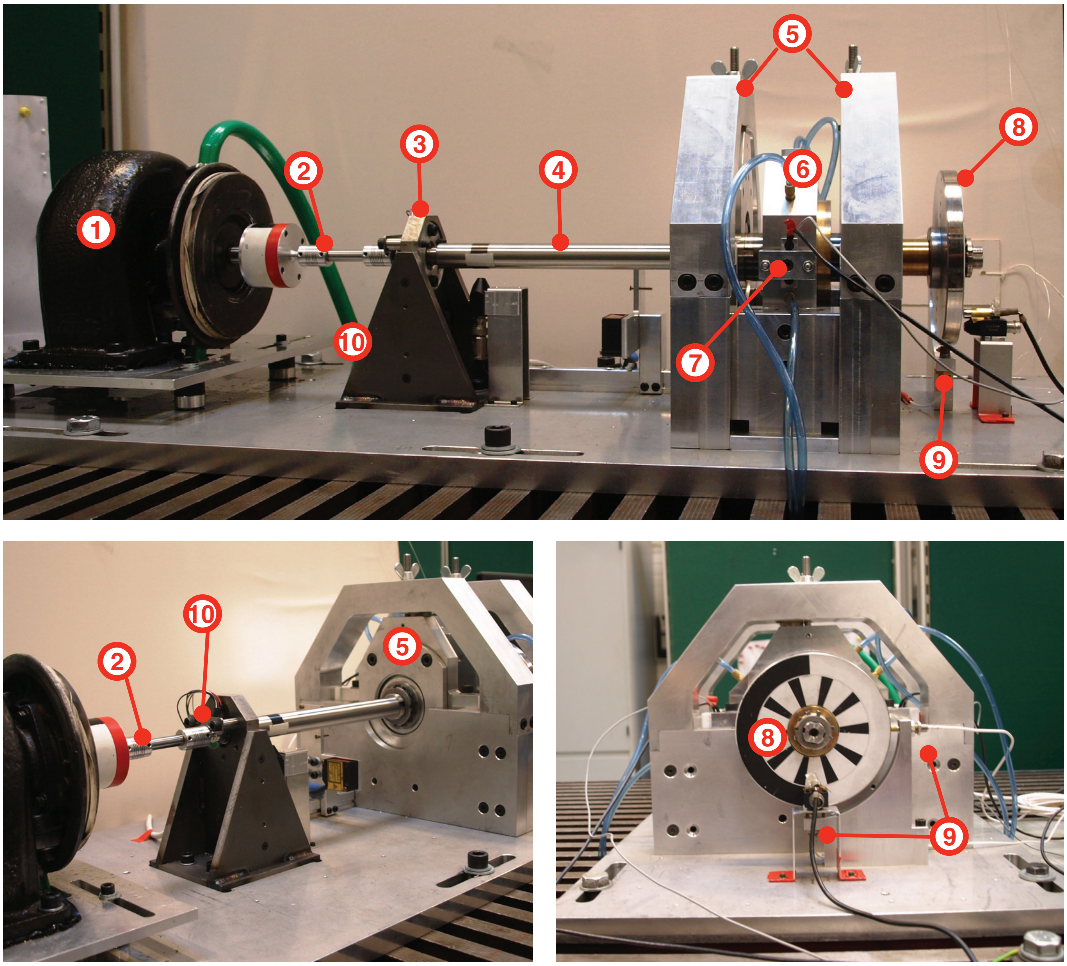

Figure 2.1: Test rig overview. 1 - Turbine, 2 - Flexible coupling, 3 - Ball bearing, 4 - Shaft, 5 - Magnetic bearings, 6 - Gas bearing, 7 - Piezo actuator, 8 - Disc, 9 - Proximity sensors, 10 - Rotary encoder.

2.2 Rotor shaft and discs

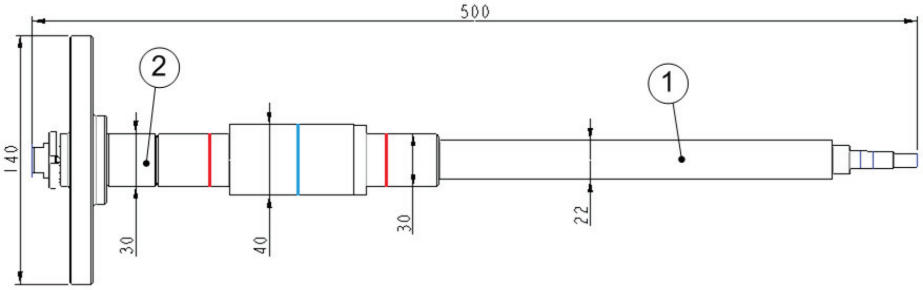

Figure 2.2: Shaft outline with principal dimensions.

An overview of the shaft is presented in Figure 2.2. In order to achieve some degree of flexibility, It is a quite slender, having a total length of 500 mm and base diameter of 22 mm. The diameter is increased at the bearing mounts location, to 30 mm for the magnetic bearings (red) and 40 mm for the gas bearing (blue). The shaft material is austenitic stainless steel type 314, however the gas bearing bushing is a shrink-fitted sleeve made of 34CrNiMo6 hardening steel, nitride treated in order to achieve a surface hardness of 800 HV. Such treatment is necessary in order to minimize damage to the component in case of contaminant entrapment during operation or touch-down events. The general circularity tolerance for the non-bearing parts (1) of the shaft is set to 1 μm. A bronze bushing (2) is fitted between the magnetic bearing on the non driven side and the disc to secure the magnetic bearing stator.

Shaft	
E	2.05e11Pa
m_{tot}	1.95 kg
l_{tot}	500 mm

Table 2.1: Summary of shaft properties.

The disc is made in carbon steel, with an outer diameter of 150 mm and total weight is 1.5 kg. Carbon steel is ferromagnetic (it is attracted by magnetic fields). This characteristic is important for this purpose, as it allows the use of inductive proximity sensors in its surface. Note, that the application of inductive sensors directly on the shaft surface is troublesome as austenitic stainless steel is paramagnetic (non-magnetic behavior). As high precision measurements are to be performed on its surface, one important design requirement is smoothness thus tight tolerances are prescribed for its circumference surface roughness.

Large disc	
m_{tot}	1.5 kg
d_{out}	150 mm
Roughness, R_a	0.39 μm

Table 2.2: Summary of disc properties.

2.3 Permanent magnetic bearing

Two passive magnetic bearings are assembled in parallel (with each other and with respect to the gas bearing). Simplicity and ease of manufacturing dictates the design of the bearings, each consisting of two concentrically mounted ring-shaped magnets with axial magnetization and radial air gap of 3mm. In Figure 2.3 a schematic overview of the general dimensions and layout of the ring magnet is shown. The magnets are made from an sintered alloy of neodymium, iron, and boron, also known as neodymium magnets, grade N48. This type of magnets offer excellent characteristics; besides having very high saturation magnetization (making them among the most powerful permanent magnets available on the market), these compounds also have high coercivity (resistance to be demagnetized). The main properties of the material are presented in Table 2.3. Sintered neodymium magnets are very brittle, thus particular care must be taken during the assembly phase and during operation. Both magnet rings are enclosed in an aluminum jacket. The choice for such jackets thickness and material are crucial parameters

N48	
Remanence, B_r	13.7 - 14.0 kG
Coercive Force, H_c	812-859 kA/m
Intrinsic Coercive Force, H_{ci}	875 kA/m
Max.Energy Product, BH_{max}	358-382 kJ/m^3
Curie Temp.	310°C
Max. Working Temp.	80°C

Table 2.3: Summary of magnets properties.

influencing the performance of the bearing. Thinness is desirable, as magnetic forces increase as the gap between the magnets is lowered; as for the material, it should be noted that a way of increasing the magnetic forces is to shield the sides and back of the magnetic rings with a soft ferromagnetic material with high permeability (typically, soft iron). This lowers the reluctance of the magnetic flux paths outside the bearing, while concentrating in the gap region. A different magnetic flux density field results in a redistribution of forces, however one should be careful as while in case of rings with radial magnetic polarization radial forces are increased - thus providing a beneficial effect - in case of axial polarization only unwanted axial forces are increased, whereas radial forces are greatly reduced. Radially magnetized magnetic rings were of course the first choice being considered for the project, however due to the difficult magnetization process for these geometries (requiring custom made tooling) the cost is extremely elevated.

Figure 2.4 shows how the magnetic bearing is assembled in the jackets, with the inner ring (1) and outer ring (2) pressed in the respective aluminum fittings, (3) and (4). These sub-assemblies are bolted to the magnetic bearing housing, see Figure 2.5. The housing is then placed into the frame, see Figure 2.6 (1), which allows the vertical displacement to be adjusted vertically by a butterfly nut (2). This feature makes it possible to change the bearing eccentricity, thus to adjust the verse of vertical resultant of the magnetic forces, which can be either pointing upwards or downwards.

Moreover application of neodymium magnet is limited by the temperature. Those magnets begin to lose magnetic properties and strength, when they are heated or when they are operating in environments above their maximum working temperature. The complete decline of magnetization occurs when they are heated above Curie temperature, and in this case magnets become paramagnetic. Note, that this phenomenon is reversible, when the temperature decreases below Curie temperatures - then magnetization properties return. For analysis of the theoretical model of the passive magnetic bearing, calculation of the magnetic flux density B and magnetic force Fm are crucial. In Chapter 4 a detail mathematical model of magnetic bearing is presented.

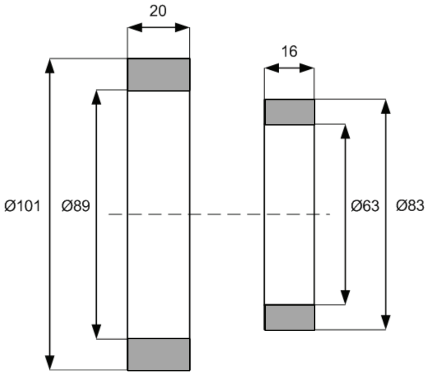

Figure 2.3: Permanent magnetic bearing outline and principal dimensions.

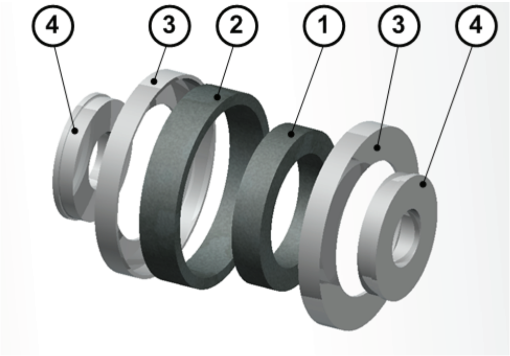

Figure 2.4: PMB components view. 1 - Inner ring, 2 - Outer ring, 3,4 - Aluminium casing.

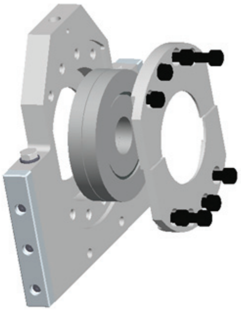

Figure 2.5: PMB assembly and housing.

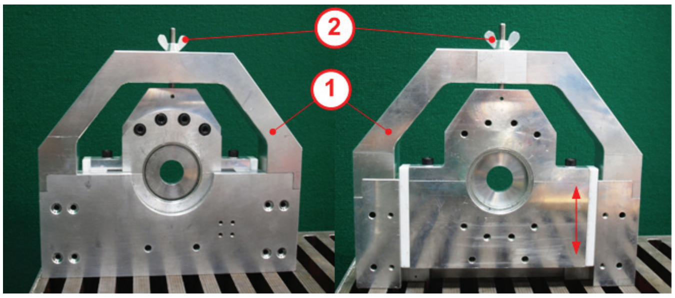

Figure 2.6: PMB in housing, front/back. 1 - stator top frame, 2 - vertical offset adjusting nut.

2.4 Active gas journal bearing

A cylindrical, hybrid aerostatic/aerodynamic gas journal bearing constitutes the system main support element. In Figure 2.7 the main components of the bearing are illustrated: sleeve, housing, adjustable mounts and a sub-plate. The sleeve is made of bronze alloy, the remaining parts of aluminum. The general bearing design is relatively simple, being a cylindrical rigid sleeve with nominal radial clearance between rotor and bearing is 25 μm. On its surface, four equally spaced orifices are drilled in order to provide external pressurization, with 2 mm diameter. Injection ducts are manufactured in order to channel air through the sleeve and housing, at the back of which piezoelectric actuated valves are placed. Note that for alignment purposes the bearing housing can be adjusted horizontally and vertically as the connecting mounts feature grooves for adjusting bolt connection.

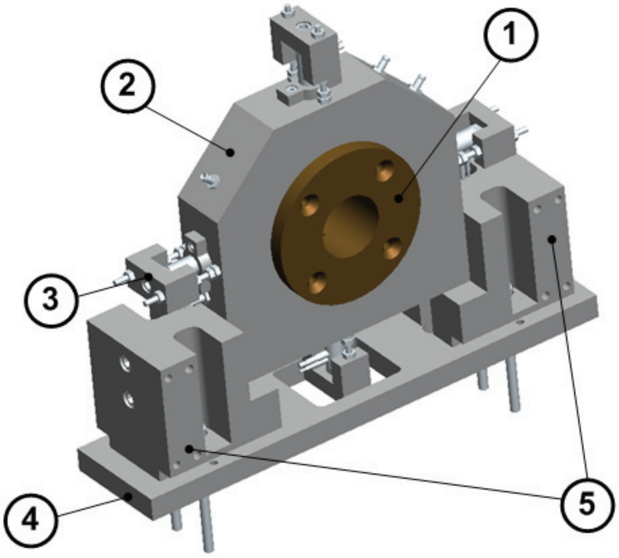

Figure 2.7: Isometric view of assembled gas journal bearing with four piezo actuators. 1 - Bronze sleeve, 2 - Aluminum housing, 3 - One of the piezo actuator, 4 - Sub-plate, 5 - Adjustable mounts.

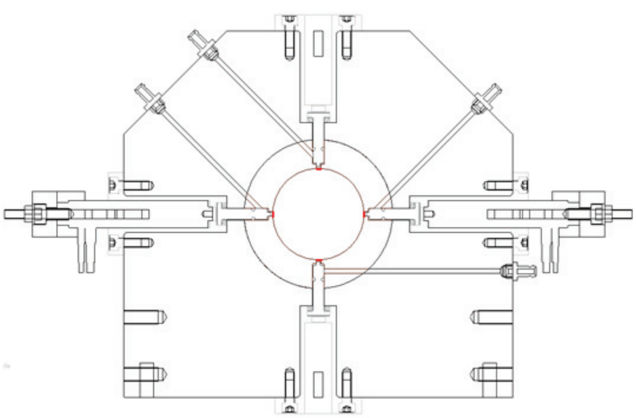

Figure 2.8: Gas journal bearing cross-section with hidden lines. The final assembly with two piezo actuators; red lines indicate location of the injection orifices.

2.4.1 Injection system

Figure 2.8 shows the assembly cross section of the bearing, providing an overview of the injection system in place. Pressurized air injection for each of the four orifices is provided by an independent injection subsystem, which schematic is presented in Figure 2.9. The pressurized air is supplied through 2 mm diameter channel (1). To close the valve, the piezo actuator mounted on the back of the assembly (2) pushes the pin (4) in the direction of the gas bearing center. Note that the piezo actuator is not capable of pulling the pin back to its initial (open) position, thus a Belleville springs assembly is placed (3) in order to provide the necessary restoring force. Additionally, O-ring seal (5) is used to ensure that the pressurized air discharges only trough the orifice and not via the upper assembly. On the lower surface of the pin, a rubber sealing (6-marked blue) is glued, in order to avoid air leakage to the gas bearing sleeve when the orifice is closed. The injection of the air is controlled by changing the distance between the rubber sealing and the bottom of chamber (7-marked red). The tip of the pin (8) goes into the injection orifice in order to minimize the surface discontinuity of the sleeve. This feature is added to provide a near-smooth surface on the bearing sleeve, in order to avoid fluid film discontinuities while operating in aerodynamic mode.

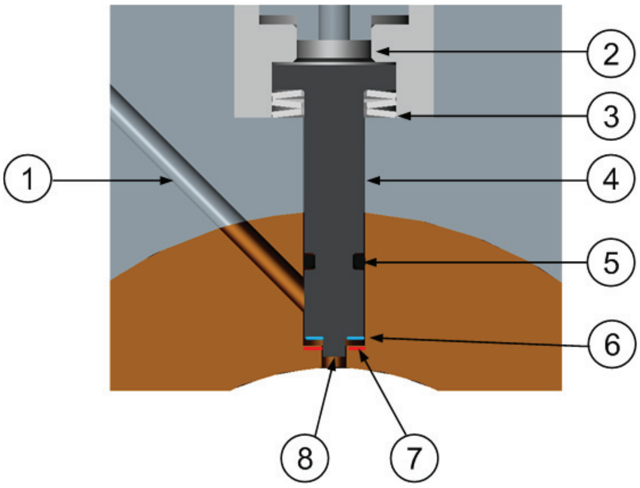

Figure 2.9: Injection subsystem. 1 - Supply channel, 2 - Piezo actuator, 3 - Belleville washers, 4 - Plastic pin, 5 - O-ring seal, 6 - Rubber sealing, 7 - Bottom of the injection chamber, 8 - Tip of the pin.

2.5 Ball bearing and coupling

On the driven end the shaft is supported by a spherical ball bearings, SKF type 1200ETN9. The bearing is assembled in a pressure plate, ensuring uniform axial load distribution on the bearings and a solid attachment to the housing. The housing is designed to have high rigidity in both lateral and axial direction, as this is the only location of the test rig where the axial load (mainly originating from magnetic forces) are supported. The assembly is presented in Figure 2.10.

2.6 Drive Train

The rotor bearing system is driven by an air turbine. The component is derived from a turbocharger, model Holset HX42F commonly used in medium size diesel engines. In order to reduce vibrations arising from the operation, the turbine is mounted on an aluminum plate which is isolated from the based plate of the test rig with the aid of rubber bushings, see Figure 2.12.

Operation of the turbine requires an external lubrication system for the oil lubricated bearing. During the experiments the lubrication is provided by an oil pump placed under the test rig

Figure 2.10: Ball bearing assembly.

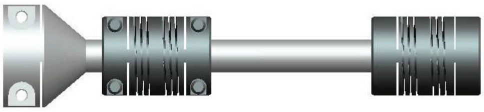

Figure 2.11: Flexible coupling arrangement.

table. As the oil pump does not include heating element, in order to heat up the oil to the operating temperature (60°C) it is recommended to run the oil pump for around one hour before the turbine can be launched. The turbine is driven by compressed air; a steady supply is provided by a 3 m^3, 64 bar pressure tank. The tank is fed by reciprocating compressor Burckhardt Basel C4N3F. Both units are located in the basement of DTU building 414. The high pressure line consists of of a 10mm (inside diameter) metal pipe that can withstand air pressures up to 200 bar. It is possible to manually regulate the rotational speed of the turbine thanks to a pressure reduction valve.

In the preliminary test, the turbine was tested without external load (rotor disconnected). The angular velocity was gradually increased up to 50,000rpm. The duration of such test was reasonably long in order to simulate a typical experimental time frame. However, it should be noticed that the operational time of the air turbine is limited by the pressurized air supply tank. Useful runtimes are on the order of 15-20 min.

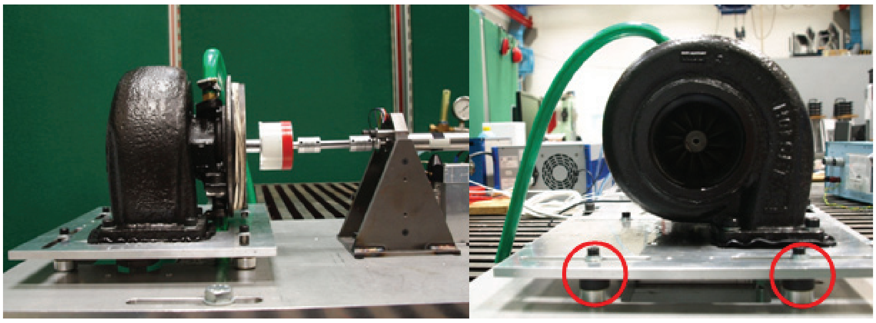

Figure 2.12: Turbine assembly. Note the the isolation rubber bushings (red circles).

2.7 Measuring Equipment

2.7.1 Displacements sensors

The most crucial aspect in measurements of operating rotor bearing system is accurate estimation of the rotor displacement. An inductive proximity sensor allows contactless measurement of the relative displacement of moving machine elements. Commonly, this type of sensors are used for measuring the relative vibration and axial position of rotating machine shafts, such as those found in steam, gas and hydraulic turbines, as well as in alternators, turbo-compressors and pumps.

Considerations about measured surface material

This type of sensors provide very accurate measurement and can be applied for measurements of ferromagnetic and non-ferromagnetic metals. However, the ferromagnetic targets absorb more energy compared to non-ferromagnetic materials. Hence, the operating range for the sensors is significantly wider in case of ferromagnetic targets. In the test rig under investigation the shaft was made of non-ferromagnetic stainless steel, and therefore application of inductive proximity sensors directly on the shaft surface is troublesome, as the gap between the shaft and the inductive proximity sensors should be less than 100 μm. In fact, although the nominal clearance of the gas bearing is 25 μm, flexibility of the shaft must be accounted for in order to ensure no touch-downs between shaft and sensors. As a conservative strategy, displacements of the rotor are measured at the disc location, as it is manufactured in common steel. In this case, the necessary gap between the discs and the sensors is much higher, up to 1 mm.

In the experiment, two types of sensors manufactured by Vibro-Meter are used. The horizontal displacement of a disc was measured by a TQ 401 Proximity Transducer (probe) with IQS451

Signal Conditioner, and the displacement in vertical direction by TQ 102 Proximity Transducer (probe) with IQS603 Signal Conditioner, see Figure 2.13.

Considerations about calibration of inductive sensors in the proximity of strong magnetic fields

The test rig under investigation is equipped with very powerful magnet rings, which are able to magnetize the discs (location of measurement). Thus, the calibration has to be done directly on the discs mounted to the shaft in order to take into account any influence of the magnetic field created by the magnetic rings.

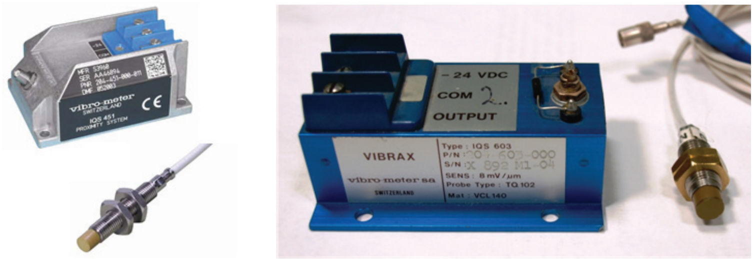

Figure 2.13: Inductive sensors.

2.7.2 Rotational speed and angular position measurements

For active control applications, a real-time reliable knowledge of system states is essential for correct implementation. The objective is to define a reference measure of the shaft surface and, for each time instant of the raw measure, subtract the corresponding part of the reference measure. This is accomplished by keeping track of the shaft rotational speed and angular position. The solution adopted for precise monitoring of the shaft position and angular velocity is a 3-channel incremental encoder, see Figure 2.14. This type of incremental encoder consists of an encoded wheel with 500 cpr (counts per revolution) and an optical sensor. With such dense triggering, a very accurate monitoring of the shaft position is ensured, as the sensor can track the rotor position every 0.72°.

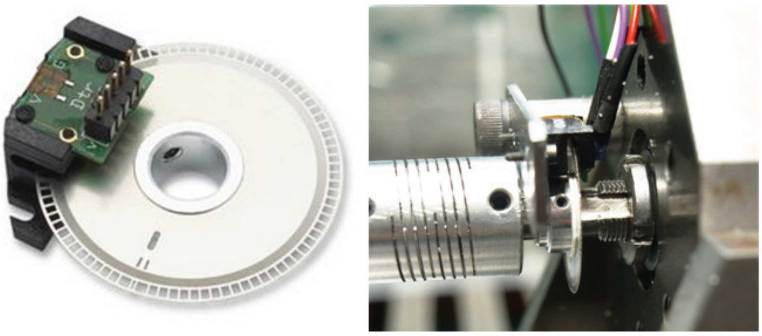

Figure 2.14: Rotary encoder.

2.8 Piezoelectric air injection system

A general description of the injection system principle of operation is described in details in section 2.4. A total of four injectors can be mounted on the bearing. For the present project only two units were available, mounted in the horizontal direction orifice, as seen in Figure 2.9 and 2.15. The orifices in the vertical direction are locked in fully open position. The moving parts of the injection subsystem are shown in Figure 2.16, where piezo actuator with mount, fitting and pin with Belleville springs can be identified. The core of the injection system is the piezo actuator; two Physik Instrumente P-841.3B units are used. Technical specification are summarized in table 2.4.

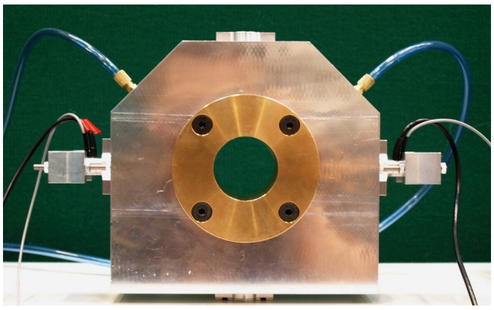

Figure 2.15: Gas bearing with assembled piezo actuators.

Figure 2.16: Elements of the injection system, from left to right: Piezo actuator with mount, fitting between housing and piezo actuator, pin with O-ring seal and Belleville spring.

Open/close loop travel @ 0-100 V	45 μm
Static large signal stiffness	19 N/μm ± 20%
Pushing Force	up to 1000 N
Pulling Force	50 N
Unloaded resonant freq.	10 kHz ± 10%
Length	68 mm

Table 2.4: Main properties of piezo actuator of type P-841.3B.

Due to tight assembly tolerances due to the minimum travel of the actuators, the assembly of the injection system itself is a crucial stage for obtaining the best possible performance. Sealing of the injection chamber, tightening of the adjustable injector mounts, and Belleville spring configuration all play a decisive role with respect to regulating the amount of air flow to the bearing.

Preliminary tests conducted without the rotor installed revealed that the elastomeric sealing glued on the tip of the pin is too "soft" for ensuring effective opening/closing operation. When pushing the pin towards the bearing (closing the valve) the presence of rubber efficiently blocks the flow from entering the bearing. It should be noted that the sealing effect is largely due to the rubber being compressed by the piezoelectric forces. However, despite careful attempts of calibration, it is very difficult to ensure a complete opening of the valve while pulling the pin. That is because the effective travel of the piezo actuator is reduced from the nominal 45 μm by the fraction lost in the compression of the seal. It was finally decided to eliminate the rubber sealing. This choice has significant implications for the operation of the injection system, as in such configuration it is not possible to prevent a leakage flow when the valve is closed. It means that if the pressurized air flow is connected effectively the bearing always operates in hybrid mode, while the relative contribution of such aerostatic pressure can be addressed by regulating the flow. If aerodynamic operation needs to be investigated, the pressurized supply line needs to be closed.

Other parameters that influence air flow into the bearing - both for the active and passive orifices - concerns the tightening of the assembly and Belleville springs arrangement. The mount of the piezo actuators are adjustable in the axial direction, and can be regulated by screwing nuts, see 2.17. Each of the piezo actuators needs to be assembled and tested individually, in order to achieve the best compromise between the large air flow when the orifice in open and as small flow as possible when the piezo actuator has the maximum displacement. The main

issue during this set up phase is to ensure the same air flow rate for all four orifices when they are fully opened. In order to measure the flow rate in the orifices a specially fitted flow meter was used in order to ensure near equal flow rate with tolerance of ±10%. The final setup and dimensions of Belleville washers are presented in Figure 2.18. The vertical orifices consist of stacks of four identical washers, with thicknesses of 0.5mm, set up opposite to each other.
It needs to be emphasized that the adjustment of the piezo actuators is a time-consuming activity and the procedure needs to be repeated whenever the injection systems assembly is altered or dismounted.

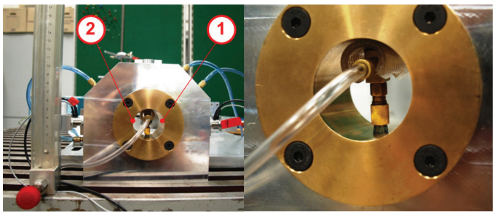

Figure 2.17: Measurement of the flow in the bottom orifice. 1-Right orifice, 2-Left orifice.

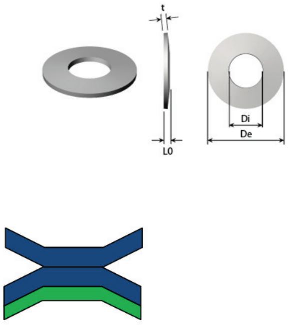

Figure 2.18: Belleville washers: dimensions and setup for vertical orifices.

Considerations on the piezo actuators dynamics

The frequency bandwidth of the piezoelectric injector system is limited due to the considerations concerning the charging/discharging of the piezo stack and the dynamics of the mechanical subsystem, as discussed in section 3.4.1. Moreover, the electronics of the piezoelectric actuators charge amplifier can have a significant impact on the actuators response. It is then fundamental to perform an initial assessment of the actuator/control system dynamics in order to determine the frequency ranges suitable for proper operation. Generally speaking, for control purposes the frequency bandwidths of the actuators must be larger than the highest frequency of the system intended to be controlled. If such conditions are not satisfied, the actuator dynamics will significantly limit the performance of the controlled system and may even induce instability. In this context, it should be remarked that the objective of the control system under investigation is to

address synchronous and eventual whirl instabilities of the rotor bearing system. Experimental facility limitations define an operational upper ceiling of 15,000 rpm (250 Hz).
The operating limits of a piezo amplifier depend on the amplifier power, the amplifier design, and of course, the piezo's electrical capacitance. Two sets (of two) charge amplifiers were available; a high power amplifier E-617 (open loop only) and a high resolution piezo servo controller and driver E-621 (open/closed loop).

Considerations on piezo actuators open/closed loop operation

The piezo actuators in use, P-841.3B, are equipped with integrated high-resolution strain gauge position sensors, providing high precision for closed-loop operation. In closed loop operation the amplifiers use the position feedback signal for controlling the voltage output send to the piezo actuators. Position servo control eliminates nonlinear behavior of piezoceramics such as hysteresis and creep and is the key to highly repeatable motion. Moreover, position controlled systems show a high linearity, stability, and accuracy; they can also compensate for varying load and forces, a feature that is relevant for the dynamic aerodynamic loads.
Open-loop piezo actuators can exhibit large degree of hysteresis in their dielectric and electromagnetic large-signal behavior. Hysteresis is based on crystalline polarization effects and molecular effects within the piezoelectric material. The amount of hysteresis increases with increasing voltage (field strength) applied to the actuator, see Figure 2.19.

Preliminary tests evaluating the piezo actuators/amplifiers performance was conducted in closed-loop mode. Note that closed loop operation is possible with the E-617 amplifier only by using the feedback position sensor signal drawn from the E-621 module (it means that both units must be online). A random voltage signal varying from 0 to 10V. The feedback position signal and input signal were stored in order to obtain Frequency Response Function of the piezo actuators. Results are shown in Figure 2.20. From the experimental FRFs results, it can be immediately noticed that the attenuation produced by the E-621 amplifier is very high for the range in consideration (250 Hz, as above), dropping to 10% of the amplitude and phase-shifting 180° at 200 Hz. On the other hand, the advantages of the high power unit E-617 are evident, maintaining an overall linear behavior within the working range.

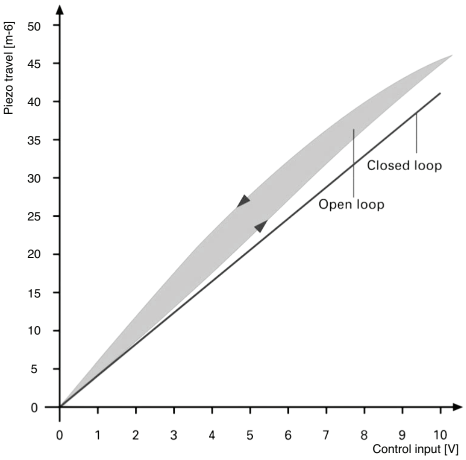

Figure 2.19: Open loop vs closed loop performance of P.841.3B actuator.

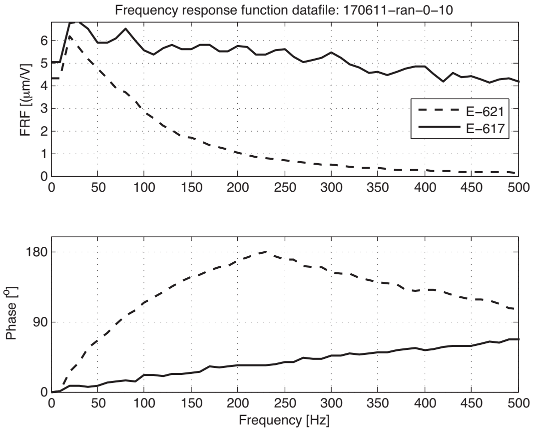

Figure 2.20: Frequency Response Function of P.841.3B actuator driven by different amplifiers.

2.8.1 Data acquisition and signal processing

For data acquisition and piezo actuator control a dSPACE DS1104 R&D Controller Board with CP1104 Connector Panel was utilized. This system is a powerful tool for rapid control prototyping and along with Real Time Interface, it allows to use Matlab/Simulink blocks for graphical I/O configuration. In practice, acquisition and control software runs directly on the Controller Board microprocessor, however it can be developed in Matlab/Simulink environment, and then loaded on the board after having been compiled in C++. For management and control of an experiment, ControlDesk software is used. This software allows to modify experimental parameters in real-time and monitoring current status of the control system and data acquisition via virtual instrumentation. The CP1104 Connector Panel serves as an interface between the DS1104 Board and all external hardware. It has connectors for eight Analog- to-Digital inputs (ADCH), eight Digital-to-Analog (DACH) outputs, and six other Sub-D Connectors including two for incremental encoders. During the experiment, the measurement and control instrumentation was connected to CP1104 Connector Panel, as follows:

- Two inductive proximity sensors are connected to: ADCH1 (vertical) and ADCH2 (horizontal) channels.
- Two piezo actuators are connected to: ADCH6 and ADCH8 channels (control of displacement); DACH1 and DACH2 channels (position feedback).

- Incremental encoder is connected to: Inc1 connector.

The operating range for all Analog-to-Digital and Digital-to-Analog connectors is from -10 to +10V.

Considerations on filtering

Analog passband filters have been also used for conditioning the displacement sensor signals; the high-pass cutting frequency has been set to 1 Hz; mainly this is to eliminate the DC level. The low-pass cut-off is set to 250 Hz (corresponding to a rotational speed of 15,000 rpm).

The use of a low-pass filter serves two purposes: on the one hand, it is important to have low-noise signals when these are meant to be fed-back, especially if the actuators have high frequency response dynamics. This is especially true if such signals are also differentiated (as in the present case, in order to obtain the velocity feedback signal) and subsequently amplified (as high frequency noise is also amplified). On the other hand, low-pass filtering is common practice in order to minimize aliasing phenomena. Aliasing is an important problem to consider both when recording data and doing FFT, because discrete sampling is involved in both. When sampling data, aliasing occurs if the continuous signal measured by the analogue sensor has an considerable energy content at frequencies higher than half the sampling-rate (the Nyquist frequency). Too low sampling rates will cause the high frequency content to be mistaken for low frequency content. In the frequency domain this can be thought of as higher frequency content spilling over into the low-frequency domain.

It should be noticed that in engineering control the influence of a filter must not be neglected when designing the feedback gains, because it may influence the gain- and phase-margin of the system. An ideal low-pass filter completely eliminates all frequencies above the cutoff frequency while passing those below unchanged; in mathematical terms, it can be defined as the convolution of signal and its impulse response. Real filters for real-time applications approximate the ideal filter by truncating and windowing the infinite impulse response to make a finite impulse response. The operations produces an unwanted delay, which is manifested as a phase shift between original and filtered signals. In general, the lower the cutoff frequency, the higher the delay. Applying a filter is then a compromise between having a reasonably smooth signal, which calls for the lowest possible cutoff frequency, and the shortest possible delay, which calls for the highest.

2.8.1.1 Encoder implementation

The dSPACE system is equipped with dedicated incremental encoder channels which run at an internal variable clock (depending on the rotating frequency), which can offer sampling up to 1.65MHz. The output from the encoder-channel can then be fitted by interpolation to the sampling frequency of the program. This is very useful for keeping track of the rotor position which has the tangible effect that the measurement program can work faster and thereby more precise, especially when compared to traditional ways to keep track of the rotational speed such as photoelectric probes or induction type triggering; in these cases for obtaining accurate real-time measurements it is necessary to use global extremely high sampling frequencies (that in a rotating machine are proportional to its angular velocity), which essentially pose a controller hardware limit on the speed at which it can be applied.

2.8.1.2 Real time surface noise compensation

In section 2.7.1 the inductive proximity displacement sensors were introduced. They provide high precision measurements and are therefore sensitive to the rotating surface irregularities. Such irregularities can easily be compensated in post processing, however for control purposes it is necessary to eliminate them in real-time, otherwise their component is embedded in the displacement signals and consequently fed back to the the controller, adding to the spill over effect.

The objective is then to define a reference measure of the shaft surface and, for each time instant of the raw measure, subtract the corresponding part of the reference measure. This is accomplished by keeping track of the shaft angular position.

Surface noise can be thought as mainly due to ovality or even surface roughness of the rotor. These parameters can be described as the raw sensor measurement $\tilde{y}(t,\phi)$ as:

$$\tilde{y}(t,\phi) = y(t) + DC + O(\phi) \tag{2.1}$$

where $y(t)$ is the shaft displacement, DC is the sensor DC-level, and $O(\phi)$ is surface-noise. The measure of interest is $y(t)$, but depending on the operational conditions, $O(\phi)$ can be comparable or even larger than $y(t)$, dominating the response.

If the angular positions is known, then a reference can be made. The reference contains both the DC-level and the noise level. To obtain a good reproduction of the DC-level and the noise level a mean value is found for a certain number of points per revolution.

$$\widehat{DC}(\phi) = DC + \hat{O}(\phi) \tag{2.2}$$

Where $\hat{O}(\phi)$ is the mean surface noise and $\widehat{DC}(\phi) = DC_{mean}$.

The compensated signal can then be found by subtracting DC_{mean} from the raw-data:

$$y(t) = \tilde{y}(t, \phi) - \widehat{DC}(\phi) \tag{2.3}$$

Practically, a reference is made by rotating the rotor at a low constant speed. By doing so, only the surface-noise and the DC-level is obtained. Note that if the angular velocity is too high, then the reference measurement will be containing also a component of the dynamic response of the rotor bearing system. For capturing the reference data the angular velocity was set to 80rpm and sampling frequency to 10kHz. In Figure 2.21a an example of raw measurement is shown. To compensate sensor noise each data point has been defined as the average of 500 periods, which will smoothen the reference measure, see Figure 2.21b. Here, the top plot presents the same raw measurement as a function of the rotor position, the DC_{mean} is indicated by the red-line. The error between the raw-measurement and the DC_{mean} is shown in the lower part of Figure 2.21b. As the error is showed in [μm], it is possible to notice that it is reduced to the minimum resolution of the instruments, which for the inductive proximity sensors used is of ± 1 μm.

2.8.2 Experimental Setup

The way the various components interact with each other within the experimental setup can be visually summarized in Figure 2.22. The nodal point of the experiment is the dSpace controller board; for passive operation, its purpose is to collect analog signals of displacement and rotational velocity from the sensors mounted on the test rig and convert them in digital form; the dSpace board has a direct interface with the computer which is responsible of performing online real-time surface noise compensation, measurement display and offline post processing. In active operation, the computer is also responsible of performing the necessary calculation in order to build a control signal, which is sent back to the controller board to be digital-to-analog converted. This signal is then sent to the piezo actuators, before being amplified by the piezo actuators charge amplifiers, closing the feedback loop.

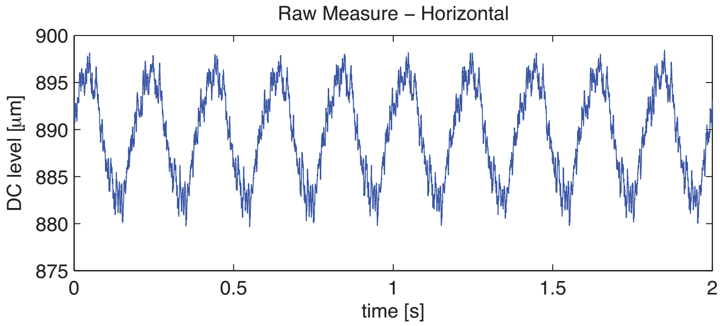

(a) Raw data.

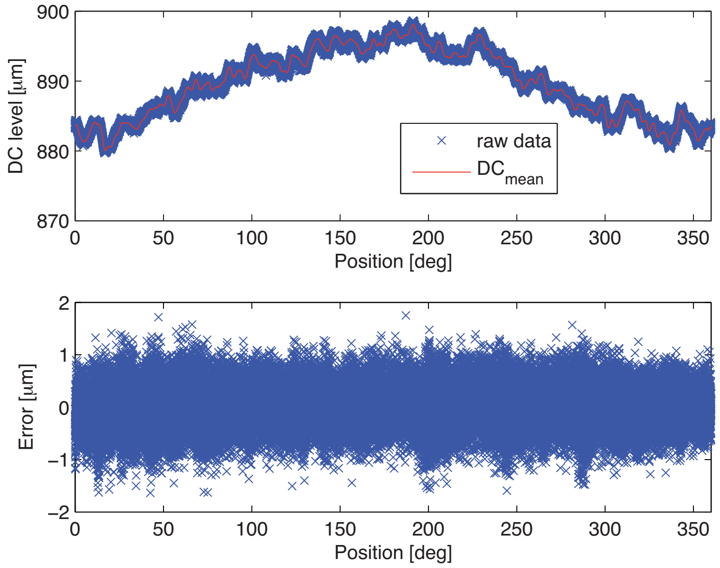

(b) Reference.

Figure 2.21: Examples of raw data and reference compensation and absolute error.

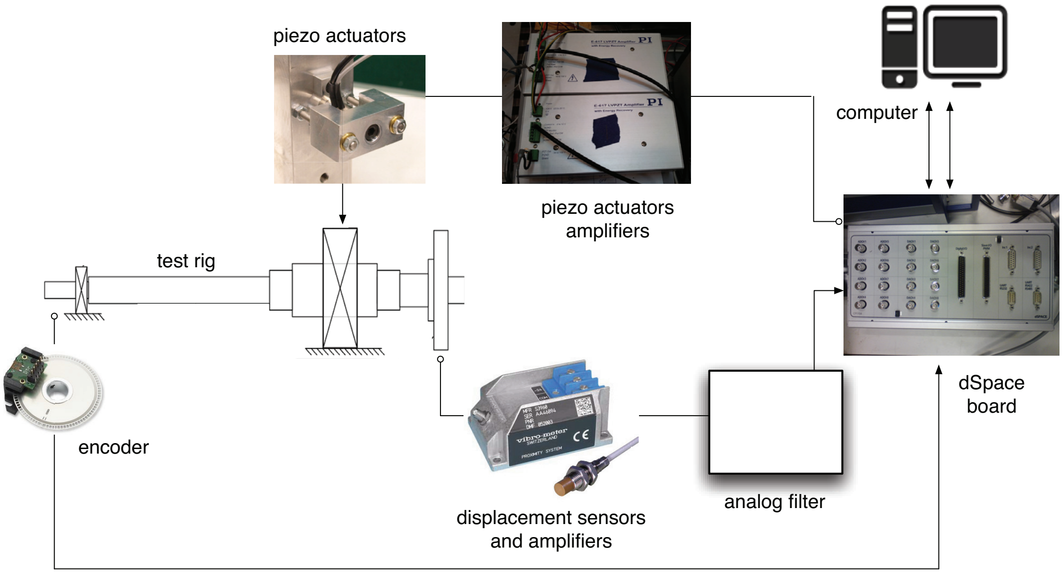

Figure 2.22: Schematic layout of the experimental setup.

3

Active Hybrid Journal Bearing

This chapter provides the mathematical and physical background to the fluid film problem. It is organized as follows:

- Discussion of mathematical foundation of the Reynold's equation.
- Application on radial gas journal bearings and introduction of perturbation equations for the simple case: aerodynamic lubrication.
- Introduction in the Reynold's equation of a simplified model for external radial injections.
- Including thermal effects: coupling the pressure-temperature problem.
- Mathematical modeling of the piezoelectric air injection system linked to the pressure problem.
- Review of the numerical methods used to solve the fluid problem.
- Validation with published results and discussion of selected numerical examples aim at modeling the prototype bearing.

3.1 Plain cylindrical aerodynamic journal bearing

Upon the introduction of customary lubrication assumptions for laminar, Newtonian, inertia-less, thin-film flows, in the Navier-Stokes equations, the Reynold's equation for compressible lubricants is written as:

$$\frac{\partial}{\partial y}\left(\rho\frac{h^3}{\mu}\frac{\partial p}{\partial y}\right)+\frac{\partial}{\partial z}\left(\rho\frac{h^3}{\mu}\frac{\partial p}{\partial z}\right)=6v_j\frac{\partial \rho h}{\partial y}+12\frac{\partial(\rho h)}{\partial t} \tag{3.1}$$

Note, for a comprehensive derivation of the Reynold's equation from the general Navier-Stokes is given in Appendix A.
In this general form it is not possible to solve the Reynold's equation for the pressure as - without introducing any assumptions - the viscosity and density fields are also unknown functions.

Viscosity can be considered as function of pressure and temperature. In gases this parameter is marginally affected by variations of pressure: for temperature ranges of 300-500 K the isothermal viscosity variation is approximately in the range of 10-25% per 10 Mpa pressure increase [43]. As for the temperature relationship, while liquids get "runnier" as they get hotter, gases get "thicker" [66]. As explained in Elert [25], the viscosity of gases increases as temperature increases and is approximately proportional to the square root of temperature. This is due to the increase in the frequency of intermolecular collisions at higher temperatures. Since most of the time the molecules in a gas are flying freely through the void, anything that increases the number of times one molecule is in contact with another will decrease the ability of the molecules as a whole to engage in the coordinated movement. The more these molecules collide with one another, the more disorganized their motion becomes.

The density of dry air can be calculated using the ideal gas law, expressed as a function of temperature and pressure. Note that the equation of state given here formally applies only to an ideal gas, or as an approximation to a real gas that behaves sufficiently like an ideal gas. The ideal gas law states that:

$$\rho = \frac{p\tilde{M}}{RT} \tag{3.2}$$

where $\tilde{M}$ is the molar mass of the gas, R is the universal gas constant and T the gas temperature. In this first approximation, one can make use of the customary literature assumption that gas bearings work in near-isothermal conditions, as frictional heat generation is generally considered to be low. Thus all terms except for the pressure term p in eq. (3.2) are constant and since the viscosity loses its variable dependency, eq. (A.57) can be written in its standard form:

$$\frac{\partial}{\partial y}\left(ph^3\frac{\partial p}{\partial y}\right) + \frac{\partial}{\partial z}\left(ph^3\frac{\partial p}{\partial z}\right) = 6\mu v_j\frac{\partial(ph)}{\partial y} + 12\mu\frac{\partial(ph)}{\partial t} \tag{3.3}$$

which is a nonlinear parabolic equation for the pressure.

Film thickness. The location of the minimum film thickness is defined by the attitude angle Φ, see Fig. 3.1.

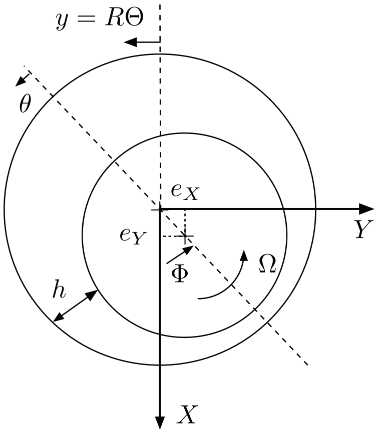

Figure 3.1: Journal bearing schematic.

An absolute circumferential coordinate is therefore defined taking into account the attitude angle as:

$$y = \Theta R, \quad \Theta = \theta + \Phi \tag{3.4}$$

The journal center is displaced a distance e from the bearing center. Such journal eccentricity cannot exceed the bearing clearance, to avoid solid contact between the surfaces. Its components in the inertial coordinate system are:

$$e_X = e\cos\Phi, \quad e_Y = e\sin\Phi \tag{3.5}$$

The film thickness function $h = h(y,t)$ depends on the position of the center of the shaft according to:

$$h = C + e_X\cos\Theta + e_Y\sin\Theta \tag{3.6}$$

where $C = R_b - R_j$ is the nominal radial clearance of the bearing.

In high speed applications, centrifugal shaft growth may give a significant contribution, especially considering the relative small radial clearance of gas bearings. The centrifugal growth of the solid shaft is obtained by assuming cylindrical plane stress model and given by:

$$s_{cg} = \frac{\rho_s R^3 \omega^2}{4E}(1-\nu) \tag{3.7}$$

where ρ_s is the shaft density, E is Young's modulus, and ν is Poisson's ratio of the shaft. In this case, the shaft nominal clearance must be corrected as:

$$C = R_b - (R_j + s_{cg}) \tag{3.8}$$

Perturbation equations. Seeking to investigate the dynamic performance of the bearing, a harmonic perturbation method is employed. This linearized approach is a common method, introduced by Lund [57] and widely accepted, upon the understanding of the limitations imposed by the underlying assumptions. The general motion of the rotor at frequency (ω) with small amplitude harmonic motion ($\Delta e_X, \Delta e_Y$) around an equilibrium position (e_{X_0}, e_{Y_0}) is:

$$e_X = e_{X_0} + \Delta e_X e^{i\omega t} \qquad e_Y = e_{Y_0} + \Delta e_Y e^{i\omega t} \tag{3.9}$$

leading to the following perturbation expression for the film thickness function and pressure field:

$$h = C + e_{X_0}\cos\Theta + e_{Y_0}\sin\Theta + (\Delta e_X \cos\Theta + \Delta e_Y \sin\Theta)\, e^{i\omega t} \tag{3.10}$$

$$p = p_0 + (\Delta e_X p_X + \Delta e_Y p_Y)\, e^{i\omega t} \tag{3.11}$$

Separating steady state (zeroth order) and perturbed (first order) terms:

$$h = h_0 + \Delta h e^{i\omega t} \tag{3.12}$$

$$p = p_0 + \Delta p e^{i\omega t} \tag{3.13}$$

Equation (3.12) and (3.13) can be inserted into (3.3), yielding (neglecting higher order terms) the zeroth and first order lubrication equations:

- Zeroth order

$$\frac{\partial}{\partial y}\left(p_0 h_0^3 \frac{\partial p_0}{\partial y}\right) + \frac{\partial}{\partial z}\left(p_0 h_0^3 \frac{\partial p_0}{\partial z}\right) = 6\mu U \frac{\partial (p_0 h_0)}{\partial y} \tag{3.14}$$

- First order

$$\begin{gathered} X : \frac{\partial}{\partial y}\left(p_0 h_0^3 \frac{\partial p_X}{\partial y} + p_X h_0^3 \frac{\partial p_0}{\partial y}\right) + \frac{\partial}{\partial z}\left(p_0 h_0^3 \frac{\partial p_X}{\partial z} + p_X h_0^3 \frac{\partial p_0}{\partial z}\right) + 6\mu U \frac{\partial}{\partial y}(p_X h_0) + 12\mu i\omega (h_0 p_X) \\ 0 \\ = -\frac{\partial}{\partial y}\left(3 p_0 h_0^2 \frac{\partial p_0}{\partial y}\cos\Theta\right) - \frac{\partial}{\partial z}\left(3 p_0 h_0^2 \frac{\partial p_0}{\partial z}\cos\Theta\right) + 6\mu U \frac{\partial}{\partial y}(p_0 \cos\Theta) + 12\mu i\omega (p_0 \cos\Theta) \end{gathered} \tag{3.15}$$

$$\begin{aligned}Y:\ &\frac{\partial}{\partial y}\left(p_0h_0^3\frac{\partial p_Y}{\partial y}+p_Yh_0^3\frac{\partial p_0}{\partial y}\right)+\frac{\partial}{\partial z}\left(p_0h_0^3\frac{\partial p_Y}{\partial z}+p_Yh_0^3\frac{\partial p_0}{\partial z}\right)+6\mu U\frac{\partial}{\partial y}(p_Yh_0)+12\mu i\omega(h_0p_Y)\\ &\qquad\qquad\qquad\qquad\qquad\qquad 0\\ &=-\frac{\partial}{\partial y}\left(3p_0h_0^2\frac{\partial p_0}{\partial y}\sin\Theta\right)-\frac{\partial}{\partial z}\left(3p_0h_0^2\frac{\partial p_0}{\partial z}\sin\Theta\right)+6\mu U\frac{\partial}{\partial y}(p_0\sin\Theta)+12\mu i\omega(p_0\sin\Theta)\end{aligned} \tag{3.16}$$

The pressure distribution in the bearing is continuous in the circumferential coordinate and equal to the atmospheric value at the bearing sides. The boundary conditions for the steady state, eq. (3.14), and perturbation equations (3.15) and (3.16) are defined by:

$$p_0:\begin{cases}p_0(y,0)=p_0(y,L)=p_{atm}\\ p_0(0,z)=p_0(2\pi R,z)\\ \dfrac{\partial p_0(0,z)}{\partial y}=\dfrac{\partial p_0(2\pi R,z)}{\partial y}\end{cases}\qquad p_{X,Y}:\begin{cases}p_{X,Y}(y,0)=p_{X,Y}(y,L)=0\\ p_{X,Y}(0,z)=p_{X,Y}(2\pi R,z)\\ \dfrac{\partial p_{X,Y}(0,z)}{\partial y}=\dfrac{\partial p_{X,Y}(2\pi R,z)}{\partial y}\end{cases} \tag{3.17}$$

Zeroth order equation. For given operation conditions $U=\Omega R_j$ and excentricity, the nonlinear PDE (3.14) is solved using a finite difference approximation on a discretized domain of dimension $m\times n$ in the y and z coordinate respectively. Details of the numerical method are give in section 3.5.

The zeroth order pressure field is integrated over the bearing surface, which in turn imposes vertical and horizontal lubrication reaction forces:

$$\begin{aligned}F_X&=\int_0^L\int_0^{2\pi}(p_0-p_{atm})\cos\Theta Rd\Theta dz\\ F_Y&=\int_0^L\int_0^{2\pi}(p_0-p_{atm})\sin\Theta Rd\Theta dz\end{aligned} \tag{3.18}$$

First order equations. The solution of the first order perturbation Eq. (3.15) and (3.16) for the perturbed pressures (p_X,p_Y) is straightforward, as these are linear PDEs. Given a zeroth order field p_0 they are solved via a finite difference scheme and subsequently integrated over the bearing surface to determine the stiffness and damping coefficients:

$$K+i\omega D=\int_0^L\int_0^{2\pi}\begin{bmatrix}p_X\cos\Theta & p_X\sin\Theta\\ p_Y\cos\Theta & p_Y\sin\Theta\end{bmatrix}Rd\Theta dz \tag{3.19}$$

It is important to notice that the dynamic coefficients are dependent on the excitation frequency and that the model assumes small amplitude of perturbations.

3.2 Hybrid Aerostatic - Gas Journal Bearings

In order to take into account the fluid dynamic contribution of radial external air injection, a modified form of the standard Reynold's equation is proposed.

A hybrid form of the Reynolds equation can be derived upon introducing a simple modification to the standard reduction of the Navier-Stokes equations, as shown also in [88]. Note that this formulation has an advantage over the classical method of including aerostatic contributions [35], as mass conservation is implicitly respected without the need of iterating for mass flow balancing. There are, however, some limiting assumptions. Most prominently, it is assumed that the radial injection flow is laminar and fully developed; moreover the injection ducts are also considered to be short.
The derivation of a hybrid modified from of the Reynold's equation is as follows. Assuming an isoviscous, Newtonian, compressible fluid in a laminar regime, one can write the Navier-Stokes equations as (for details see in eqs. (A.34) - (A.36)):

$$\begin{aligned}
\frac{\partial}{\partial x}\left(\mu\frac{\partial u}{\partial x}\right) &= 0\\
\frac{\partial}{\partial x}\left(\mu\frac{\partial v}{\partial x}\right) &= \frac{\partial p}{\partial y}\\
\frac{\partial}{\partial x}\left(\mu\frac{\partial w}{\partial x}\right) &= \frac{\partial p}{\partial z}
\end{aligned} \tag{3.20}$$

Where x is the across-film coordinate, y the circumferential, z the axial, as presented in Figure 3.2. Note that the pressure is assumed to be constant across the film, and it solely considered the variation of tangential stresses upon the normal to the surface. However, in order to take into account the external radial flow from the orifices, the following boundary conditions are imposed:

$$\begin{aligned}
&u_b(0,y,z) = V_{inj} \quad && u_j(h,y,z) = V\\
&v_b(0,y,z) = 0 && v_j(h,y,z) = U = \Omega R\\
&w_b(0,y,z) = 0 && w_j(h,y,z) = 0
\end{aligned} \tag{3.21}$$

Note that compared to the regular form of the Reynold's equation, only the radial boundary conditions have been modified. Formally, $u_j(h,y,z) = V$ is the radial velocity of the journal, $V = \partial h/\partial t$, whereas $u_b(0,y,z) = V_{inj}$ is the velocity profile of the injection flow.

Integrating twice eq. (3.20) upon applying the boundary conditions above, one obtains:

$$
\begin{aligned}
u &= \frac{x}{h}V + \left(\frac{h-x}{h}\right)V_{inj} \\
v &= -x\left(\frac{h-x}{2\mu}\right)\frac{\partial p}{\partial y} + \frac{x}{h}U \\
w &= -x\left(\frac{h-x}{2\mu}\right)\frac{\partial p}{\partial z}
\end{aligned}
\tag{3.22}
$$

External radial injection. Regarding the external air injection, a velocity profile is defined in the domain comprised between the supply chamber and the bearing. A schematic view can be seen in Figure 3.3. A simplified analytical expression is easily obtained by simplifying the N-S equations, expressed in cylindrical coordinates [63]:

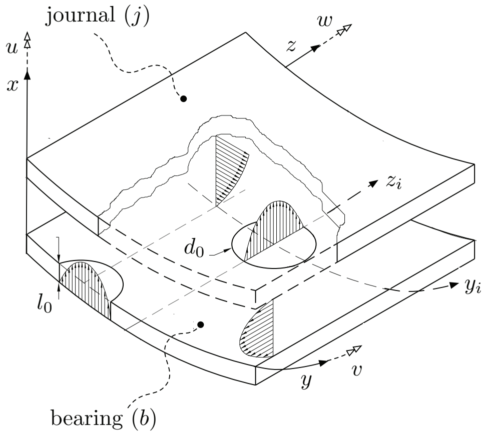

Figure 3.2: Coordinate system schematic.

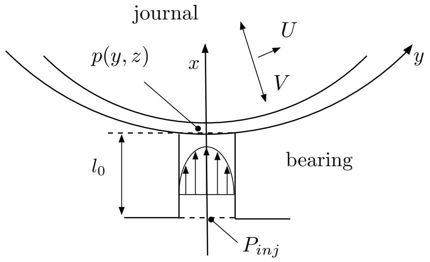

Figure 3.3: Model of the injection flow.

$$
V_{inj}(y,z,t) = -\frac{1}{4\mu}\left(\frac{\partial p}{\partial x}\right)\left[\frac{d_o^2}{4} - (y-y_i)^2 - (z-z_i)^2\right] \tag{3.23}
$$

Equation (3.23) is known as Hagen-Poeiseuille formula and despite formally it applies to incompressible fluids, if one considers only an infinitesimal length dx of the feeding pipe, the change of density of the fluid within this distance can be neglected. This assumption allows a further simplification, by assuming the variation of injection pressure along the duct length (l_0, along the $-x$ direction) to be linear and proportional to the difference between supply and journal pressures:

$$
\frac{\partial p}{\partial x} = \frac{P_{inj} - p(y,z,t)}{l_0} \tag{3.24}
$$

The injection velocity is zero outside the orifice region. Note that if length of the injection feeding ducts is appreciable, the flow density changes as the pressure changes, so that although the mass flow rate is constant, the volumetric flow is not and the compressibility effect ought to be taken in consideration. Moreover, it should be noted that such formulation is in general valid for steady conditions; however, in case of high injection frequencies, the rapid opening and closing of the orifice might render necessary the inclusion of fluid inertia effects. It is worth to highlight that a in depth analysis of the limitations of the presently developed theory are ongoing; Solutions of the problem based on full 3D Navier-Stokes equations are being investigated within a collaboration project with Dr. Braun and Horvat at the University of Akron, with the aim of precisely define the application limit of the simplified theory.

Modified Reynolds equation. Introducing the velocity profiles of Eq. (3.22), upon the inclusion of Eq. (3.23), into the general form of the continuity equation:

$$\int_0^h \left[\frac{\partial \rho}{\partial t} + \frac{\partial}{\partial x}(\rho u) + \frac{\partial}{\partial y}(\rho v) + \frac{\partial}{\partial z}(\rho w)\right] dx = 0 \tag{3.25}$$

After the integration of eq. (3.25) the velocity profiles become coupled, meaning that the lubrication film is continuous.

In the case of a compressible lubricant obeying the ideal gas law, the pressure distribution p in near-isothermal conditions is governed by the modified general form of the Reynolds equation:

$$\frac{\partial}{\partial y}\left(ph^3\frac{\partial p}{\partial y}\right) + \frac{\partial}{\partial z}\left(ph^3\frac{\partial p}{\partial z}\right) = 6\mu U\frac{\partial (ph)}{\partial y} + 12\mu\frac{\partial (ph)}{\partial t} + 12pV_{inj} \tag{3.26}$$

Note that the extra term $12pV_{inj}$ is only to be included in orifice areas, whereas it is zero elsewhere. Substituting the expression presented in Eq. (3.23) and introducing an auxiliary function $\mathcal{F}_i$ which describes the velocity profile while taking into account the position of the orifices:

$$V_{inj}(y,z,t) = -\frac{1}{4\mu l_0}(P_{inj}-p)\cdot\mathcal{F}_i(y,z) \tag{3.27}$$

$$\mathcal{F}_i(y,z) = \begin{cases} \dfrac{d_0^2}{4} - (y-y_i)^2 - (z-z_i)^2, \quad (y-y_i)^2 - (z-z_i)^2 \leqslant \dfrac{d_0^2}{4} \\ 0, (y-y_i)^2 - (z-z_i)^2 \geqslant \dfrac{d_0^2}{4} \end{cases} \tag{3.28}$$

Note that the form function $\mathcal{F}_i$ is used to describe the parabolic velocity profile in the orifice region, whereas is zero elsewhere. Equation 3.26 can be then rewritten as:

$$\frac{\partial}{\partial y}\left(ph^3\frac{\partial p}{\partial y}\right) + \frac{\partial}{\partial z}\left(ph^3\frac{\partial p}{\partial z}\right) - \frac{3}{l_0}\sum_{i=1}^{s}\mathcal{F}_i p^2 = 6\mu U\frac{\partial (ph)}{\partial y} + 12\mu\frac{\partial (ph)}{\partial t} - \frac{3}{l_0}\sum_{i=1}^{s}\mathcal{F}_i P_{inj} p \tag{3.29}$$

For a cylindrical, rigid sleeve bearing, the boundary conditions for eq. (3.29) impose that the pressure at the bearing sides equals the atmospheric pressure p_{atm} and the pressure is continuous and periodic in the circumferential direction.

Perturbation equations. Expressions for the static and dynamic pressure equations are derived by the perturbation method, as introduced earlier. Equations (3.10) and (3.11) can be inserted into eq. (3.29), yielding (neglecting higher order terms) the zeroth and first order lubrication equations:

- Zeroth order

$$\frac{\partial}{\partial y}\left(p_0 h_0^3 \frac{\partial p_0}{\partial y}\right) + \frac{\partial}{\partial z}\left(p_0 h_0^3 \frac{\partial p_0}{\partial z}\right) - \frac{3}{l_0}\sum_{i=1}^{s} \mathcal{F}_i p_0^2 = 6\mu U \frac{\partial (p_0 h_0)}{\partial y} - \frac{3}{l_0}\sum_{i=1}^{s} \mathcal{F}_i p_0 P_{inj} \tag{3.30}$$

- First order

$$\begin{aligned}
X :\ & \frac{\partial}{\partial y}\left(p_0 h_0^3 \frac{\partial p_X}{\partial y} + p_X h_0^3 \frac{\partial p_0}{\partial y}\right) + \frac{\partial}{\partial z}\left(p_0 h_0^3 \frac{\partial p_X}{\partial z} + p_X h_0^3 \frac{\partial p_0}{\partial z}\right) - 6\mu U \frac{\partial}{\partial y}(p_X h_0) \\
& - 12\mu i\omega (h_0 p_X) - \frac{3}{l_0}\sum_{i=1}^{s} 2\mathcal{F}_i p_0 p_X = \\
& - \frac{\partial}{\partial y}\left(3 p_0 h_0^2 \frac{\partial p_0}{\partial y}\cos\Theta\right) - \frac{\partial}{\partial z}\left(3 p_0 h_0^2 \frac{\partial p_0}{\partial z}\cos\Theta\right) + 6\mu U \frac{\partial}{\partial y}(p_0 \cos\Theta) \\
& + 12\mu i\omega (p_0\cos\Theta) - \frac{3}{l_0}\sum_{i=1}^{s} \mathcal{F}_i p_X P_{inj}
\end{aligned} \tag{3.31}$$

$$\begin{aligned}
Y :\ & \frac{\partial}{\partial y}\left(p_0 h_0^3 \frac{\partial p_Y}{\partial y} + p_Y h_0^3 \frac{\partial p_0}{\partial y}\right) + \frac{\partial}{\partial z}\left(p_0 h_0^3 \frac{\partial p_Y}{\partial z} + p_Y h_0^3 \frac{\partial p_0}{\partial z}\right) - 6\mu U \frac{\partial}{\partial y}(p_Y h_0) \\
& - 12\mu i\omega (h_0 p_Y) - \frac{3}{l_0}\sum_{i=1}^{s} 2\mathcal{F}_i p_0 p_Y = \\
& - \frac{\partial}{\partial y}\left(3 p_0 h_0^2 \frac{\partial p_0}{\partial y}\sin\Theta\right) - \frac{\partial}{\partial z}\left(3 p_0 h_0^2 \frac{\partial p_0}{\partial z}\sin\Theta\right) + 6\mu U \frac{\partial}{\partial y}(p_0 \sin\Theta) \\
& + 12\mu i\omega (p_0\sin\Theta) - \frac{3}{l_0}\sum_{i=1}^{s} \mathcal{F}_i p_Y P_{inj}
\end{aligned} \tag{3.32}$$

Boundary conditions for eqs. (3.30), (3.31) and (3.31) are given in eq. (3.17).

3.3 Thermal effects

If thermal effect ought to be included in the model, the Reynold's equation assumes the following form.

Introducing the ideal gas law, eq. 3.2 into the general form of the Reynold's equation and simplifying the constant terms yields:

$$\frac{\partial}{\partial y}\left(\frac{p}{\mu T}h^3\frac{\partial p}{\partial y}\right)+\frac{\partial}{\partial z}\left(\frac{p}{\mu T}h^3\frac{\partial p}{\partial z}\right)=6U\frac{\partial}{\partial y}\left(\frac{p}{T}h\right)+12\frac{\partial}{\partial t}\left(\frac{p}{T}h\right) \tag{3.33}$$

which is a non-linear parabolic equation in p for compressible, non-isothermal lubrication regime. If hybrid radial lubrication is included:

$$\frac{\partial}{\partial y}\left(\frac{p}{\mu T}h^3\frac{\partial p}{\partial y}\right)+\frac{\partial}{\partial z}\left(\frac{p}{\mu T}h^3\frac{\partial p}{\partial z}\right)-\frac{3}{\mu l_0}\sum_{i=1}^{s}\mathcal{F}_i\frac{p^2}{T}=6U\frac{\partial}{\partial y}\left(\frac{p}{T}h\right)+12\frac{\partial}{\partial t}\left(\frac{p}{T}h\right)-\frac{3}{\mu l_0}\sum_{i=1}^{s}\mathcal{F}_i\frac{P_{inj}p}{T} \tag{3.34}$$

Recalling that the ideal gas law (3.2) establishes a relation between density and the other state variables as:

$$\rho=\frac{p\tilde{M}}{\tilde{R}T} \tag{3.35}$$

in the above statement is an assumption of the temperature, hence the viscosity, being independent of x. This conclusion owes to the fact that one of the assumptions of the Reynold's equation as formulated is to neglect the pressure gradient in the radial direction.

A simplified model for accounting thermal deformations introduced by the thermal effect assumes that thermal growth of the shaft and bearing sleeve are linear and given by:

$$s_{tg}=\alpha_s R\left(T_s-T_A\right) \tag{3.36}$$

$$Bs_{tg}=\alpha_{Bs} R\left(T_{Bs}-T_A\right) \tag{3.37}$$

where α is the material linear coefficient of thermal expansion and the subscripts s and Bs refers to the shaft and bearing sleeve respectively. Note that, similarly to the work of [51] this model assumes that both shaft and bearing sleeve are free to expand in the radial direction.

The shaft nominal clearance then updated as:

$$C=R_b-\left(R_j+s_{cg}\right)-\left(s_{tg}-Bs_{tg}\right) \tag{3.38}$$

Perturbation equations The perturbation equations for the pressure lubrication equation in non-isothermal regime become:

- Zeroth order

$$\frac{\partial}{\partial y}\left(\frac{p_0}{\mu T}h_0^3\frac{\partial p_0}{\partial y}\right)+\frac{\partial}{\partial z}\left(\frac{p_0}{\mu T}h_0^3\frac{\partial p_0}{\partial z}\right)=6U\frac{\partial}{\partial y}\left(\frac{p_0}{T}h_0\right) \tag{3.39}$$

- First order

$$\begin{aligned}X:\ &\frac{\partial}{\partial y}\left(\frac{p_0}{\mu T}h_0^3\frac{\partial p_X}{\partial y}+\frac{p_X}{\mu T}h_0^3\frac{\partial p_0}{\partial y}\right)+\frac{\partial}{\partial z}\left(\frac{p_0}{\mu T}h_0^3\frac{\partial p_X}{\partial z}+\frac{p_X}{\mu T}h_0^3\frac{\partial p_0}{\partial z}\right)-6U\frac{\partial}{\partial y}\left(\frac{p_X}{T}h_0\right)\\ &-12i\omega\left(h_0\frac{p_X}{T}\right)=-\frac{\partial}{\partial y}\left(3\frac{p_0}{\mu T}h_0^2\frac{\partial p_0}{\partial y}\cos\Theta\right)-\frac{\partial}{\partial z}\left(3\frac{p_0}{\mu T}h_0^2\frac{\partial p_0}{\partial z}\cos\Theta\right)\\ &+6U\frac{\partial}{\partial y}\left(\frac{p_0}{T}\cos\Theta\right)+12i\omega\left(\frac{p_0}{T}\cos\Theta\right)\end{aligned} \tag{3.40}$$

$$\begin{aligned}Y:\ &\frac{\partial}{\partial y}\left(\frac{p_0}{\mu T}h_0^3\frac{\partial p_Y}{\partial y}+\frac{p_Y}{\mu T}h_0^3\frac{\partial p_0}{\partial y}\right)+\frac{\partial}{\partial z}\left(\frac{p_0}{\mu T}h_0^3\frac{\partial p_Y}{\partial z}+\frac{p_Y}{\mu T}h_0^3\frac{\partial p_0}{\partial z}\right)-6U\frac{\partial}{\partial y}\left(\frac{p_Y}{T}h_0\right)\\ &-12i\omega\left(h_0\frac{p_Y}{T}\right)=-\frac{\partial}{\partial y}\left(3\frac{p_0}{\mu T}h_0^2\frac{\partial p_0}{\partial y}\sin\Theta\right)-\frac{\partial}{\partial z}\left(3\frac{p_0}{\mu T}h_0^2\frac{\partial p_0}{\partial z}\sin\Theta\right)\\ &+6U\frac{\partial}{\partial y}\left(\frac{p_0}{T}\sin\Theta\right)+12i\omega\left(\frac{p_0}{T}\sin\Theta\right)\end{aligned} \tag{3.41}$$

Notice that there is no allowance for perturbation dependency of μ and T in the first order equations. The pressure distribution in the bearing is continuous in the circumferential coordinate and equal to the atmospheric value at the bearing sides. The boundary conditions for the steady state, eq. (3.39), and perturbation equations (3.40) and (3.41) are equivalent as defined in eq. (3.17).

It should be noticed that in gas thermohydrodynamic problems, the Reynold's equation is linked to the temperature field directly, as the term T appears explicitly in the equation due to the ideal gas law substitution, and indirectly through the viscosity field, which is assumed to be function of the temperature. The viscosity-temperature relationship of air is given by:

$$\mu = a\left(T - T_{ref}\right) \tag{3.42}$$

where $a = 4e-8$ and $T_{ref} = -458.75$ when T is in C.

The above considerations make the approach different from that of incompressible lubricants, where the only relationship between pressure and temperature is given by the viscosity field.

3.3.1 The energy equation

In order to determine the thermal behavior of the fluid, it is necessary to introduce a relationship that links the fluid dynamic problem with the effect of heat transfer, the energy equation. By involving both the effect of pressure and thermal, such expression allows the determination of the temperature distribution in the fluid problem, provided however that its pressure distribution is known. Therefore, a solution of the energy equation (and vice versa of the Reynold's equation with thermal effects) cannot be obtained directly, but iterated until convergence of the results.

The energy equation involves the physic principle of energy conservation; it means that in a closed system the energy transferred to the system must be conserved. By doing an energy balance in a system containing a fluid particle in movement, it can be established that:

$$\underbrace{\text{Rate of variation of internal energy}}_{\mathbf{1}} = \underbrace{\text{Heat flux through the system}}_{\mathbf{2}} +$$

$$\underbrace{\text{Work of body and surface forces on the sytem}}_{\mathbf{3}}$$

The rate of variation of internal energy inside the system containing the fluid (**1**) can be expressed as the derivative of the total internal energy of the fluid per unit mass. This energy can be defined as the sum of the internal energy of the fluid (e) and its kinetic energy ($V^2/2$):

$$\mathbf{1} : \rho \frac{D}{Dt}\left(e + \frac{V^2}{2}\right) dx\,dy\,dz \tag{3.43}$$

The second term (**2**) involves the total heat exchange of the system per unit volume through conduction.:

$$\mathbf{2} : \left[\frac{\partial}{\partial x}\left(k\frac{\partial T}{\partial x}\right) + \frac{\partial}{\partial y}\left(k\frac{\partial T}{\partial y}\right) + \frac{\partial}{\partial z}\left(k\frac{\partial T}{\partial z}\right)\right] dx\,dy\,dz \tag{3.44}$$

where k is the conductivity coefficient of the fluid.

The third term accounts for the work of body and surface forces acting on the system (**3**). By body forces, one needs to account for example those generated by gravitational and eventual magnetic fields, or other eventual forces that can influence the particle of fluid in the system. By surface forces, one can account for the effect of pressure as well as the viscosity, as both act on the boundaries of the system considered. By grouping these components:

$$\begin{gathered}\mathbf{3} : \Bigg[-\left(\frac{\partial v_x p}{\partial x} + \frac{\partial v_y p}{\partial y} + \frac{\partial v_z p}{\partial z}\right) + \frac{\partial (v_x \tau_{xx})}{\partial x} + \frac{\partial (v_x \tau_{yx})}{\partial y} + \frac{\partial (v_x \tau_{zx})}{\partial z} + \frac{\partial (v_y \tau_{xy})}{\partial x} + \\ \frac{\partial (v_y \tau_{yy})}{\partial y} + \frac{\partial (v_y \tau_{zy})}{\partial z} + \frac{\partial (v_z \tau_{xz})}{\partial x} + \frac{\partial (v_z \tau_{yz})}{\partial y} + \frac{\partial (v_z \tau_{zz})}{\partial z} dx\,dy\,dz + \rho(\mathbf{f}\cdot\mathbf{V}) dx\,dy\,dz\end{gathered} \tag{3.45}$$

where $\mathbf{V}$ is the vector of the velocity components of the fluid (v_x , v_y, v_z) and $\mathbf{f}$ represents the body forces acting on the system (τ_{xx}, τ_{yy}, τ_{zz}, τ_{xy}, τ_{xz}, τ_{yx}, τ_{yz}, τ_{zx}, τ_{zy}).

In this form, obtained reuniting the expressions (**1**, **2** and **3**) represent the energy equation in its non-conservative form, as it involves the terms of total energy ($e + V^2/2$), thus also the velocity component. However it is possible to isolate the contribution given by the kinetic energy; By applying the definition of total derivative:

$$\frac{D\alpha}{Dt} = \frac{\partial \alpha}{\partial t} + (\mathbf{V} \cdot \bigtriangledown)\alpha \tag{3.46}$$

the total derivative of the term related to the kinetic energy is:

$$\rho \frac{D}{Dt}\left(\frac{V^2}{2}\right) = -v_x \frac{\partial p}{\partial x} - v_y \frac{\partial p}{\partial y} - v_z \frac{\partial p}{\partial z} + v_x \left(\frac{\tau_{xx}}{\partial x} + \frac{\tau_{yx}}{\partial y} + \frac{\tau_{zx}}{\partial z}\right) + v_y \left(\frac{\tau_{xy}}{\partial x} + \frac{\tau_{yy}}{\partial y} + \frac{\tau_{zy}}{\partial z}\right) +$$
$$+ v_z \left(\frac{\tau_{zx}}{\partial x} + \frac{\tau_{zy}}{\partial y} + \frac{\tau_{zz}}{\partial z}\right) + \rho(v_x f_x + v_y f_y + v_z f_z) \tag{3.47}$$

Thus, for a conservative form of the energy equation, the terms derived in eq. 3.47 can be subtracted from eq. 3.43, yielding:

$$\rho \frac{De}{Dt} = \frac{\partial}{\partial x}\left(k \frac{\partial T}{\partial x}\right) + \frac{\partial}{\partial y}\left(k \frac{\partial T}{\partial y}\right) + \frac{\partial}{\partial z}\left(k \frac{\partial T}{\partial z}\right) - p\left(\frac{\partial v_x}{\partial x} + \frac{\partial v_y}{\partial y} + \frac{\partial v_z}{\partial z}\right) +$$
$$\tau_{xx}\frac{\partial v_x}{\partial x} + \tau_{yx}\frac{\partial v_x}{\partial y} + \tau_{zx}\frac{\partial v_x}{\partial z} + \tau_{xy}\frac{\partial v_y}{\partial x} + \tau_{yy}\frac{\partial v_y}{\partial y} + \tau_{zy}\frac{\partial v_y}{\partial z} + \tau_{xz}\frac{\partial v_z}{\partial x} + \tau_{yz}\frac{\partial v_z}{\partial y} + \tau_{zz}\frac{\partial v_z}{\partial z} \tag{3.48}$$

Introducing the thermodynamic identity:

$$\mathrm{d}h' = c\ \mathrm{d}T + (1 - \beta T)\frac{dp}{\rho} \tag{3.49}$$

where $e = c\ \mathrm{d}T$. The terms h', ρ, and k are the enthalpy, density and the thermal conductivity of the fluid respectively. The total derivative of the internal energy is written as:

$$\frac{De}{Dt} = \frac{\partial e}{\partial t} + v_x \frac{\partial e}{\partial x} + v_y \frac{\partial e}{\partial y} + v_z \frac{\partial e}{\partial z} = c\left(\frac{\partial T}{\partial t} + v_x \frac{\partial T}{\partial x} + v_y \frac{\partial T}{\partial y} + v_z \frac{\partial T}{\partial z}\right) \tag{3.50}$$

With eqs (3.49) and (3.50), the energy equation (3.48) can be rewritten as:

$$\rho c \frac{DT}{Dt} = \beta T \frac{Dp}{Dt} + k \nabla^2 T - p \cdot \nabla u + \Phi \tag{3.51}$$

where β and c are the coefficient of thermal expansion and the heat capacity respectively; Φ is viscous dissipation. For an ideal gas β is exactly equal to $\frac{1}{T}$. If only steady state problems are considered and the fluid is assumed to obey the ideal gas law, the energy equation then be reduced to:

$$\rho c\left(u\cdot\nabla T\right)-u\cdot\nabla p-k\nabla^2T+p\cdot\nabla u=\Phi \tag{3.52}$$

note that eq. (3.52) is the customary form of the energy equation for compressible fluids [69], plus the term $p\cdot\nabla u$, which is usually simplified due to the thin film lubrication assumptions, see eq. (3.54). Specifically, note that in hydro/aerodynamic lubrication regime $\partial v_x/\partial x$ is zero, whereas for hybrid lubrication is not (in the orifice region), see eq. (3.22). Such contribution is therefore retained.

The main difference between the energy equation for compressible and incompressible fluids is the compression work term $u\cdot\nabla p$. This contribution is generally negligible for incompressible fluid lubricated bearings. In gas journal bearings on the other hand, the lubricant is continuously subjected to compression and expansion. When the gas is compressed in the convergent region of the film, it does positive work and releases heat; while in the divergent region, the gas expands and absorbs heat.

The viscous dissipation for a newtonian fluid is given by:

$$\Phi=\tau_{ij}\frac{\partial u_i}{\partial x_j}=\mu\left[2\left(\frac{\partial u}{\partial x}\right)^2+2\left(\frac{\partial v}{\partial y}\right)^2+2\left(\frac{\partial w}{\partial z}\right)^2+\left(\frac{\partial v}{\partial x}+\frac{\partial u}{\partial y}\right)^2+\left(\frac{\partial w}{\partial y}+\frac{\partial v}{\partial z}\right)^2+\left(\frac{\partial u}{\partial z}+\frac{\partial w}{\partial x}\right)^2\right]+\lambda\left(\frac{\partial u}{\partial x}+\frac{\partial v}{\partial y}+\frac{\partial w}{\partial z}\right)^2 \tag{3.53}$$

According to Stokes hypothesis, see eq. (A.20), the bulk viscosity can be expressed as λ= -2/3 μ.

In its extended form, eq. (3.52) is rather complex, however - upon the introduction of certain simplifications - it can be considerably simplified.

First, one should note that, following the assumption made in section A and 3.2, the following can be assumed:

$$\begin{aligned}\frac{\partial v_x}{\partial y}&\approx\frac{\partial v_x}{\partial z}\ll\frac{\partial v_x}{\partial x} && v_x\approx v_x(x)\\ \frac{\partial v_y}{\partial y}&\approx\frac{\partial v_y}{\partial z}\ll\frac{\partial v_y}{\partial x} && v_y\approx v_y(x)\\ \frac{\partial v_z}{\partial y}&\approx\frac{\partial v_z}{\partial z}\ll\frac{\partial v_z}{\partial x} && v_z\approx v_z(x)\end{aligned} \tag{3.54}$$

Moreover, if one considers only a bidimensional case:

$$T=T(y,z)\quad;\quad\mu=\mu(y,z) \tag{3.55}$$

The integral form of the energy equation for thin gas films and accounting injection is written as:

$$
\begin{aligned}
&-\rho ch\frac{\partial T}{\partial t}+\rho c\left(V_{inj}-\frac{\partial h}{\partial t}\right)(T_{inj}-T)-\left(\frac{\rho ch^3}{12\mu}\frac{\partial p}{\partial y}-\frac{\rho chU}{2}\right)\frac{\partial T}{\partial y}-\frac{\rho ch^3}{12\mu}\frac{\partial p}{\partial z}\frac{\partial T}{\partial z}=\\
&k\left.\frac{\partial T}{\partial x}\right|_0+kh\frac{\partial^2 T}{\partial y^2}+kh\frac{\partial^2 T}{\partial z^2}-p\left(V_{inj}-\frac{\partial h}{\partial t}\right)+\left(v\frac{\partial p}{\partial y}+w\frac{\partial p}{\partial z}\right)+\\
&\frac{4}{3}\frac{\mu}{h}\left(V_{inj}-\frac{\partial h}{\partial t}\right)^2+\frac{h^3}{12\mu}\left[\left(\frac{\partial p}{\partial y}\right)^2+\left(\frac{\partial p}{\partial z}\right)^2\right]+\frac{\mu U^2}{h}
\end{aligned}
\tag{3.56}
$$

The term $\partial T/\partial x|_0$ refers to the thermal conduction within the feeding orifices. Considering the length relatively short, one can linearize such term as:

$$k\left.\frac{\partial T}{\partial x}\right|_0\approx\frac{T_{inj}-T}{l_0}\cdot\mathcal{G}_i \tag{3.57}$$

where $\mathcal{G}_i$ is a form function taking into account the position of the orifices:

$$\mathcal{G}_i(y,z)=\begin{cases}1,(y-y_i)^2-(z-z_i)^2\leqslant\dfrac{d_0^2}{4}\\[2mm] 0,(y-y_i)^2-(z-z_i)^2\geqslant\dfrac{d_0^2}{4}\end{cases} \tag{3.58}$$

Equation (3.56) is expression of the energy balance of a fluid element. Dissipation arises from viscous effect, see eq. (3.53), and can only happen in circumferential and axial coordinates, due to how the bidimensional assumption is expressed. However, a radial heat flux exists and is the prime responsible of heat removal. In order to take into account the net heat conduction through the wall-fluid interface (q), one can think of modify the source term as:

$$S=\Phi+q \tag{3.59}$$

In order to establish a mathematical expression of the net heat conduction through the fluid-wall interface, the following assumptions are made:

- It is assumed that the conduction through the bearing walls are dominant, therefore heat conduction through the shaft, radiation etc. are neglected. Regarding the adiabatic condition imposed on the shaft boundary, one should notice that in thermal steady state conditions the net radial thermal conduction is zero; in practice in the pressure convergent region temperature builds up and a heat flows into the shaft, whereas the contrary takes place in the divergent part. Nevertheless, this assumption leads to an overestimation of the fluid temperatures, as axial thermal flows are neglected.

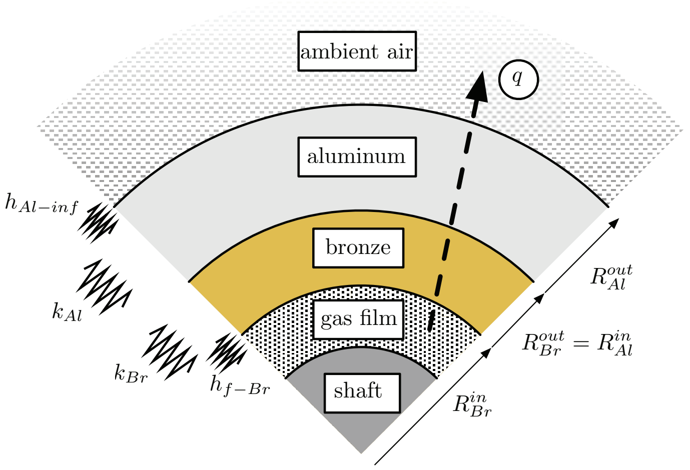

Figure 3.4: Schematic model for heat flow and convection/conduction coefficients.

- Heat conduction in the bearing sleeve is assumed to obey the one-dimensional Fourier's law. It means that the general geometry of the bearing is small and that the dominant temperature gradient in the walls of the bearing housing is in the radial direction, thus conduction in the other directions are neglected. Furthermore it is assumed that the temperature profile in the housing can be approximated by a linear function.

The heat transfer from the fluid film to the environment is assumed to happen by natural convection and conduction into the bearing through its layers. The one-dimensional energy flux through the bearing radial direction per unit area per unit time is:

$$q = -k_{eq}\frac{\mathrm{d}T}{\mathrm{d}z} \tag{3.60}$$

where k_{eq} is an equivalent convection/conduction coefficient. A simplified schematic model is presented in Figure 3.4 In the present case the bearing inner sleeve and the outer case are modeled as bronze and aluminum rings respectively, with thickness of 30 and 50 mm. It can be calculated as:

$$\frac{1}{k} = \frac{1}{h_{f-Br}} + \frac{R_{Br}^{in}\ln\left(\frac{R_{Br}^{out}}{R_{Br}^{in}}\right)}{k_{Br}} + \frac{R_{Br}^{in}\ln\left(\frac{R_{Al}^{out}}{R_{Al}^{in}}\right)}{k_{Al}} + \frac{R_{Br}^{in}}{R_{Al}^{out}}\frac{1}{h_{Al-\mathrm{inf}}} \tag{3.61}$$

where $k_{Br,Al}$ are the thermal conduction coefficients of bronze (60 W / m K) and aluminum (200 W / m K) , $h_{Al-\mathrm{inf}}$ the natural heat convection coefficient from flat surfaces to a stagnant fluid (which for the temperature range under investigation can be assumed to be constant, at

8 W / m^2 K). The convection coefficient from the fluid film to the bearing sleeve, h_{f-Br} is derived for laminar conditions from the Nusselt number as in [85].

$$Nu = \frac{Ch_{f-Br}}{k} = 3Pr^{1/3} \tag{3.62}$$

where $Pr = \mu c/k$ is the Prandtl number. For the sake of completeness, although as mentioned the convection to the ambient air is considered constant in the present case, natural heat convection coefficients to a stagnant fluidic medium can derived from [36] as:

$$Nu = \frac{R_{Al}^{out} h_{Al-inf}}{k} = 0.53(Gr \cdot Pr)^{1/4} \tag{3.63}$$

Where Gr the Grashof number.

The radii at the various locations are indicated by R_i^j, where the subscript $i = Br, Al$ indicates either the bronze or aluminum layer and the superscript $j = in, out$ indicates either the inner or outer radius. Note that $R_{Al}^{in} = R_{Br}^{out}$. As boundary condition for Eq. (3.60), it has been assumed that the temperature at the inner borders of the bearing is equal to the fluid temperature T, while the temperature outside the bearing is constant and equal to the ambient temperature T_A. As boundary conditions for the fluid film, governed by Eq. (3.52), it has been assumed that the temperature in areas where the pressure is lower than ambient pressure is a mixing temperature T_{mix} between the fluid at ambient temperature entering from the bearing sides and the warmer recirculating air. Similarly to the approach presented in [69] it can be approximated as:

$$T_{mix} = \frac{\dot{M}'T' + \dot{M}_A T_A}{\dot{M}' + \dot{M}_A} \tag{3.64}$$

where $\dot{M}'$ and T' indicates the mass flux and temperature of the recirculating fluid and $\dot{M}_A$ is the mass flux of ambient fluid entering a control volume at the border of concern. In areas where the pressure is higher than the ambient pressure, the temperature at the border is a fraction c between the temperature just inside the bearing sides and the ambient temperature. This fraction is dependent on the Péclet number and $c = Pe/100$ if $Pe \leq 100$, otherwise $c = 1$. The boundary conditions for the energy equation (3.52) can be then summarized as:

$$T : \begin{cases} T_{mix} \text{ for } (y,z) = \left(y|_{p \leq p_A}, \{0, L\}\right) \\ T_A(1-c) + cT(y, z \pm \delta z) \text{ for } (y,z) = \left(y|_{p \geq p_A}, \{0, L\}\right) \\ T(0,z) = T(2\pi R, z) \\ \dfrac{\partial T(0,z)}{\partial y} = \dfrac{\partial T(2\pi R, z)}{\partial y} \end{cases} \tag{3.65}$$

3.4 Active Control

Attenuation of mechanical vibrations can be generally achieved by two kinds of approaches: passive suppression or active control techniques. Passive control methods are the most widely used in rotating machines because they are relatively simple to implement, they are extremely reliable and do not require a power source. Vibrations are usually addressed either by adding passive absorbing devices, such as frictional dampers, damping wires, under platform dampers or by a structural redesign of the system. The drawback of such techniques is that they are usually designed to work at certain operational conditions (e.g. a particular rotational speed or system configuration) and they are difficult to be adapted when these conditions are changed. Problems could for example arise in the start-up phase of a rotating machine, when critical speeds must be crossed before reaching the operational speed or if wear introduces unbalance. Passive solutions have been developed, in gas lubrication most prominently with foil bearings; however, it is hard to rely on the friction coefficient between foils and housing walls, and because of that their performance is sometimes difficult to predict and particularly sensitive to operational and environmental parameters. The only way to overcome these problems is to implement an active control system.

Active control is based on the principle of monitoring and sensing some of the system parameters such as displacements and velocities and based on these data consequently producing a controlling reaction. A typical active control scheme is showed in figure 3.5. Depending on the type of sensors employed a signal conditioning (filtering) or amplification may be necessary before the measured variables signals are sent to the control system. Additional amplification may also be employed before the control signals are sent to the actuators. Active control system

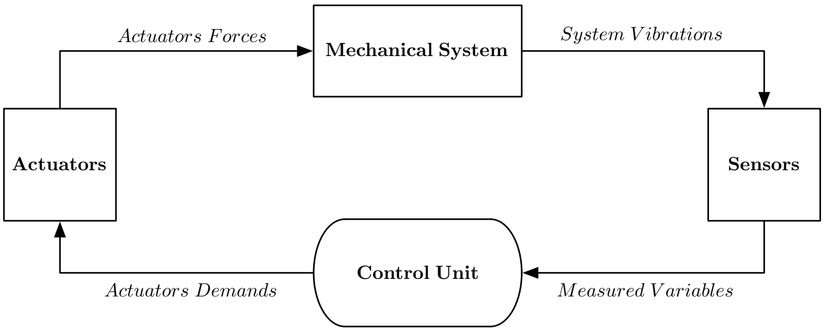

Figure 3.5: Schematic drawing of an active control system.

have the advantage of being more adaptable to changing operational conditions than passive methods. On the other hand, they have the disadvantage of requiring an external power supply and, depending on the degree of sophistication, number of sensors and actuators, they are more expensive and less reliable.

In this project, a hybrid gas journal bearing with controllable radial injection is evaluated. The main idea is that injection of air can be used to actively modify the pressure profile over the bearing, which in turn changes the thickness of the fluid film, thus creating an active force on the rotor that can be used to suppress vibrations of the rotor-bearing system.

3.4.1 Piezoelectric Injection System

The air injection is physically performed by the means of piezo actuators. Piezoceramic actuators have been subjects of increasing research in the last two decades; a comprehensive comparative study was performed by Ulbrich [99], underlying the advantages of such components. In general, piezoelectric actuators are characterized by a more compact design and faster response when compared to other types of actuators [64] - [97]. A schematic view of the piezoelectric air injection system is presented in Figure 3.6. In this system, the air injection is regulated by the activation of the piezoelectric stack. When a voltage signal is sent to this stack, the attached injection pin can be moved vertically, allowing or blocking the passage of air from the supply reservoir at P_{sup} to the injection chamber of volume V_{inj}at pressure P_{inj} and subsequently to the journal bearing at P_{JB}. Note the Belleville washers positioned between the injection pin and its casing to aid the backwards stroke of the pin and the O-rings.

For the sake of simplify the modeling, some effects are neglected and the following general assumptions are made:

- The air supply pressure P_{sup} is constant.
- Elastic deformations of solid parts due to pressure changes are neglected.
- Internal leakages are neglected.

The main governing equations for the electrical, mechanical and pneumatic subsystems are presented next. In the present configuration, up to four actuators are employed, these can operate independently from each other. The following mathematical description refers to either of them.

3.4.2 Modeling of the Piezoelectric Stack

Material strain and electrical charge density displacement of a piezoelectric stack are affected both by the mechanical stress and electrical field the material is subjected to. The ANSI-IEEE 176 Standard on Piezoelectricity [2] declares the linear constitutive law for piezoelectrical materials. Considering a stack consisting of several layers of piezoelectric material, from the constitutive law the resultant piezoelectric force F_{piezo} and electric charge Q_{piezo} can be derived as:

$$F_{piezo} = -k_{piezo}\, y(t) + k_{piezo}\, c_{piezo}\, N_{stack} u(t) \tag{3.66}$$

$$Q_{piezo} = -k_{piezo}\, c_{piezo}\, y(t) + \epsilon_{piezo}\, N_{stack}\, E_{piezo}^{-1}\, u(t) \tag{3.67}$$

where k_{piezo} is the elastic stiffness of the piezoelectric stack, $y(t)$ is the total displacement, c_{piezo} the piezoelectric coupling coefficient, $u(t)$ the feeding voltage, ϵ_{piezo} the dielectric permittivity of the material, E_{piezo} its elastic modulus and N_{stack} the number of layers of piezoelectric material that constitute the piezo actuator stack. It should be noted that this model does not include the effect of hysteresis nonlinearities, which would limit the performance of the actuator (both static and dynamic). Depending on whether such effect are relevant for each individual system, one could compensate it using one of several strategies developed in recent years; a review can be found in [19]. As a practical note, several piezoelectric motion control unit on the market are equipped with closed loop hysteresis feedback compensation, where a near linear response between $u(t)$ and $y(t)$ can be obtained, as noted in [12].

3.4.3 Modelling of the Mechanical Subsystem

In order to model the main mechanical components of the piezoelectric injection system, a simplified model is proposed, see Figure 3.8. It consists of a basic 1 degree of freedom system, which dynamic behavior is described by:

$$m_{pin}\, \ddot{y}(t) = F_{piezo} - k_{mech}\, y(t) - d_{mech}\, \dot{y}(t) \tag{3.68}$$

where m_{pin} is the mass of the injector pin plus that of the piezoelectric stack, k_{mec} is the stiffness of the Belleville washers and d_{mech} the combined equivalent viscous friction coefficient of the Belleville springs and O-rings. Note that the stiffness of the O-ring is not included in this analysis, as its magnitude is negligible for the configuration under consideration, where its contribution would be in parallel with the larger one due to the Belleville washers.

3.4.4 Modelling of the Pneumatic Subsystem

The pneumatic subsystem, see Figure 3.9 is considered as a container of unknown pressure and volume V_{inj}, with cross sectional area greater than the inlet and outlets ducts. From the definition of mass conservation:

$$\frac{dm}{dt} = \rho\left(-\dot{Q}_{in} + \dot{Q}_{out}\right) \tag{3.69}$$

where $\dot{Q}_{in}$ and $\dot{Q}_{out}$ are the in- and outlet volumetric flow rates, respectively. If inertia is neglected and only the elasticity effect is taken into account, it can be assumed that the control volume has uniform pressure. Compressibility of the fluid needs also to be accounted for; the pressure change within a control volume of the pneumatic subsystem can be expressed by substituting the definition of the (isothermal) bulk modulus of elasticity. Equation (A.1) can then be modified, expressing the variation of pressure as:

$$\frac{dP}{dt} = \frac{\beta}{V_{inj}}\left(\frac{dV_{inj}}{dt} - \dot{Q}_{in} + \dot{Q}_{out}\right) \tag{3.70}$$

where β is the bulk modulus of elasticity and the term dV_{inj}/dt takes into account the variation of volume due to the motion of the injector pin. The intake and outtake volumetric flows can be derived by the Bernoulli's law, modified by introducing an expansion factor to account for the compressibility of gases [29]. By assuming steady-state, incompressible (constant fluid density), inviscid, laminar flow with negligible frictional losses and head differences, Bernoulli's equation reduces to an equation relating the conservation of energy between two points on the same streamline an expression for the volumetric flow can be written:

$$\dot{Q} = c_D A(y(t))\sqrt{2(P_{up} - P_{dwn})/\rho} \tag{3.71}$$

where the subscripts *up* and *dwn* refer to the fluid properties upstream and downstream the control volume respectively. In general, eq. (3.71) is only valid for incompressible flows, however It can be modified by introducing the expansion factor to account for the compressibility of gases. Using the ideal gas law and the compressibility factor (which corrects for non-ideal gases), a practical equation is obtained for the non-choked [1] flow of real gases: Their expressions are

---

[1] Choked flow is a fluid dynamic condition associated with the Venturi effect. When a flowing fluid at a given pressure and temperature passes through a restriction (such as the throat of a convergent-divergent nozzle or a valve in a pipe) into a lower pressure environment the fluid velocity increases. At initially subsonic upstream conditions, the conservation of mass principle requires the fluid velocity to increase as it flows through the smaller cross-sectional area of the restriction. At the same time, the Venturi effect causes the static pressure, and therefore the density, to decrease downstream past the restriction. Choked flow is a limiting condition which occurs when the mass flow rate will not increase with a further decrease in the downstream pressure environment while upstream pressure is fixed.

also function of the speed of the flow (sub/supersonic). For subsonic flows:

$$\dot{Q} = c_D A(y(t)) \sqrt{2RT \left(\frac{k}{k-1} \right) \left[\left(\frac{P_{dwn}}{P_{up}} \right)^{2/k} - \left(\frac{P_{dwn}}{P_{up}} \right)^{(k+1)/k} \right]} \tag{3.72}$$

For supersonic (chocked) flows:

$$\dot{Q} = c_D A(y(t)) \sqrt{kRT \left(\frac{2}{k+1} \right)^{(k+1)/(k-1)}} \tag{3.73}$$

Where c_D is the discharge coefficient, $A(y(t))$ the area of the orifice, R the specific gas constant for air, T the absolute upstream temperature of the gas, k is specific heat ratio (c_p / c_v), P_i are the downstream and upstream pressures, respectively. Note that the last two quantities interchange their places whether the flow is directed form the supply tank towards the journal bearing or vice versa (backflow). As for the volume change due to the motion of mechanical parts, it holds that:

$$V_{inj} = \pi \frac{d_0^2}{4} [l_0 + y(t)] \quad \Longrightarrow \quad \frac{dV_{inj}}{dt} = \pi \frac{d_0^2}{4} \dot{y}(t) \tag{3.74}$$

3.4.5 State Space representation of global mathematical model of the injection system

For each piezoelectric injector system, the mechanical and pneumatic subsystems are coupled. All the equations that describe the mathematical model of each piezo-actuated injector can be rewritten in state space form as:

$$\dot{\mathbf{y}}(t) = f(t, \mathbf{y}(t), \mathbf{u}(t)) \tag{3.75}$$

where $\mathbf{y} = [y \; \dot{y} \; P_{inj}]^T$. In state space representation then:

$$\begin{bmatrix} \dot{y} \\ \ddot{y} \\ \dot{P}_{inj} \end{bmatrix} \Leftrightarrow \begin{bmatrix} \dot{x_1} \\ \dot{x_2} \\ \dot{x_3} \end{bmatrix} = \begin{bmatrix} x_2 \\ \dfrac{(k_{piezo}\, x_1 + k_{piezo}\, c_{piezo}\, N_{stack}\, u - k_{mech}\, x_1 - d_{mech}\, x_2)}{m_{pin}} \\ \dfrac{\beta}{V_{inj}(x_3)} \left(\dot{V}_{inj}(x_1) - \dot{Q}_{in}(x_1, x_3) + \dot{Q}_{out}(x_3, P_{JB}) \right) \end{bmatrix} \tag{3.76}$$

Note that each piezoelectric subsystem is linearly independent with respect to each other, but coupling arises through the journal pressure P_{JB}.

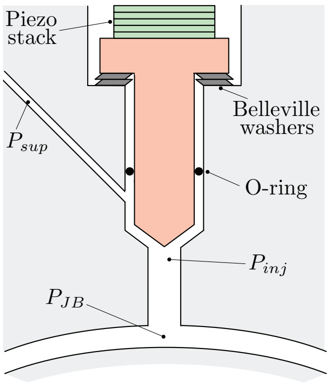

Figure 3.6: Schematic view of the piezoelectric air injection system.

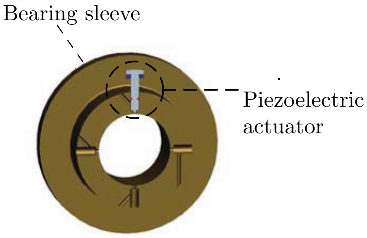

Figure 3.7: 3D view of the piezoelectric injection system inside the bearing sleeve.

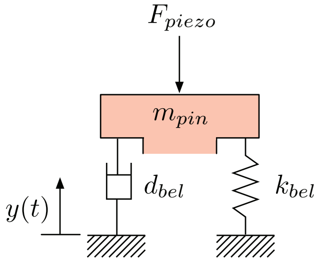

Figure 3.8: Schematic view of the piezoactuator mechanical subsystem.

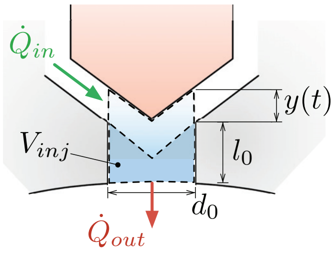

Figure 3.9: Schematic view of the piezoactuator pneumatic subsystem.

3.4.6 Modeling of the Control System

Once the mathematical model for the hybrid bearing and piezo actuated injection system is formulated, the next step is to develop the control system. It is assumed that the instantaneous position and velocity of the journal is measured by sensors mounted on the bearing. First, the objective of the controller needs to be defined. In order to minimize the response of the system subjected to some kind of excitation, one could for instance increase the stiffness or damping coefficients. With this objective in mind, it is then necessary to establish a feedback control law in order to construct the signal to send to the piezo actuators as function of the information received by the sensors. General input signals can be defined as a combination of displacement and velocity, for either the vertical (X) or horizontal (Y) coordinates as:

$$\mathbf{u}(t) = \mathbf{G}^k\mathbf{q}(t) + \mathbf{G}^d\dot{\mathbf{q}}(t) \quad \Rightarrow \quad \begin{aligned} u_X &= G_X^k e_X + G_X^d \dot{e}_X \\ u_Y &= G_Y^k e_Y + G_Y^d \dot{e}_Y \end{aligned} \tag{3.77}$$

where $G_{X,Y}^{k,d}$ are the gains of the control system. The superscripts k, d refer respectively to the proportional or derivative gain. Depending on the goal of the control system, the gain coefficients should be calculated and optimized with the help of the developed model.

Despite not included in the present modeling, one should be aware that under certain operation conditions and parameters, an active controlled system could be affected by lag or lead times, which could result in poor performance or even instability. Delays often arise mechanical in systems (in the present case for example due to the dynamic of the actuator), as well as in measurement and computation (for example due to filtering or coarse sampling frequencies).

3.5 Numerical Implementation

3.5.1 Discrete formulation of the Reynold's equation

The pressure distribution in the gas journal bearing is obtained through the solution of the compressible Reynold's equation, either the isothermal aerodynamic form (3.3), or hybrid (3.29), or with thermal effects (3.33). Either these equations are nonlinear partial differential equations, hence there is no analytical solution, but it is necessary to develop a numerical method. A common way is to approximate the solution with a finite difference method. With this method it is possible to transform a system of differential equations into an equivalent system of algebraic equations, where the number of equations depends on the refinement of the discretization grid. Generally, mesh size is one of the main parameters determining the accuracy of the method, the other being the oder of the finite difference scheme.

Traditionally, the Reynold's equation is solved on uniformly spaced grids, which require a straightforward set-up where the difference coefficients are constant at every discretization point. This is a relatively simple formulation, convenient when approaching problems without particular geometrical features, e.g. plain cylindrical/elliptic/lobed bearings, conventional foil bearings or plain flexure pivot/tilting pad bearings. However, appropriately including the hybrid aerostatic term in a finite difference formulation, see eq. (3.29), would require the generation of extremely fine grids in order to produce adequate discretization of the orifice areas (particularly when such orifices are round). Moreover, finer discretization is also desirable in region around the orifice, as steep pressure gradients are generally expected. Such high degree of refinement would produce great accuracy, however also severely increase computational time. In order to keep fine discretization where needed while keeping the computational effort at a manageable level, in this project a non-uniform variant of the standard finite difference formulation is employed. Its derivation stems from a standard version applied to uniformly spaced grids. This approach is different from what is generally adopted in literature, where aerostatic contribution are treated as point sources [55].

The calculation of the gradient of an an arbitrary function $\Psi = \Psi(x)$ can be approximated writing the r-term Taylor series expansion of $\Psi(x)$, about the point $x = x_i$ and evaluating the result at each point on the stencil:

$$\Psi(x) = \sum_{m=0}^{\infty} \frac{(x - x_i)^m}{m!} \Psi_i^{(m)} \tag{3.78}$$

Using a 3 point stencil in order to obtain the centered finite difference coefficients scheme (CDS), the system of Taylor expansions has the form:

$$\begin{bmatrix} 1 & -1 & 1/2 \\ 1 & 0 & 0 \\ 1 & 1 & 1/2 \end{bmatrix} \begin{Bmatrix} \Psi_i^0 \\ \Delta x \Psi_i^1 \\ \Delta x^2 \Psi_i^2 \end{Bmatrix} = \begin{Bmatrix} \Psi_{i-1} \\ \Psi_i \\ \Psi_{i+1} \end{Bmatrix} \tag{3.79}$$

Which is readily solved for the coefficients:

$$\begin{Bmatrix} \Psi_i^0 \\ \Delta x \Psi_i^1 \\ \Delta x^2 \Psi_i^2 \end{Bmatrix} = \begin{bmatrix} 0 & 1 & 0 \\ -1/2 & 0 & 1/2 \\ 1 & -2 & 1 \end{bmatrix} \begin{Bmatrix} \Psi_{i-1} \\ \Psi_i \\ \Psi_{i+1} \end{Bmatrix} \tag{3.80}$$

Thus the approximation for the first order derivative:

$$\Psi_i^1 = \left. \frac{\partial \Psi}{\partial x} \right|_i \simeq \frac{1}{2\Delta x} \left(\Psi_{i+1} - \Psi_{i-1} \right) \tag{3.81}$$

and the second order:

$$\Psi_i^2 = \left. \frac{\partial^2 \Psi}{\partial x^2} \right|_i \simeq \frac{1}{\Delta x^2} \left(\Psi_{i-1} - 2\Psi_i + \Psi_{i+1} \right) \tag{3.82}$$

If one wants to consider that the grid spacing Δx is not constant, the above procedure needs to be slightly modified. For an arbitrarily spaced set of points x_i, $i = 1, 2, ..., N$, each point will have its own scheme with coefficients computed exactly as above. The only difference is that $x - x_i$ in the Taylor expansion cannot be replaced by an integer times Δx. Note that when computing these coefficients, it is important to scale each term in the Taylor expansion by the appropriate power of a representative grid spacing in order to avoid generating a singular matrix when points are clustered closely together. Thus the general expression for the Taylor series coefficient should look like:

$$\frac{\left(\dfrac{x_j - x_i}{\Delta x_{min}} \right)^m}{m!} \qquad m = 0, 1, ...r - 1; \quad j = i - sl, ..., i, ..., i + sr \tag{3.83}$$

where sl is the number of stencil points to the left, sr the number of stencil points to the right and $r = sl + sr + 1$. As each term has been scaled by the minimum grid spaing Δx_{min}, once the system is solved the resulting coefficients for the m^{th} derivative must be divided by the factor $(\Delta x_{min})^m$.

This technique can be used to solve the Reynold's equation on a discretized domain of dimension

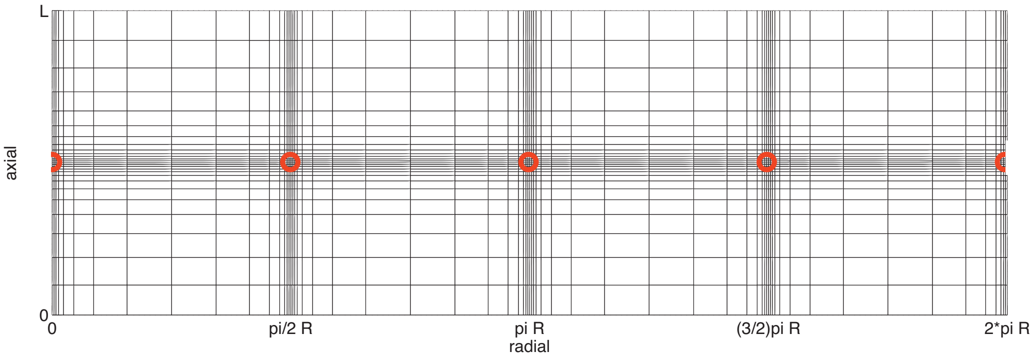

Figure 3.10: Non-uniform mesh of the bearing domain (orifices highlighted in red).

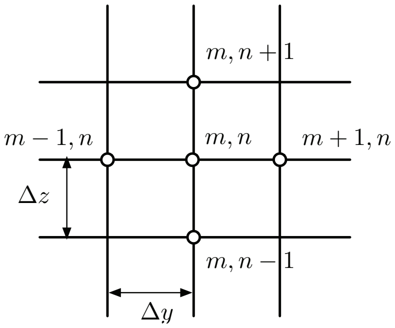

Figure 3.11: Discretization of the bearing domain

$m \times n$ in the y and z coordinate respectively, as shown in Figures 3.10 and 3.11. As an example, the numerical procedure is detailed for the solution of the compressible Reynold's equation, for aerodynamic operation, and considering thermal effects. It is written for the steady-state case as:

$$\frac{\partial}{\partial y}\left(\frac{p}{\mu T}h^3\frac{\partial p}{\partial y}\right)+\frac{\partial}{\partial z}\left(\frac{p}{\mu T}h^3\frac{\partial p}{\partial z}\right)=6U\frac{\partial}{\partial y}\left(\frac{p}{T}h\right) \tag{3.84}$$

Assuming the temperature profile to be known, eq. (3.84) is nonlinear in p, therefore the solution cannot be achieved directly. A common way to solve nonlinear systems is to employ an iterative method in which attempts to solve a problem are made by finding successive approximations to the solution starting from an initial guess.

In the present case, a solution strategy of this kind is developed rewriting the Reynolds equation

(3.85) splitting the pressure terms into zeroth and first order terms as:

$$\left[\frac{\partial}{\partial y}\left(\frac{p_0^\alpha}{\mu T}h^3\frac{\partial}{\partial y}\right)\right]p_0^\beta+\left[\frac{\partial}{\partial z}\left(\frac{p_0^\alpha}{\mu T}h^3\frac{\partial}{\partial z}\right)\right]p_0^\beta=6U\left(\frac{p_0^\alpha}{T}\frac{\partial h}{\partial y}-\frac{p_0^\alpha h}{T^2}\frac{\partial T}{\partial y}\right)+6U\left(\frac{h}{T}\frac{\partial}{\partial y}\right)p_0^\beta \tag{3.85}$$

Starting with an initial guess for p_0^α, the problem becomes linear in p_0^β and thus can be solved directly, which is then used to update the guess for the next iteration. This is repeated until the difference between the solutions of two successive iterations is smaller than a set tolerance. For a better understanding of the procedure, the method can be divided in a series of steps:

1. Starting with a good initial guess can dramatically decrease the number of iterations necessary. Thus it has been decided to initially calculate the solution of the linear, isothermal Reynolds equation, which physically correspond to the incompressible case:

   $$\frac{\partial}{\partial y}\left(h^3\frac{\partial p}{\partial y}\right)+\frac{\partial}{\partial z}\left(h^3\frac{\partial p}{\partial z}\right)=6\mu U\frac{\partial(h)}{\partial y} \tag{3.86}$$

   which is a linear elliptic equation for p that can be solved directly to give us the first guess for p_0^α.

2. The differential operators are defined as described in eqs. (3.78) - (3.82) witht the appropriate coefficeints calculated with eq. (3.83) so that:

   - First and second derivative in y direction:

     $$D_y: \quad D_y p=\frac{\partial p}{\partial y},\quad D_y h=\frac{\partial h}{\partial y},\quad D_y\frac{1}{T}=\frac{\partial T}{\partial y},\quad D_y\frac{1}{\mu}=\frac{\partial \mu}{\partial y} \tag{3.87}$$

     $$D_{yy}: \quad D_{yy}p=\frac{\partial^2 p}{\partial y^2} \tag{3.88}$$

     where the coefficients of the differential operators related to $m-1, n$ lie on the n^{th} lower subdiagonal, m, n on the main diagonal and $m+1, n$ on the n^{th} upper subdiagonal.

   - First and second derivative in z direction:

     $$D_z: \quad D_z p=\frac{\partial p}{\partial z},\quad D_z\frac{1}{T}=\frac{\partial T}{\partial z},\quad D_z\frac{1}{\mu}=\frac{\partial \mu}{\partial z} \tag{3.89}$$

     $$D_{zz}: \quad D_{zz}p=\frac{\partial^2 p}{\partial z^2} \tag{3.90}$$

     where the coefficients of the differential operators related to $m, n-1$ lie on the 1^{st} lower subdiagonal, m, n on the main diagonal and $m, n+1$ on the 1^{st} upper subdiagonal

3. The difference equations are calculated. To do so eq. (3.85) is rewritten as:

$$\underbrace{\left[\frac{\partial}{\partial y}\left(\frac{p_0^\alpha}{\mu T}h^3\frac{\partial}{\partial y}\right)\right]p_0^\beta}_{\text{term A}}+\underbrace{\frac{\partial}{\partial z}\left(\frac{p}{\mu T}h^3\frac{\partial p}{\partial z}\right)}_{\text{term B}}=\underbrace{6U\left(\frac{p_0^\alpha}{T}\frac{\partial h}{\partial y}-\frac{p_0^\alpha h}{T^2}\frac{\partial T}{\partial y}\right)+6U\left(\frac{h}{T}\frac{\partial}{\partial y}\right)p_0^\beta}_{\text{term C}} \tag{3.91}$$

   - term A

$$\begin{aligned}\left[\frac{\partial}{\partial y}\left(\frac{p_0^\alpha}{\mu T}h^3\frac{\partial}{\partial y}\right)\right]p_0^\beta = {} & \underbrace{3h^2p_0^\alpha D_y h\frac{1}{\mu T}}_{\text{A1}}D_y p_0^\beta+\underbrace{h^3D_y p_0^\alpha\frac{1}{\mu T}}_{\text{A2}}D_y p_0^\beta+\underbrace{h^3p_0^\alpha\frac{1}{\mu T}}_{\text{A3}}D_{yy}p_0^\beta - \\ & \underbrace{h^3p_0^\alpha\frac{1}{\mu T^2}D_yT}_{\text{A4}}D_y p_0^\beta-\underbrace{h^3p_0^\alpha\frac{1}{\mu^2T}D_y\mu}_{\text{A5}}D_y p_0^\beta\end{aligned} \tag{3.92}$$

   - term B

$$\begin{aligned}\left[\frac{\partial}{\partial z}\left(\frac{p_0^\alpha}{\mu T}h^3\frac{\partial}{\partial z}\right)\right]p_0^\beta = {} & \underbrace{h^3D_z p_0^\alpha\frac{1}{\mu T}}_{\text{B1}}D_z p_0^\beta+\underbrace{h^3p_0^\alpha\frac{1}{\mu T}}_{\text{B2}}D_{zz}p_0^\beta-\underbrace{h^3p_0^\alpha\frac{1}{\mu T^2}D_zT}_{\text{B3}}D_z p_0^\beta - \\ & \underbrace{h^3p_0^\alpha\frac{1}{\mu^2T}D_z\mu}_{\text{B4}}D_z p_0^\beta\end{aligned} \tag{3.93}$$

   - term C

$$\begin{aligned}6U\left(\frac{p_0^\alpha}{T}\frac{\partial h}{\partial y}-\frac{p_0^\alpha h}{T^2}\frac{\partial T}{\partial y}\right)+6U\left(\frac{h}{T}\frac{\partial}{\partial y}\right)p_0^\beta = {} & \underbrace{6Up_0^\alpha D_y h\frac{1}{T}}_{\text{C1}}-\underbrace{6Up_0^\alpha h\frac{1}{T^2}D_yT}_{\text{C2}} + \\ & \underbrace{6Uh\frac{1}{T}}_{\text{C3}}D_y p_0^\beta\end{aligned} \tag{3.94}$$

4. The p_0^α components of each term are calculated for every grid point m, n and arranged into diagonal matrices. As an example, the matrix of terms A1 has the form:

$$A1_{m\times n,m\times n}=\begin{bmatrix}\left.\left(3h^2p_0^\alpha D_y h\frac{1}{\mu T}\right)\right|_{1,1} & & \\ & \ddots & \\ & & \ddots & \\ & & & \left.\left(3h^2p_0^\alpha D_y h\frac{1}{\mu T}\right)\right|_{m\times n,m\times n}\end{bmatrix} \tag{3.95}$$

and similarly for the other components A2 - A5, B1- B4 and C3. As for C1 - C2, one should notice that they do not depend on p_0^β, thus they are constant terms and arranged into vector form. As an example, C1 has the form:

$$C1_{m\times n,1} = \begin{bmatrix} \left(6Up_0^\alpha D_y h\frac{1}{T}\right)\big|_{1,1} \\ \vdots \\ \vdots \\ \left(6Up_0^\alpha D_y h\frac{1}{T}\right)\big|_{m\times n,m\times n} \end{bmatrix} \tag{3.96}$$

5. The matrices and vectors calculated in point 4 are arranged into a linear system of the form:

   $$\Lambda(p_0^\alpha)p_0^\beta = \Gamma(p_0^\alpha) \tag{3.97}$$

   where:

   $$\Lambda = A1D_y + A2D_y + A3D_{yy} + A4D_y + A5D_y + B1D_z + B2D_{zz} + B3D_z + B4D_z - C3D_y \tag{3.98}$$

   and:

   $$\Gamma = C1 + C2 \tag{3.99}$$

6. The system given in eq. 3.97 is solved for p_0^β upon imposing the boundary conditions given in eq. (3.17).

The procedure is performed iteratively from point 3 to 6. At the end of each iteration, the solution p_0^β becomes the guess p_0^α for the new iteration, until the norm of the difference between the solution of two consecutive iterations is less than a prescribed tolerance value (the default value is set to 10^{-5}).

3.5.2 Discrete formulation of the energy equation

The determination of the fluid temperature distribution over the bearing surface is related to the solution of the energy equation, (3.56). Rearranging the terms it is rewritten in steady state form as:

$$\underbrace{\left(\frac{\rho ch^3}{12\mu}\frac{\partial p}{\partial y} - \frac{\rho chU}{2}\right)\frac{\partial T}{\partial y} + \frac{\rho ch^3}{12\mu}\frac{\partial p}{\partial z}\frac{\partial T}{\partial z}}_{\text{convective terms}} + \underbrace{kh\frac{\partial^2 T}{\partial y^2} + kh\frac{\partial^2 T}{\partial z^2}}_{\text{diffusive terms}} + \left(\frac{k}{l_0}\mathcal{G}_i + \rho cV_{inj}\right)T =$$
$$\left(\frac{k}{l_0}\mathcal{G}_i + \rho cV_{inj}\right)T_{inj} + pV_{inj} - \frac{4}{3}\frac{\mu}{h}V_{inj}^2 - \frac{h^3}{12\mu}\left[\left(\frac{\partial p}{\partial y}\right)^2 + \left(\frac{\partial p}{\partial z}\right)^2\right] - \frac{\mu U^2}{h} \tag{3.100}$$

A solution is obtained employing a finite difference scheme, analogous to that employed for the solution of the Reynold's equation. Therefore the present section does not offer the same detailed description, however it is focused on the differences in the approach. Note that in order to ease the numerical matching of the two solutions, the same discretization meshing is maintained.

Two main differences can be identified:

1. The energy equation is a linear partial differential equation in T, thus the recursive scheme is not necessary and a solution can be obtained by direct inversion of the FD system.
2. Due to the strong convective terms, a central difference scheme can produce numerical instabilities, thus it is replaced by an upwind (or upstream) approach.

In order to clarify the statement of point 2. the following argument should be considered.

The Peclet number relative to the thin film flow is defined as:

$$Pe = \frac{\rho c U C}{k} \tag{3.101}$$

Physically, it represent the ratio between convective transport and diffusive transport phenomena. For many geometrical and operational conditions in fluid film bearings, the Peclet number is high, meaning that convective transport dominates. In such situations, the dependency of the flow upon downstream locations is diminished with respect to those upstream.

Outside an orifice region, in a central difference schemes the fist order approximation of the convective terms yields small coefficients on the main diagonal, exactly zero for uniform discretization, see (3.81). Thus, the main contribution is given by diffusive terms. As the transport is mainly convective these are also small. However, on the sub- and super-diagonals, both convection and diffusion concur to yield large coefficients. The resulting CDS matrix is then weakly diagonally dominant, which originates imprecise results and ”wiggle” numerical instability [103].

The solution proposed is then to utilize another type of finite difference approximation for the first order terms. Instead of a central scheme, an upstream one-sided can be used:

$$\Psi_i^1 = \left.\frac{\partial \Psi}{\partial x}\right|_i \simeq \frac{1}{\Delta x}\left(\Psi_i - \Psi_{i-1}\right) \tag{3.102}$$

Note that the truncation error of the above one-sided scheme (3.102) is first order, compared to the second order accurate central difference (3.81).

Equation (3.100) is then to be solved with an upstream scheme; considering the reference of frame in use, the first order approximation can vary locally, depending on the sign of the circumferential and axial velocities, v and w. In detail four cases arise (note that to ease the notation these refer to a uniform discretization):

$$v > 0: \quad \left.\frac{\partial T}{\partial y}\right|_{m,n} \simeq \frac{1}{\Delta y}\left(T_{m,n} - T_{m-1,n}\right) \tag{3.103}$$

$$v < 0: \quad \left.\frac{\partial T}{\partial y}\right|_{m,n} \simeq \frac{1}{\Delta y}\left(T_{m+1,n} - T_{m,n}\right) \tag{3.104}$$

$$w > 0: \quad \left.\frac{\partial T}{\partial y}\right|_{m,n} \simeq \frac{1}{\Delta y}\left(T_{m,n} - T_{m,n-1}\right) \tag{3.105}$$

$$w < 0: \quad \left.\frac{\partial T}{\partial y}\right|_{m,n} \simeq \frac{1}{\Delta y}\left(T_{m,n+1} - T_{m,n}\right) \tag{3.106}$$

Once the all the matrix of coefficients are determined, a difference equations can be written and a linear system analogous to (3.97) setup:

$$\Xi T = \Upsilon \tag{3.107}$$

where Ξ and Υ contain all the terms related to the right and left hand side of eq. (3.100) respectively. Equation (3.107) can be solved directly to determine the temperature field.

Note that pressure gradients present $\partial p/\partial y$ and $\partial p/\partial z$ in eq. (3.100) are assumed to be known, being solution of the Reynold's equation.

3.5.3 Pressure - temperature convergence

The pressure - temperature problems constitute a nonlinear system in which the solution of each system is a dependent variable for the other:

$$\begin{aligned} \text{Reynold's equation:} \quad & P = P(\mu, T) \\ \text{Energy equation:} \quad & T = T(P) \end{aligned}$$

To solve such problem the following strategy has been adopted:

1. Assume a temperature and viscosity distribution.
2. Calculate pressure
3. Calculate temperature

When both the pressure and temperature distributions are known, the fluid properties are updated and the pressure and temperature are recalculated. This procedure continues until all properties converge, respecting set tolerances. Once convergence is obtained, the zeroth order pressure field is integrated over the bearing surface, which in turn imposes vertical and horizontal lubrication reaction forces.

The bearing reaction forces are expressed in the fixed (X, Y) coordinate system:

$$\begin{aligned} F_X &= \int_0^L \int_0^{2\pi} (p_0 - p_{atm}) \cos \Theta R d\Theta dz \\ F_Y &= \int_0^L \int_0^{2\pi} (p_0 - p_{atm}) \sin \Theta R d\Theta dz \end{aligned} \tag{3.108}$$

Numerical integration is performed numerically by the means of a standard Simpson's method.

3.5.4 Calculating the equilibrium position

For the bearing to be in steady state equilibrium the reaction forces must equilibrate the loading. Assuming that this load W is only due to gravity, it only acts on the vertical (X) direction, this means:

$$\begin{aligned} &W + F_X(e_X, e_Y) = G_X(e_X, e_Y) = 0 \\ &F_Y(e_X, e_Y) = G_Y(e_X, e_Y) = 0 \end{aligned} \tag{3.109}$$

Equation 3.109 constitute a nonlinear system which has to be solved for the values e_X and e_Y that zero these functions: the equilibrium position of the bearing. This solution of this system can be done by a Newton-Raphson procedure. Due to the large amount of calculations needed in order to achieve full convergence of pressure, temperature and equilibrium position, it is very important to take any possible strategy in order to reduce the computational load. A modified version of the standard algorithm is therefore applied.

3.5.4.1 The Newton-Raphson method with reduced step

Starting from a guessed equilibrium position $(e_X e_Y)^i$, the functions can be Taylor expanded around the guessed value as:

$$\begin{aligned} G_X(e_X^i + de_X, e_Y^i + de_Y) &= G_X(e_X, e_Y)^i + \frac{\partial G_X}{\partial e_X} de_X + \frac{\partial G_X}{\partial e_Y} de_Y \\ G_Y(e_X^i + de_X, e_Y^i + de_Y) &= G_Y(e_X, e_Y)^i + \frac{\partial G_Y}{\partial e_X} de_X + \frac{\partial G_Y}{\partial e_Y} de_Y \end{aligned} \tag{3.110}$$

rearranging and writing in matrix notation:

$$\begin{bmatrix} G_X(e_X^i + de_X, e_Y^i + de_Y) \\ G_Y(e_X^i + de_X, e_Y^i + de_Y) \end{bmatrix} = \begin{bmatrix} G_X(e_X, e_Y)^i \\ G_Y(e_X, e_Y)^i \end{bmatrix} + \begin{bmatrix} \frac{\partial G_X}{\partial e_X} & \frac{\partial G_X}{\partial e_Y} \\ \frac{\partial G_Y}{\partial e_X} & \frac{\partial G_Y}{\partial e_Y} \end{bmatrix} \begin{bmatrix} de_X \\ de_Y \end{bmatrix} \tag{3.111}$$

or:

$$\begin{bmatrix} G_X(e_X^i + de_X, e_Y^i + de_Y) \\ G_Y(e_X^i + de_X, e_Y^i + de_Y) \end{bmatrix} = \begin{bmatrix} G_X(e_X, e_Y)^i \\ G_Y(e_X, e_Y)^i \end{bmatrix} + J \begin{bmatrix} de_X \\ de_Y \end{bmatrix} \tag{3.112}$$

where J is the Jacobian matrix evaluated at the guessed position. Defining:

$$\begin{aligned} (e_X, e_Y)^{i+1} &= (e_X^i + de_X, e_Y^i + de_Y) \\ (e_X, e_Y)^{i+1} &= (e_X^i + de_X, e_Y^i + de_Y) \end{aligned} \tag{3.113}$$

if one wants it to be a better approximation of the solution then:

$$\begin{aligned} G_X(e_X, e_Y)^{i+1} &= 0 \\ G_Y(e_X, e_Y)^{i+1} &= 0 \end{aligned} \tag{3.114}$$

Substituting eq. (3.114) with (3.113) into (3.112) one obtains:

$$-\begin{bmatrix} G_X(e_X, e_Y)^i \\ G_Y(e_X, e_Y)^i \end{bmatrix} = J \begin{bmatrix} de_X \\ de_Y \end{bmatrix} \tag{3.115}$$

which is a linear system that can be solved for the values of (de_X, de_Y).

The reduced step scheme. The trajectory that the solution follows to reach this minimum can however be very erratic, especially when the initial guess is very far from the solution. To avoid this problem, instead of taking a full Newton-Raphson step, one can look along the direction of the step for a point where the error is less than that at the starting point. The standar Newton-Raphson procedure can then be modified.

The definition of the norm of the residual of (3.109) reads:

$$||G_X(e_X, e_Y), G_Y(e_X, e_Y)|| = \left(G_X(e_X, e_Y)^2 + G_Y(e_X, e_Y)^2\right)^{(1/2)} \tag{3.116}$$

This implies that:

$$||G_X(e_X, e_Y), G_Y(e_X, e_Y)|| \geqslant 0 \tag{3.117}$$

which means that the solution is a global minimum in $||G_X(e_X, e_Y), G_Y(e_X, e_Y)||$.
The new scheme follws:

1. Calculate the function values at the guessed value of $(e_X e_Y)^i$
2. Calculate the Jacobian matrix using the current guess
3. Solve the linear system of eq. (3.115)
4. Enter the reduced step loop:
    - Initialize the index j=1
    - Calculate:

    $$||G_X(e_X + 0.5^j de_X, e_Y + 0.5^j de_X), G_Y(e_X + 0.5^j de_X, e_Y + 0.5^j de_Y)|| \tag{3.118}$$

    - Update the index $j = j + 1$

    Repeat until:

    $$\begin{aligned} &||G_X(e_X + 0.5^j de_X, e_Y + 0.5^j de_X), G_Y(e_X + 0.5^j de_X, e_Y + 0.5^j de_Y)|| < \\ &\qquad ||G_X(e_X, e_Y), G_Y(e_X, e_Y)|| \end{aligned} \tag{3.119}$$

5. Updated the guessed value as

    $$(e_X, e_Y)^{i+1} = (e_X^i + 0.5^j de_X, e_Y^i + 0.5^j de_Y) \tag{3.120}$$

The procedure should be iterated using the updated value as the new guess until the norm of the residual of eq. (3.109) is below a predefined tolerance (10^{-10}).

3.5.5 First order equations

The solution of the first order perturbation eqs. (3.15) and (3.16) (plain aerodynamic bearing), (3.31) and (3.32) (hybrid bearing), or (3.41) and (3.41) (with thermal effects) is straightforward, as these are linear partial differential equations with respect to the perturbed pressures variables (p_X, p_Y).

A discrete formulation of the perturbation equations can be obtained by using the same differential operators described in Section 3.5.1. This leads to the definition two linear systems comprising of the matrices of coefficients determined. A difference equations can be written and a linear system analogous to (3.97) and (3.107) setups:

$$\begin{aligned} \Lambda_X P_X &= \Gamma_X \\ \Lambda_Y P_Y &= \Gamma_Y \end{aligned} \tag{3.121}$$

where $\Lambda_{X,Y}$ and $\Gamma_{X,Y}$ contain all the terms related to the right and left hand side of the first order pressure perturbation equations respectively, where zeroth order (steady state) pressure field, temperature and viscosity are assumed to be known. Equation (3.121) can be solved directly to determine the temperature field. Once solutions are obtained, they can be numerically integrated over the bearing surface to determine the stiffness and damping coefficients:

$$\mathbf{K} + i\omega\mathbf{D} = \int_0^L \int_0^{2\pi} \begin{bmatrix} p_X \cos\Theta & p_X \sin\Theta \\ p_Y \cos\Theta & p_Y \sin\Theta \end{bmatrix} R d\Theta dy \tag{3.122}$$

3.5.6 Global solution of fluid film problem

Depending on the kind of system under analysis and which level of approximation one is to obtain, solutions of the fluid film problem can be generated for:

- aerodynamic journal bearing, isothermal or THD;
- hybrid journal bearing, isothermal or THD;
- active bearing.

3.5.6.1 Passive bearing

As for the passive case, aerodynamic or hybrid bearing, full THD solutions are those numerically more cumbersome and demanding; a full flow chart of the full THD-model is shown in Fig. 3.12. The first order computation of dynamic perturbation coefficients does not involve the energy equation per se; all temperature-dependent quantities are designated to be those determined in the converged full-THD computation. The necessary steps in order to determine the static and dynamic properties at an equilibrium position of the rotor-bearing system are as follows:

1. Initialize the problem: load geometrical and operational inputs. Initial assumption of pressure and temperature distribution.

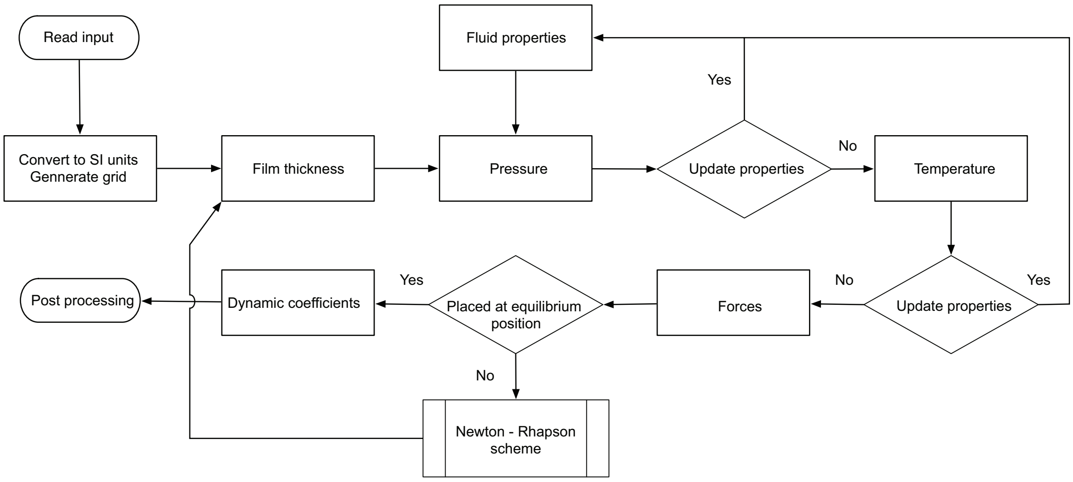

Figure 3.12: General sketch of the solution procedure.

2. Convert to SI units and generate computational grid. In general the discretization of the domain is non-uniform, however if the problem is for a plain aerodynamic bearing the computational effort can be minimized by choosing an uniform mesh.
3. Determine an analytical expression for the film thickness function, (3.10), depending on the instantaneous position of the rotor, e_{X_0}, e_{Y_0}.
4. Estimate pressure field (3.39) with boundary conditions indicated in eq. (3.17). The discrete formulation is given in section 3.5.1.
5. Estimate temperature filed, eq (3.56) with boundary conditions eq. (3.65). The discrete formulation is given in section 3.5.2.
6. Update fluid properties. For every given journal position, steps 4-6 are repeated until the pressure-temperature solution has converged.
7. Numerically integrate the zeroth-order pressure distribution to obtain the fluid forces, eq (3.108).
8. Calculate the steady state equilibrium of the rotor-bearing system as described in section 3.5.4. Steps 3-7 are then repeated in an iterative scheme until the equilibrium is reached.
9. Calculate the dynamic properties of the bearing, by solving eq. (3.40) and (3.41) as indicated in section 3.5.5.

10. Terminate and post-process.

3.5.6.2 Active bearing

In principle, dynamic analysis of the rotor-bearing system operating with active lubrication could be performed bypassing the dynamic of the piezoelectric injection system described in Section 3.4.1, under the assumption that the injection pressures P_{inj} are known as a function of time. As it has been shown, see Eq. (3.76), these pressures depend on the actuators dynamics and the gain coefficients of the feedback law. For calculating the dynamic response it is then necessary to take into account Eqs. (3.75) and (3.77), which provide the coupling between rotor-bearing system and piezo actuators. The numerical procedure is essentially similar to that described in the previous section for the equilibrium position. In this case, starting from a calculated equilibrium position, the dynamic solution in time domain is obtained by numerically integrate the dynamic equations of the rotor bearing system, injector dynamic and feedback law. A simple Runge-Kutta scheme has been implemented for this purpose.

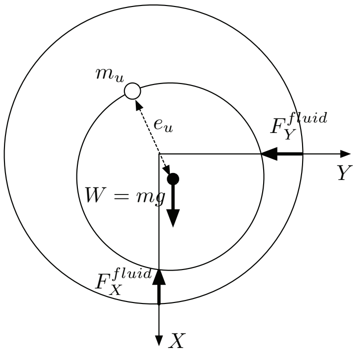

Figure 3.13: Physical representation of the forces acting on the rotor.

In the present context, for the sake of keeping a very simple mathematical description of the rotordynamic system, the rotor is assumed to be rigid, yielding to a 2 degrees of freedom mathematical model. When modeling a flexible system however, the size of the model is sensibly increased; alternatively in order to minimize the computational effort, a modal reduction can be implemented, see section 5.1.5. The equation of motion of the rotating system is expressed by:

$$\mathbf{M}\ddot{\mathbf{q}}(t) + \mathbf{D}\dot{\mathbf{q}}(t) + \mathbf{K}\mathbf{q}(t) = \mathbf{F}^{ext}(t) + \mathbf{F}^{fluid}(t) \tag{3.123}$$

where $\mathbf{M}$, $\mathbf{D}$ and $\mathbf{K}$ are the mass, damping and stiffness matrices of the rotor, $\mathbf{q}(t) = [e_X \, e_Y]^T$ the displacement vector. $\mathbf{F}^{ext}(t)$ is the vector of externally applied forces, which accounts for gravity and eventual unbalance, and $\mathbf{F}^{fluid}(t)$ the vector of (nonlinear) dynamic reaction forces of the bearing, defined by (3.18). Considering an unbalanced rigid disc interacting with the fluid film forces, $\mathbf{D}$ and $\mathbf{K}$ can be neglected, and one can rewrite Eq. 3.123 in matrix form as:

$$\begin{bmatrix} m & 0 \\ 0 & m \end{bmatrix} \left\{ \begin{array}{c} \ddot{e}_X \\ \ddot{e}_Y \end{array} \right\} = \left\{ \begin{array}{c} mg + m_u e_u \Omega^2 \cos(\Omega t) \\ m_u e_u \Omega^2 \sin(\Omega t) \end{array} \right\} + \left\{ \begin{array}{c} F_X^{fluid}(e_X, \dot{e}_X, e_Y, \dot{e}_Y) \\ F_Y^{fluid}(e_X, \dot{e}_X, e_Y, \dot{e}_Y) \end{array} \right\} \tag{3.124}$$

In a time marching integration algorithm, in practice the following equations are solved at each time step:

1. The equation of motion of the rotor bearing system:

   $$\ddot{\mathbf{q}}(t) = \mathbf{M}^{-1}\mathbf{F}^{ext}(t) + \mathbf{M}^{-1}\mathbf{F}^{fluid}(t) \tag{3.125}$$

2. The dynamic nonlinear fluid film forces:

   $$\mathbf{F}^{fluid}(t) = \left\{ \begin{array}{c} F_X^{fluid}(e_X, \dot{e}_X, e_Y, \dot{e}_Y) \\ F_Y^{fluid}(e_X, \dot{e}_X, e_Y, \dot{e}_Y) \end{array} \right\} = \int \int_A (p - p_{atm}) dA \tag{3.126}$$

   Note that in the dynamic case, in order to obtain the correct pressure profile, Eq. 3.3 must be solved taking into account the transient term, which is implicitly integrated as:

   $$12 \frac{\partial (ph)}{\partial t} = 12 \left[\frac{(p_t - p_{t-1}) h_t}{\Delta t} + \frac{\partial h}{\partial t} p_t \right] \tag{3.127}$$

   Where $\frac{\partial h}{\partial t}$ is the squeeze component, which can be obtained by analytical differentiation of Eq. 3.6

3. The injector dynamic set:

   $$\dot{\mathbf{y}}(t) = f(t, \mathbf{y}(t), \mathbf{u}(t)) \tag{3.128}$$

4. The feedback law:

   $$\mathbf{u}(t) = \mathbf{G}^k \mathbf{q}(t) + \mathbf{G}^d \dot{\mathbf{q}}(t) \tag{3.129}$$

   which provides the essential coupling between the rotor bearing system degrees of freedom, $\mathbf{q}(t)$, and the injector ones $\mathbf{y}(t)$, through the input signal $\mathbf{u}(t)$

3.6 Validation and selected numerical examples

This section covers the validation of the developed numerical model and presents selected case studies aimed at defining the general characteristics of the fluid film bearing, which is the foundations for a more thorough experimental analysis presented in chapter 5. Although the main goal of the project is ultimately to evaluate the design and performance of an active lubricated gas bearing, such analysis cannot be performed regardless of validation of the mathematical numerical model for the passive operation.

3.6.1 Grid convergence

In order to determine a proper discretization of the domain, a grid convergence analysis has been performed. The parameter of concern is the relative deviation of a coarser solution compared to a fine one:

$$\xi = max\left(\frac{\varphi - \varphi_{fine}}{\varphi_{fine}}\right) \cdot 100 \tag{3.130}$$

where $\varphi \in \{p, T\}$. The fine grid solution has been obtained with $N = \sqrt{m \cdot n}$=501 grid points. The result of the analysis is shown on Fig. 3.14. It can be inferred that a discretization of $N = 40$ is sufficient to ensure that the discretization error of both the Reynolds and energy equation is less than 1%. Thus, unless otherwise stated, for computational speed reasons a coarser grid has been utilized for the numerical analysis. Note the different slopes of the convergence curves; while the pressure solution is obtained with second order finite difference approximation, the temperature solution contains elements of first order.

3.6.2 Comparison with published results

The solution of the compressible Reynolds equation has been validated against experimental results presented by Powell [72] shown in Fig. 3.15. The calculations are made with for the aerodynamic equation with the full THD-model and air as lubricant. From the figure, a good agreement between the experimental results and the numerical calculations is seen, even though the maximum pressure for a bearing number of $\Lambda = 1.15$ is slightly underestimated. As pressure solutions depend on the applied load rather than the temperature, the equilibrium position, which determine the pressure distribution, depends on the viscosity field, thus indirectly the temperature. The fact that the pressure solutions are equivalent thus reasonably suggests the validity of the model.

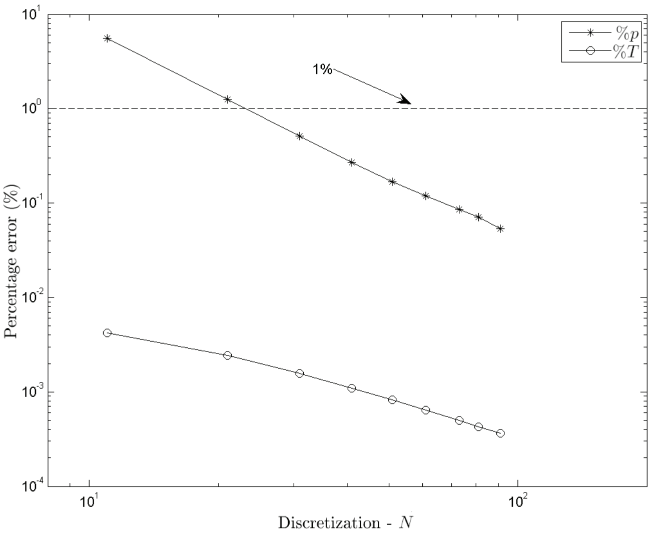

Figure 3.14: Analysis of grid dependency on the compressible Reynold's and energy equation respectively.

Another parameter used for the validation of the aerodynamic Reynold's equation solution, is to compare attitude angle results. Figure 3.16 compares the results from Dimofte [21] (which also includes validation with Raimondi [76]) with those obtained with the present program. Such results are obtained by fixing the value of eccentricity, while increasing the bearing number value. Note, the bearing number is an non-dimensional quantity defined as:

$$\Lambda = \frac{6\mu UR}{(p_{atm}C^2)} \tag{3.131}$$

A substantial correlation is observed, adding confidence on the presently developed numerical implementation.

Further comparisons of pressure solutions are provided in order to validate the results obtained with the modified Reynold's equation accounting for radial fluid injection. In this case the comparison benchmark is [53], as good overview of pressure profiles are provided. The validity of this article's benchmarks is also corroborate by its own validation with the results of Lo et al [54]. The configuration of the test bearing under investigation is shown in Figure 3.17. Two sets of eight orifices are arranged in the circumferential direction at an angular distance of 45 deg with each other. Geometrical and operational parameters are matched as indicated. In general, good agreement is obtained when comparing the parametric variation of parameters in the reference. Figure 3.18 presents the comparison of the circumferential

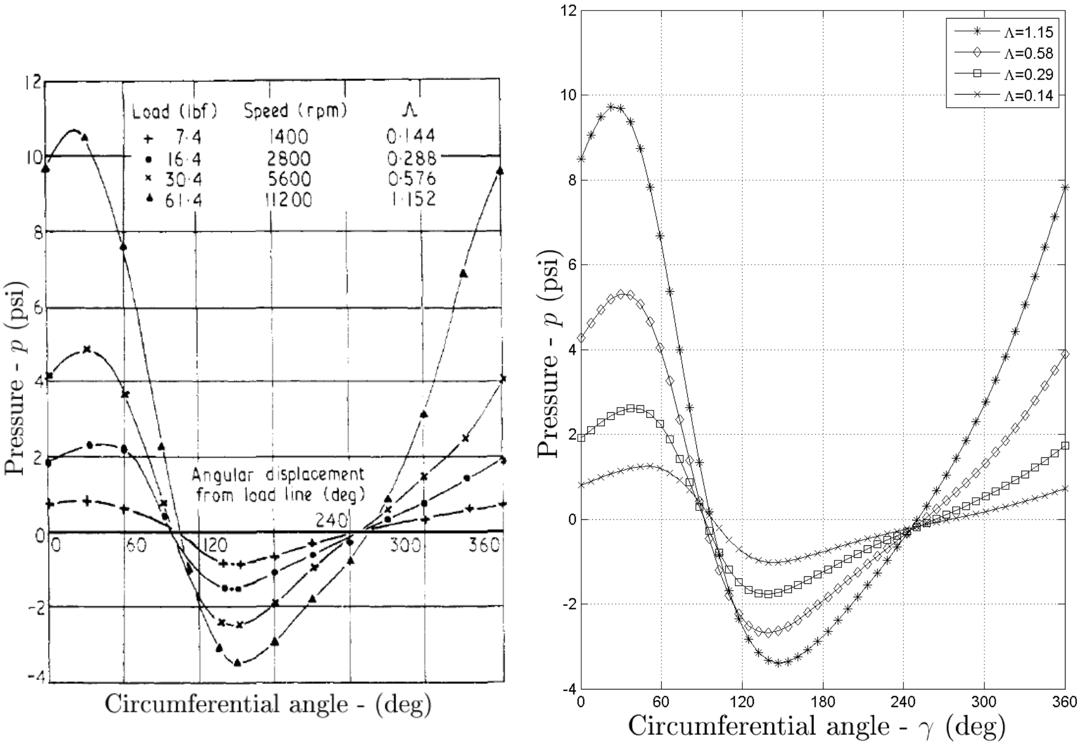

(a) Results from Powell [72]. **(b)** Numerical calculated attitude angles.

Figure 3.15: Comparison between experimental results from Powell [72] and numerical calculations. $L = 101.6$ mm, $D = 50.8$ mm, $C = 26.54$ μm.

pressure profile taken at the location of one of the two rows of orifices plane in the axial direction. The journal is vertically displaced from the center at 90% of the clearance, so that the eccentricity ratio e=0.9. Single contribution of aerodynamic component (obtained solving the aerodynamic Reynold's equation) and aerostatic (Solving the modified Reynold's equation without rotation) as well as the hybrid solution are provided and show a reasonable agreement.

A comparison of computed dynamic perturbation coefficients is made against results presented by Arghir et al. [3] as shown in Fig. 3.19. The results show the evolution of stiffness and damping as function of perturbation (excitation) frequency; while a convincing qualitative agreement is observed, some quantitative disparity can be seen. There is a stark contrast between the smoothness of all curves in Figs. 3.19a and 3.19b to the jaggedness of those in Fig. 3.19c, especially in the range 1.0 to 1.5 of the abscissa. Since in the stability analysis of a rotor-bearing system, determination of the neutral state of instability require numerical root-finding

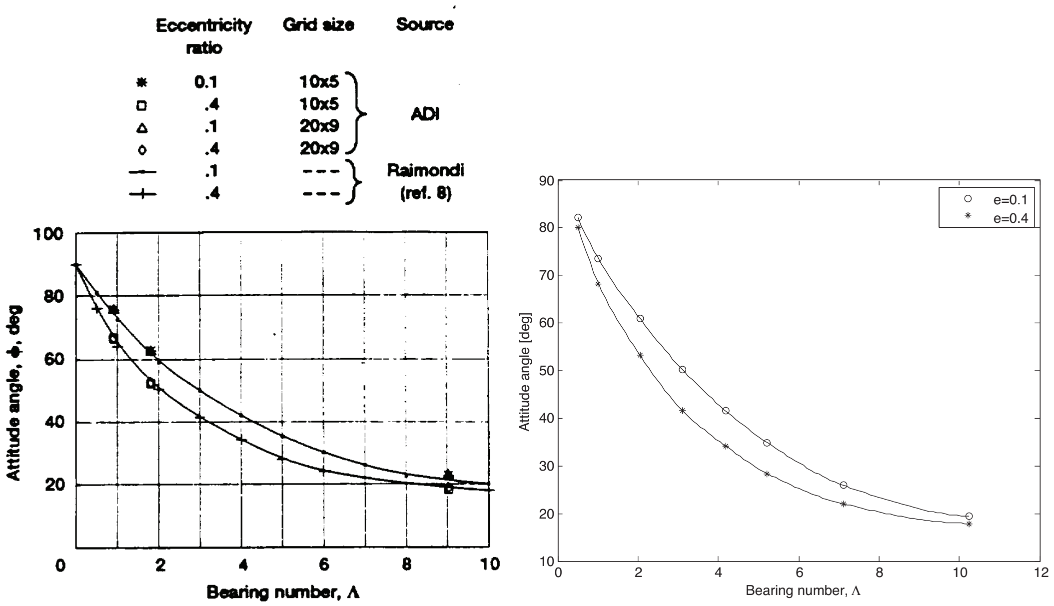

(a) Results from Dimofte [21].

(b) Numerical calculated attitude angles.

Figure 3.16: Comparison between experimental results from Dimofte [21] and numerical calculations.

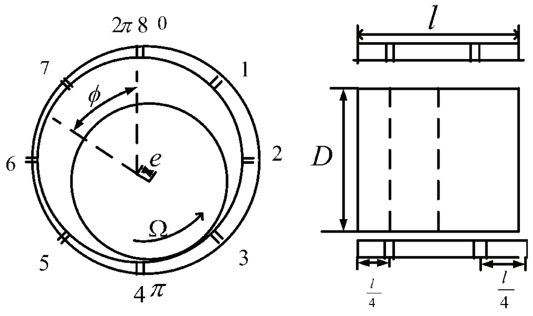

Figure 3.17: Bearing configuration as in [53].

of the characteristic determinant formed by the dynamic perturbation coefficients, a significant improvement in the numerical precision of the present scheme can be reasonably asserted.

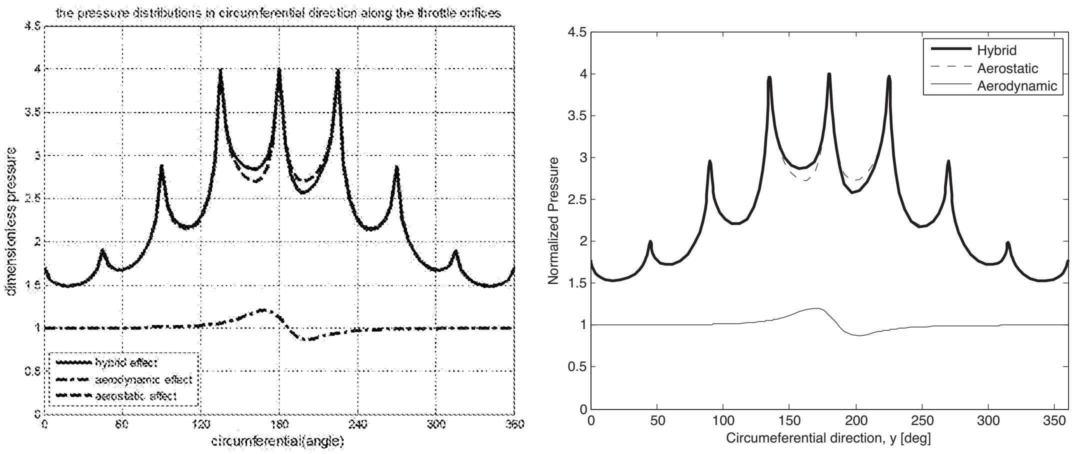

(a) Results from Liu et al. [53].

(b) Numerical calculated pressure profiles.

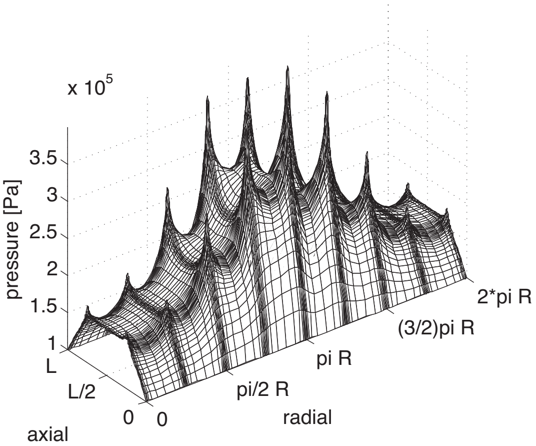

(c) Numerical calculated pressure profiles, 3D view (hybrid).

Figure 3.18: Comparison between experimental results from Liu et al. [53] and numerical calculations. $L = 7.5$ mm, $D = 7.5$ mm, Ω=10000 rpm, $e = 0.9$, $d_0 = 0.2$ mm, $p_{inj} = 4$ atm.

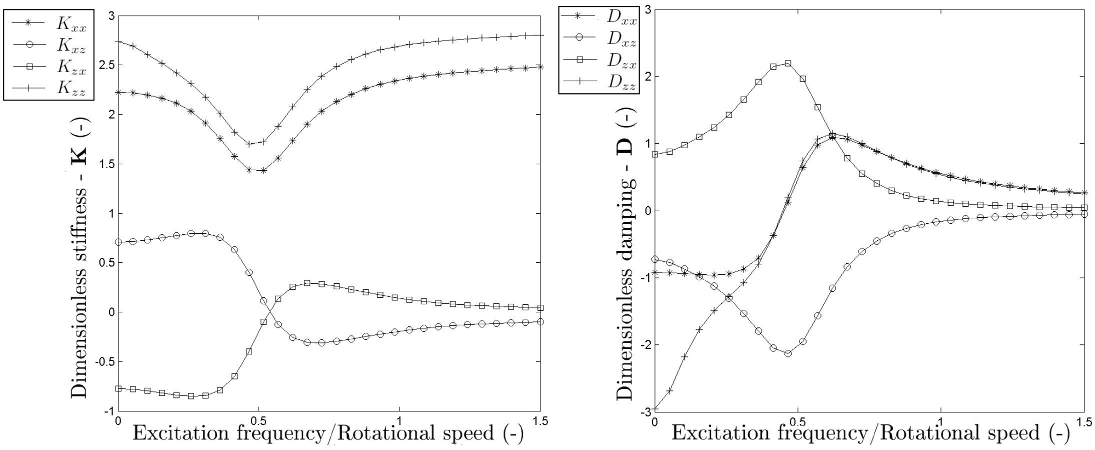

(a) Dimensionless stiffness for a cylindrical air bearing. $\Lambda = 10$, $e = 0.3$ and $L/D = 1$.

(b) Dimensionless damping for a cylindrical air bearing. $\Lambda = 10$, $e = 0.3$ and $L/D = 1$.

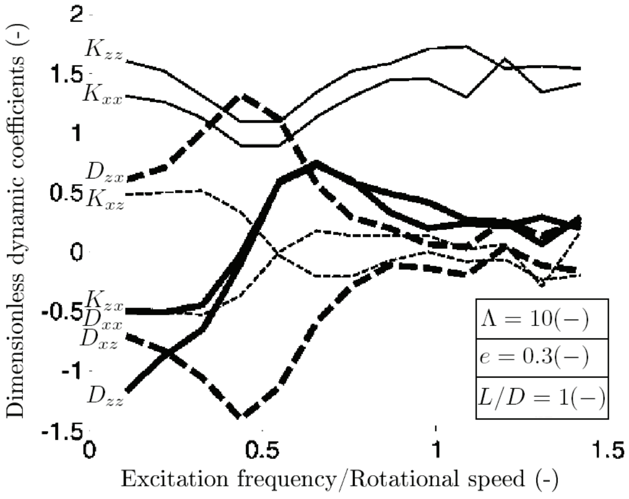

(c) Dimensionless damping and stiffness for a cylindrical air bearing calculated by Arghir et al.. [3].

Figure 3.19: Comparison between calculated dimensionless dynamic coefficients and calculations presented by Arghir et al. [3].

3.6.3 Numerical examples

Selected numerical examples are presented, with the aim of establishing the general characteristics and performance of the prototype bearing built during this project. The number of different analyses that can be performed with the developed numerical methods are almost countless, as the number of possible parameter variations one can put to test. In this framework it is chosen to focus the research effort towards quantities that should be possible to identify with the available experimental setup, tools and time constraints. Parametric analysis mainly involves two quantities: rotational speed and supply pressure.

The reference bearing simulation parameters are as detailed in table 3.1.

Baering diameter	D	40 mm
Bearing length	L	40 mm
Nominal clearance	C	25 μm
Number of orifices		4 (0°, 90°, 180°, 270°)
Diameter of orifices	d_0	0.25 mm
Air viscosity (at 15°)	μ	1.78e-5 Pa.s
Air density (at 15°)	ρ	1.204 kg/m^3
Air ambient temperature	$T_A = T_{inj}$	293° K
Air specific heat capacity (at 15°)	c	1.005 kJ/kg.K
Air thermal conductivity (at 15°)	k	0.257 W/m.K

Table 3.1: Reference bearing properties for numerical analysis.

3.6.3.1 Passive operation

Pressure distribution and equilibrium position. Pressure distributions are presented for 4 different scenarios, see Figure 3.20. All results are obtained for a nominal rotational speed of Ω= 10,000 rpm and for the journal at the corresponding equilibrium position. Case **a)** corresponds to the bearing operating in aerodynamic mode, e.g. without any orifices or orifices closed. In case **b)** the orifices are open, however no pressurized air is fed. It is relevant for the present case to establish the differences between these two scenarios: once the gas bearing is assembled in its final configuration with the piezoactuators, it is in practice not feasible to close all four orifices, thus the closest approximate condition to test aerodynamic mode is to close the pressurized supply feed line valve. Note that the pressure distribution, maximum pressure value and circumferential location are similar for the first two scenarios; for identical operation conditions these parameters are mainly related to the equilibrium position. It means than that it is marginally different, which is confirmed by the analysis presented in Figure 3.21, showing a comparison between equilibrium positions calculated for different scenarios as function of rotational velocity. Returning to Figure 3.20, in cases **c)** and **d)** the bearing operates in hybrid mode, with different injection pressures, 3 and 8 atm respectively. For $p_{inj} = 3$ atm the aerodynamic effect is more pronounced, making the pressure generation mechanism truly "hybrid", whereas at $p_{inj} = 8$ atm the operation becomes dominated by the aerostatic contribution. This behavior is due to two reasons; at lower injection pressures, on one hand the difference between aerodynamic and aerostatic contribution is smaller and on the other the load carrying capacity is lower. Thus eccentricity values are higher (see also Figure 3.21) and in turn the maximum aerodynamic pressure is also higher.

Temperature distribution. Temperature distribution for different bearing case studies and rotational velocities are presented in Figures 3.22, 3.23 and 3.24. These graphs are obtained solving the coupled pressure-temperature problem and represent the predicted fluid film temperatures at the corresponding equilibrium positions. In Figure 3.25 a comparison between equilibrium positions as function of rotational velocity is presented, calculated with isothermal theory and including the energy balance.

The first set, see Figure 3.22, refers to the bearing operating in aerodynamic mode; in case **a)** the speed is limited to 2,000 rpm, which is the lower limit for the pressure solution convergence. Note that at lower velocities aerodynamic lift may be still achievable in practice, however numerical solution is cumbersome at high eccentricities, due to the generation of steep gradients (both pressure and film thickness). At such low velocity, the temperature distribution is closely related to the film thickness profile, as viscous dissipation is mainly due to the presence of pressure gradients. Referring to the energy equation (3.56), it is clear that heat generation is mainly due either to the Couette or Poiseuille contributions. It means that large heat generation is associated either with high eccentricities and/or high rotational velocities. For the bearing and conditions under analysis, it will be shown how the latter mechanism prevails. As the speed increases, see cases **b)**, **c)** and **d)**, average temperature increases accordingly, while it also noticed that the location of maximum temperature also changes, reaching a maximum angular value for the 20,000 rpm case. This behavior is parallel to the evolution of equilibrium positions as analyzed in Figure 3.21 and 3.25. Note that at 30,000 rpm the lowest value of attitude angle is expected, however it is difficult to see from the temperature profile presented for case **d)**, as

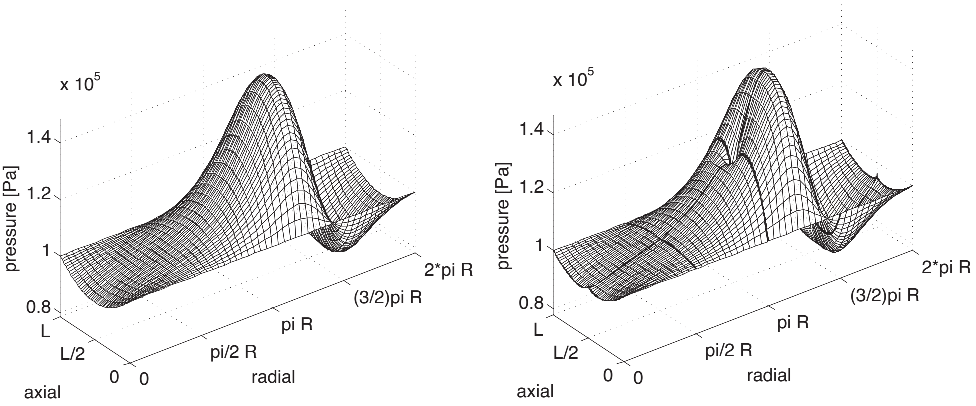

(a) Pressure distribution, aerodynamic mode.

(b) Pressure distribution, $p_{inj} = p_{atm}$.

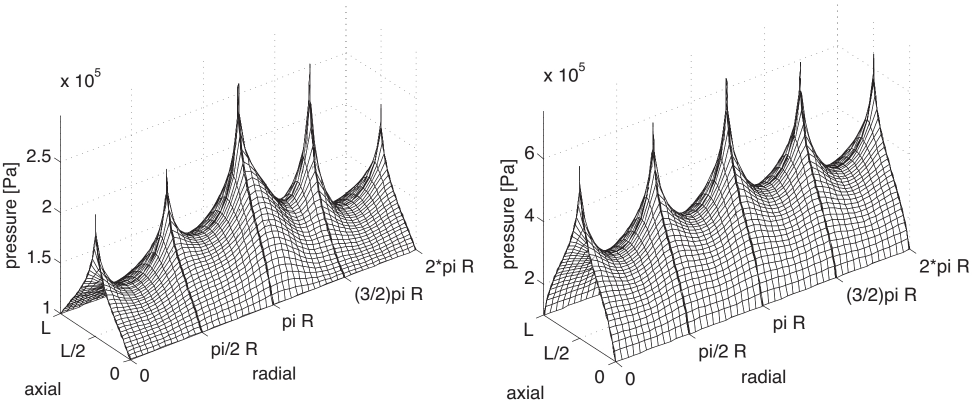

(c) Pressure distribution, p_{inj} = 3 atm.

(d) Pressure distribution, p_{inj} = 8 atm.

Figure 3.20: Comparison between pressure profiles calculated for different scenarios at Ω= 10000 rpm.

the maximum temperature range is distributed over a much longer circumferential portion of the bearing when compared for example to case **a)**. The reason is as follows: as noted earlier, at low speed heat generation is mainly due to steep pressure gradients, which in turn are due to high eccentricity ratios. At higher speeds however, while it is true that tangential velocity becomes the main heat source, the eccentricity values are smaller, thus pressure gradients are smoother (less steep), determining also a "smoothening" of the temperature distribution.

Moving to Figure 3.23, the same parametric study is performed for the hybrid mode case, where the injection pressure is 3 atm. At 2,000 rpm, case **a)**, the temperature distribution

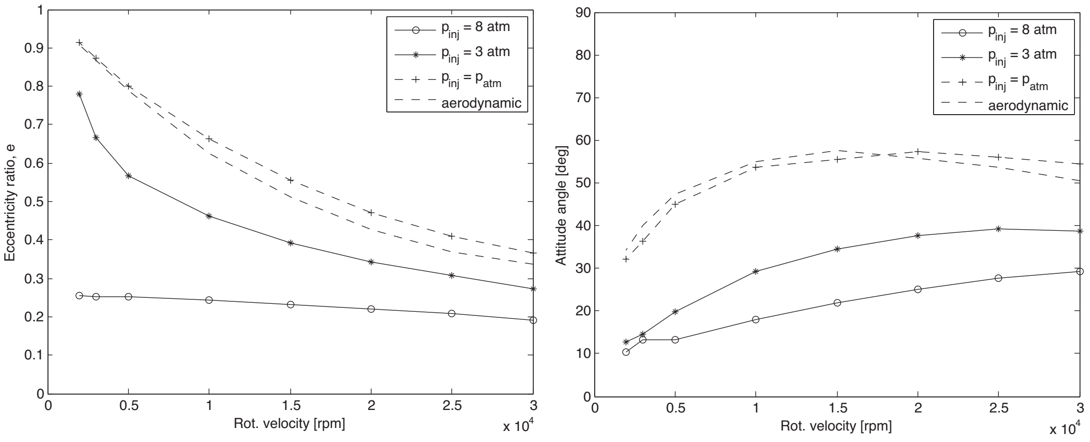

(a) Eccentricity ratios.

(b) Attitude angles.

Figure 3.21: Comparison between equilibrium positions calculated for different scenarios as function of rotational velocity.

is remarkably similar to the aerodynamic case discussed earlier. Indeed, at this lower supply pressure aerodynamic pressure generation is a strong component. Eccentricity is also at level similar to the aerodynamic case, whereas the attitude angle is quite lower. These informations explain why the position of the maximum temperature has moved closer to be aligned with the vertical. The reduction of air temperature in the hybrid bearing occurs locally, in areas forward the orifices. This is particularly true in areas where values of film thickness are lower. The reason for that is the local predominance of the flow in the circumferential direction (velocity components in y direction are larger than those in z direction). Thus, heat transfer in the axial direction is less significant. Where the film thickness is larger, however, differences in magnitude between velocity components in either direction are less pronounced, allowing a larger heat transfer in the axial direction. Such effect can be easily detected by comparing cases **a)** and **b)** at higher angular velocity.

Similar analysis and conclusions can be drawn for Figure 3.24, where the injection pressure is raised to 8 atm. Larger aerostatic forces increase the carrying capacity and move the journal closer to the center of the bearing, yielding lower eccentricity. Combined with more air at T_{inj} being supplied through the orifice, the temperature rise at 2,000 rpm, case **a)**, is practically absent. Low eccentricity values determine also more modest temperature rises at higher speeds, **b)**, and in general explain why the heat transfer is relevant both in circumferential and axial directions. From the analysis of Figure 3.25 the following general observations can be made:

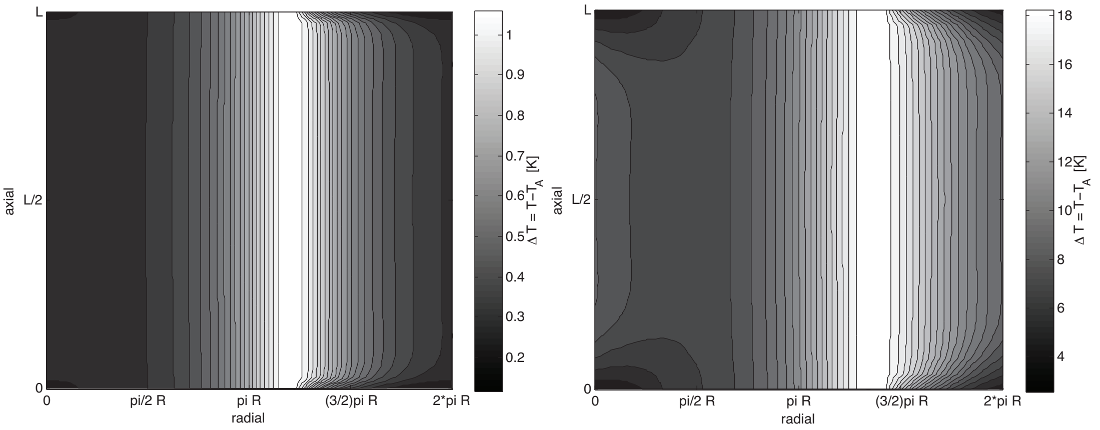

(a) Temperature distribution, aerodynamic mode, Ω= 2,000 rpm.

(b) Temperature distribution, aerodynamic mode, Ω= 10,000 rpm.

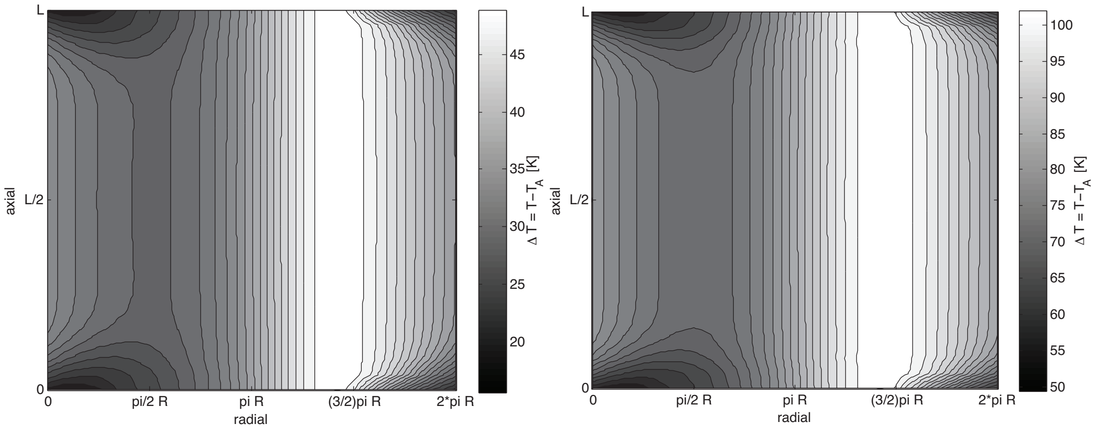

(c) Temperature distribution, aerodynamic mode, Ω= 20,000 rpm.

(d) Temperature distribution, aerodynamic mode, Ω= 30,000 rpm.

Figure 3.22: Comparison between temperature profiles calculated in aerodynamic operation at different rotational velocities.

at low speed thermal effects are negligible, regardless of the pressure generation mode (aerodynamic or hybrid). As velocity increases and temperature rises, eccentricity and attitude angles start to deviate towards larger values. The behavior can be interpreted as follows: as explained in section A, unlike for liquid lubricants the viscosity of gases increases with the temperature. this in turn causes an increase in the load carrying capacity introduced by the thermal wedge. Such conclusions are consistent, among others, with the work of Peng and Khonsari [69].

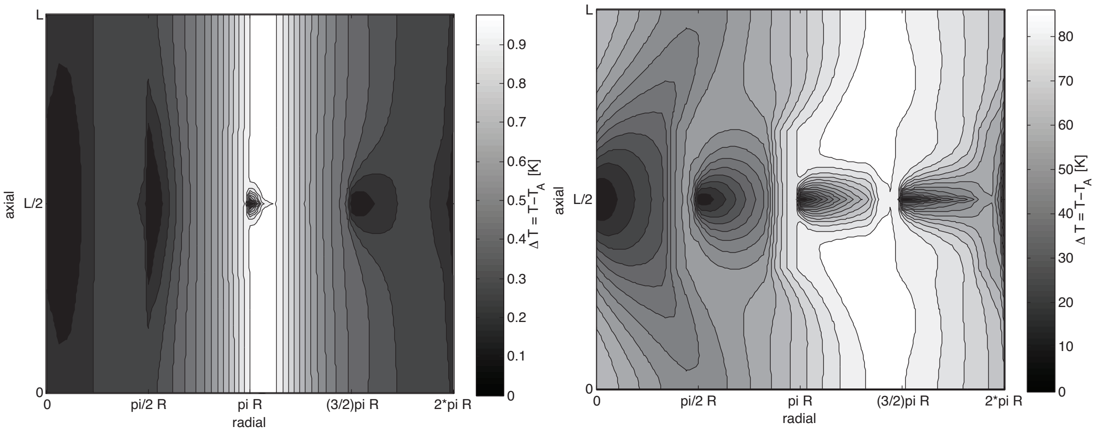

(a) Temperature distribution, $p_{inj} = 3$ atm, $\Omega = 2,000$ rpm.

(b) Temperature distribution, $p_{inj} = 3$ atm, $\Omega = 30,000$ rpm.

Figure 3.23: Comparison between temperature profiles calculated in hybrid operation, $p_{inj} = 3$ atm, at different rotational velocities.

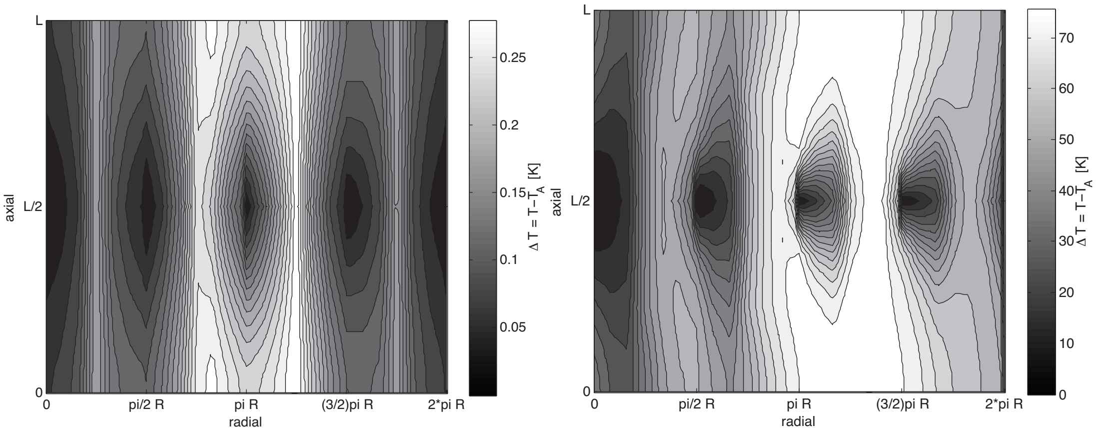

(a) Temperature distribution, $p_{inj} = 8$ atm, $\Omega = 2,000$ rpm.

(b) Temperature distribution, $p_{inj} = 8$ atm, $\Omega = 30,000$ rpm.

Figure 3.24: Comparison between temperature profiles calculated in hybrid operation, $p_{inj} = 8$ atm, at different rotational velocities.

Dynamic coefficients. The variation of synchronous[1] stiffness and damping coefficients for the bearing under analysis is evaluated as function of the rotational speed. Formally, the dynamic coefficients calculated with small perturbation theory is only valid for infinitesimal

---

[1] It is worth reminding that unlike in the incompressible fluid film lubrication, the dynamic coefficients of compressible fluids are (strongly) dependent on the excitation frequency.

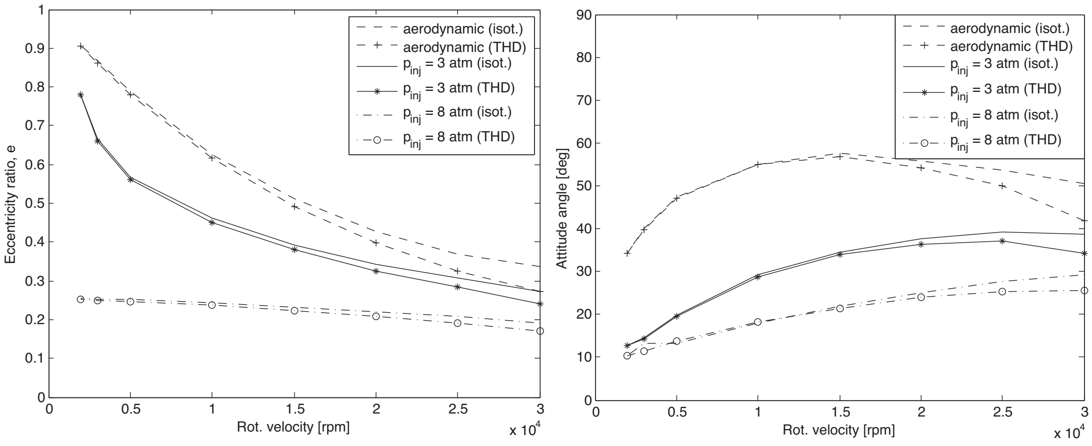

(a) Eccentricity ratios. **(b)** Attitude angles.

Figure 3.25: Comparison between equilibrium positions calculated for with and without THD analysis as function of rotational velocity.

amplitudes. However, in practice it holds for amplitudes as large as up to one half the radial clearance, thus covering the range of interest in most applications.

Figures 3.26, 3.27, 3.28 and 3.29 refer to aerodynamic, open orifices $p_{inj} = p_{atm}$, hybrid $p_{inj} = 3$ atm and hybrid $p_{inj} = 8$ atm respectively. For the bearing operating in aerodynamic mode, it can be noticed that stiffness and damping coefficients assume large values at low rotational velocities. As previously analyzed, in such operational region the bearing equilibrium position is set at very large eccentricity values. Physically, increasing eccentricity increases the direct stiffness with respect to the cross-coupled stiffness. This is also evidenced by a decreasing attitude angle with increasing eccentricity. In addition, squeeze-film damping becomes stronger when the separation between surfaces is reduced. As the velocity increases, damping and direct stiffness are greatly reduced. Note that at higher speeds the cross-coupled damping assumes an antisymmetric configuration, diverging from zero; such behavior is generally not desirable, as the destabilizing property of bearings stems from the lack of symmetry of cross-coupled coefficients. The behavior of the bearing dynamic coefficients with open orifices, see Figure3.27 is substantially equivalent to the aerodynamic case, and no macroscopically different physical characteristic can be inferred limited to this analysis.

Certain similarities with respect to hybrid operation are also identifiable to the lower injection pressure case, see Figure 3.28. The damping characteristics particularly follow the general behavior of the aerodynamic case, even so the magnitude is slightly reduced. The stiffness however has quite different characteristics, with the direct terms rapidly increasing with the rotational speed. It is noticed that at the lowest speed the direct vertical term K_{XX} tends to increase sharply; this is due to the high eccentricity in such conditions. As for the cross-coupled stiffness, the asymmetric configuration is more marked, with a maximum between 12,000 and 15,000 rpm. This will be reflected in the experimental results, where whirling instability onsets. As the aerostatic component is increased further, see Figure 3.29, the bearing becomes noticeably stiffer, with asymmetric behavior of the cross-coupled terms, with the spreading of the two curves accentuating at higher speed. Also, the damping coefficients are sensibly reduced in this case, with the squeeze film damper effect disappearing for lower velocities. Again, this is consistent with the equilibrium position analysis, see Figure 3.21, which shows low eccentricities even at low speeds.

Regarding influence on stability of dynamic force coefficient of the bearing for the operational range under analysis, a qualitative eigenvalue analysis based on the dynamic coefficients of Figures 3.26 - 3.29 is presented in Figure 3.30. It shows the evolution as function of the rotational speed of the real part of the lowest eigenvalue for a simple 2 degrees of freedom system with unit mass:

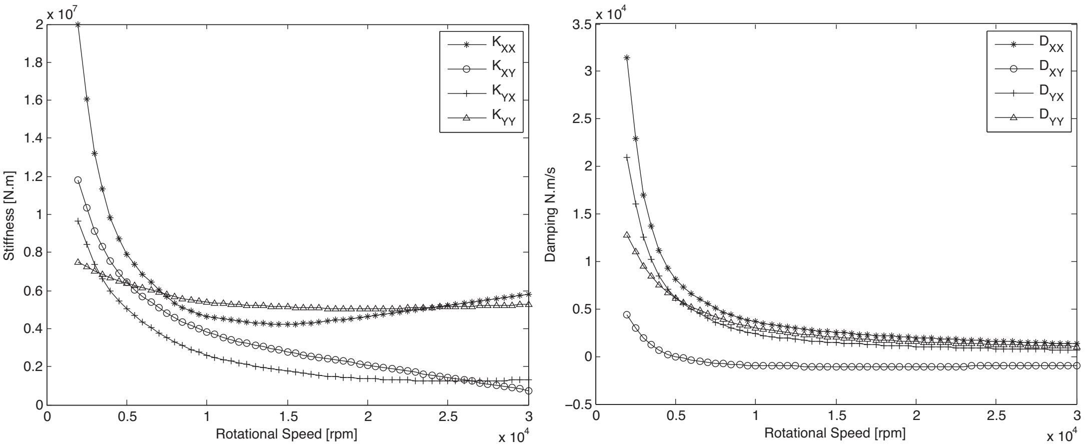

(a) Stiffness.

(b) Damping.

Figure 3.26: Components of the rotordynamic coefficients matrices as function of rotational velocity, aerodynamic operation.

$$\begin{bmatrix} 1 & 0 \\ 0 & 1 \end{bmatrix} \begin{bmatrix} \ddot{X} \\ \ddot{Y} \end{bmatrix} + \begin{bmatrix} D_{XX} & D_{XY} \\ D_{YX} & D_{YY} \end{bmatrix} \begin{bmatrix} \dot{X} \\ \dot{Y} \end{bmatrix} + \begin{bmatrix} K_{XX} & K_{XY} \\ K_{YX} & K_{YY} \end{bmatrix} \begin{bmatrix} X \\ Y \end{bmatrix} = \begin{bmatrix} 0 \\ 0 \end{bmatrix} \tag{3.132}$$

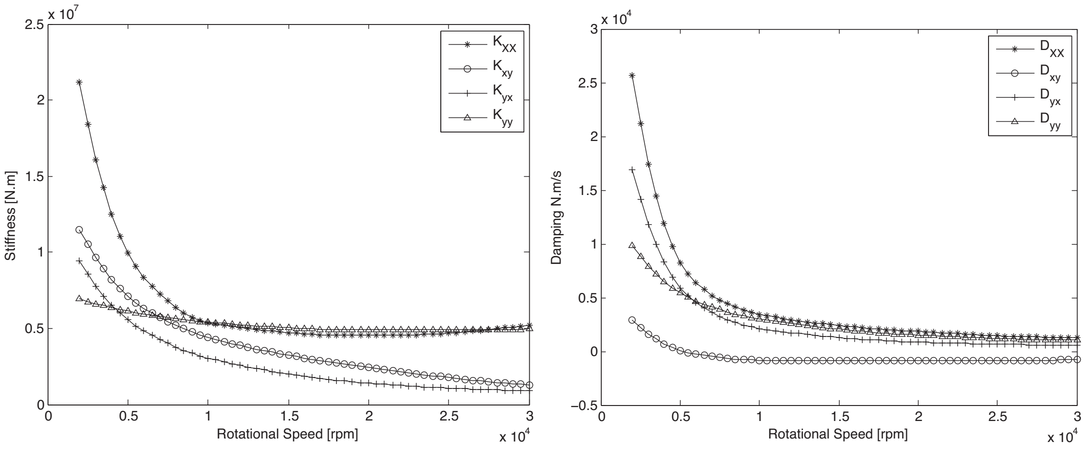

(a) Stiffness. **(b)** Damping.

Figure 3.27: Components of the rotordynamic coefficients matrices as function of rotational velocity, open orifices $p_{inj} = p_{atm}$.

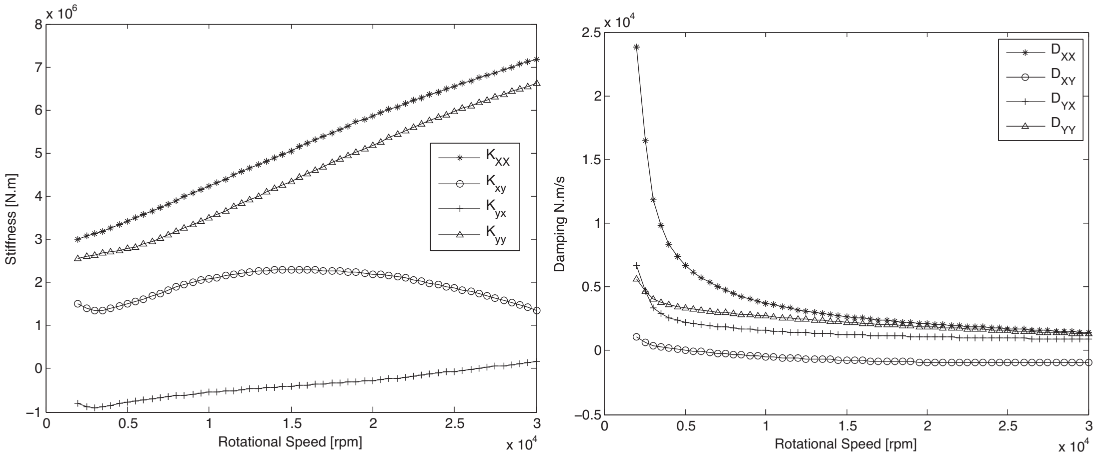

(a) Stiffness. **(b)** Damping.

Figure 3.28: Components of the rotordynamic coefficients matrices as function of rotational velocity, hybrid operation $p_{inj} = 3$ atm.

Note that physically this system can be interpreted as a spinning rigid disc, where gyroscopic effects are neglected. It should be remarked that the real part of the system eigenvalues are associated with the damping level of the system; moreover an equilibrium is stable if the real part of the eigenvalues are negative. The more negative the values, the more the system is damped.

Following an analysis of Figure 3.30. the following observation can then be summarized:

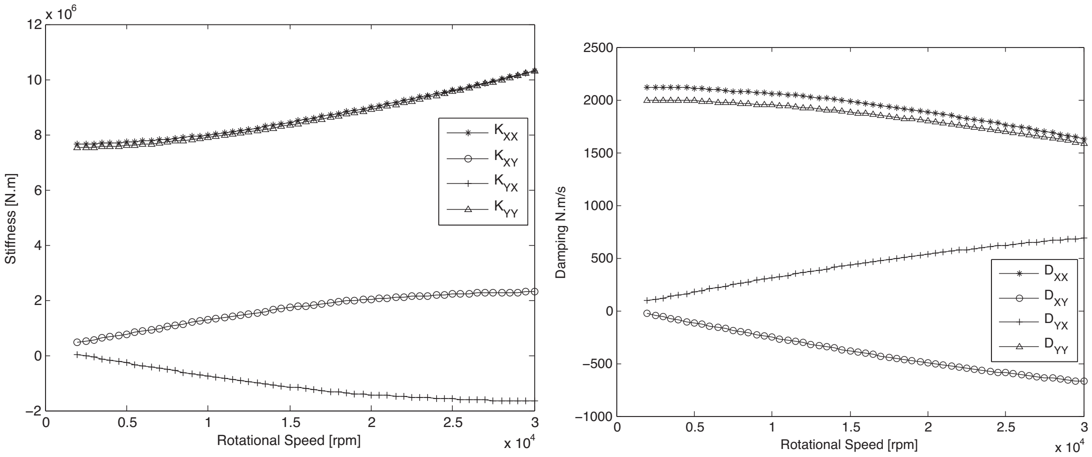

(a) Stiffness.

(b) Damping.

Figure 3.29: Components of the rotordynamic coefficients matrices as function of rotational velocity, hybrid operation $p_{inj} = 8$ atm.

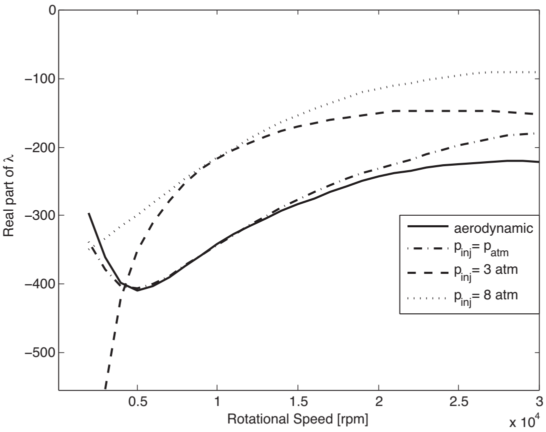

Figure 3.30: Qualitative stability analysis for the bearing in different scenarios, consisting of real part of eigenvalues as function of the rotational speed.

1. Aerodynamic operation: the damping plays the main detrimental role, as cross coupling damping is antisymmetric, D_{XY} = -D_{YX}, see Figure 3.26b. The effect is most noticed at lower speed where the separation between these coefficients is the largest. An optimum value (eigenvalues are most "negative") can be identified just over 5,000 rpm; it should be noted that as the speed increases the damping cross coupling decreases sensibly (thus theoretically yielding a more stable operation), however the direct damping also decreases; moreover the stiffness cross coupling effect asymmetry is increased, see Figure 3.26a.

2. Open orifices, p_{inj}= 1 atm: generally, the same discussion as for the aerodynamic case can be made, as the two curves show an analogous overall behavior, consistent in fact to what observed and commented for Figure 3.21. It should be however mentioned that the system appears slightly more damped at lower speeds, whereas it loses this advantage as the rotation is increased. Physically one could interpret that at low speed extra squeeze film damping effect can be generated by pressing the air out of the journal through the orifices, whereas at higher speed where the damping is mainly due to air compressibility this beneficial mechanism is reverted.

3. Hybrid operation, p_{inj}= 3 atm: both stiffness and damping cross coupling coefficients are antisymmetric, K_{XY} = -K_{YX} and D_{XY} = -D_{YX} although their magnitude, especially damping, remains limited throughout the speed range. The main destabilizing effect arises then from the stiffness contribution. Looking at Figure 3.30, one notices that at low speed the stability margin[1] is the largest: one could argue that stiffness cross coupling is compensated by the high magnitude of direct damping coefficients.

4. Hybrid operation, p_{inj}= 8 atm: both stiffness and damping cross coupling coefficients are antisymmetric, K_{XY} = -K_{YX} and D_{XY} = -D_{YX} and their magnitude markedly increases with the rotational speed. As a result the stability margin decreases throughout the whole speed range.

The influence of temperature effects on the dynamic coefficients of the bearing is presented in Figure 3.31. A detailed view is also shown in Figure , as at speed below 10000 rpm, the deviation between the results obtained with isothermal and THD models is unappreciable. For the same reason, only the aerodynamic bearing coefficients are analyzed here, as for the hybrid case the deviation is even smaller.

Firstly, it shall be noticed that the deviation between the two models is generally small and constant in the entire domain. Physically, the dynamic coefficients are used to obtain a linear representation of the aerodynamic force. Therefore, the integral of the aerodynamic pressure is the fundamental field to obtain such dynamic coefficients. The pressure distribution in a journal bearing is directly affected by the temperature distribution as well as the equilibrium position at which the dynamic coefficients are calculated, as these quantities enter directly in their mathematical expressions. Moreover, viscosity increases driven by the heating of the air

---

[1] Here by stability margin it is intended the magnitude of the distance of the real part of an eigenvalue from the zero line.

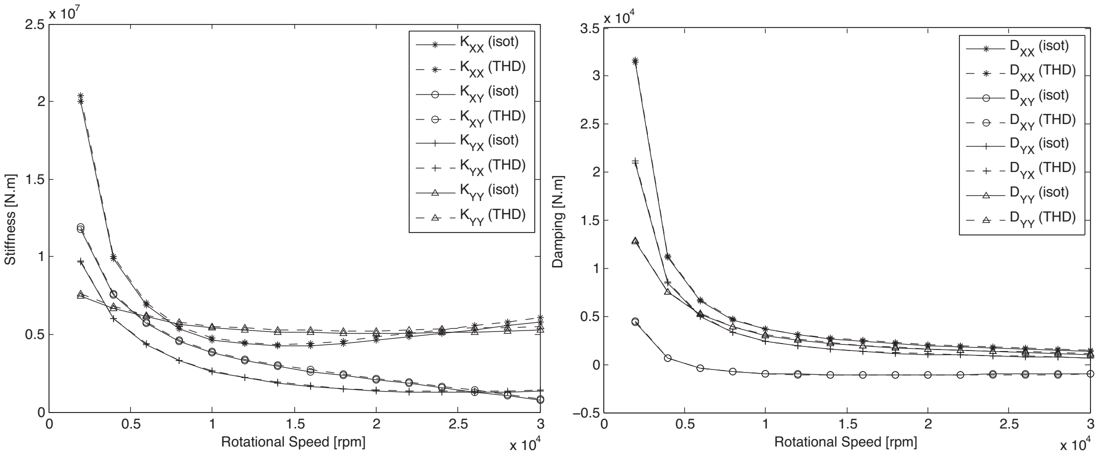

(a) Stiffness. **(b)** Damping.

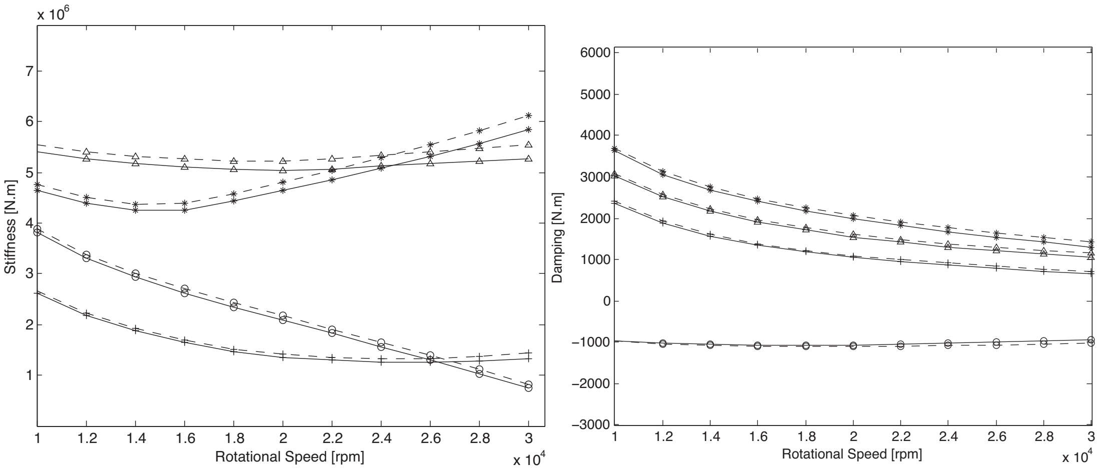

(c) Stiffness (detail). **(d)** Damping (detail).

Figure 3.31: Components of the rotordynamic coefficients matrices as function of rotational velocity, aerodynamic operation, with and without THD analysis.

film indirectly affects the equilibrium position, as the aerodynamic forces also increase. As for the heat generation, one should consider that it is essentially driven by the two phenomena described in the previous section; Poiseuille terms especially relevant at high loads or low rotational speeds and a Couette term that dominates the energy equation at higher rotational speeds. Then, the deviation between isothermal and THD calculated dynamic coefficients is given by a combination of the shifting of the equilibrium position and the different mechanisms that drive the heat generation; at low speed the deviation must be mostly driven by temperature and viscosity gradients caused by the Poiseuille dissipation, because little deviation are observed in the eccentricity and attitude angles values. At high speed, although the temperatures and viscosity fields are subjected to larger variations, the equilibrium position is shifted more towards the center of the bearing, where the pressure fields tend to assume asymptotic values.

Further thermal analysis is presented in journal contribution **J1**, where analysis is extended for bearing with different geometries and operational variables.

3.6.3.2 Active operation

Selected numerical examples are presented for the journal bearing operating in passive and active mode. An overview of the simulations parameters is presented in Table 3.2. The passive mode refers to regular hybrid aerostatic/aerodynamic operation, with the piezoelectric actuators fixed in the open position. In the active mode the actuators receive the feedback control signal as an input, regulating the closing and opening of the valves. As an example with obvious practical purposes, the goal of the PD controller is set to minimize the vibration amplitude of the system. In general, when the system is excited by an unbalance or subjected to a shock it will start oscillate around its equilibrium with a certain amplitude and at frequencies depending on the excitation and the system itself. In order minimize the response, one strategy is to direct the

Piezoactuator pin mass	m_{pin} = 0.05 kg
Belleville spring stiffness	k_{mech} = 5$\cdot$ 10^6 N/m
Piezoactuator equivalent damping	d_{mech} = 2000 N/m s
Piezoelectric element stiffness	k_{piezo} = 3$\cdot$ 10^7 N/m
Piezoelectric coupling coefficient	$c_{piezo} = 65 \cdot 10^{-8}$ C/N
N. of piezoelectric elements in stack	N_{stack} = 100
Gas constant of air	R = 287 J/kg K
Specific heat ratio	k = 1.4
Proportional gains	$G_X^k = G_Y^k$ = -10^{-5} V/m
Derivative gains	$G_X^d = G_Y^d = 10^{-3}$ Vs/m
Time step	$\Delta t = 10^{-7}$ s
Unbalance mass	m_u = 0.0025 kg
Unbalance eccentricity	e_u = D/2

Table 3.2: General simulations parameters.

active forces against these movements around the equilibrium. The term active forces here refers to the portion of aerostatic force contribution that can be adjusted by regulating the movement of the piezo actuators. In practice the following solution has been adopted: according to a given displacement and velocity of the rotor, the piezo actuators are selectively open or closed in order to generate a resultant force in the appropriate direction, see Figure 3.32 . In this case, one should note that by closing one of the piezo valves, its net contribution to the active force is "negative", as its aerostatic component is suppressed. Moreover, the piezo actuators aligned on the horizontal ($-X$) direction are fed back with the horizontal displacement and velocity components (e_X, $\dot{e}_X$) and similarly for the vertical direction.

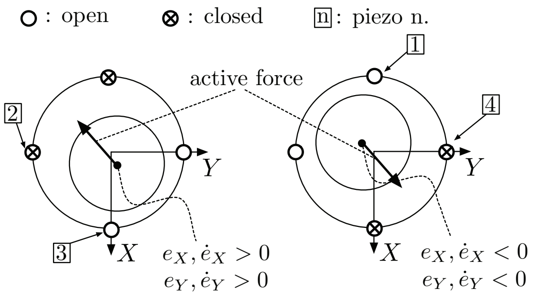

Figure 3.32: Schematic view of the control strategy adopted.

A first test is performed at a rotational speed of 12,000 rpm. Starting from the equilibrium position of the passive system for this operation parameters, the equation of motion is integrated and after ensuring that the transient has decayed, the controller is turned on. Figure 3.33 presents the time history of the rotor vertical displacement compared to the displacement of the piezo actuator 3. Prior to the controller switch on, the rotor appears to have a periodic behavior, which is typical linear synchronous response to unbalance excitation. Note the vibration amplitude is limited to less than 10% of the radial clearance and the equilibrium position is taken as a reference value. As the controller is switched on, the response is significantly altered. Most importantly, it is noticed that after an initial settling time the steady vibrations of the active system are noticeably reduced compared to the passive case. Secondly, it is possible to observe another, higher, frequency component overlapped to the fundamental one. The situation becomes more clear when analyzing the harmonic content of the passive and active signals as function of the normalized frequency (with respect to the rotational one), see Figure 3.34.

While it is confirmed the ability of the controller to efficiently reduce the synchronous vibration component, it becomes evident how the system responds to another, higher one. This frequency is in fact a new characteristic of the mechatronic system composed by the rotor-bearing and piezoelectric injection system; its value is a function of the physical and operational parameters of rotor-bearing system, the characteristics of the piezoelectric actuators and the mechanical subsystem they are mounted within and, most importantly, the controller gains. As the speed is increased to 13,000 rpm, the passive system response sees a marked change. Starting from the equilibrium position, the vibrations show an unstable behavior which lead to a growth to much larger amplitudes, spanning much of the bearing nominal clearance, Figure 3.35. The corresponding frequency spectrum analysis, Figure 3.36, reveals the nature of this motion, which, besides the synchronous response due to the unbalance, is dominated by a subharmonic, half period component: the half-speed whirl. This feature is characteristic of rigid sleeve, gas lubricated journal bearings and it is perhaps the primary factor that limits their performance and usefulness [6], as the journal is characterized by extremely large motion amplitudes, spanning as much as the whole clearance. However, when the controller is turned on, the vibration level is dramatically reduced and, the half frequency whirl motion suppressed and the steady state motion assumes similar qualitative and quantitative characteristics to those described earlier for the 12,000 rpm case, with a higher system frequency superimposed to a limited synchronous component. Note that although for both of the cases examined the vibrations response with ac-

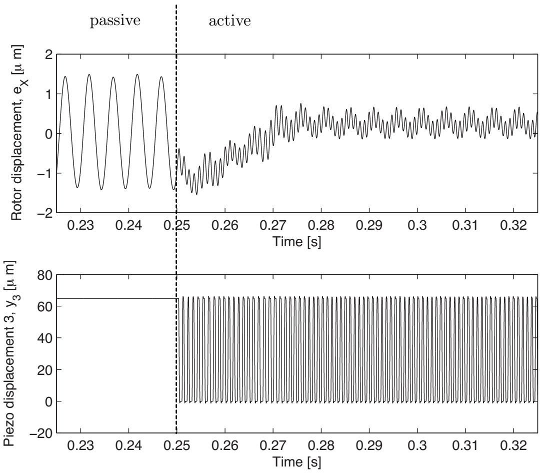

Figure 3.33: Rotor and piezo actuator displacement responses around the equililbrium, passive and active mode, Ω=12,000 rpm.

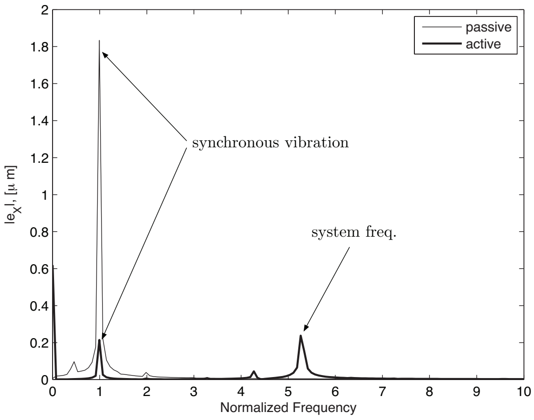

Figure 3.34: Single-sided power spectra of rotor displacement responses, passive and active mode, Ω=12,000 rpm.

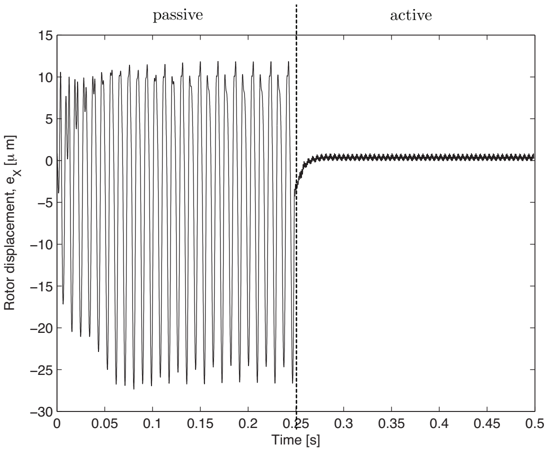

Figure 3.35: Rotor and piezo actuator displacement responses around the equilibrium, passive and active mode, Ω=13,000 rpm.

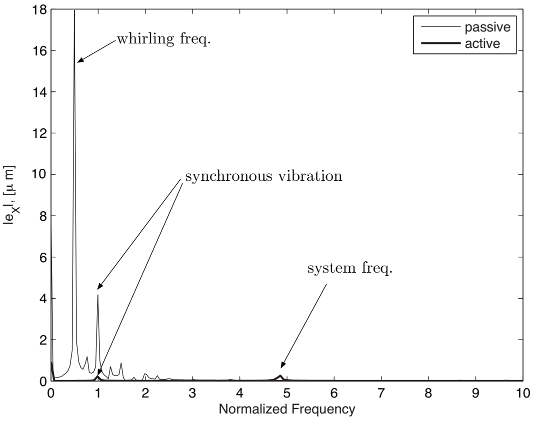

Figure 3.36: Single-sided power spectra of rotor displacement responses, passive and active mode, Ω=13,000 rpm.

tive lubrication settles to similar steady state values, the performance compared to the passive mode appears sensibly different from case to case, due to the largely different passive system response.

For a final example of the qualities of the active lubrication in addressing the unbalance response of the system, the speed is further increased to 18,000 rpm, well above the whirling threshold. For the passive operation, at this speed the sub-synchronous motion amplitude is not contained within the bearing clearance anymore, but large enough to cause touch-down between rotor and bearing. With the controller on, however, the vibrations are kept to limited values, see Figure 3.37 while the whirling motion is eliminated, see Figure 3.38, and only low-energy synchronous and system frequencies are retained.

Typical industrial rotating machinery environments may induce sudden shocks which result in sudden large amplitude responses. Therefore it is utmost favorable that the rotating system is well damped and able to quickly reduce or possibly limit such vibrations. Figure 3.39 compares passive and active unbalance responses when an initial condition of displacement is applied to the rotor, $e_X|_{t=0}$=5μm. While the passive system shows a typical logarithmic decrement of the transient vibrations, remarkably the active system is able to suppress the largest - and most dangerous - amplitudes faster and more efficiently.

The above examples compare operation either with the control system either switched on or off. One however could imagine a working situation in which active lubrication is only applied when a shock is detected.

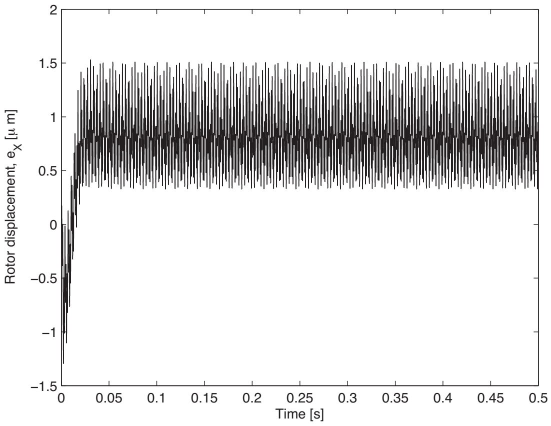

Figure 3.37: Rotor displacement response around the equilibrium, active mode, Ω=18,000 rpm.

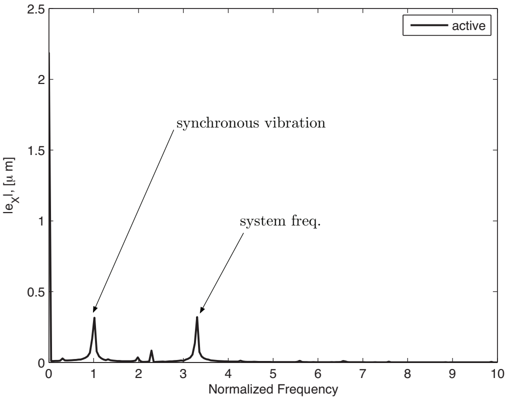

Figure 3.38: Single-sided power spectra of rotor displacement responses, active mode, Ω=18,000 rpm.

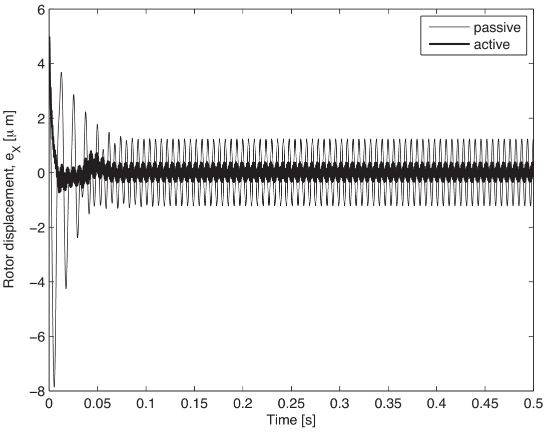

Figure 3.39: Rotor displacement responses around the equilibrium, passive active mode, $e_X|_{t=0}$=5μm; Ω=10000 rpm.

4

Permanent Magnetic Bearing

This chapter provides the mathematical background and modeling necessary for the physical characterization of simple permanent magnetic bearings. Analytical expressions for calculating the magnetic flux density and forces are derived for the characterization of a magnetic bearing consisting of two concentric, axially magnetized rings. The procedure for obtaining such parameters is based on that presented in [8]. Moreover, the effect of ferromagnetic shielding is evaluated as proposed by Mayer and Vesley, [59], with the aim of enhancing the bearing stiffness and load carrying capacity. Numerical and experimental validation is provided.

In the last part of the chapter, the performance of a novel hybrid permanent magnetic - aerodynamic gas bearing is evaluated with numerical examples.

4.1 Mathematical Model

4.1.1 The Earnshaw stability criterion

According to Earnshaw's theorem [24], a body cannot be maintained in a state of stable equilibrium if it is solely supported by magnetic or electrostatic interaction of charges. This concept was firstly proved by the English mathematician in 1842 and originally applied to electrostatic fields, however it was subsequently shown it can be more broadly applied to all inverse square law forces (electric and gravitational), in addition to the magnetic one.

The proof stems directly from the Gauss's law for magnetism, which states that the divergence of any possible magnetic field **B** is zero in free space. A magnetic force deriving from a potential will then always satisfy Laplace's equation:

$$\nabla \cdot \mathbf{B} = \nabla \cdot (-\nabla U) = \nabla^2 U = 0 \tag{4.1}$$

Condition for a magnetic dipole to be stable is the energy to have a minimum. Firstly, in order to have a stationary point it must be verified that:

$$\frac{\partial U}{\partial x} = \frac{\partial U}{\partial y} = \frac{\partial U}{\partial z} = 0 \tag{4.2}$$

For a minimum, it must also hold that:

$$\nabla^2 U > 0 \rightarrow \frac{\partial^2 U}{\partial x^2} + \frac{\partial^2 U}{\partial y^2} + \frac{\partial^2 U}{\partial z^2} > 0 \tag{4.3}$$

However, according to the Laplace equation applied to the magnetic dipole, its Laplacian is equal to zero. Thus, at best only two of the partial differentials in eq. (4.3) can be positive, while the third must be negative. Mathematically, stationary points which are neither local maxima or minima exist: saddle points. Physically, it means that a magnetic levitated body can only achieve (static) stable equilibrium in two directions, while the third remains unstable.

For magnetic bearing applications, stability can be still achieved in all direction, however it is necessary to add the contribution from a dynamic contribution, either electromagnetic or mechanical. Adding an electromagnetic term will effectively transform the Laplace's equation into the Poisson's equation. This is principle used for example in active magnetic bearings. In permanent bearing, mechanical constraints can be added, typically ball bearings. However, for the bearing to be of the non-contact type the preferred mechanical forces are either gyroscopic or fluid dynamic. Note that for a mechanical force to be used for stabilizing purposes, it must have substantial spatial derivatives; gravity for instance cannot be used, whereas the hydrodynamic effect in fluid film bearings is. In some special cases, the interaction of magnetic, gravitational and gyroscopic forces can be used to achieve spin stabilized magnetic levitation: since the early 90s it is possible to buy a toy magnetic spinning top which levitates in a stabilized equilibrium above a magnetic base. The physical principle behind this interesting phenomenon - which does not contradict Earnshaw's theorem, since the top is not static, but spinning, are detailed in [32] and [95].

4.1.2 Characterization of magnetic field and force

For the calculations of the magnetic field, or magnetic flux density **B**, a permanent magnetic bearing consisting of two radially magnetized rings is considered. The dimensions, the coordinate system arrangement and relationship between spontaneous magnetization and equivalent surface current density are shown in Fig. 4.1. Three coordinate systems are used for the analysis: the cylindrical system (r_m, α_m, z_m), the cartesian moving system (x_m, y_m, z_m) attached to the outer ring and the cartesian stationary system (u_m, v_m, w_m) attached to the inner ring. Essentially, the magnetic field can be defined as the curl of the magnetic vector potential $\mathbf{A}$:

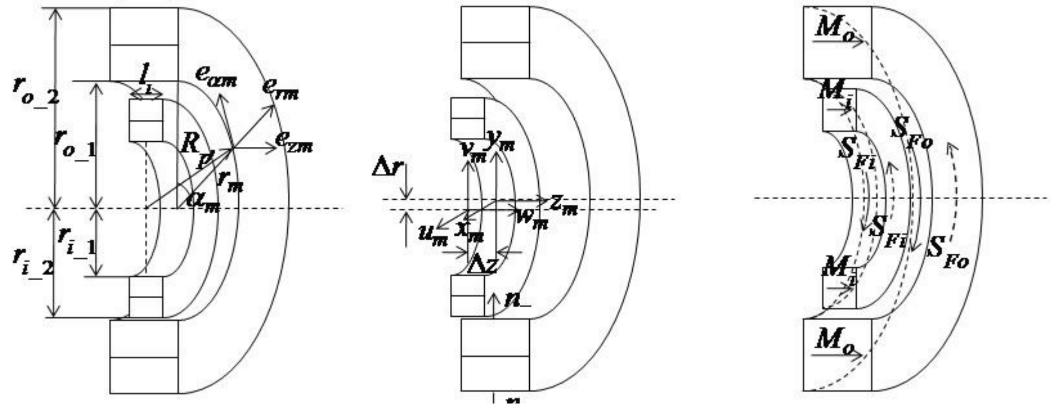

Figure 4.1: Characterization of the permanent magnetic bearing. From [8].

$$\mathbf{B} = \nabla \times \mathbf{A} \tag{4.4}$$

Outer ring. The equivalent surface current density for the outer ring is defined as the cross product of magnetization vector $\mathbf{M}_o$ and a normalized vector perpendicular to magnetization direction $\mathbf{n}_\pm$:

$$\mathbf{S}_{F_o} = -\mathbf{n}_\pm \times \mathbf{M}_o \tag{4.5}$$

where:

$$\mathbf{n}_\pm = \pm \begin{bmatrix} \cos\alpha_m \\ \sin\alpha_m \\ 0 \end{bmatrix} \qquad ; \qquad \mathbf{M}_o = M \begin{bmatrix} 0 \\ 0 \\ 1 \end{bmatrix} \tag{4.6}$$

with M being the spontaneous magnetization constant of the material. The magnetic flux density $\mathbf{B}_o$ can then be obtained through the Biot-Savart law:

$$\mathbf{B}_o = \frac{\mu_0}{4\pi} \int \int_A \frac{S_{F_o} \times R_{P'P}}{\|R_{P'P}\|^3} dA \tag{4.7}$$

where the vector $R_{P'P}$ is the distance between a generic point P on the inner ring magnet and a source point P' on the outer ring magnet:

$$\mathbf{R}_{P'P} = \begin{bmatrix} X_m - r_m \cos\alpha_m \\ -r_m \sin\alpha_m \\ Z_m - z_m \end{bmatrix} \tag{4.8}$$

Inserting Eq. (4.5), (4.6) and (4.8) into (4.9), one obtains:

$$\mathbf{B}_o = \frac{\mu_0}{4\pi} \int_{\alpha_m=0}^{2\pi} \int_{r_m=r_{o_{in}}}^{r_{o_{out}}} \frac{\begin{bmatrix} \cos\alpha_m(Z_m - z_m) \\ \sin\alpha_m(Z_m - z_m) \\ -X_m\cos\alpha_m + r_m \end{bmatrix}}{[(X_m - r_m\cos\alpha_m)^2 + (r_m\sin\alpha_m)^2 + (Z_m - z_m)^2]^{3/2}} \Bigg|_{z_m=-l_a/2}^{z_m=+l_a/2} r_m dr_m d\alpha_m \tag{4.9}$$

Inner ring. If the magnetic poles are arranged in contiguous pairs, the magnetization vector of the inner ring is equivalent to that of the outer one, see Eq. (4.6), see Fig. 4.1:

$$\mathbf{n}_{\pm} = \pm \begin{bmatrix} \cos\alpha_m \\ \sin\alpha_m \\ 0 \end{bmatrix} \quad ; \quad \mathbf{M}_i = M \begin{bmatrix} 0 \\ 0 \\ 1 \end{bmatrix} \tag{4.10}$$

With this quantity it is possible to calculate the equivalent surface current density on the inner ring:

$$\mathbf{S}_{F_i} = -n_{\pm} \times M_i \tag{4.11}$$

Magnetic bearing force. The magnetic force between the two rings depends both on the magnetization of the inner ring, Eq. (4.10) and the magnetic field of the outer one, Eq. (4.9). If the surrounding of the bearing is filled with a material of unitary relative permeability, the force of a single current-carrying conductor within a magnetic field is given by:

$$\mathbf{F} = \int_{\beta=0}^{2\pi} \int_{\rho_m=r_{i_{in}}}^{r_{i_{out}}} (S_{F_i} \times B_o) \Bigg|_{w_m=-l_i/2}^{w_m=+l_i/2} \rho_m d\rho_m d\beta_m \tag{4.12}$$

In order to correctly describe the magnetic force for any point P of the moving reference of frame (x_m, y_m, z_m) in the fixed one, (u_m, v_m, w_m), this should be rotated as show in Fig. 4.2. The distances X_m and Z_m are function of the position of ring magnets in relation to each other. Thus, these can be defined as:

$$\begin{gathered} X_m = \sqrt{(\Delta r_m + \rho_m\cos\beta)^2 + (\rho_m\sin\beta)^2} \\ Z_m = w_m + \Delta z_m \end{gathered} \tag{4.13}$$

Note that if the rings are perfectly axially aligned, $Z_m = w_m$. The angle δ between the two coordinate systems is defined as:

$$\delta = \pm \arccos \frac{\rho_m\cos\beta + \Delta r_m}{X_m} \tag{4.14}$$

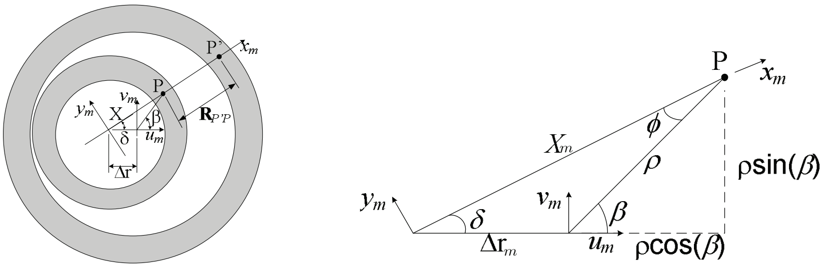

Figure 4.2: Magnetic bearing cross section, with displacement and coordinate system definition.

$+$ for $0 \leq \beta \leq \pi$ and $-$ for $\pi \leq \beta \leq 2\pi$. The angle ϕ between X_m and ρ_m is also given as:

$$\phi = \begin{cases} \beta - \delta, & 0 \leq \beta \leq \pi \\ 2\pi - \beta + \delta, & \pi \leq \beta \leq 2\pi \end{cases} \tag{4.15}$$

The magnetic flux density of the outer ring given in Eq. (4.9) is also rewritten in the fixed reference as:

$$\mathbf{B}_o = \begin{bmatrix} B_{xo}\cos\delta \\ B_{xo}\sin\delta \\ B_{zo} \end{bmatrix} \tag{4.16}$$

It is finally possible to rewrite Eq. (4.12) as:

$$\mathbf{F} = M_i \int_{\beta=0}^{2\pi} \int_{\rho_m = r_{i_{in}}}^{r_{i_{out}}} \left[\begin{array}{c} B_{zo}\cos\beta \\ B_{zo}\sin\beta \\ -B_{xo}\cos\phi \end{array} \right] \Bigg|_{w_m=-l_i/2}^{w_m=+l_i/2} \rho_m d\rho_m d\beta \tag{4.17}$$

4.2 Numerical solutions

In this section selected numerical analysis is presented, aimed at provide validation of the mathematical model and give an overview of the performance of the permanent magnetic bearing used in the test rig. The overall dimensions of the magnetic bearing rings are as indicated in Figure 2.3, the material properties can be found in table 2.3.

4.2.1 Preliminary validation

Numerical solutions for the developed model are provided; These results are positively validated in two ways:

1. Comparison of radial and axial magnetic forces between numerical solution presented in [8], see Figure 4.3 and 4.4, and those obtained with the current model - based on Eq. (4.17), see Figure 4.5 and 4.6. Note that the bearing dimensions and parameters are in this case adapted to match the reference data; moreover, the analytical expressions need to be slightly modified as the magnetization of the reference bearing is in the radial direction and not axial, as in the present project.

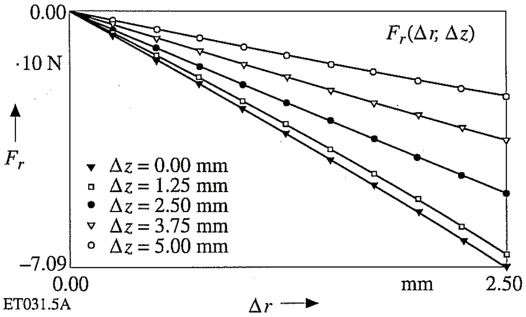

Figure 4.3: Reference radial forces at various radial and axial offsets, from [8].

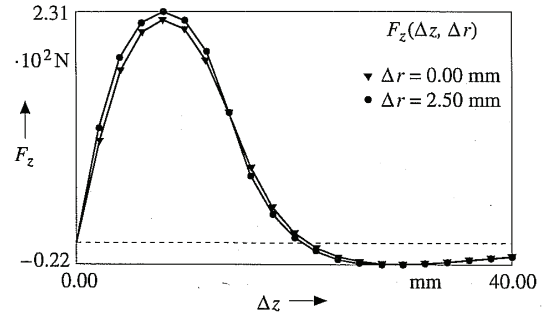

Figure 4.4: Reference axial forces at various radial and axial offsets, from [8].

2. Comparison axial magnetic forces between numerical analysis of current model and magnetic FE based software FEMM, see Figure 4.7. In this case, bearing parameters are defined according to the physical characteristics of the prototype bearing. Note that FEMM has only 2D capability, hence the comparison is restricted to the sole axial case.

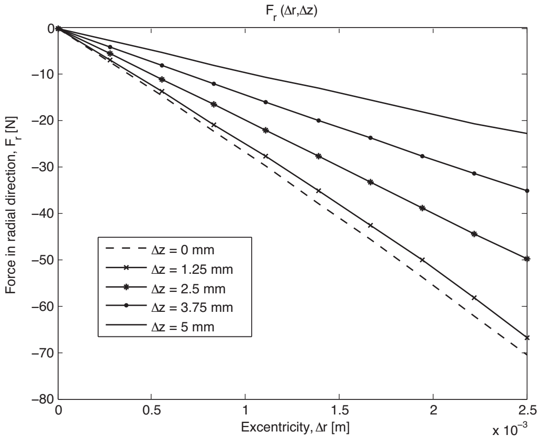

Figure 4.5: Calculated radial forces at various radial and axial offsets.

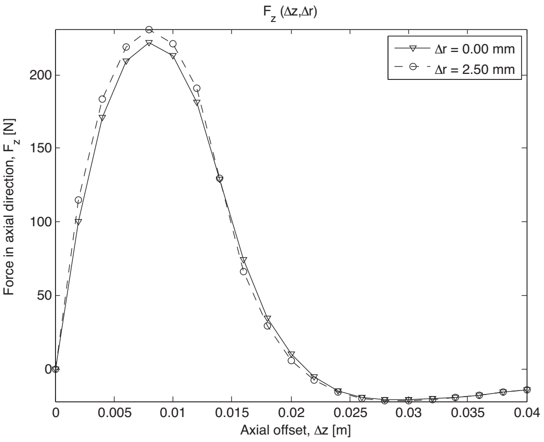

Figure 4.6: Calculated axial forces at various radial and axial offsets.

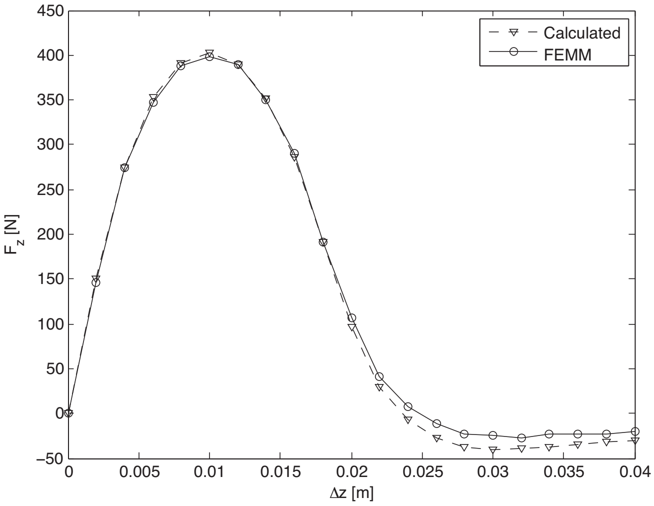

Figure 4.7: Comparison between calculated and FEMM axial forces at various offsets.

4.2.2 Evaluation of shielding effect

According to [59], in order to increase the magnetic force, which in turns improves the load carrying capacity of the magnetic bearing, a possible strategy is to lower the reluctance paths of the magnetic flux outside the bearing, causing an increase of magnetic flux density in the air gap. This can be achieved by shielding the magnets with a soft ferromagnetic material of high permeability, see Figures 4.8 and 4.9. Note that the flux lines are concentrated in radial section of the air gap. The improvement of the characteristic curve (radial force vs. eccentricity) of the bearing is shown in Figure 4.10. For either case, the radial force increases linearly, making it possible to calculate a "shielding factor". Note that the slope of the characteristic curve is the radial stiffness of the bearing. The drawback of the aforementioned shielding solution is however that it only applies to magnets with characteristics analogous to those in the reference, with radial magnetization. If the same strategy is used for axially magnetized bearings - the configuration adopted for the prototype bearing - the shielding with high permeability material increases the magnetic flux density, however the flux lines are concentrated in the axial direction, see Figures 4.11 and 4.12. This produces an increase of (unwanted) axial forces, whereas radial forces are greatly reduced. Therefore, the jacket is manufactured in aluminum alloy; its characteristic low permeability has a limited effect on the magnetic field distribution, see Figure 4.13.

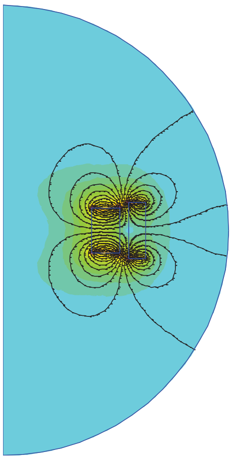

Figure 4.8: Qualitative magnetic flux density plot, no shielding - radial magnetization.

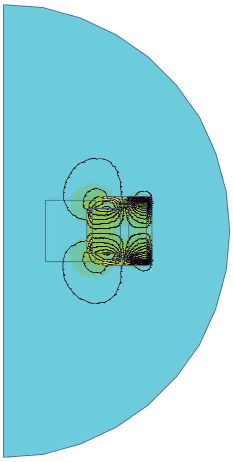

Figure 4.9: Qualitative magnetic flux density plot, iron shielding - radial magnetization.

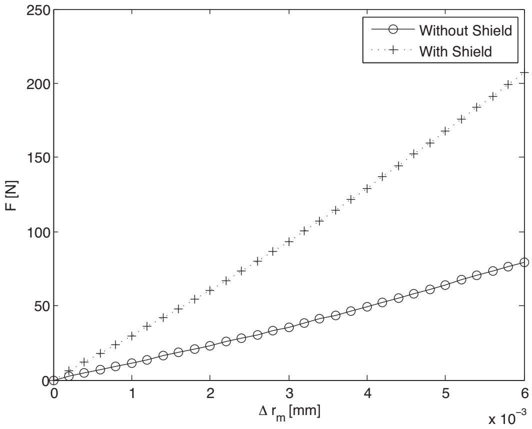

Figure 4.10: Characteristic curve of the magnetic bearing with and without shielding.

4.3 Experimental validation

A simple experiment is carried out in order to validate the numerical results presented in Section 4.2. The idea is to load the bearing with known forces in the radial direction and measure the displacement produced. The rotor bearing test rig is used for the test, however assembled without gas bearing, see Figure 4.14. To ease the identification precess, only one of the two

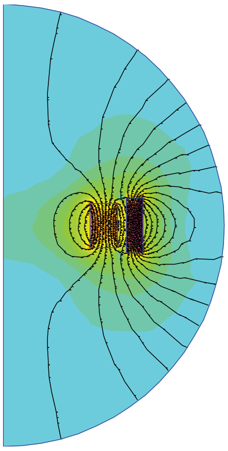

Figure 4.11: Qualitative magnetic flux density plot, no shielding - axial magnetization.

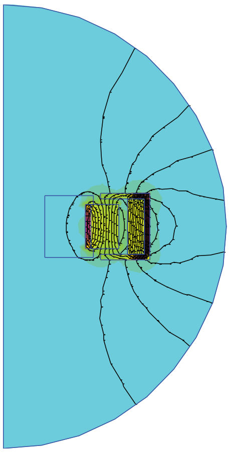

Figure 4.12: Qualitative magnetic flux density plot, iron shielding - axial magnetization.

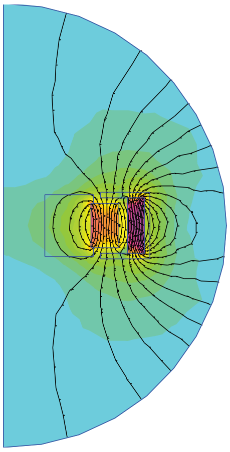

Figure 4.13: Qualitative magnetic flux density plot, aluminum shielding - axial magnetization.

magnetic bearings is considered at a time. Radial load in the vertical direction is applied by attaching known masses to the shaft, see Figure 4.15. The displacements are measured by the means of a high precision laser sensor. Note that in unloaded conditions, the shaft shows an initial displacement, given by the load resulting from the weight of the rotor itself. Moreover, due to the relatively small loading and the fact that the displacements measurement and the load application line is at negligible distance from the bearing, flexibility of the shaft is not considered. The experimental procedure is repeated for both the magnetic bearings. The results are presented in Figure 4.16 and 4.17, where radial eccentricity values are recorded at

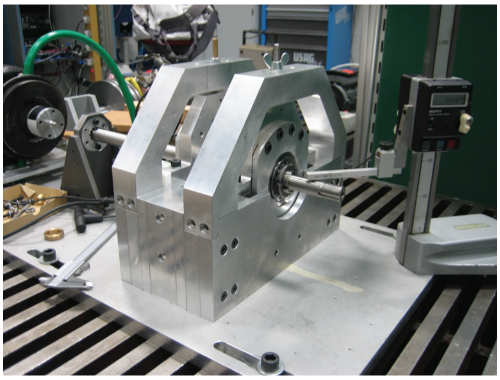

Figure 4.14: Test rig during magnetic stiffness testing.

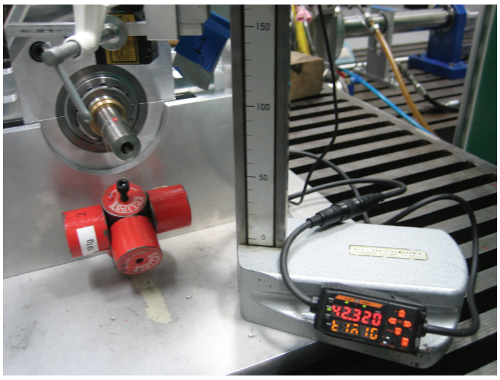

Figure 4.15: Validation of magnetic load/stiffness capacity.

different loading steps. Qualitative and overall quantitative agreement is observed. For both cases, the experimental data linear fit averages show a slight underestimation of the carrying capacity (and therefore radial stiffenss), when compared to the analytical results. Discrepancies are mainly attributed to two factors:

- uncertainty in the nominal value for the magnetic remanence B_r and thus the spontaneous magnetization M of the Neodymium rings;
- the effect of aluminum jackets and stainless steel shaft on the reluctance paths of the magnetic flux outside the bearing clearance is not considered in the numerical model.

The first factor can also explain why the two bearing show a slightly different behavior, despite being geometrically identical. A reasonable assumption is that imprecise manufacturing process left the four rings with slightly difference magnetization. Average radial stiffness values are also summarized in Table 4.1. Note that the passive magnetic bearing has only direct stiffness coefficients, meaning that the response to a displacement in a given direction produces a reaction

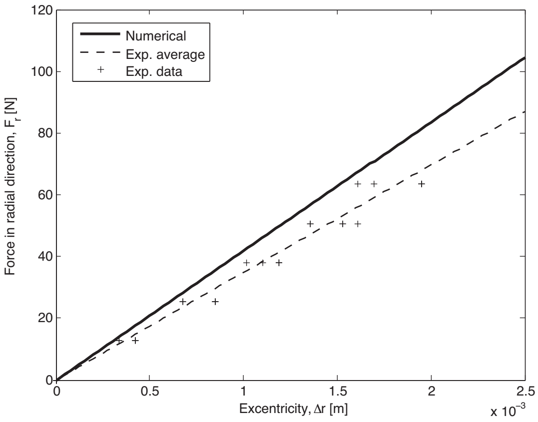

Figure 4.16: Experimental radial force characteristic of magnet 1, with numerical reference.

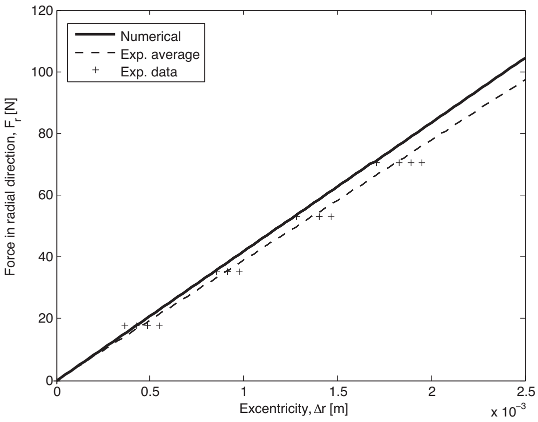

Figure 4.17: Experimental radial force characteristic of magnet 2, with numerical reference.

	Mag. bearing 1	Mag. bearing 2
Numerical	41130 N/m	41130 N/m
Experimental	34810 N/m	38940 N/m

Table 4.1: Magnetic bearings numerical and experimental stiffness.

in that direction only. The mathematical expression of the stiffness matrix is then written as:

$$\mathbf{K}^{bb} = \begin{bmatrix} K_{XX}^{mag} & 0 \\ 0 & K_{YY}^{mag} \end{bmatrix} \tag{4.18}$$

4.4 Combining magnetic and aerodynamic effects

Magnetic and aerodynamic lubrication technologies are combined with the aim of developing a new kind of hybrid permanent magnetic - gas bearing. Such bearing is intended to exploit the benefits of the two technologies while minimizing their drawbacks.

Aerodynamic bearings offer good load carrying capacity and stiffness at high rotational speed, however they do not work if such velocity is too low. Thus they offer poor start-up and shut-down operation characteristics, where rubbing between journal and bearing surfaces accelerates wear and may even cause bearing failures.

Passive magnetic are a simple and economic solution for providing contact-free support. Magnetic forces can be generated in static and dynamic conditions, however magnetic dynamic coefficients properties are poor.

The idea is then to combine the two bearings as follows:

- the lack of carrying capacity at low speeds of the gas bearing is provided by the magnetic one;
- at higher speed, when the aerodynamic lift suffices to carry the load, the magnetic bearing can be used to improve the dynamic characteristics by offsetting the stator ring magnet.

Practically, this can be achieved simply by offsetting the stator ring of the permanent magnetic bearing. At zero and low speed such force should be directed at lifting the rotor, whereas at higher speed it may be possible to use it to push the rotor, effectively ”preloading” the aerodynamic bearing, see Figure 4.18. Note that the offsetting of the magnetic bearing is necessary, as if the ring were concentric the resultant magnetic force would be zero. Moreover, the offset provided by purely aerodynamic operation - the eccentricity - is much too small (of the order of tens of microns) compared to the range of the magnetic forces in the present configuration (of the order of thousands of microns), see for example Figure 4.16.

4.4.1 Numerical analysis

As the magnetic bearing is mounted on moveable supports, it is rather easy to act towards creating an offset between the stator ring (solidal to the bearing case) and the rotor (solidal to

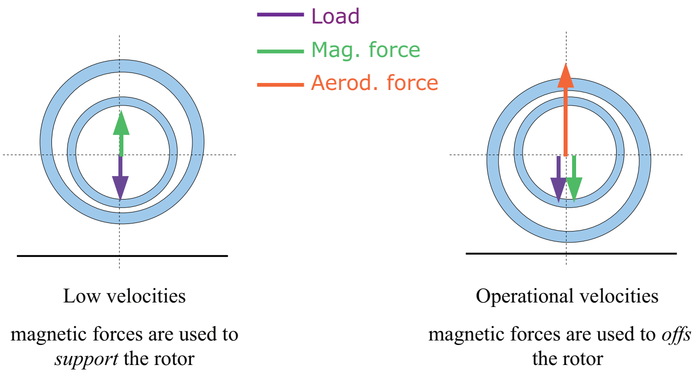

Figure 4.18: Principle of operation of hybrid aerodynamic - permanent magnetic bearing with adjustable offset.

the rotor). The simplest way to attack the problem is to calibrate such offset in order to offer enough support at zero velocity (or during start-up and shut-down phases) and to modify it once the machine reaches the continuous operation speed. Note that in this way the operation should not be considered as "active", but simply "adjustable", although formally a feedback law is established through the book-keeping of the rotational speed. This is an important point, as the developed magnetic-gas bearing should be regarded as a passive element.

The hybrid bearing is composed of one gas and two magnetic bearings in parallel; The schematic layout of the hybrid: bearing is presented in Figure 4.19.

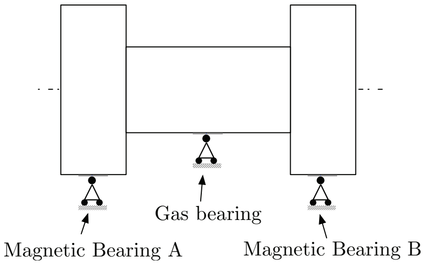

Figure 4.19: Schematic layout of the hybrid bearing.

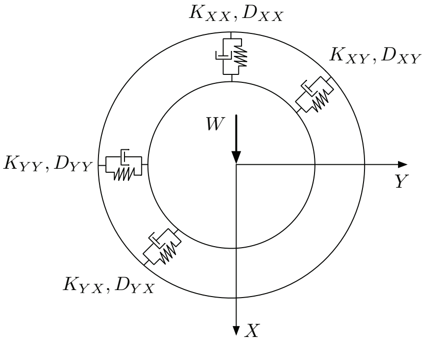

Figure 4.20: Physical representation of the dynamic coefficients of the bearing.

For a given position of the journal (e_X, e_Y), the Reynolds equation can be solved for the pressure, which in turn imposes vertical and horizontal lubrication forces on the shaft, see eq. (3.18). Similarly, it is possible to calculate the magnetic forces on the shaft, as given in eq. (4.17). Note that formally a further coordinate transformation is necessary in order to express the magnetic forces in the same reference as the gas ones. For the purpose of this numerical analysis, one can think of regulating the offset in order to modify the total load on the bearing; this in turn has also an effect on the eccentricity.

For a bearing to be in equilibrium the lubrication forces must equilibrate a given load W acting on the vertical direction:

$$\begin{cases} W + F_X^{gas}(e_X, e_Y) + F_X^{mag-A}(e_X, e_Y) + F_X^{mag-B}(e_X, e_Y) = 0 \\ F_Y^{gas}(e_X, e_Y) + F_Y^{mag-A}(e_X, e_Y) + F_Y^{mag-B}(e_X, e_Y) = 0 \end{cases} \tag{4.19}$$

which is a nonlinear system that can be solved by a Newton-Rhapson scheme.

Now, it is clear that depending on the relative direction of the offset compared to the bearing center, one can either apply a force that acts with a lifting effect (negative contribution in the $-X$ coordinate, in the bearing reference of frame) or a force that acts as a pushing effect (positive contribution in the $-X$ coordinate), see Figure 4.18. In practice a negative force contribution is subtracted from the load applied on the bearing W; it is physically equivalent as a more lightly loaded bearing. A positive contribution is added to the load, meaning that the bearing is more heavily loaded.

The physical representation of the dynamic coefficients of the hybrid bearing is presented in 4.20. The effective stiffness constant of the bearing is given by:

$$\mathbf{K} = \mathbf{K}^{gas} + \mathbf{K}^{mag-A} + \mathbf{K}^{mag-B} \tag{4.20}$$

However one should notice that the stiffness contribution of the magnetic bearing is around two orders of magnitude smaller than the gas bearing, for most of the operational speed range[1] analyzed numerically in chapter 3. As for the damping coefficient, it is assumed that the contribution of the passive magnetic bearing is negligible compared to the gas one:

$$\mathbf{D} = \mathbf{D}^{gas} \tag{4.21}$$

In Figures 4.21 and 4.22 a comparison between the synchronous dynamic coefficients as func-

---

[1] Although at zero or very low rotational speed the aerodynamic effect is not able to carry the load and formally fluid dynamic coefficients cannot be defined; in this case the magnetic stiffness is the dominating contribution.

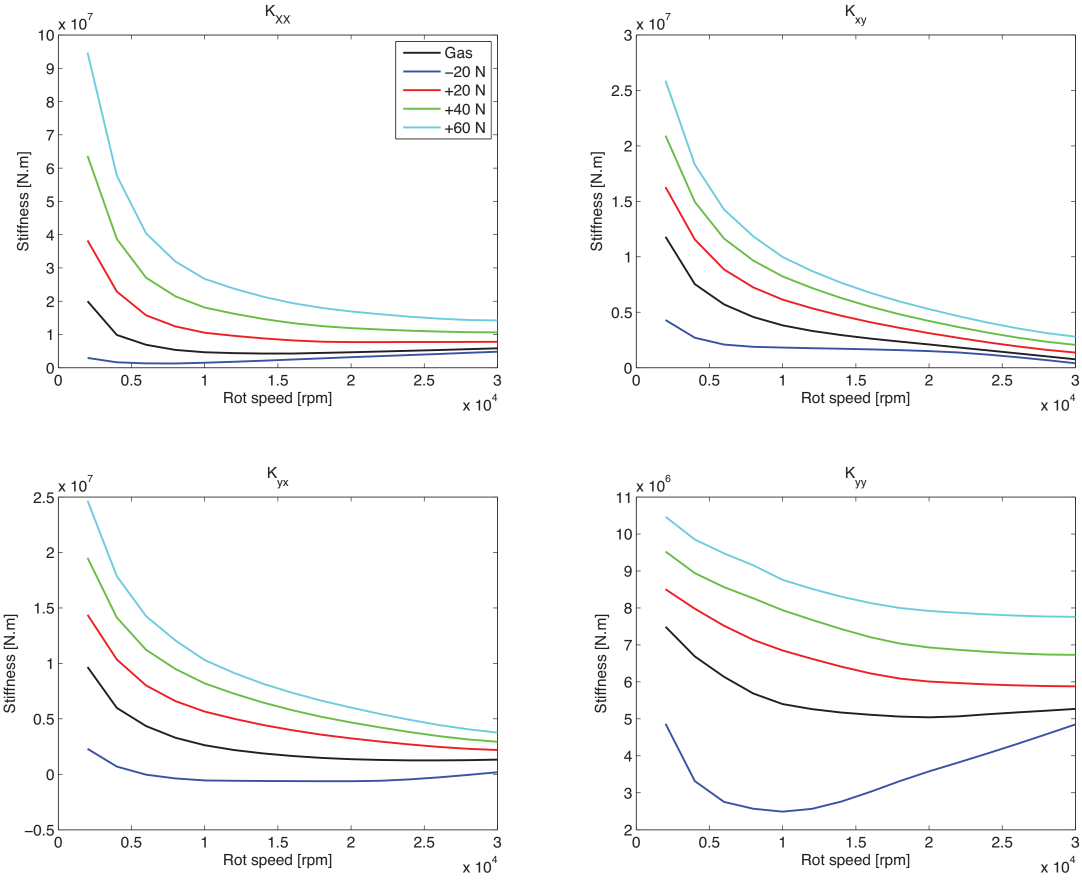

Figure 4.21: Components of the stiffness coefficients matrices as function of rotational velocity, gas bearing vs. hybrid bearing.

tion of the rotational speed of the gas bearing and hybrid bearing is presented. In both cases the simulations span at an operational range of 2,000 - 30,000 rpm. The influence of the hybrid bearing is evaluated at different magnetic loads (-20, +20, +40, +60 N).

The stiffness coefficients, Figure 4.21 are those which see the most marked changes; In general, one can observe that the higher the bearing is loaded, the larger its damping coefficients become. Moreover, larger differences between the parametric analysis is especially noticed at lower rotational speeds. This behavior can be referred to the that of the equilibrium position of the bearing. At low operational speed the aerodynamic force is weak, thus variation of magnetic force have the largest influence. The higher the magnetic load, the more the bearing equilibrium positions becomes eccentric, and the journal becomes very close to the bottom of the bearing. These operational conditions are characterized by a steep convergence effect into

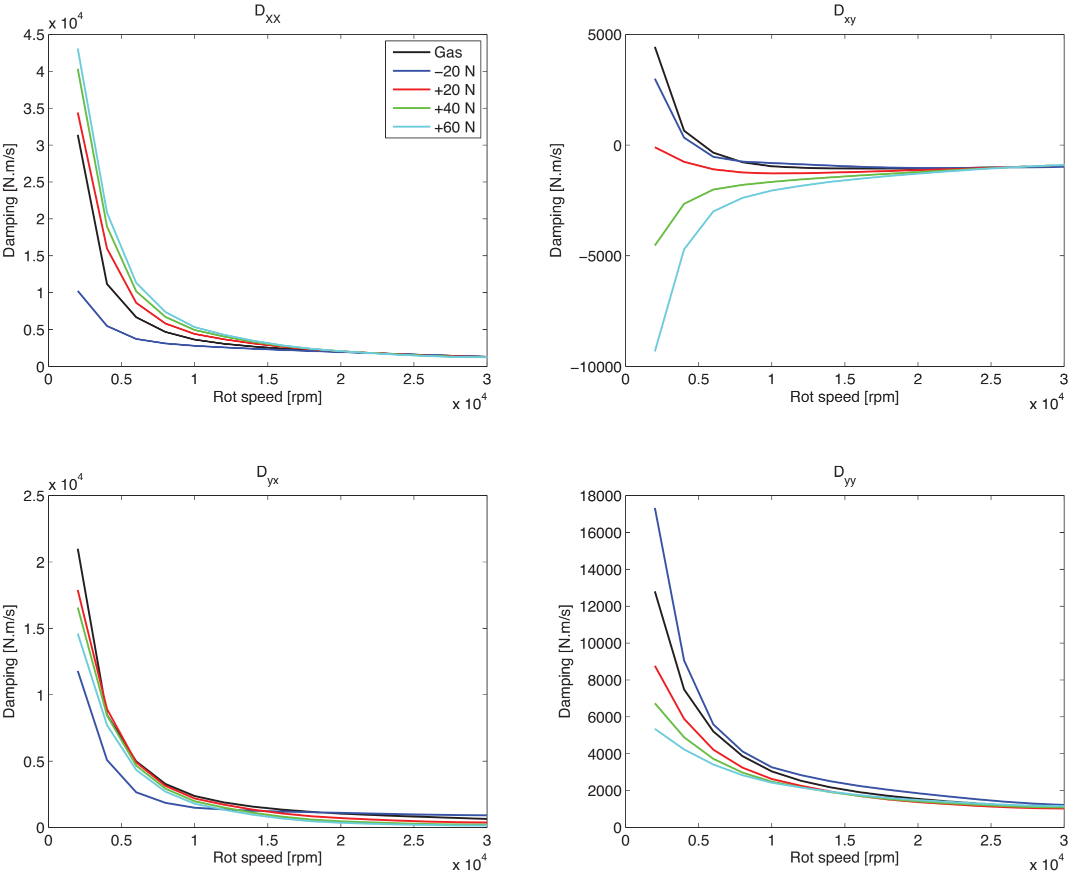

Figure 4.22: Components of the damping coefficients matrices as function of rotational velocity, gas bearing vs. hybrid bearing.

which the lubricant is forced by its viscosity and adhesion, creating a strong pressure wedge, hence the high stiffness values.

At the same time, squeeze-film damping effect becomes stronger when the separation between surfaces is reduced and rotational speed low, see Figure 4.22. This then also explains why direct vertical damping (D_{XX}) at low velocities is higher if the magnetic load is larger. It also explains why the opposite happens for the horizontal direct damping (D_{YY}). As the journal is pushed towards the bottom of the bearing, it yields smaller minimum film thicknesses in the vertical direction, while in the horizontal direction are large, hence at high loads the horizontal the squeeze-film damping effect is weak; when however the magnetic force is reduced, the vertical thickness increases, whereas it is reduced in the horizontal direction, hence the larger damping. As the velocity increases, direct stiffness is progressively decreased, as the pressure wedge is boosted by the Couette contribution. As for the damping, note that for the largest magnetic loads the cross-coupled terms assume an asymmetric configuration, however at high speed it is close to zero, which in principle should not contribute to the destabilizing effect from the lack of symmetry of cross-coupled coefficient. It is also noticed that the bearing loses its damping with increasing speed; this is a feature typical of gas lubricated bearings, and it is related not much to the equilibrium position, but rather to the compressibility effect [57].

5

A Flexible Rotor-Bearing System

Theoretical and experimental analyses

In this chapter all the models developed and discussed in the previous part of the thesis are combined and applied in order to perform a characterization of a flexible rotor-bearing system. Analytical results are first presented and discussed, successively compared and validated with experimental findings.

It is a well known fact that the dynamic performance of a rotating machine depends not only on its geometrical and physical parameters, but also on the operational conditions. It is then of outmost importance to perform an accurate and rigorous analysis at the design stage, in order to determine whether or not they will be performing satisfactorily at the intended operation. For the purpose of this analysis, it should be remarked that unbalance is regarded as the main source of excitation.

In general, the dynamic characteristics of a mechanical system, such as natural frequencies, mode shapes and damping ratios can be analytically and or numerically obtained. When dealing with rotating systems, one should be aware that such characteristics are highly influenced by the angular velocity, making the model parameters dependent on the rotation of the machine. Namely, the gyroscopic effect is responsible for coupling the linear and angular movements of the system. In presence of such effect, the motion of a rotor can be thought as a superposition of the rotation around the axis itself and the so called precession, a phenomenon where the geometrical axis of the rotor describes orbits around the the axis of rotation. If the rotor-bearing system is symmetric, these orbits are circular and can only happen in the same direction of rotation - the forward synchronous whirl - whereas any asymmetry introduces a degree of ellipticity and a contra rotating motion may be observed - the backward synchronous whirl. Note that the mentioned asymmetry is not necessarily associated by the rotor and/or discs geometry, but more often by the nature of the bearings; frequently used hydro/aerodynamic bearings used in rotating machines exhibit a high degree of anisotropy with respect to lateral motion axes. The speed of precession is proportional to the angular momentum: this is an important consideration, as it explains the relation between natural frequencies, whirling and rotational velocity. As the gyroscopic matrix is skew-symmetric, for each rotational velocity $2n$ distinct natural frequencies appear, a larger, forward component, and a smaller, backward component, as opposed to the n frequencies of the corresponding system without rotation. When the rotational velocity coincides with one of the natural frequencies, the system is said to reach a critical speed. Thus, it is of utmost importance to predict when these critical speeds occur - usually through the Campbell diagram - as any synchronous excitation force, such as unbalance, can lead to large and potentially destructive responses.

5.1 Mathematical model

The mathematical model of the mechanical system under investigation can be divided in the following components:

- Flexible shaft
- Rigid discs
- Bearings

The first two items are object of the present chapter, where a comprehensive model is developed in order to accurately describe the lateral dynamic behavior of the rotating machine, based - upon reasonable simplifications - on the structural drawings of the machine prototype.

Such mathematical analysis is based on the Finite Element Method. Using the FE method, the shaft is modeled by dividing it into multiple elements, to which discs and bearings can be assembled. Once a global model is defined, the structure dynamic response can be calculated, such as natural frequencies, mode shapes, unbalance response, critical speed analysis.

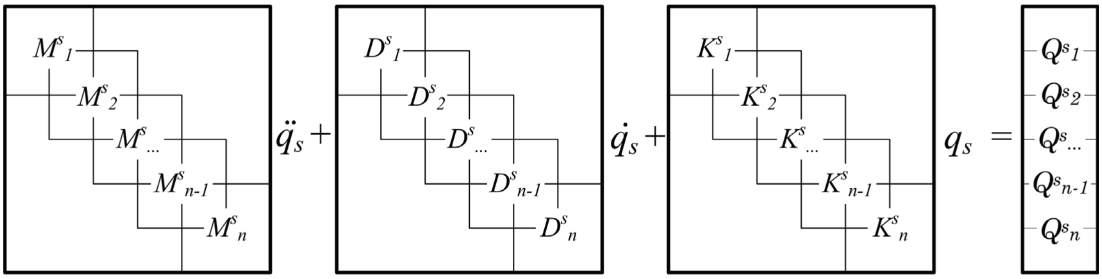

Figure 5.1: Visualization of the matrices structure of the global shaft FE model.

5.1.1 Modeling the flexible shaft and rigid disc

In order to account for lateral displacements and tilting oscillations of the rotor, the shaft is modeled as a flexible body using a finite element formulation where the rotor bearing system is assumed to be supported by flexible supports, and the gyroscopic and rotational inertia effects are included. Overall, the mathematical modeling is developed as described by Nelson and McVaugh [65]. Note that in the present model, only lateral and tilting motions are modeled, yielding 8 degrees of freedom beam elements (4 dofs per node). Here a general outline of the modeling is presented; details are given in Appendix B.

5.1.1.1 Flexible shaft

The equation of motion of each element can be derived via Lagrange's energy formulation; mass, gyroscopic and stiffness matrices can be defined for each element. In order to assemble each element matrices into a global model for the shaft, each individual elements contribution is added to the degrees of freedom on which it influences. Graphically the local matrices can be considered 'overlapped' to formulate the global matrices, see Figure 5.1.The global contribution is then:

$$\underbrace{\left(\mathbf{M}_T^S + \mathbf{M}_R^S\right)}_{\mathbf{M}^S} \ddot{\mathbf{q}} + \mathbf{D}^S \dot{\mathbf{q}} + \mathbf{K}^S \mathbf{q} = \mathbf{Q}^S \tag{5.1}$$

where the superscript $.^S$ refers to the Shaft, $\mathbf{M}_T^S$ is the mass matrix contribution of the translational dofs and $\mathbf{M}_R^S$ of the rotational dofs. The damping matrix $\mathbf{D}^S = -\Omega\mathbf{G}^S$ is given by the gyroscopic effect and $\mathbf{K}^S = \mathbf{K}_B^S$ the bending stiffness.

5.1.1.2 Rigid disc

The derivation of the equation of motion for discs is somehow simpler, as these can generally be considered as rigid bodies. Similarly to the previous case, the equation of motion is obtained by solving the Lagrange's equation; to do so on has to define expressions for the potential and kinetic energy. Assuming the disc to be rigid, no potential energy due to deformation is store, therefore the equation of motion does not include a stiffness contribution:

$$\mathbf{M}^D \ddot{\mathbf{q}}^D - \Omega \mathbf{G}^D \dot{\mathbf{q}}^D = \mathbf{f}^D \tag{5.2}$$

5.1.2 Modeling the bearings

Modeling of bearing dynamics differs greatly depending the bearing type, but can in general be interpreted by a basic mechanical model, see Figure 5.2.

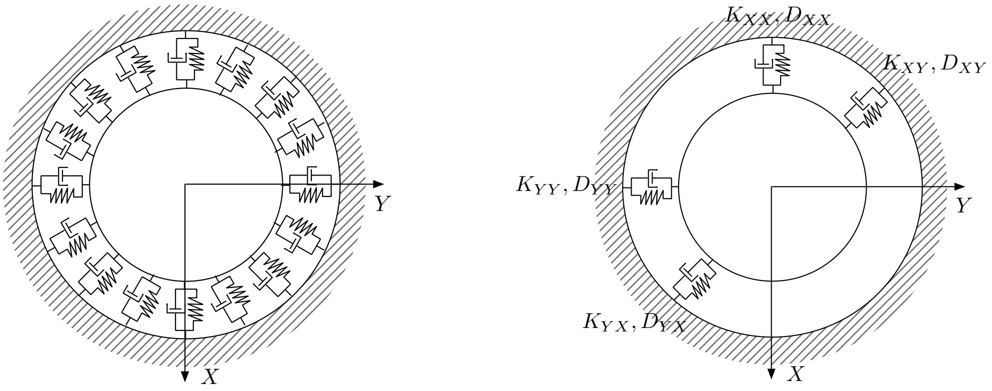

Figure 5.2: Mechanical model of bearings – Representation of bearing by means of springers and dampers.

Whenever the housing can be considered as clamped and not moving, the mass contribution can be neglected, i.e. $\mathbf{M}^B \ddot{\mathbf{q}}_b = 0$. Moreover, the bearing is assumed to have only an insignificant influence on the rotation in the node, hence additional stiffness and damping is added only to the translational dofs.

The equation of motion can then be written as:

$$\mathbf{f}^B = -\mathbf{D}^B \mathbf{q}^B - \mathbf{K}^B \mathbf{q}^B$$

$$\begin{bmatrix} f_X^b \\ f_Y^b \end{bmatrix} = - \begin{bmatrix} D_{XX}^b & D_{XY}^b \\ D_{YX}^b & D_{YY}^b \end{bmatrix} \begin{bmatrix} \dot{X} \\ \dot{Y} \end{bmatrix} - \begin{bmatrix} K_{XX}^b & K_{XY}^b \\ K_{YX}^b & K_{YY}^b \end{bmatrix} \begin{bmatrix} X \\ Y \end{bmatrix} \tag{5.3}$$

Where $\mathbf{f}^B$ is the static force acting on the bearing. The coefficients of $\mathbf{D}^B$ and $\mathbf{K}^B$ are specifically obtained for each bearing type through different methods and theories. For the ball bearing, a short descriptions follows; for the test bearings, see the relative chapter.

Similarly to the disc case, for any bearing, its dofs coincide to the dofs of the shaft element at the given location where the bearing is placed, $\mathbf{q}_i^B = [X_i, Y_i]^T$, where $_i$ denotes a specific node on the shaft.

5.1.2.1 Gas and magnetic bearings

For the dynamic coefficients of the test bearing, see chapters 3 and 4.

5.1.2.2 Ball bearing

It is assumed that the stiffness of the bearing can be considered to be linear elastic, and that the damping can be modeled as viscous, i.e. proportional to the velocity of the shaft. The contributions added to the global matrices are:

$$\mathbf{D}^{bb} = \begin{bmatrix} D^{bb}_{XX} & 0 \\ 0 & D^{bb}_{YY} \end{bmatrix} \quad , \quad \mathbf{K}^{bb} = \begin{bmatrix} K^{bb}_{XX} & 0 \\ 0 & K^{bb}_{YY} \end{bmatrix}$$

5.1.3 Assembly of the global matrices

To form the global equations of motion, the superposition principle can be used, since the model is considered linear. As already anticipated in the previous sections, shaft, discs and bearings are coupled placing each subsystem at nodes strategically located at points where discs and bearings are mounted on the shaft. The generalized coordinates for the global model are $\mathbf{q}_i = [V_i, W_i, \Gamma_i, \beta_i]^T$, where the subscript i refers to the nodes in the FE model, $i = 1, 2, ..N$, and N is the total number of degrees of freedom, ndof. The total ndof is then $N = 4(N_e + 1)$, where N_e is the number of shaft elements.

$$\mathbf{q}^G = \begin{bmatrix} \boldsymbol{q}_1 \\ \boldsymbol{q}_2 \\ \cdot \\ \cdot \\ \cdot \\ \boldsymbol{q}_N \end{bmatrix} \tag{5.4}$$

The global equation of motion is written in standard form as:

$$\mathbf{M}^G \ddot{\mathbf{q}}^G + \mathbf{D}^G \dot{\mathbf{q}}^G + \mathbf{K}^G \mathbf{q}^G = \mathbf{Q}^G \tag{5.5}$$

Where:

$$\begin{aligned} \mathbf{M}^G &= \mathbf{M}^S + \mathbf{M}^D \\ \mathbf{D}^G &= \mathbf{D}^S + \mathbf{D}^D + \mathbf{D}^B \\ \mathbf{K}^G &= \mathbf{K}^S + \mathbf{K}^B \end{aligned} \tag{5.6}$$

To make a generalization of the system matrices, for the 2-node elements, one can see that it results in a banded matrix as illustrated in figure 5.3. The contributions of the discs and bearings can now simply be placed at the respective nodes in the mesh.

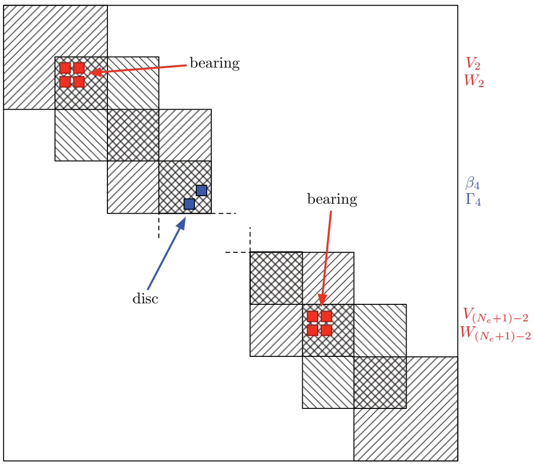

Figure 5.3: Band structure and element overlap for global damping matrix. Structure of the matrix $\mathbf{D}^G$ for a flexible rotor with 2 bearings (node 2 and (N_e+1)-2) and 1 disc (node 4).

5.1.4 Eigenvalue problem and mode shapes

In order to solve this system with respect to the natural frequencies and mode shapes it is convenient to rearrange it into a state space formulation reducing the original second order system to first order, providing a standard form to pose an eigenvalue problem:

$$\underbrace{\begin{bmatrix} \mathbf{M}^G & \mathbf{0} \\ \mathbf{0} & \mathbf{M}^G \end{bmatrix}}_{\mathbf{M}_{glob}} \underbrace{\begin{bmatrix} \dot{\mathbf{q}}^G \\ \ddot{\mathbf{q}}^G \end{bmatrix}}_{\dot{\mathbf{z}}} + \underbrace{\begin{bmatrix} \mathbf{K}^G & \mathbf{G}^G \\ -\mathbf{M}^G & \mathbf{0} \end{bmatrix}}_{\mathbf{K}_{glob}} \underbrace{\begin{bmatrix} \mathbf{q}^G \\ \dot{\mathbf{q}}^G \end{bmatrix}}_{\mathbf{z}} = \underbrace{\begin{bmatrix} \mathbf{Q}^G \\ \mathbf{0} \end{bmatrix}}_{\mathbf{Q}_{glob}} \tag{5.7}$$

$$\mathbf{M}_{glob}\dot{\mathbf{z}} + \mathbf{K}_{glob}\mathbf{z} = \mathbf{Q}_{glob}$$

Where $\boldsymbol{z} = [\boldsymbol{q}^g, \dot{\boldsymbol{q}}^g]$. Or, equivalently:

$$\begin{bmatrix} \dot{\mathbf{q}}^G \\ \ddot{\mathbf{q}}^G \end{bmatrix} = \underbrace{\begin{bmatrix} \mathbf{0} & \mathbf{I} \\ \textbf{-}\mathbf{M}^{G(-1)}\mathbf{K}^G & \textbf{-}\mathbf{M}^{G(-1)}\mathbf{D}^G \end{bmatrix}}_{\mathbf{A}_{glob}} \underbrace{\begin{bmatrix} \mathbf{q}^G \\ \dot{\mathbf{q}}^G \end{bmatrix}}_{\mathbf{z}} + \underbrace{\begin{bmatrix} \mathbf{0} \\ \mathbf{M}^{G(-1)}\mathbf{Q}^G \end{bmatrix}}_{\mathbf{Q}_{glob}} \tag{5.8}$$

$$\dot{\mathbf{z}} = \mathbf{A}_{glob}\mathbf{z} + \mathbf{Q}_{glob}$$

Considering the unforced unforced system, governed by the equation of motion $\dot{\mathbf{z}} = \mathbf{A}_{glob}\mathbf{z}$, the solution is assumed to be harmonic of the form:

$$\mathbf{z} = \boldsymbol{\varphi_k} e^{\lambda_k t} \tag{5.9}$$

Where λ_k and $\boldsymbol{\varphi_k}$ are the k-th of $2N$ time-invariant eigenvalues and right hand eigenvectors of the system. Introducing the solution (5.9) in the equation of motion, the eigenvalue problem is defined:

$$[\mathbf{A}_{glob} - \lambda_k \mathbf{I}]\boldsymbol{\varphi_k} = 0 \tag{5.10}$$

The solution yields the complex conjugate pairs:

$$\begin{aligned} \lambda_k &= \alpha_k \pm j\,\omega_k \\ \boldsymbol{\varphi_k} &= \mathbf{r}_k \pm j\,\mathbf{s}_k \end{aligned} \tag{5.11}$$

For each eigenvalue pair, only one component is retained, where the imaginary part represents the mode eigenfrequency, whereas the real part is associated with the damping level. Similarly, only one of the eigenvectors (mode shapes) is used for the analysis; here the presence of real and imaginary part indicates the presence of a certain damping level. Each vector contains both the states (displacements) and their time derivative (velocities). Furthermore, it is common practice to normalize the vectors by their largest component. Inserting the eigenpair, eq. (5.11) into the solution, eq. 5.9:

$$\mathbf{z}_k = (\mathbf{r}_k \pm j\,\mathbf{s}_k)e^{(\alpha_k \pm j\,\omega_k)} \tag{5.12}$$

In order to characterize the mode shapes, the movement of each node can be thought as made of the two components in the horizontal and vertical directions, thus eq. (5.12) can be rewritten so that the i-th translation of an arbitrary node in the k-th vibration mode is:

$$\mathbf{z}_{i,\,k} = C_k e^{\alpha_k t}\left[r_{i,\,k}\sin(\omega_k t + \gamma_k) + s_{i,\,k}\cos(\omega_k t + \gamma_k)\right] \tag{5.13}$$

Setting the initial conditions at unitary displacement amplitude ($C_k = 1$), zero phase lag (γ_k=0) and neglecting the change of amplitude ($\alpha_k = 0$), eq (5.13) can be written as:

$$\begin{aligned} V_k(t) &= r_k^V \sin(\omega_k t) + s_k^V \cos(\omega_k t) \\ W_k(t) &= r_k^W \sin(\omega_k t) + s_k^W \cos(\omega_k t) \end{aligned} \tag{5.14}$$

Hence, the resulting path describes orbits that are generically of elliptical shapes, which can reduce to be circular or lie on a straight line as extreme cases, see Figure 5.4 Moreover, they can be either forward or backward in relation to the spin of the rotor. In order to predict direction of rotation, the complex displacement is introduced as:

$$z_k(t) = V_k(t) + jW_k(t) \tag{5.15}$$

Substituting eqs. (5.14) into eq. (5.15), one can define the path of each node as a sum of two vectors rotating with the same angular velocity, but in opposite direction:

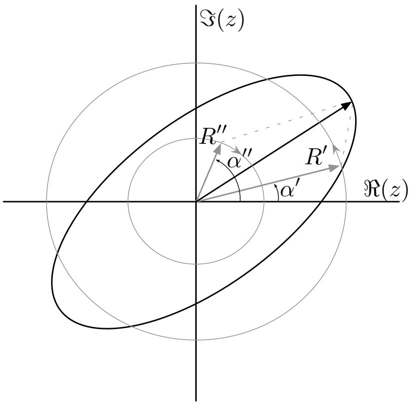

Figure 5.4: Elliptic orbits traced in the complex plane.

$$z(t) = R' e^{j(\omega t + \alpha')} + R'' e^{-j(\omega t + \alpha'')} \tag{5.16}$$

Where:

$$(R',\, R'') = \frac{1}{2}\sqrt{(\pm r_k^W + s_k^V)^2 + (\mp r_k^V + s_k^W)^2} \tag{5.17}$$

$$(\alpha',\, \alpha'') = \tan^{-1}\left(\frac{\pm r_k^V + s_k^W}{\mp r_k^W + s_k^V}\right) \tag{5.18}$$

The amplitude ratio R'/R'' determines whether the orbits are forward or backward. For $R' > R''$ the result is a forward motion, whereas $R' < R''$ results in a backward motion. $R' = R''$ describe a motion lying along a straight line.

5.1.5 Pseudo modal reduction of the flexible rotor-bearing system for time integration

One may argue that the 2 degrees of freedom model simplification introduced in section 3.5.6.2 is only valid in case the rotor is truly rigid and does not account for additional rotational speed effects, such as the gyroscopic. In principle then, if one has to combine the dynamic of the flexible rotor and disc and the active gas bearing dynamic problem, the system must account for all dofs defined in the respective models. This generally results in the setup of relatively large problems which, while they can be readily solved in frequency domain analysis, make a time domain approach rather heavy with respect to the computational effort. In these situations it may be then useful to employ a pseudo modal reduction to decrease the number of degrees of freedom of the rotor bearing problem and limit them to the minimum number necessary in order to give an satisfactory representation of the physical phenomena of interest.
The necessary steps in order to implement this procedure can be summarized as:

- Set up the global mathematical model, including flexible rotor and disc, but NOT the bearings; these will be included as external forces, as described in section 3.5.6.2.

$$\mathbf{M}^G\ddot{\mathbf{q}}^G + \mathbf{D}^G\dot{\mathbf{q}}^G + \mathbf{K}^G\mathbf{q}^G = \mathbf{Q}^G \tag{5.19}$$

- Select the number of relevant dofs Nr that the reduced model should account for. For example, in the range of application of the available test rig, the dynamic of the rig up to its first two critical speeds is relevant. This reduces the number of degrees of freedom to the first two bending modes.

- Extract the relevant eigenevectors from eq (5.11) and split them in left $\mathbf{L}$ and right $\mathbf{R}$ vectors:

$$\begin{aligned}\mathbf{L} &= [\varphi_1^L \cdots \varphi_{Nr}^L]' \\ \mathbf{R} &= [\varphi_1^R \cdots \varphi_{Nr}^R]\end{aligned} \tag{5.20}$$

  Note that the solution of the eigenvalue problem (5.10) as set up produces the right eigenvector column $\boldsymbol{\varphi}_k^R = \mathbf{R}$. The left eigenvector is defined as a row vector satisfying:

$$\boldsymbol{\varphi}_{\boldsymbol{k}}^{\boldsymbol{L}}\mathbf{A}_{glob} = \lambda_k\boldsymbol{\varphi}_{\boldsymbol{k}}^{\boldsymbol{L}} \tag{5.21}$$

  It follows that $\mathbf{R} \cdot \mathbf{L} = \mathbf{I}$.

- Define the pseudo modal vector $\boldsymbol{\eta}$ as $\mathbf{q}^G = \mathbf{R} \cdot \boldsymbol{\eta}$. Note that $\boldsymbol{\eta}$ has dimension $Nr \times 1$.

- Setup the reduced system:

$$\mathbf{L}^T\mathbf{M}^G\mathbf{R}\ddot{\boldsymbol{\eta}} + \mathbf{L}^T\mathbf{D}^G\mathbf{R}\dot{\boldsymbol{\eta}} + \mathbf{L}^T\mathbf{M}^G\mathbf{R}\boldsymbol{\eta} = \mathbf{L}^T\mathbf{Q}^G \tag{5.22}$$

  or simply:

$$\mathbf{M}^r\ddot{\boldsymbol{\eta}} + \mathbf{D}^r\dot{\boldsymbol{\eta}} + \mathbf{K}^r\boldsymbol{\eta} = \mathbf{Q}^r \tag{5.23}$$

  Note that the size of the system is now $Nr \times Nr$.

When applying pseudo modal reduction for rotating system one should be aware that the gyroscopic matrix is function of the rotational speed, thus the reduced system given in eq. (5.22) must be recalculated whenever this parameter is varied.

It should be stressed that by applying a modal reduction one introduces a relevant approximation, thus one should select carefully the number of modes to retain and discard.

5.2 Static analysis of Rotor in free-free conditions

In order to validate the computational program, a comparison between natural frequencies obtained from experiments and from numerical calculation is performed. To ensure that the numerical model reflects the real system, an adjustment of the number of elements, dimensions, and the material properties (Young's modulus, density) of the rotor was made for each considered configuration. The adjustment is necessary as the numerical model is simplified version of the real rotor and it does not take into account grooves, threads and rounding.

5.2.1 Experimental procedure

For a stationary shaft, the easiest way to perform modal identification is a simple impact test. This test allows to determine the natural frequencies of the shaft with different configurations:

- Shaft only
- Shaft with disc
- Shaft with disc and magnetic rings

In each case the shaft is hung on flexible strings which allow free-free movements. By using a impact hammer equipped with a force transducer, the shaft is excited and transient response recorded with an accelerometer. For each configuration, the experiment is repeated in order to ensure repeatability. Figure 5.5 shows the impacts position on the rotor, and the position of the attached accelerometer for one of the test. By digital signal processing, namely Fast Fourier Transforms (FFT), it is possible to obtain from the recorded data signals, in time, an experimental Frequency Response Function (FRF).

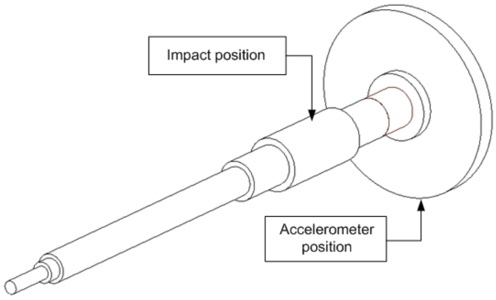

Figure 5.5: Impact test procedure.

The autocorrelation, R_{xx}, and crosscorrelation, R_{xf}, functions are given as:

$$R_{xx}(\tau) = \lim_{T\to\infty} \frac{1}{T} \int_0^T x(t)x(t+\tau)dt \tag{5.24}$$

$$R_{xf}(\tau) = \lim_{T\to\infty} \frac{1}{T} \int_0^T x(t)f(t+\tau)dt \tag{5.25}$$

Where $x(t)$ and $f(t)$ are the response and force signal, respectively. The correlation functions shows how fast the signal varies in time, by the use of convolution integrals. The Power Spectral Density (PSD) and the Cross Spectral Density (CSD) are then given, respectively, by the following Fourier transforms:

$$S_{xx}(\omega) = \frac{1}{2\pi} \int_{-\infty}^{\infty} R_{xx}(\tau)e^{-i\omega\tau}d\tau \tag{5.26}$$

$$S_{xf}(\omega) = \frac{1}{2\pi} \int_{-\infty}^{\infty} R_{xf}(\tau)e^{-i\omega\tau}d\tau \tag{5.27}$$

Notice that $S_{xf} = S_{fx}$ due to, among other reasons, the orthogonality property of the Fourier transform.

There is a direct link between the spectral densities and the frequency response function:

$$H_1(\omega) = \frac{S_{fx}}{S_{ff}} \tag{5.28}$$

$$H_2(\omega) = \frac{S_{xx}}{S_{xf}} \tag{5.29}$$

Each of them have their advantages and faults. $H_1(\omega)$ is a better estimator in areas around the antiresonance, since the force applied will be large whereas $H_2(\omega)$ is best used around resonance, because the response signal will be very high.
As a test of the data quality, the coherence function is given by the following:

$$\gamma = \frac{|S_{fx}|^2}{S_{xx}S_{ff}} \tag{5.30}$$

Since the time history is recorded as discrete points, a discrete FFT is used to calculate the spectral densities. This facilitates splitting the time history into overlapped segments. A Hanning-window is applied to the segment in order to avoid leakage. The segment is processed and the result is used to update the spectral average. The number of spectral averages possible depends on the length of the time history record, and generally the more averages used, the more smooth the resulting frequency response will be.

An example of the transient signals for a single impact of one of the impact tests is presented in Figure 5.6. As more impact test signals are recorded for the same tests, the FRF response with coherence and phase plots can be produced, as shown in Figure 5.7.

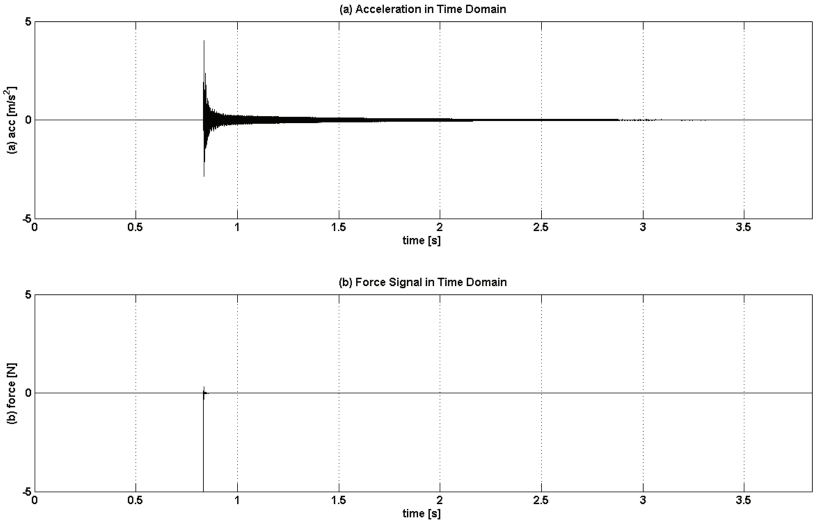

Figure 5.6: Analysis in time domain; acceleration and force.

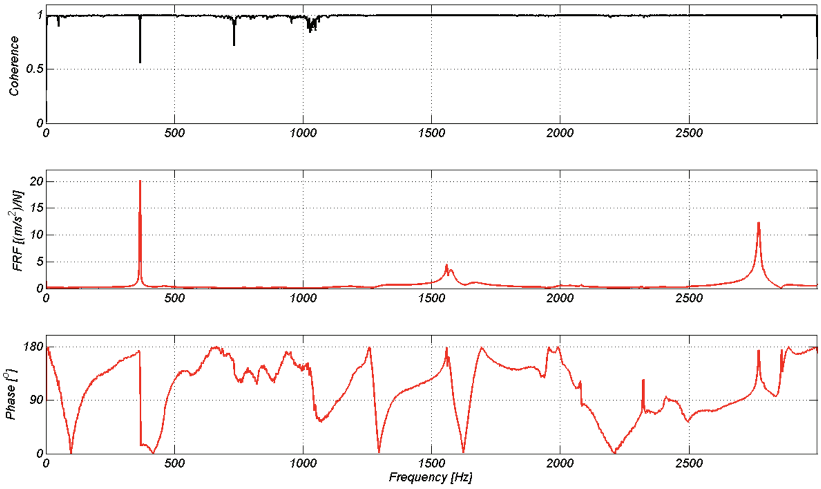

Figure 5.7: Analysis in frequency domain; coherence, FRF amplitude and phase for the shaft and disc.

5.2.2 Summary of numerical and experimental results

For the analysis in free-free conditions, It is considered as acceptable a deviation of up to 5% between numerical and experimental values. The natural frequencies are identified as following illustrated.

Consideration on model updating. Note that in general numerical results needed some degree of adjustment in order to match the experimental measurements. Mostly, numerical parameters such as material density and elasticity modulus have been updated, however radii averages and element lengths have also been varied in order to obtain the best possible match. The updating procedure needs to be repeated for each shaft/disc configuration.

Also, it should be mentioned that minimum number of elements that ensure convergence has been investigated and respected. Increasing the number of elements does not necessarily result in more precision. When discretizing with a large number of elements, the roundoff error will increase and therefore the accuracy of the model is decreased.

ω_i	ω_{num} [Hz]	ω_{exp} [Hz]	Deviation [%]
ω_1	518.5	518.2	0.1
ω_2	1570.1	1540.3	2

Table 5.1: Numerical and experimental natural frequencies for the shaft only in free-free conditions.

ω_i	ω_{num} [Hz]	ω_{exp} [Hz]	Deviation [%]
ω_1	371.4	366.7	1.3
ω_2	759.6	734.9	3.4
ω_3	1633.8	1567.2	4.2

Table 5.2: Numerical and experimental natural frequencies for the shaft with disc in free-free conditions.

ω_i	ω_{num} [Hz]	ω_{exp} [Hz]	Deviation [%]
ω_1	330.3	340.0	-2.9
ω_2	702.2	699.5	0.4
ω_3	1520.5	1546.3	-1.7

Table 5.3: Numerical and experimental natural frequencies for the shaft with disc and magnetic rings in free-free conditions.

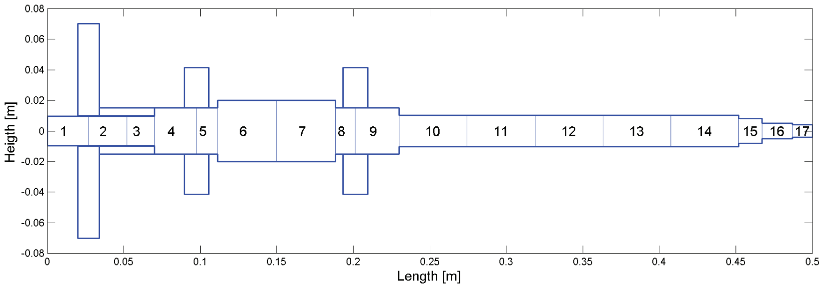

Figure 5.8: Numerical model for shaft with disc and magnetic rings.

5.3 Dynamic Analysis

Mathematical concepts necessary for rotordynamic analysis are introduced here in this section. Numerical analysis is performed for various system configurations in passive operation, aimed at defining the baseline performance characteristics of the prototype machine. Experimental validation is presented in the following chapter.

5.3.1 Adding unbalance

Generally rotating machine are characterized by the presence of some degree of unbalance. Such unbalance can be related to a specific design feature, however some residual amount is unavoidably present even when manufactured with the tightest tolerances. In many cases, it is possible to model unbalance as a concentrated mass m_u rotating with the shaft at a distance e_u from its center, see Figure 5.9. Mathematically, this effect can be included by a simple addition to the equation of motion of the system, eq. (5.5) as for the linear model, the superposition principle holds. Specifically, the the vector of externally applied loads, $\mathbf{Q}^G$ would change, taking the contribution:

$$\mathbf{Q}^G_{unbal.} = \mathbf{f}_c \cos(\Omega t + \phi) + \mathbf{f}_s \sin(\Omega t + \phi) \tag{5.31}$$

In the global model, the vectors $\mathbf{f}_c$ and $\mathbf{f}_s$ contain $m_u e_u \Omega^2$ only at the (translational) degrees of freedom where unbalance is present, otherwise they are equal to zero.

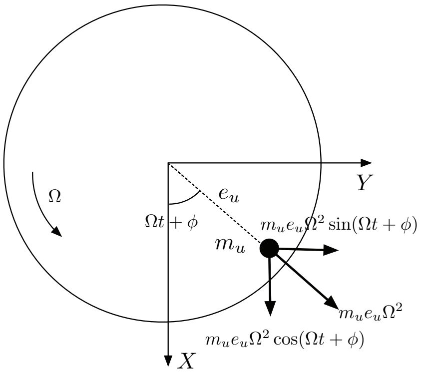

Figure 5.9: Physical representation of rotating unbalance forces.

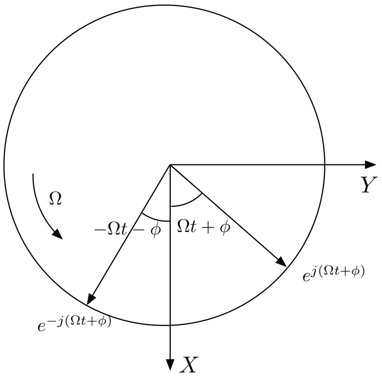

Figure 5.10: Mathematical representation of rotating unbalance in complex form.

In order to ease notation, one can write $\mathbf{Q}^G_{unbal.}$ in complex form and disregard ϕ:

$$\mathbf{Q}^G_{unbal.} = \mathbf{f}_+ e^{j\Omega t} + \mathbf{f}_- e^{-j\Omega t} \tag{5.32}$$

Where:

$$\mathbf{f}_+ = \frac{\mathbf{f}_c}{2} + \frac{\mathbf{f}_s}{2j} \quad \text{and} \quad \mathbf{f}_- = \frac{\mathbf{f}_c}{2} - \frac{\mathbf{f}_s}{2j} \tag{5.33}$$

Solving the equation of motion with respect to the stationary solution, and applying the superposition principle the forward (+) and backward (−) contributions are defined:

$$\mathbf{Q}^G = \hat{\mathbf{q}}_+ e^{i\Omega t} + \hat{\mathbf{q}}_- e^{-i\Omega t} = \hat{\mathbf{q}}_+ + conj(\hat{\mathbf{q}}_-) \tag{5.34}$$

Where:

$$\begin{aligned} \hat{\mathbf{q}}_+ &= \left[-\Omega^2\mathbf{M} + \mathbf{K} + j\Omega\left(\mathbf{D} + \mathbf{G}(\Omega)\right)\right]^{-1}\mathbf{f}_+ \\ \hat{\mathbf{q}}_- &= \left[-\Omega^2\mathbf{M} + \mathbf{K} - j\Omega\left(\mathbf{D} + \mathbf{G}(\Omega)\right)\right]^{-1}\mathbf{f}_- \end{aligned}$$

5.3.2 Campbell diagrams, stability maps and unbalance responses

In rotordynamics analysis, Campbell diagram plots are often used to characterize the response of the system as a function of the rotational speed. In such systems, eigenfrequencies generally vary with speed due to gyroscopic effects and variable dynamic coefficients. Campbell diagrams for different configurations of the system are calculated by varying the angular velocity of the rotor, and for each velocity computing the corresponding first damped natural frequencies; whenever the rotational speed of the rotor crosses a natural frequency a critical speed is reached, which may result in increasing the amplitude of the rotor vibrations, as the natural frequencies are excited (for the machine under analysis it is reasonable to assume that synchronous excitation is mainly due to residual unbalance in the system). The magnitude of vibrations amplification and, in the case of critical speeds, the rate of change of the phase-angle with respect to speed, are related to the amount of damping in the system.

Figure 5.11 shows the Campbell diagram relative to the machine operating with the gas bearing in aerodynamic mode. The first six natural frequencies are plotted; Note that the range of interested is limited to the band 2,000-12,000 rpm. These values are chosen a result of considerations of experimental nature; the lower bound is related to the minimum velocity to ensure aerodynamic lift of the journal bearing, whereas the upper bound is threshold velocity that the

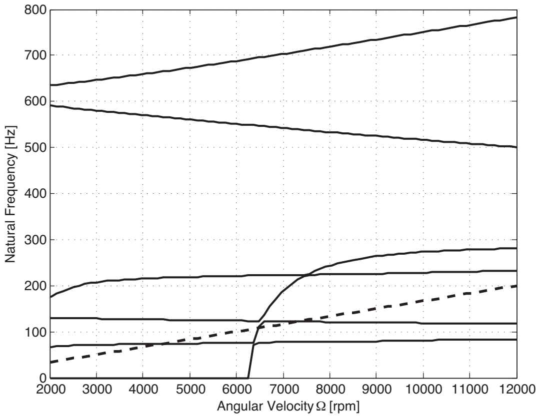

Figure 5.11: Numerical Campbell diagram, aerodynamic mode.

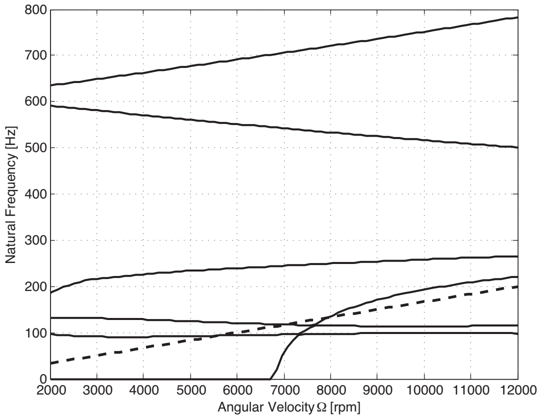

Figure 5.12: Numerical Campbell diagram, hybrid mode, p_{inj}= 3 atm.

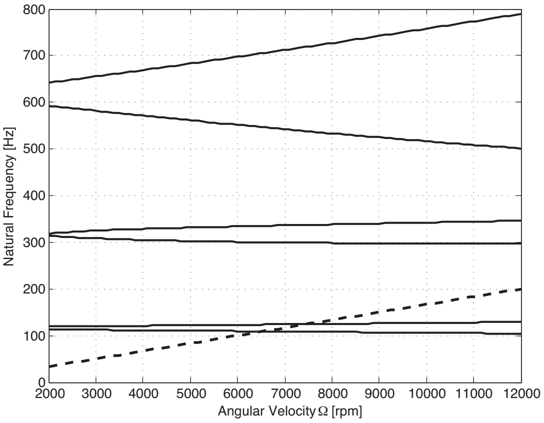

Figure 5.13: Numerical Campbell diagram, hybrid mode, p_{inj}= 8 atm.

experimental setup can deliver. Note that the modal interaction appears as veering regions in which different natural frequencies come close to each other, but the corresponding modes keep their orthogonality. In practice no crossing occurs, but as they approach each other, they veer the other's frequency path.

Figure 5.12 present an analogous analysis, however relative to the bearing operating in hybrid mode, with injection pressure of $p_{inj} = 3$ atm. The overall behavior is similar to that presented for the aerodynamic case; as the geometrical and physical properties of rotating machine are identical for the two analyses, the only source of discrepancies stems form the dynamic coefficients of the gas bearing. Under this light, such trend is then consistent with the considerations discussed in section 3.6.3.1, particularly when comparing Figures 3.26 and 3.28; at the consid-

ered speed range, the curves (thus the absolute values of the coefficients) are similar. Referring to the Campbell diagram, one notices that the spreading between first backward and forward modes is more pronounced for the aerodynamic case; in general this suggests a higher degree of anisotropy in the stiffness coefficients.
The hybrid case at the higher injection pressure, $p_{inj} = 8$ bar is finally presented in Figures 5.13. Compared to the previously discussed case, the system shows a markedly different behavior. The first two critical speeds are increased, moreover the over-damped mode present in both aerodynamic and lower pressure hybrid modes disappears.

A stability analysis corresponding to the same operation conditions studied for the Campbell diagrams is presented in Figures 5.14 - 5.16, where stability maps are shown. Here the real part of the eigenvalues of the system are plotted as function of the angular velocity. Note that the real component is associated to the damping level of the mode, and instability occurs if any of these components assumes positive value. Note that in this case study, all modes are stable within the operating region boundaries.

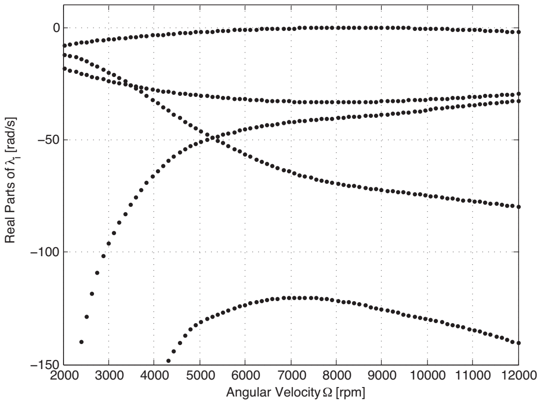

Figure 5.14: Stability map, aerodynamic mode.

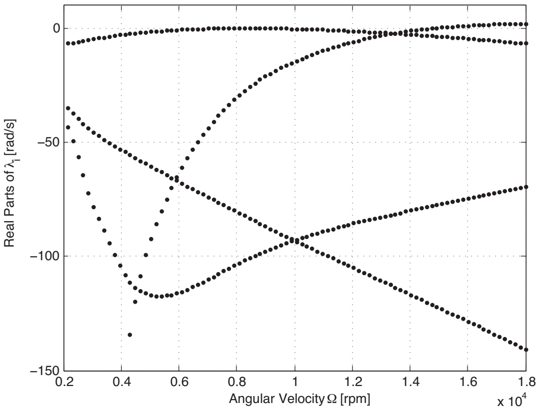

Figure 5.15: Stability map, hybrid mode, p_{inj}= 3 atm.

For aerodynamic operation, the analysis suggests that stable operation is maintained throughout the entire operational speed range, up to 12,000 rpm. Comparing these results for the stability map for the hybrid operation at p_{inj}= 3 atm, see Figure 5.15, it should be noticed that the analysis is extended up to 18,000 rpm; it is then possible to show that the real part

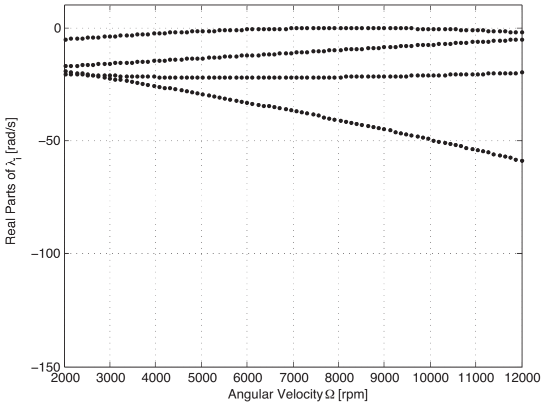

Figure 5.16: Stability map, hybrid mode, p_{inj}= 8 atm.

of one of the system eigenvalues becomes positive (just above 14000 rpm), inducing instability. This will be later confirmed by experimental results. However, at lower speed the stability map is more "negative", suggesting overall slightly higher modal damping with respect to aerodynamic case. On the other hand, by increasing the injection pressure the system becomes stiffer, as observed in the Figure 5.13, but also significantly less damped, as confirmed by the lower stability margin (the real part of the eigenvalues are closer to zero). These observation are consistent with the behavior of the damping coefficients presented in section 3.6.3.1, Figure 3.29.

The analysis of the general behavior of the system at different operating conditions is furthermore confirmed and completed by a study of the damped unbalance response, see Figures 5.17 - 5.18. For this analysis a number of assumption are made:

- It is assumed that the unbalance mass is concentrated and lumped to the nodal coordinates of the rigid disc. Such choice is made after consideration of experimental nature, where it is found that the disc has by far the largest influence on the unbalance response of the system; moreover such placement generally corresponds to the location of maximum displacement nearest to the journal bearing (thus, as API 617 recommendations).
- The magnitude of the unbalance is also derived from experimental identification; it is chosen to match the unbalance level of the system in regions away form resonances.

The stability maps suggest that the most favorable configuration is the hybrid bearing at low injection pressure, p_{inj}= 3 atm. This claim is confirmed by lower energy unbalance response when crossing the critical speeds, see Figure 5.18 compared to 5.17. Such behavior might suggest a contradiction with the analysis of damping coefficients, which show higher direct damping coefficients for the aerodynamic case, however one should also notice that for the hybrid case the cross-coupled terms are also closer to zero. For higher pressurization values, see Figure 5.19, the amount of damping introduced into the system by its support is significantly smaller. As a result, the unbalance diagram shows a much larger response, with amplitudes across the first forward critical speed that seem to suggest potential bearing-journal touchdown scenario.

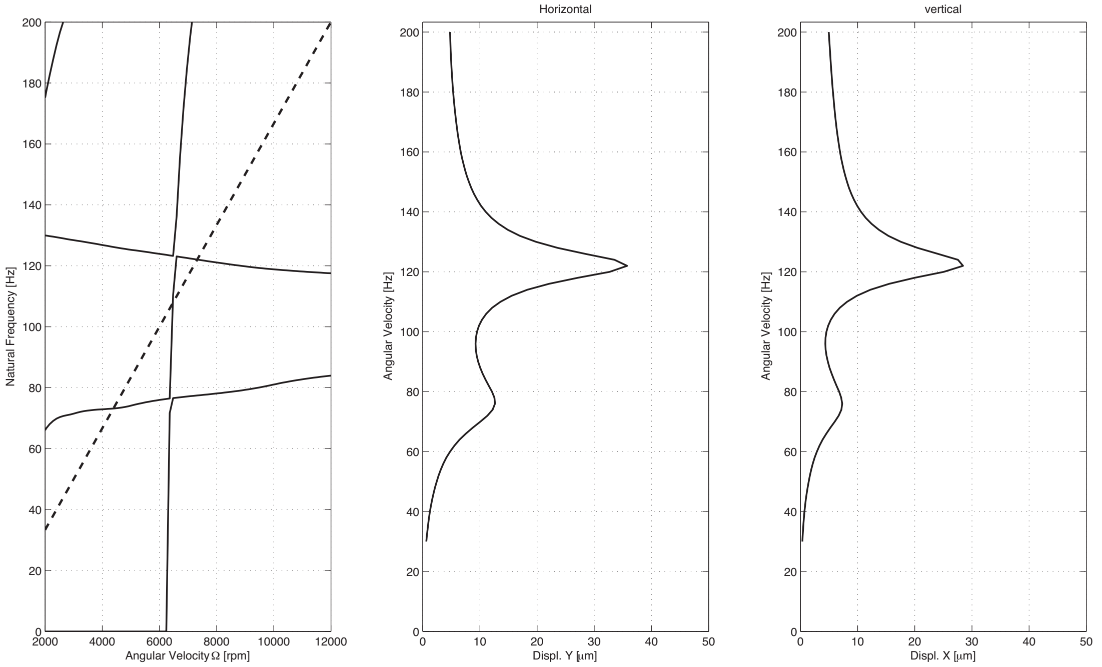

Figure 5.17: Numerical evaluation of unbalance response, aerodynamic mode.

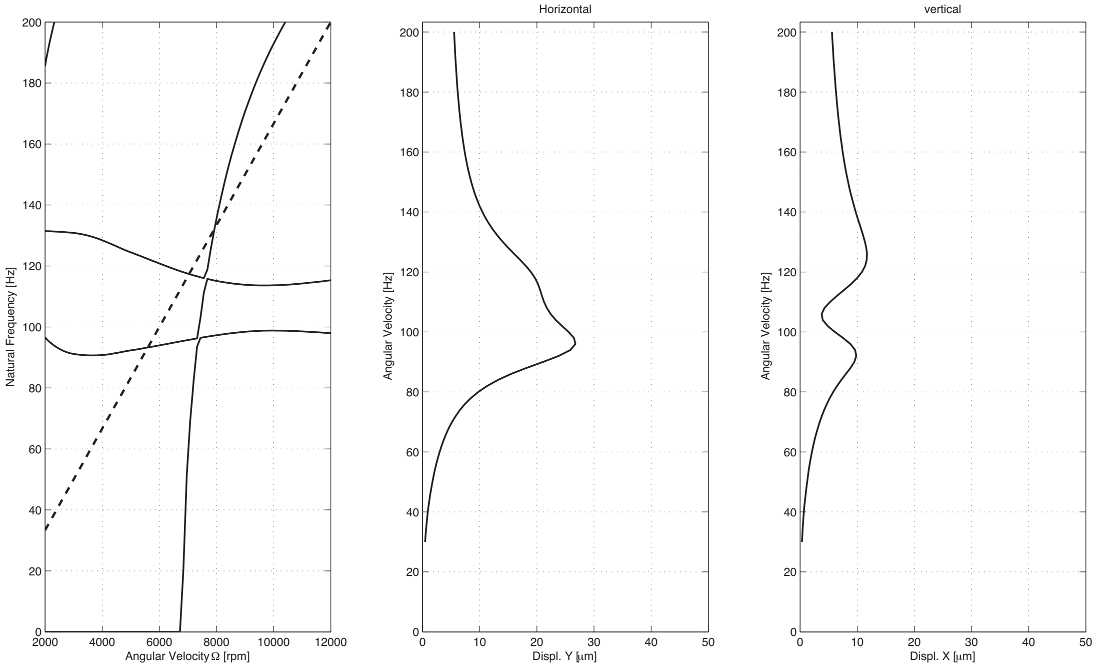

Figure 5.18: Numerical evaluation of unbalance response, hybrid mode, p_{inj}= 3 atm.

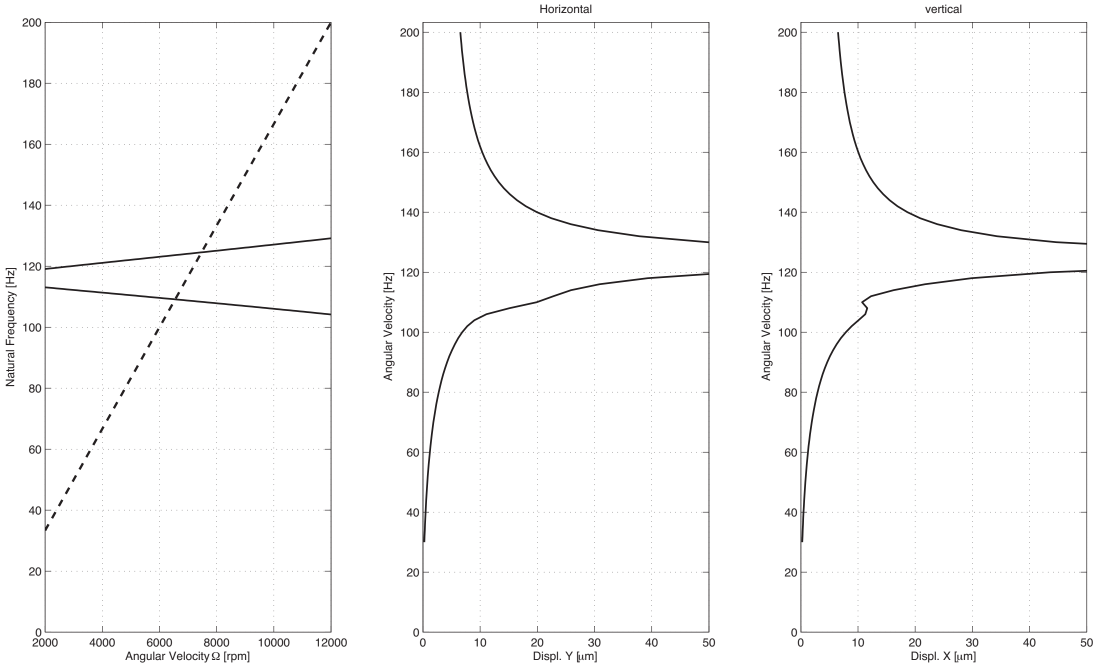

Figure 5.19: Numerical evaluation of unbalance response, hybrid mode, p_{inj}= 8 atm.

5.4 Rotodynamic experimental Results

The following section deals with the results of the experimental analysis and verification of the rotor-bearing system.
Experimental rotordynamic results are presented, both concerning the passive system and with active lubrication. Differences with numerical results are evaluated and the sources of such discrepancies explained.

5.5 Model validation: passive hybrid aerostatic-aerodynamic bearing

Before the active control schemes are implemented in the test rig and evaluated, the dynamics of the system running in passive, non-controlled mode is experimentally studied. Such preliminary study has two important purposes:

1. to tune and validate the mathematical modeling and numerical predictions;
2. to asses the operational range of the machine and identify the operating conditions where the control system can be most suitably implemented.

For this purpose, selected numerical examples for the bearing operating in hybrid mode are presented and discussed. Note that during this phase, the permanent magnetic bearings are dismounted.

The issues of model tuning and updating have been the first concern of the early experimental assessments. In order to obtain reasonable agreement between numerical and experimental results a systematic variation of the model parameters (particularly concerning the fluid film bearing) has been performed. Perhaps the most challenging discrepancies between idealized model and the real setup was managing an equal flow through the orifices equipped with piezo actuators, as discussed in section 2.8. Other challenges included keeping consistent pressurization levels in the bearing. As the feeding line is directly connected to the laboratory centralized system, considerable variations can be expected and need to be carefully monitored; moreover with the pressure regulation equipment it resulted to be difficult to make fine pressure adjustments. Alignment between the air turbine and flexible shaft has also proven to be an issue, as well as the minimization and estimation of residual unbalance.

5.5.1 Unbalance response and critical speed analysis

Several rotordynamic performance parameters can be practically evaluated by performing coast down rotor speed tests. Among these, it is possible to obtain clear identification of the system critical speeds, the overall residual level of unbalance and the instability threshold speed, if present. Moreover, by varying the radial injection pressure, it is also possible to evaluate the effect of this parameter on the overall performance of the machine.

5.5.1.1 Experimental procedure

Each coast down test follows the same procedure:

1. Run-up the machine to the maximum reachable speed (without instability or excessive vibration amplitude).
2. Close the air supply of the air turbine and start measurements. Note that the data acquisition hardware allows a maximum continuous recording time of 70 s (at the minimum sampling frequency allowable for providing good results). In case the coast down run is longer than this value, a re-run up is required to the speed where the last measurement are recorded (plus overlapping).

Note that for each operation conditions several complete tests have been performed, to insure repeatability. However, it should be mentioned that no averaging is made in the following results, each consisting of single test measurement.

5.5.1.2 Selected results

Figure 5.20 shows a waterfall plot for the rotor horizontal response consisting of spectral lines of vibration versus speed while coasting down from a top speed of 12,500 rpm at injection pressure of p_{inj}= 3 atm.

The results show that the main frequency component corresponds to the synchronous 1X vibration due to unbalance excitation (A). Notice the increased response during crossing of the first two critical speeds, (B) and (C). A smaller supersynchronous 2X component is also observed (D); its presence is related to coupling misalignment between rotor and turbine. Such phenomenon is greatly studied and explained in literature; among references, one could cite Sekhar and Prabhu [92], who numerically evaluated the effects of coupling misalignment on

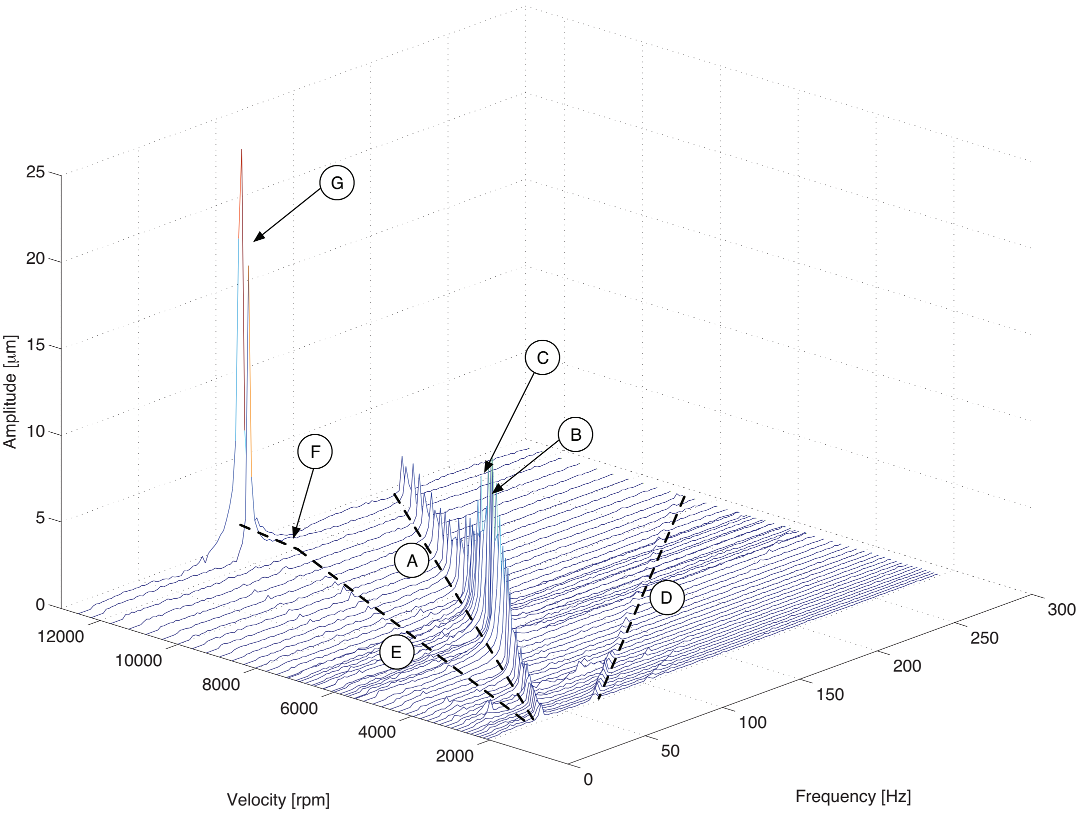

Figure 5.20: Waterfall diagram for a coast-down rotor speed test, p_{inj}= 3 bar.

the 2X vibration response of rotor-coupling- bearing system. Dewell and Mitchell [20] showed experimentally that 2X and 4X vibration components are largely dependent upon coupling misalignment. Moreover, a subsynchronous 0.5X whirling component is also observed throughout the speed range (E). At low speed such contribution is very limited, and can be only partially detected. However, at a speed just above 12,000 rpm such subsynchronous frequency suddenly becomes excited, sending the rotor into whirl instability (G). Note that the whirling instability frequency is around half the rotational speed, but also coincides with one of the system critical speeds. The whirl instability is a well understood phenomenon, which is mainly caused by cross-coupled force effects [55]. It is a severe problem in gas bearings as sustained operation of the rotor at this speeds can lead to severe mechanical damage where the vibration motion spans the entire bearing clearance. Note that instability persists also at speeds above the threshold, as the whirl becomes locked to the system natural frequency in a whip phenomenon (F). Moreover, it should be mentioned that the useful operational range can be extended by reducing the rotating unbalance, as the whirling instability threshold also relates to this parameter [82], [83]. Although the waterfall plot gives a good overview of the global dynamic of the rotor-bearing system, it it difficult to identify some characteristics, such as the location and response amplitude of the critical speeds. Figure 5.21 shows the unbalance response of the coast down in the same conditions as for Figure 5.20. Note that only the stable operation region is considered. In this case the experimental unbalance response values are given by the maximum amplitude of recorded displacement signals either in horizontal and vertical directions. It should be remarked that as the measurement location is at the disc and not at the bearing, values exceeding the nominal clearance can be observed without being in touch-down conditions (without considering bending the limit clearance at the disc station is ca. 33 μm). It is seen that numerical predictions and experimental results are in good agreement with each other. The crossing of the two critical speeds can be noticed, particularly in the vertical response; the theoretical curve shows a marked decrease of response between the two peaks; such behavior is less evident in the experimental curve, however it should be noted that the theoretical predictions are based on steady state assumptions, whereas during a coast down such conditions may not be satisfied, particularly considering a situation where the deceleration is not slow enough compared to the damping level of the system.

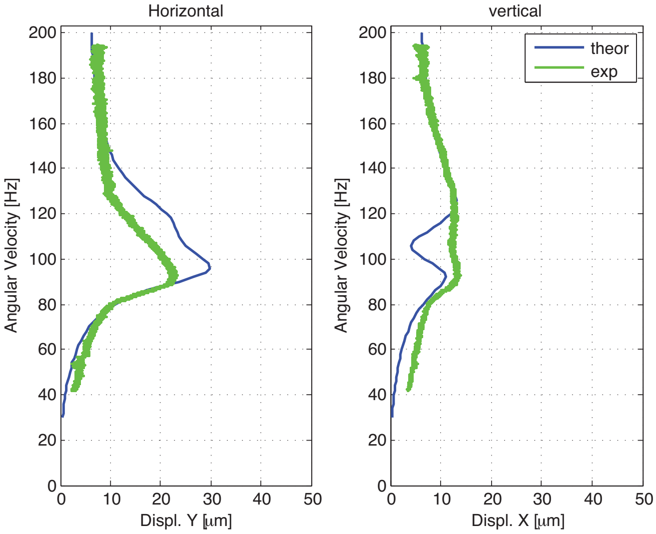

Figure 5.21: Theoretical and experimental unbalance responses (peak to peak), passive operation, p_{inj}= 3 bar.

Regarding the comparison between theoretical and experimental results, further general observations can be made:

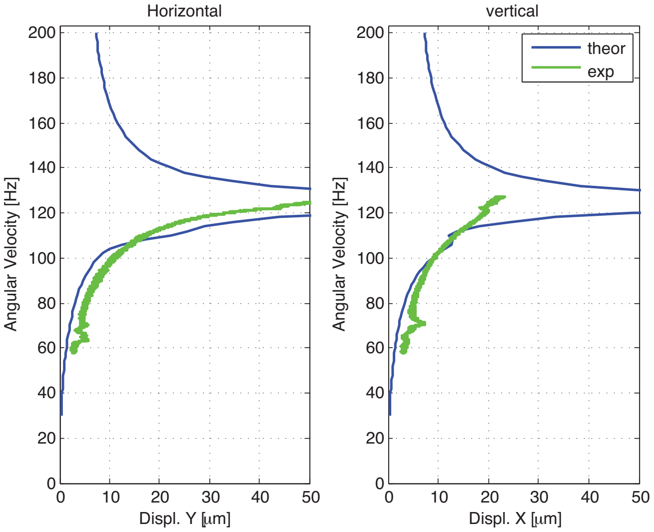

Figure 5.22: Theoretical and experimental unbalance responses (peak to peak), passive operation, p_{inj}= 8 bar.

- The values of experimental unbalance response in the supercritical region are used for parameter identification (both for geometrical data of rotor-bearing system, such as the manufactured radial clearance, as well as unbalance in the system) in order to tune the numerical model.

- Theoretical results are based on predictions of bearing dynamic coefficients obtained with a linearized theory (small perturbations). In general then, predicted response around resonance should not be considered as reliable, as in theses regions amplitudes are large.

The procedure described above for the hybrid bearing at low injection pressure, p_{inj}= 3 atm is repeated when increasing the pressure to p_{inj}= 8 atm. Figure 5.22 depicts the unbalance amplitudes of rotor in these conditions. Firstly, it should be noticed that the critical speeds cannot be crossed, as when the velocity of the rotor approaches the critical value, the vibration amplitude increases dramatically, causing touch-down between journal and bearing. This is mainly due to the loss of damping caused by the increase of external pressurization. Similar behavior was observed and studied by Osborne and San Andres [67], where they experimentally observed an increase of the critical speed resulting from higher injection pressures. These observations can be explained for example when looking at the calculated damping coefficients, which decrease considerably as the injection pressure is increased, compare Figures 3.28 and 3.29. Rotordynamic numerical predictions are also consistent with this claim, see the narrower margins in Figure 5.16 compared to 5.15. Moreover, it should be noticed that theoretical results show how external pressurization into the gas bearing increases its direct stiffnesses, thereby raising the system critical speeds, as seen in Figures 5.12 and 5.13. Again, this seems to be confirmed when analyzing the experimental responses; moreover, it should be mentioned that as the backward and forward speeds are now closer to each other compared to the lower pressurization case, it is more difficult to identify separation between them.

5.5.2 Identification of damping ratios: least squares complex exponential method

Modal parameters are usually identified by curve fitting a set of Frequency- or Impulse Response Functions, FRFs or IRFs. By curve fitting it is intended the process of matching a mathematical expression to a set of empirical data points. Commonly, this implies to minimize the squared error (or squared difference) between the analytical function and the measured data.

Depending on the type of system under analysis, several techniques can be employed, with varying level of complexity. Simple systems, which can be approximated by Single Degree Of Freedom (SDOF) mechanical equivalents or Multi Degrees Of Freedom Systems (MDOF) that present relatively uncoupled modes (light modal density) can be approached by simple methods, such as SDOF least square techniques. Such methods estimate modal parameters in independent instances and are thus straightforward to use. However, when modal coupling is strong, in order to account for the modal interaction, the identification technique need to be able to simultaneously estimate modal parameters for two or more modes at a time [90].

In the region of interest, high modal coupling is present between the first two critical speeds (first backward and forward modes), thus a time domain IRF identification method is set up with the aim of evaluating the damping ratios of the system, the least squares complex exponential method. The method follows the procedure introduced by Brown et al [11]. The mathematics is omitted here, however it is summarized in Appendix D.

5.5.2.1 Experimental procedure

A series of impact tests measurements are performed for both static and dynamic conditions, gradually increasing the rotational speed. Note that at least 5 impacts are recorded at each speed, to ensure repeatability. The experimental procedure is as follows:

1. For each rotational speed, launching the test rig and achieving steady state conditions.
2. Exciting the rotor at disc location with impact hammer with a plastic head.
3. Measuring window of 5 s.
4. For each rotational speed, repeating the measurements without excitation, in order to obtain reference measurement.

Note that point 4) is necessary as the raw signal is not only the sum of impact displacement and surface noise, but the unbalance component as well.

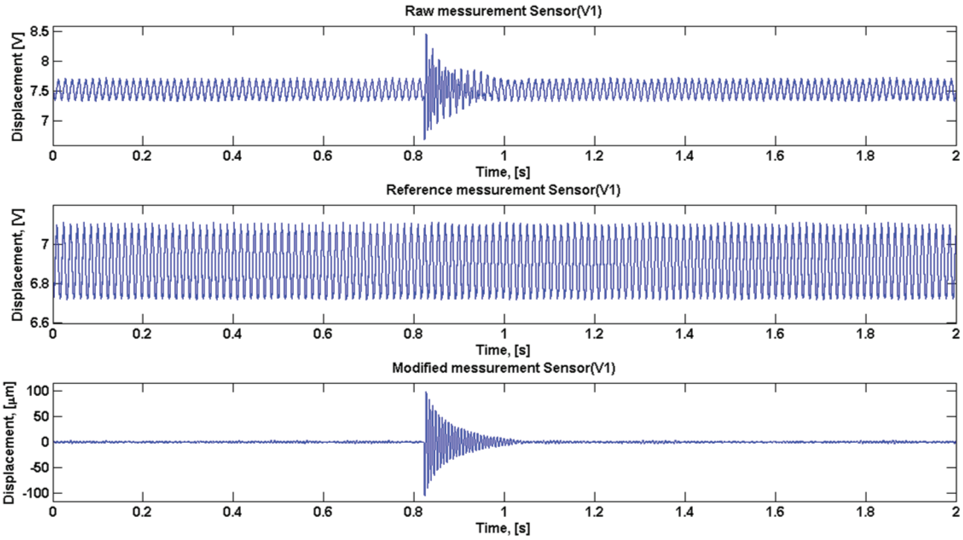

Figure 5.23: Impact testing: measurement procedure of damping factor for rotor bearing system with small disc and injection pressure of 8 atm, Ω= 4500 rpm.

Figure 5.23 shows an example of measurement and method of calculating of the damping factor for velocity of 4,500rpm. The top two time series plots represents the raw measurement of the impact test and reference measurement. These signals are subtracted from each other and, upon multiplying by the sensitivity of the sensors, converted in displacement. For each impact response, the damping factor was calculated by the least squares complex exponential procedure and subsequently averaged for all measured impacts. Figure 5.24 shows an example of the high modal interaction, with the response ”jumping” between forward and backward modes.

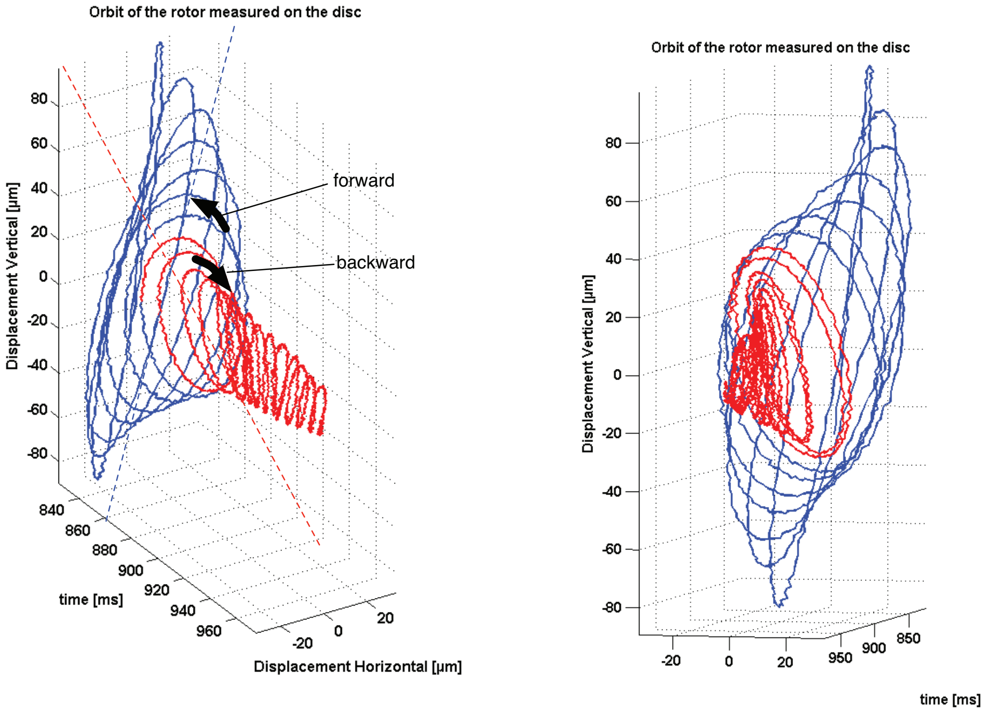

(a) (b)

Figure 5.24: Impact testing: time series showing rotor orbits, identifying 2 modes excitation (blue and red portions of curve), hybrid mode, p_inj= 8 atm .

Numerically calculated and experimental values of damping ratios of the first two modes are presented in Figures 5.25 and 5.26. They refer to the bearing operating in hybrid mode, with injection pressure of 3 and 8 atm, respectively.

Regarding the lower injection pressure, it should be mentioned that for rotational speeds up to ca. 6700 rpm the first damping ratio is actually relative to an over-damped mode[1], therefore omitted. Such over-damped mode can be easily visualized in the critical speed analysis, see Figure 5.18, where it can be noticed one natural frequency that has a zero constant value until 6700 rpm. Experimentally, this mode has too little energy to be detected. As for the first backward and forward modes, despite the correspondence between theory and experiment cannot be inferred in absolute values, the general trend and order of magnitude are at least comparable (especially for the forward mode).

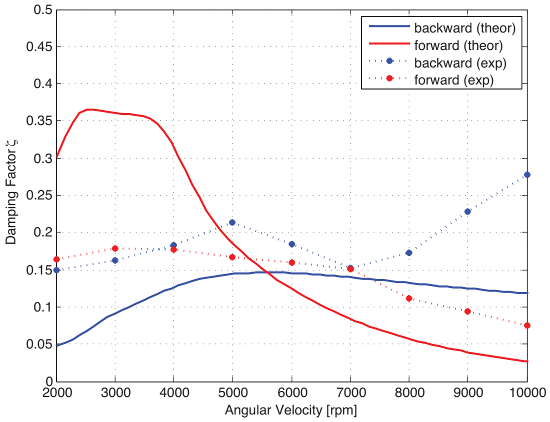

Figure 5.25: Theoretical and experimental values of the damping factor as a function of angular velocity for rotor bearing system, passive operation, p_{inj}= 3 atm.

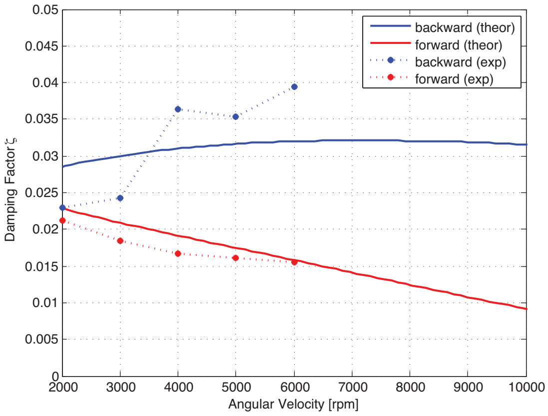

Figure 5.26: Theoretical and experimental values of the damping factor as a function of angular velocity for rotor bearing system, passive operation, p_{inj}= 8 atm.

At higher injection pressure, firstly it should be noticed that measurements are possible up to 6,000 rpm; above this value the system gets very close to its critical speed, where the amplitude of vibrations increases dramatically, until touch-down between journal and bearing occurs. Such conditions are indeed a confirmation of what observed numerically, see Figure 5.19 where it was suggested possible difficulties in crossing the critical speed. Indeed, the observed damping factor (both theoretically and experimentally) show very low values, around one order of magnitude lower than for the previous case. The general trends of the forward component seem to be in agreement, however establishing a good validation for the backward mode is more problematic.

---

[1] Mathematically, the solution of an over-damped system is of two different real roots; it means the mode has zero imaginary part, i. e. $\lambda = \lambda_{real} \pm \lambda_{imag}$, $\lambda_{imag} = 0$.

It should be mentioned that the backward mode is much harder to identify and in fact the least square identification procedure failed to produce meaningful results for many of the data sets, thus also increasing the uncertainty level of the results.

Note that the values of identified damping ratios relative to the forward mode are consistent to the results presented in [67] for a hybrid gas bearing of similar characteristics.

5.6 Summary of experimental results with active control

As observed in experimental analyses of the passive system, from a rotordynamic point of view there are two characteristics that limit the widespread of traditional gas lubrication:

1. Low damping makes operation across critical speed dangerous, as even low level of unbalance can generate large vibration responses. This is especially problematic for gas bearing applications, which often operate in the supercritical region. Damping deficiency is also detrimental for safe operation away from resonance, as the ability to cope with sudden shocks and excitations is poor.
2. The combination of low damping and large asymmetric, cross-coupled stiffness coefficients poses an upper bound also to supercritical operation, determined by the appearance of subsynchronous whirl. Due to the sudden increase in amplitude with respect to speed, this most often corresponds to the maximal attainable rotational speed of the system. Postponing the onset speed of this whirling therefore poses one of the greatest challenge in a high-speed gas bearing design [102].

5.6.1 Control loop tuning

The control gains are defined by the PD rule described in section 3.4.6, eq (3.77). Figure 5.27 offers a schematic view of the applied control scheme.

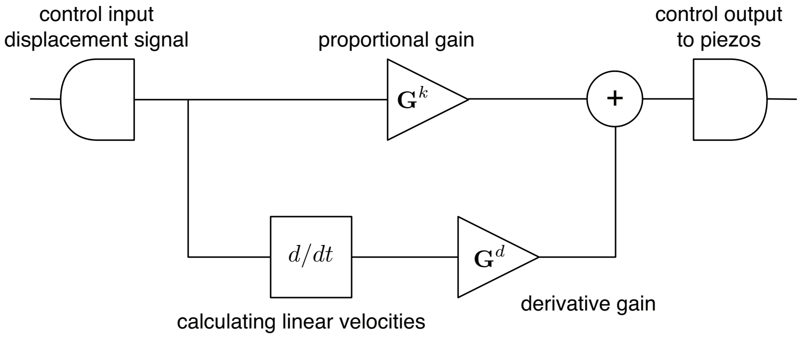

Figure 5.27: Control loop block diagram.

Tuning a control loop is the adjustment of its control parameters (gains) to the optimum values for the desired control response. In this case two goals need to be achieved; on the one hand the system should be more damped; this can be obtained by acting on the derivative gains $\mathbf{G}^d$ (velocity gains). On the other, one could be enhancing the stiffness by acting on the proportional gains $\mathbf{G}^k$ (displacement gains). In other words, by modifying the feedback gains over a certain range, one also modifies the stiffness and damping matrices and, consequently, the behavior of the system.

PD tuning is a difficult problem, even though there are only two parameters and in principle is conceptually intuitive, in practice it is relatively easy to make the controlled process to diverge by an incorrect selection of strategy; moreover, even when the strategy is chosen correctly, often instability arises caused by excess gain, particularly in the presence of significant lag. In fact, it is quite easier to design a control system to act as a shaker rather than to achieve its goal. Moreover, one should keep in mind that the optimum behavior on a process change or setpoint change may vary depending on the system; in this case, a thorough investigation is necessary regarding the operation conditions, as the controller may offer different performance when either rotational speed or injection pressure are changed. The goal is to choose a set of controller gains which offer good performance throughout the operational range, however it is in principle possible to tune the control system in order to offer better performance in any given situation by gain scheduling (using different parameters in different operating regions).

There are several methods for tuning a PD loop. Manual methods are the most direct ways, where the gains are varied in a "brute force" manner, bordering the instability boundaries until satisfactory performance is attained. Manual tuning methods can be relatively inefficient, moreover in some situations it may not be safe to send the system into unsteady behavior. Improvements can be attained by using heuristic approaches, like the Ziegler-Nicholson method. On the other side of the scale, tuning software can be used. They offer consistent tuning, can be used either online or offline and allow simulation before application. However, they often need a complex development and the tuning process may be less time efficient if optimal results are not required.

During this project the following workflow has been devised, in order to exploit advantages of both powerful software simulation capabilities and the ease of manual fine adjustments:

1. Obtain a stable and effective starting point by software simulation. Numerically, this is obtained as described in section 3.5.6.2.

2. Fine adjustment by the means of manual tuning simulations until the closed-loop system performs or compromises as desired.

One could argue why the tuning process is not completely performed via simulations; the main problem is the computing time it requires (at least in the present time-based solution form and available computing power). The current way to evaluate the controller performance consists in the time solution of a relatively complex system, involving the simultaneous solution of rotordynamic, (nonlinear) fluid film and piezoelectric set of equations. Moreover, the time step required for numerical stability are extremely small (in general 10^{-7} - 10^{-8}s). As a practical example, a 1 s transient simulation of the coupled nonlinear system requires around 36 hours. Aiming at a more efficient way to evaluate the controller performance numerically is certainly a top priority for the ongoing and future research; particularly interesting would be the possibility to perform simulations in the frequency domain. In addition, the numerical model does not account for measurement noise. Noise in the feedback loop is strongly unwanted, as it narrows the efficiency of the controller. It acts in two ways: on the one hand, as the displacement signal is used also to calculate the velocity, excessive noise can then introduce errors in the derivative. On the other hand, before being fed-back to the actuators, the control signal is amplified; thus even low noise level can be significant at the actuator input. This is especially a problem with piezo actuators, which respond to a broad range of frequencies. It is often helpful to filter the measurements with a low-pass filter in order to remove higher-frequency noise components. However, low-pass filtering introduces time lag, thus it can cancel out the derivative control contribution. Moreover, the cutting frequency also puts a ceiling to the maximum rotational speed at which the controller works; if the machine is pushed faster than the cutting frequency, the synchronous vibration components measured by the displacement signals is filtered. It means that filtering becomes an integral and substantial component of the control loop tuning.

5.6.2 Results of loop tuning

As anticipated in the previous paragraph, tuning is performed in order to investigate the influence of injection pressure and rotational speed; the experimental procedure is analogous to that presented in section 5.5.2.1. Practically, at each set pressurization and velocity values, it consists of producing a series of IRF while sweeping through the control gains. The initial control gains are obtained by numerical analysis, however during the tests the boundaries of the gain ranges are defined by changing their values until instability occurs.

It should be clarified that the goal of the tuning is to minimize the maximum amplitude of the response.

The typical outcome of such analysis is presented in Figure 5.28. Waterfall diagram of IRFs at different gains are presented; in this case the operational conditions are of zero rotational speed and injection pressure of p_{inj}= 8 atm. In Figure 5.28a the influence of the proportional gain is investigated, while setting the derivative term to zero; note that when $\mathbf{G}^k$= 0 , the system is in passive mode. Firstly, it should be noted that the variation of the proportional gain does not seem to have a great impact on the controller efficiency; its performance is slightly worsening as the gains are pushed to positive values before it reaches the threshold of stability, but this is expected as physically this means introducing energy into the system. More negative values do not produce a significant improvement either, showing rather stable IRF amplitude values. The most visible effect is however the stiffening of the system, as the natural frequencies appear to be increased. This effect is visible in the upper right detail of Figure 5.28a, showing the contour lines of the waterfall plot (the Frequency-Gain plane); again, this is physically consistent with the hardening effect that has to be expected when increasing stiffness.

A similar procedure is repeated varying the derivative gains, while setting the proportional term to zero, see Figure 5.28b. It is immediately clear that the derivative gains have a much larger influence of the dynamic amplitude response of the system; on the one hand, small increases of the gains towards positive values increase the response amplitude considerably, leading to an early onset of instability. On the other hand, decreasing the gains towards more negative values initially produces a beneficial effect, as for moderately negative gain values the maximum response amplitude is markedly reduced. Note that despite the rotational speed is set to zero, it seems to be possible to identify a separation between forward and backward modes. However, one particular feature seems to appear: as the control action becomes stronger, a pronounced shifting of the natural frequencies towards lower values becomes evident, leading to overdamping and a strong softening effect. Such effect is also accompanied by an undesired increase of the response. Moreover, it should also be noticed the appearance of a higher frequency component; it is a spill-over effect of excessive controller gain, suggesting a possible bifurcation of the eigenvalue.

Nevertheless, from this analysis it can be concluded that it is possible to identify optimum regions (marked in the red shaded ares in the contour details of Figures 5.28a and 5.28b), where both the proportional and the derivative control actions have the most beneficial contribution towards decreasing the amplitude response of the system. The combination of the identified optimal values of controller gains produces the best controller performances. Figure 5.32 presents a comparison between IRFs for the passive and active systems, showing the evident advantage of using active control. Note that the optimal gain are set to $\mathbf{G}^k$= -0.8 V/μm and $\mathbf{G}^d$= -0.015 V/μm. The same type of control loop tuning is repeated when the injection pressure is de-

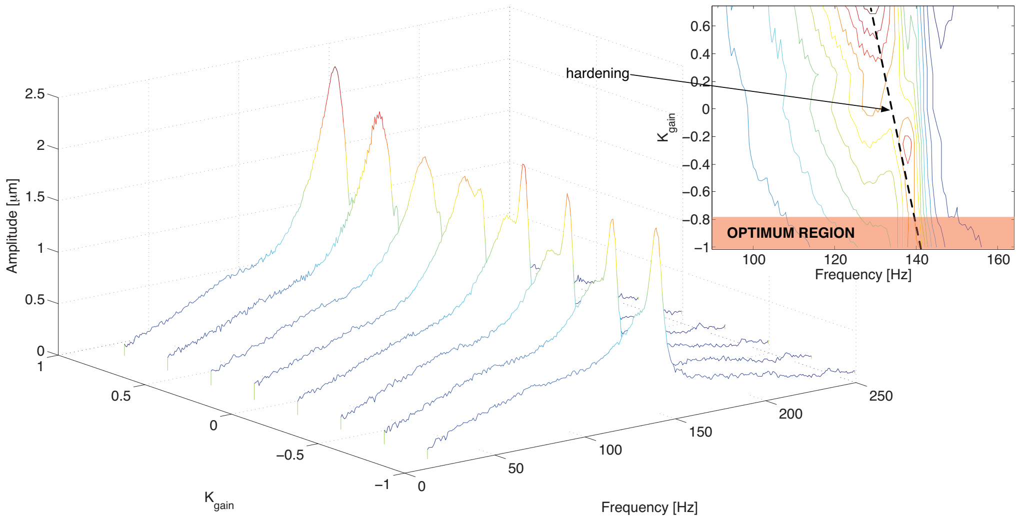

(a) Proportional gain sweep.

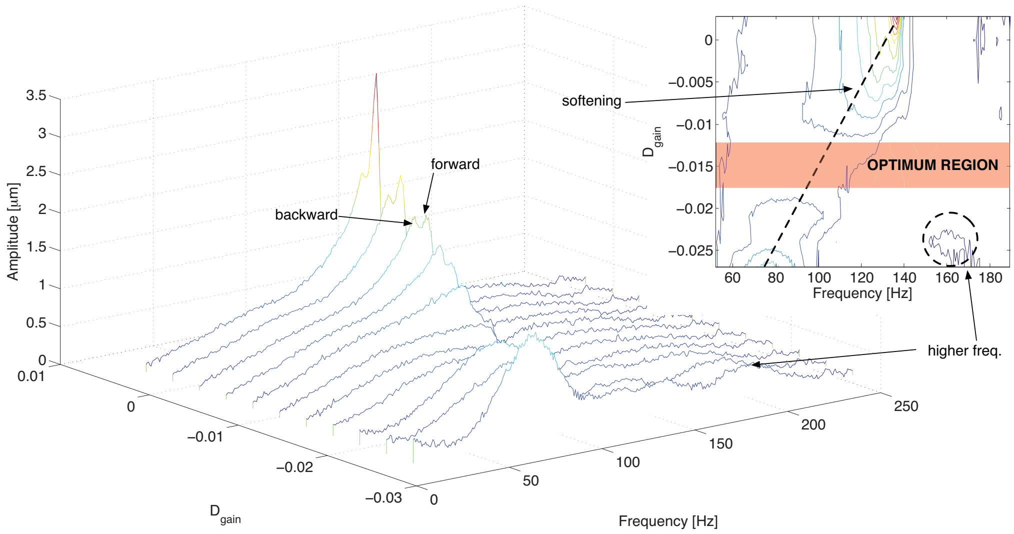

(b) Derivative gain sweep.

Figure 5.28: Waterfall diagrams of IRF with different control gains, p_{inj}= 8 atm, Ω= 0 rpm.

creased to $p_{inj}= 3$ atm. The final optimum gain results are presented in Figure 5.33. Compared to the $p_{inj}= 8$ atm case, the most noticeable difference is that the controller efficiency appears reduced. However this result is to be expected, because as previously analyzed the damping of the hybrid bearing is inversely proportional to the magnitude of injection pressure. It means that the higher is the pressurization, the better the control efficiency in damping the system. Moreover, regarding the lower pressurization case, one should be aware that although the critical frequency is reduced (and shifted towards lower frequencies), the response in the subcritical region is in fact higher than for the passive case; in the supercritical region however active and passive response are comparable.

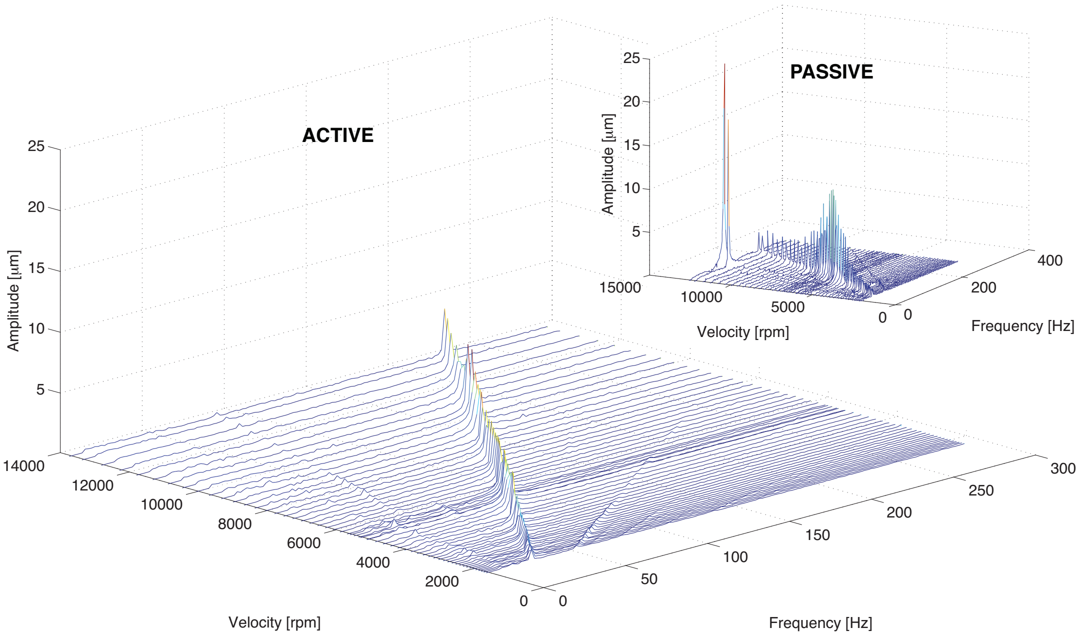

Figure 5.29: Waterfall diagram for a coast-down rotor speed test, $p_{inj}= 3$ bar, active operation, $\mathbf{G}^k= -1$ V/μm and $\mathbf{G}^d= -0.012$ V/μm. In the upper right corner, corresponding test in passive operation.

As anticipated by numerical predictions, the presently developed active control strategy has ability to address both synchronous and subsynchronous vibrations. Using the optimal gain values, Figure 5.29 is produced. It is an example of waterfall plot for the rotor horizontal response while coasting down from a top speed of 14,000 rpm at injection pressure of $p_{inj}= 3$

atm with active control. Compared to the corresponding results for the bearing operating in passive mode, see Figure 5.20, it is evident to notice the absence of any subsynchronous whirl instability and reduced synchronous response while crossing the critical speeds.

The influence of the rotational speed on the controller tuning is also investigated; This analysis reveals that the influence of this parameter is less evident compared with the variation of the pressurization level. In practice, the response of the system as function of gains sweeping (either at p_{inj}= 8 atm or p_{inj}= 3 atm) shows the same overall behavior as at 0 rpm. A typical example is presented in Figure 5.30, where an IRFs waterfall plot as function of derivative gains at a rotational speed of 3,000 rpm is presented. In Figure 5.31 the optimum values of proportional and derivative gains as function of the rotational speed is presented. Note that such optimum values are determined by analyzing the waterfall diagram as in Figure 5.30 recorded at each speed. Note that, similarly to the passive operation limitations, for the higher pressurization the experiments are possible until 6,000 rpm, due to excessive vibration levels. A more detailed clarification will follow. As for the lower pressurization, since the IRF requires manual excitation of the shaft with a impact hammer, safe (sufficiently away from whirling instability) and reliable (without "double hit" impacts) measurement are produced up to 10,000 rpm.

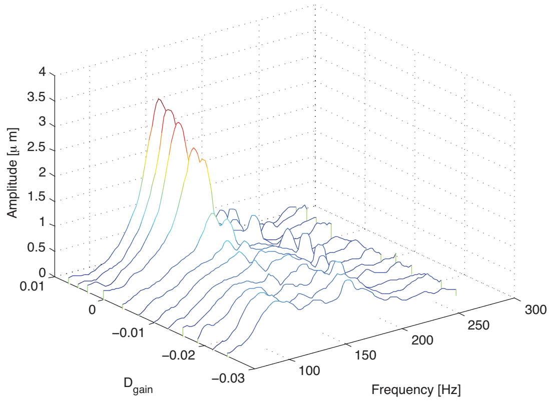

Figure 5.30: Waterfall diagrams of IRF with different control gains, p_{inj}= 8 atm, Ω= 3000 rpm..

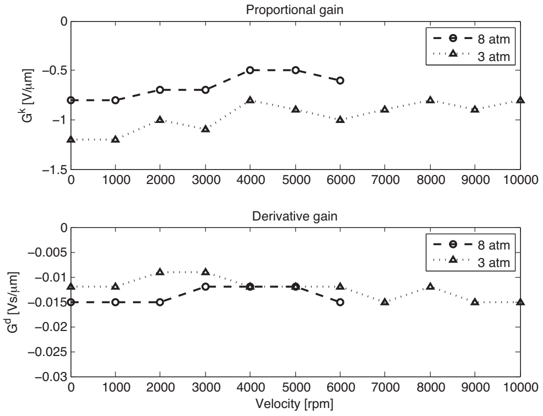

Figure 5.31: Optimum valus of proportional and derivative gains as function of rotational speed.

That the tuning of the control system does not see dramatic changes throughout the range of operation allows for a substantial simplification of the implementation of the control system, as gain scheduling is not necessary and constant gains can be used throughout the speed range. As a practical note, these gains are chosen as the average of the curves presented in 5.31. Thus, for the waterfall diagram presented in Figure 5.29, $\mathbf{G}^k$= -1 V/μm and $\mathbf{G}^d$= -0.012 V/μm.

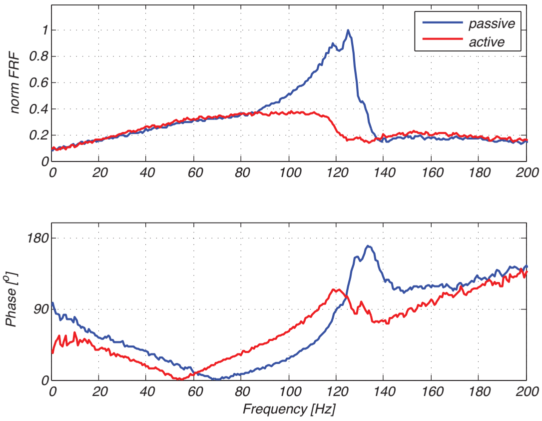

Figure 5.32: Comparison of IRFs of passive system and active with tuned gains, p_{inj}= 8 atm (Normalized to the largest amlitude).

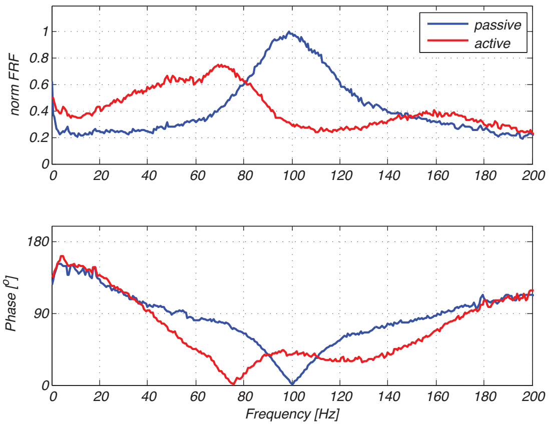

Figure 5.33: Comparison of IRFs of passive system and active with tuned gains, p_{inj}= 3 atm (Normalized to the largest amlitude).

It has been mentioned that despite the proven efficacy of the control system, when operating with high pressurization the vibration level in the proximity of the critical speeds is still too large. Looking at Figure 5.32, one expects that under active control the crossing should be smooth, with limited amplification. However, what happens reality becomes more clear looking at Figure 5.34, where the time history of the system, at p_{inj}= 8 atm, Ω= 6,300 rpm is shown. During the first 6 seconds the bearing operates in passive mode; as the control system is turned on, the vibration level is greatly reduced in the horizontal direction, whereas the response is substantially unaffected in the vertical, see Figure 5.34a. The explanation comes at no surprise; if one reminds that the two piezo actuators available are mounted in the horizontal direction, it means in the vertical direction no control action is applied. Such effect is perhaps even more dramatic seeing the orbits of the rotor, see Figure 5.34b.

The same behavior can naturally be observed at lower injection pressure; Figure 5.35 presents the waterfall diagram of coast-down test obtained in active mode for both horizontal, 5.35a and vertical 5.35b responses. Notice that the controller is effective in addressing the critical speed resonance. On the vertical direction, Figure 5.35b, control action is not applied; as a

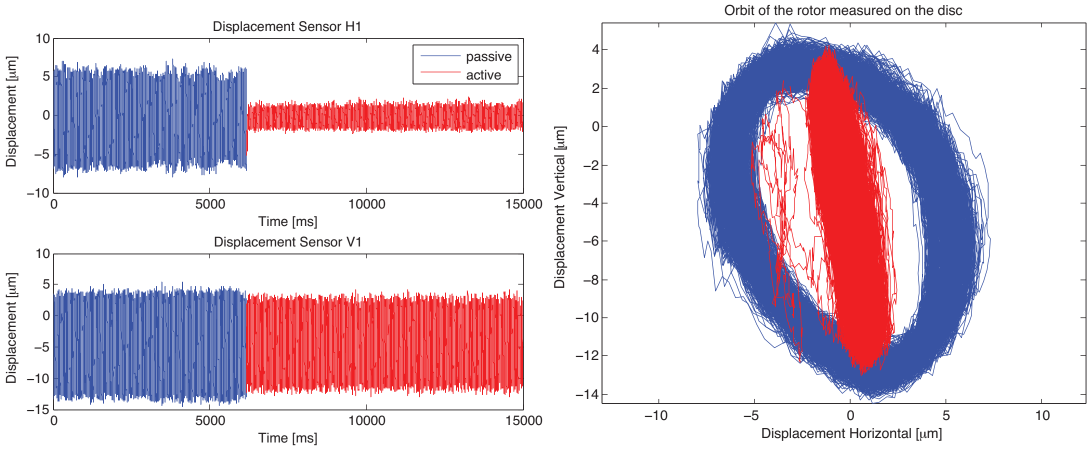

(a) Time series. **(b)** Orbits.

Figure 5.34: Time history of passive and active system, p_{inj}= 8 atm, Ω= 6300 rpm.

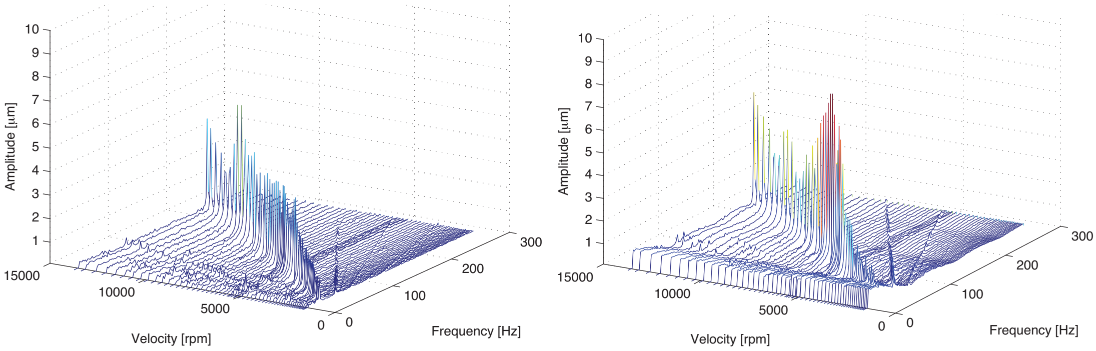

(a) Horizontal. **(b)** Vertical.

Figure 5.35: Waterfall diagram for a coast-down rotor speed test, p_{inj}= 3 bar, active operation.

consequence the critical speed amplification cannot be addressed. This explanation may then raise objection to what observed and commented regarding the ability of the active bearing to enhance the high speed capability of gas bearings by eliminating the subsynchronous whirl instability. Indeed, looking at Figure 5.36, such claims appear to be confirmed. Analogously to the previous experiment (Figure 5.34), during the first 1.7 seconds the system operates in passive mode; however the operation conditions are modified as: p_{inj}= 3 atm, Ω= 13,200 rpm. In these conditions the passive system is whirling at half the rotational frequency spanning a great part of the clearance. However, as the controller is activated, the vibration level is promptly reduced to a much lower level and, unlike for the previous case, both horizontal and

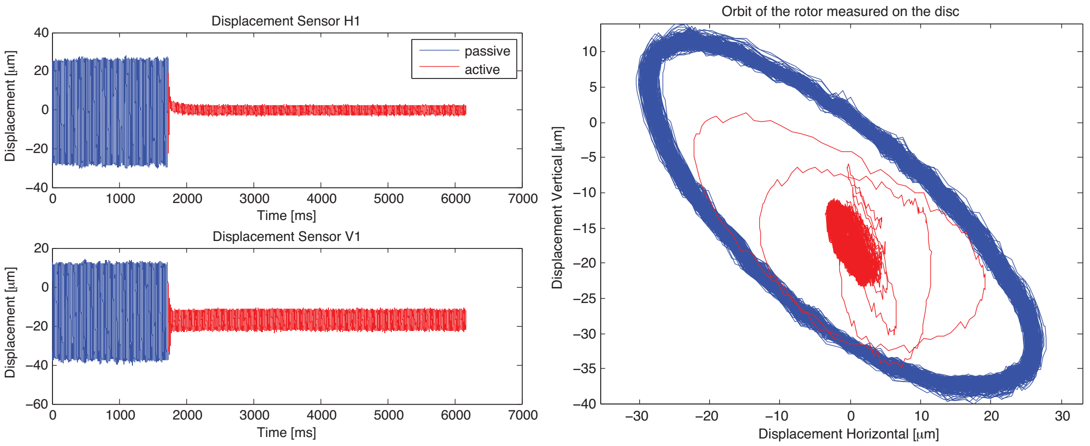

(a) Time series.

(b) Orbits.

Figure 5.36: Time history of passive and active system, p_{inj}= 3 atm, Ω= 13200 rpm.

vertical vibrations are reduced. The reason for such different behavior can be interpreted as follows: in the high pressurization previous case, high levels of amplification are due to the very low damping level when the excitation unbalance force is in proximity of the resonant frequency of the system. The action of the active bearing is then mainly of adding additional damping; it is effective, but as damping active force is only applied in the horizontal direction, the vertical remains largely unaffected (although a little effect is still observable, due to cross coupling). On the other hand, when the bearing is whirling it is not because the bearing has lost its damping, but rather because it has pasts its stability threshold; from a mathematical point of view, by turning the controller on one can increase the stability margin by making the real part of the system eigenvalues more negative. Physically, adding the active term can then be used to neutralize the destabilizing cross coupled effect of gas (and in general fluid film) bearings.

5.7 Analysis of permanent magnetic - gas bearing

The last experimental analysis concerns the feasibility of applying the hybrid configuration of permanent magnetic - gas bearing, on the basis of the numerical considerations provided in section 4.4.

The experimental setup needs to be modified for the gas bearing operating in aerodynamic mode; thus the pins that regulate the radial external injection are fixed. Note that this is a necessary step because although the left and right orifice can be open and closed via the piezo actuators, the top and bottom one can only be closed manually. Also note that closing the orifices is a better strategy than turning off the pressure supply while leaving them open. First of all, the pins are designed to occupy the whole recess (when closed), thus the pressure profile is not (in reality, far less) interrupted by abrupt changes of the bearing geometry. Moreover, when the orifices are open, pressurized air flows from the bearing through the injection system, which is at atmospheric conditions (backflow).

As for the magnetic bearings, the only necessary setup is to perform an initial calibration of the offset to define the concentric position. Practically this procedure is carried out with a laser displacement sensor mounted on a moveable support. The procedure is similar to that employed in order to define the characteristic radial force-displacement curve of the magnetic bearings, see Figures 4.16 and 4.17.

Experimental investigations are based on the results of theoretical analysis. Numerically, a great deal of informations can be inferred from the developed model. The available experimental setup on the other hand, offers more limited options. Note that the static behavior of the system is implicitly validated by the aforementioned characteristic curve analysis. The most direct way to obtain an overview of the system dynamics characteristics is through a coast-down run. Numerically, these data can be compared with unbalance response diagrams. Figure 5.37 shows theoretical unbalance responses for different magnetic loads. The physical characteristics of the rotor bearing system are analogous for each case; the only difference is the hybrid bearing dynamic coefficients; these coefficients change depending on the magnetic load as described in section 4.4, Figures 4.21 and 4.21. The goal here is to investigate whether the magnetic bearing setup can be used in order to enhance the dynamic characteristics of the aerodynamic bearing, for example if it possible to reduce the amplification while crossing the critical speeds. In order to find the optimum setup, a parametric sweep is performed (at 5 N intervals). The five presented curves (Aerodynamic, -20 N, -10 N, +20 N, +40 N) represent an overview of the evolution of the system behavior. Its interpretation can be summarized as follows. At one extreme, the -20 N curve displays an early unsteady behavior, with extreme amplifications of the backward mode. With the magnetic force providing additional lift, the equilibrium position is more centered, as in lightly loaded bearings; generally these operating conditions are not favorable from a dynamic point of view, as the magnitude of the cross coupled coefficients is comparable to that of the of the direct ones. At the other extreme, +40 N, the high response of the forward mode results in touch-down: as the magnetic load becomes substantial, the direct stiffness increases, damping is reduced and cross coupled terms are larger. Note that the natural frequencies of the system increase with increasing load, as the bearing is made stiffer.

In between these cases it can be found an optimum curve, which corresponds to the -10 N load. In this situation, a favorable combination of stiffness and damping coefficients produce the best possible response compromise. On the one hand the backward critical resonance is more amplified compared to the aerodynamic case reference, on the other the forward response is more damped, offering on overall improved performance.

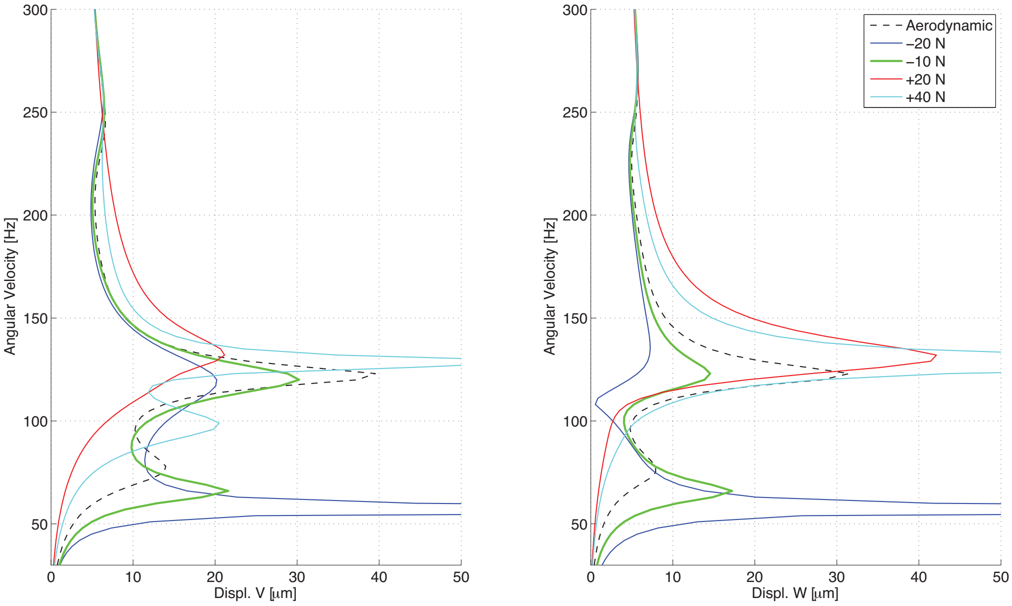

Figure 5.37: Theoretical unbalance responses for different magnetic loads.

The experimental validation proved to be particularly cumbersome. Despite numerous attempts to find optimal tuning of the parameters –mainly magnetic offset and balancing– the rotor always encountered touch-down during run-up. An example is presented in Figure 5.38; note that in this run the stator magnets are regulated so that zero (or the minimum possible) magnetic force is applied. Practically this can be checked by comparing the recorded equilibrium position time series corresponding to the system with and without magnetic bearing installed.

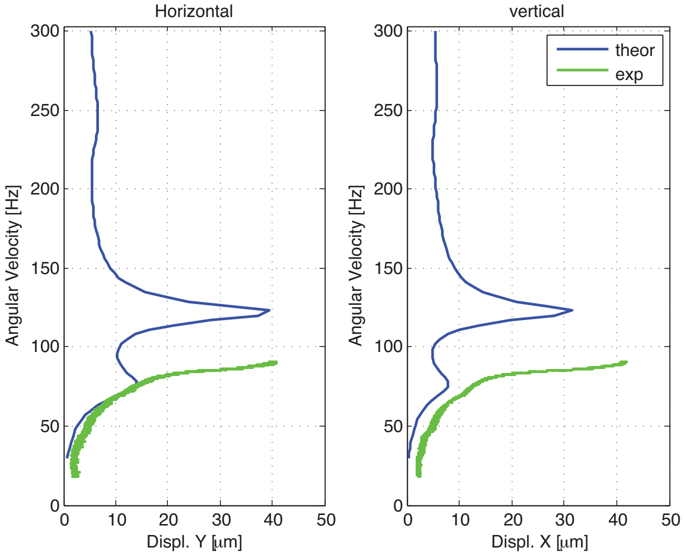

Figure 5.38: Comparison between theoretical and experimental unbalance responses for zero magnetic load.

Manufacturing related issues have been identified as prime candidates for explaining this behavior:

- The manufacturing process for the permanent magnets is beyond the controlled environment for the experimental setup, as these were purchased externally. The rings are formed by syntherization of powder material. Such process cannot guarantee stringent tolerances in circularity; this would in general affect the rotor ring, as uneven mass distribution can induce relevant level of residual unbalance.
- Also involving the manufacturing of the magnets, it should be noted that once the rings are formed these are not magnetized. In order to acquire magnetic properties, they need

> to be subjected to a strong electromagnetic field. When this field is removed, they are left with a remanent (permanent) magnetization. It is indeed possible that anomalies and unevenness in the material or the field caused a non uniform magnetization of the rings.

Significant remanent unbalance seems to be indeed present when the response is compared to the machine operating without magnetic bearings installed.

Moreover, it should be noted that the mechanism to offset the stator rings is rather crude, where adjustments can be performed simply by tightening and loosening a nut-screw mechanism. It means that a precise regulation is difficult to obtain with the present setup. Improvements of the test rigs are deemed necessary if thorough validation ought to be performed; besides the offsetting mechanism, several strategies have been considered in order to minimize the unbalance. The most promising alternative calls for a partial redesign of the rotor magnet rings and eventual substitution with ones made of machined high permeability ferromagnetic material (i.e. soft iron or alike). In order to enhance the ability to intervene on the remanent unbalance a different locking mechanism of the rotor rings would also be beneficial, eliminating the keyed joint system in favor of a tab washer[1]. These modifications would ultimately call for a redesign of the shaft; an ideal solution and a process that could benefit from the quantity of lessons and information that have been learned during the development of the project.

---

[1] A similar arrangement is used to fix the disc; its ability to successfully balance the shaft is demonstrated in Appendix C

6

Conclusions and future aspects

This thesis represents the summary of the first theoretical and experimental study on controllable gas bearing performed among the Machine Elements group at DTU. The goal of designing, prototyping and testing the concept of feasibility of applying active radial gas injection to hybrid aerostatic-aerodynamic gas journal bearing can be considered as overall met. Mathematical modeling and experimental results show reasonable agreement, however they also underline the need for refinements in several aspects of the research. The project can then be considered as a frontrunner for future development of the mathematic and numerical models and testing. From this point of view it was important to establish a solid baseline for capturing the relevant physical phenomena, both theoretically and experimentally. For this reason, an in-deep focus was devoted on some of the physical phenomena involved. Some aspects revealed more successful outcomes than others. Particularly good are the results concerning the control system; active gas journal bearing seem to give an effective answer to improving damping and extending the stability range in journal bearings. Results in this respect represent an improvement compared to the published literature. Other aspects have seen less relevant results; temperature effects within aerodynamic and hybrid gas journal bearing have been investigated, only to confirm the validity of the common assumption of isothermal conditions, at least for the considered operational range. Perhaps the most disappointing aspect of the thesis was concerning the testing of the concept of hybrid permanent magnetic-aerodynamic journal bearings. Despite promising numerical results, limitations on the available resources failed to provide experimental validation within this time frame.

The individual aspects of the thesis can be summarized as follows.

Active lubrication

In this project a method for applying active control to gas lubricated journal bearings is discussed. The principle of operation is to generate active forces by regulating radial injection of lubricant through the means of piezoelectric actuators mounted on the back of the bearing sleeves. The developed mathematical model couples the rotor-bearing system dynamics with the mechanical and fluid dynamics of the actuators through a simple proportional-derivative feedback law.

Numerical and experimental examples show how this new kind of bearing offers considerable advantages compared to conventionally lubricated bearings, not only showing a significative reduction of the synchronous vibration components, but also effectively addressing the half frequency whirling motion, thus in fact extending the range of applicability of gas lubricated bearings. Moreover, it is shown how this type of active bearing also offers improved transient response characteristics, which translated in a better ability to respond to sudden shocks and excitations the system may be subjected to.

Implementing active lubrication adds however a considerable number of parameters and variables to the system under analysis. The performance of a good control system lies most importantly on a good choice of control gains, which in general are different depending on the goal of the controller. A solution based on the developed theoretical model presents numerical challenges, as the performance can presently only be evaluated by the means of extremely time consuming transient analysis. Optimum tuning of the control loop is then addressed experimentally, showing dependency on the supply pressure and, less prominently, the rotational velocity. Experimental validation analysis is carried out with two actuators in the horizontal direction. In this configuration the controller is able to address synchronous vibrations only in the same direction as the actuators are mounted, whereas the response is unaffected in the vertical. However, the controller is able to effectively suppress the unstable motion of the system in either direction.

Thermal effects

This thesis presents an analytical model for the characterization of a compressible fluid film journal bearing under thermohydrodynamic lubrication. The solution couples the two dimensional compressible Reynolds and energy equations, taking into consideration the variations of fluid properties as well as the thermal and centrifugal growth of the shaft and bearing sleeve.

Numerical findings support the common literature assumption of the bearing being isothermal when operating in low bearing number regime. The static properties calculated with the THD and an isothermal models were compared. It was observed that larger eccentricity ratios were predicted by the isothermal model. This was expected, as the load carrying capacity dictated by the temperature changes in the lubricant viscosity. Similarly deviations between the two models were observed for the attitude angle. This behavior is of special concern for the calculation of the dynamic coefficient, which are strongly dependent on the pressure solution. On the other hand, it was observed that the difference between the dynamic coefficients calculated with isothermal- and THD model respectively were small and almost constant as a function of the rotational speed. This behavior was explained by assuming a combined effect involving the shifting of the equilibrium position and different thermal phenomena due to pressure gradients and journal velocity. It was argued that the reason why the dynamic coefficients do not show the same strong dependency upon the temperature as the static properties is related to the fact that the dynamic coefficients are coupled to the gradient of the temperature and not the temperature itself.

Due to the limited temperature variation within the operational range under consideration and the scarce influence on static and dynamic characteristics of the available test rig, experimental analysis has not been devoted on this aspect of the research.

Combining aerodynamic and magnetic effects

The concept of a novel hybrid permanent-magnetic aerodynamic journal bearing is introduced. It is an interesting solution as the two technologies combine contact free forces, suitable for high speed machinery. An analytical model for the calculations of the static and dynamic parameters of a hybrid permanent magnet - gas bearing is presented. The combination of the two technologies improves the characteristic of the single elements; the limited carrying capacity of the self-acting gas bearing at low operational velocities can be provided by the magnetic bearing by carefully offsetting the stator ring magnets; when operating at higher speed the hydrodynamic forces are strong enough to carry the load and the passive magnetic bearing can be used in order to modify its dynamic characteristics.

Despite the concept appears promising as well as the modeling delivers encouraging results, experimental validation of the theoretical results could not be carried out due to mechanical limitation of the test rig used.

6.1 Future aspects

This project is of a multidisciplinary nature; the effort has been directed at capturing the global characteristics and response of a mechatronic system. As a consequence, there of course exists wide room for improvements. Thereby future aspects are hereby summarized:

- The first priority is to improve the model for the characterization of the control system. In the present form, investigations of the active bearing are generally possible only in the time domain, and therefore long and cumbersome. Ideally, the analysis should be expanded and modified in order to allow simulations in the frequency domain.
- Also regarding the control system, different control rules and techniques should be implemented and tested. The PD scheme appeared to be effective, however the tuning was largely done via manual sweep. More sophisticated techniques can be in principle be applied. In addition, the effect of active control on the stability could be evaluated and compared.
- A second pair of piezo actuators should be acquired and tested.
- Efforts should be devoted at understanding and solving the issues regarding the experimental validation of the hybrid magnetic-aerodynamic bearing. The source of unbalance should be investigated and eliminated. Possibly, a shaft redesign could be considered.
- Concerning the fluid problem, a thorough analysis of the fluid entrance effect from the injection chamber to the bearing should be performed. Such analysis could be used firstly as an assessment of the range of validity of the simplified assumptions, and secondly in order to evaluate the feasibility of applying correction coefficients to the current model for conditions where discrepancies arise. It should be mentioned that a study with this aim is being carried out as a collaboration between the Machine Elements group at DTU and Dr. Braun's CFD-Tribology group at the University of Akron.

Appendix A

Derivation of the Reynold's equation

Fluid film lubrication problems are modeled by the means of fluid mechanics. As such, the basic assumptions of fluid mechanics theory hold. These hypothesis regard the fluid under analysis, the lubricant, which must satisfy the following:

- Conservation of mass
- Conservation of momentum
- The fluid is considered as a continuum.

Lubricants are also assumed to behave as Newtonian fluids, and laminar flow is said to exist. [3]

The Navier-Stokes Equations

The Navier-Stokes equations are used to describe the motions of viscous fluids; they can be derived considering the dynamic equilibrium of a volume of fluid.
If the mass is conserved it means that its net variation within the volume Ω is zero, that is:

$$\frac{d}{dt}\int_{\Omega}\rho d\Omega = 0 \tag{A.1}$$

The conservation of momentum basically states that the total momentum of a closed system - our volume of fluid - is constant. In other words, one can imply that the rate of change in fluid momentum is equal to the external forces applied to the fluid:

$$\frac{d}{dt}\int_{\Omega}\rho u_i d\Omega = \int_{S} T_{ij} n_j dS + \int_{\Omega} S_i d\Omega \tag{A.2}$$

where:

- $\frac{d}{dt}\int_\Omega \rho u_i d\Omega$ describes the rate of change of momentum
- $\int_S T_{ij} n_j dS$ is the term related to viscous friction
- $\int_\Omega S_i d\Omega$ are the gravity forces.

For analysis purposes, it is convenient to move the time derivatives inside the integrals of the conservation laws. This is done via the Reynolds transport theorem, an integral relation stating that the changes of an intensive property defined over a control volume Ω must be equal to the net flux through the boundaries of the volume plus what a source term inside the control volume [1]:

$$\frac{d}{dt}\int_\Omega f d\Omega = \int_\Omega \left\{ \frac{\partial f}{\partial t} + \frac{\partial}{\partial x_i}(f u_i) \right\} d\Omega \tag{A.3}$$

Applying eq. A.3 to the conservation of mass law, eq. A.1 is rewritten as:

$$\frac{d}{dt}\int_\Omega \rho d\Omega = \int_\Omega \left\{ \frac{\partial \rho}{\partial t} + \frac{\partial}{\partial x_i}(\rho u_i) \right\} d\Omega = 0 \tag{A.4}$$

which is the integral form of the conservation of mass. As the choice of the control volume is arbitrary, the relation must hold locally, yielding the differential form:

$$\frac{\partial \rho}{\partial t} + \frac{\partial}{\partial x_i}(\rho u_i) = 0 \tag{A.5}$$

Similarly, the transport theorem is applied to the conservation of momentum law, eq. A.2:

$$\int_\Omega \left\{ \frac{\partial \rho u_i}{\partial t} + \frac{\partial}{\partial x_i}(\rho u_i u_j) \right\} d\Omega = \int_S T_{ij} n_j dS + \int_\Omega S_i d\Omega \tag{A.6}$$

Applying the divergence theorem to eq. A.6, the surface stress forces can be expressed as volume integrals, leading to:

$$\int_\Omega \left\{ \frac{\partial \rho u_i}{\partial t} + \frac{\partial}{\partial x_i}(\rho u_i u_j) \right\} d\Omega = \int_\Omega \frac{\partial T_{ij}}{\partial x_j} d\Omega + \int_\Omega S_i d\Omega \tag{A.7}$$

which is the integral form of the momentum conservation law and similarly to the differential form:

$$\frac{\partial \rho u_i}{\partial t} + \frac{\partial}{\partial x_i}(\rho u_i u_j) = \frac{\partial T_{ij}}{\partial x_j} + S_i \tag{A.8}$$

The stress tensor must be expressed in terms of viscosity, density and velocity. The stresses acting on a fluid element are presented in Figure A.1. The equilibrium of moments imposes that:

$$\tau_{xy} = \tau_{yx} \quad \tau_{xz} = \tau_{zx} \quad \tau_{yz} = \tau_{zy} \tag{A.9}$$

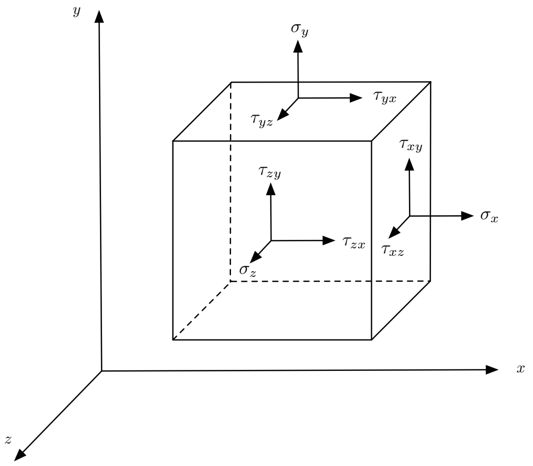

Figure A.1: Stress components acting on a fluid element

Moreover, according to Newton's definition, the shear stress is directly proportional to the velocity gradient. Stoke extended this concept for the three-dimensional case:

$$\tau_{ij} = \mu \left(\frac{\partial u_i}{\partial u_j} + \frac{\partial u_j}{\partial u_i} \right) \tag{A.10}$$

Stoke also proposed the hypothesis that the hydrostatic pressure is equal to the average of the three normal stresses components:

$$\frac{1}{3}(\sigma_x + \sigma_y + \sigma_z) = -p \tag{A.11}$$

where the minus indicates compression. [3]
The normal stress can be written as:

$$\sigma_i = -p + \lambda \left(\frac{\partial u}{\partial x} + \frac{\partial v}{\partial y} + \frac{\partial w}{\partial z} \right) + 2\mu \frac{\partial u_i}{\partial x_i} \tag{A.12}$$

The expression given in eq. A.12 is a consequence of Hooke's law. [2] The normal stress component σ_i has two contributions, the pressure $-p$ and the frictional forces τ_{ii}:

$$\sigma_i = -p + \tau_{ii} \tag{A.13}$$

Shear deformations also cause normal stress to appear:

$$E \frac{\partial u_i}{\partial x_i} = \tau_i i - \nu(\tau_{jj} + \tau_{kk}) \tag{A.14}$$

where E is the elasticity modulus and ν the Poisson's ratio.

Solving for τ_{ii} yields:

$$\tau_{ii} = \frac{E}{1+\nu}\left[\frac{\partial u_i}{\partial x_i} + \frac{\nu}{1-2\nu}\left(\frac{\partial u}{\partial x} + \frac{\partial v}{\partial y} + \frac{\partial w}{\partial z}\right)\right] \tag{A.15}$$

Comparing eq. A.15 to that for the shear stress given in eq. A.10 and neglecting the dilatation term which only contributes to the normal stress one notices that:

$$\mu = \frac{E}{2(1+\nu)} \tag{A.16}$$

since:

$$\tau_{ii} = 2\mu\frac{\partial u_i}{\partial x_i} \tag{A.17}$$

Thus, eq A.15 can be rewritten as:

$$\tau_{ii} = 2\mu\frac{\partial u_i}{\partial x_i} + \lambda\left(\frac{\partial u}{\partial x} + \frac{\partial v}{\partial y} + \frac{\partial w}{\partial z}\right) \tag{A.18}$$

where λ is the volume viscosity. In order to express λ as function of the absolute viscosity, it is simply necessary to substitute eq. A.12 into A.11:

$$\frac{1}{3}\left[-3p + 2\mu\left(\frac{\partial u}{\partial x} + \frac{\partial v}{\partial y} + \frac{\partial w}{\partial z}\right) + 3\lambda\left(\frac{\partial u}{\partial x} + \frac{\partial v}{\partial y} + \frac{\partial w}{\partial z}\right)\right] = -p \tag{A.19}$$

which gives simply:

$$\lambda = -\frac{2}{3}\mu \tag{A.20}$$

The general form of the stress tensor can therefore be written as:

$$T_{ij} = -p - \frac{2}{3}\mu\left(\frac{\partial u}{\partial x} + \frac{\partial v}{\partial y} + \frac{\partial w}{\partial z}\right) + 2\mu D_{ij} \tag{A.21}$$

where D_{ij} is the deformation tensor, defined as:

$$D_{ij} = \frac{1}{2}\left(\frac{\partial u_i}{\partial x_j} + \frac{\partial u_j}{\partial x_i}\right) \tag{A.22}$$

The conservation of momentum equation A.8 with A.21 make a system of three nonlinear differential equations with four unknowns, the fluid velocity field and pressure; they are called the Navier-Stokes equations. [3] They are valid for viscous compressible flow with generally varying viscosity. To make the system solvable another equation is supplied by the conservation of mass equation, or continuity equation A.5.

From the Navier-Stokes to the Reynold's equation

The Navier-Stokes equations in Cartesian coordinates are written as:

$$\begin{aligned}\rho\frac{Du}{Dt} &= S_x - \frac{\partial p}{\partial x} + \frac{\partial}{\partial x}\left(2\mu\frac{\partial u}{\partial x} - \frac{2}{3}\mu\left(\frac{\partial u}{\partial x} + \frac{\partial v}{\partial y} + \frac{\partial w}{\partial z}\right)\right) \\ &\quad + \frac{\partial}{\partial y}\left(\mu\left(\frac{\partial u}{\partial y} + \frac{\partial v}{\partial x}\right)\right) + \frac{\partial}{\partial z}\left(\mu\left(\frac{\partial u}{\partial z} + \frac{\partial w}{\partial x}\right)\right)\end{aligned} \tag{A.23}$$

$$\begin{aligned}\rho\frac{Dv}{Dt} &= S_y - \frac{\partial p}{\partial y} + \frac{\partial}{\partial y}\left(2\mu\frac{\partial v}{\partial y} - \frac{2}{3}\mu\left(\frac{\partial u}{\partial x} + \frac{\partial v}{\partial y} + \frac{\partial w}{\partial z}\right)\right) \\ &\quad + \frac{\partial}{\partial x}\left(\mu\left(\frac{\partial u}{\partial y} + \frac{\partial v}{\partial x}\right)\right) + \frac{\partial}{\partial z}\left(\mu\left(\frac{\partial v}{\partial z} + \frac{\partial w}{\partial y}\right)\right)\end{aligned} \tag{A.24}$$

$$\begin{aligned}\rho\frac{Dw}{Dt} &= S_z - \frac{\partial p}{\partial z} + \frac{\partial}{\partial z}\left(2\mu\frac{\partial w}{\partial z} - \frac{2}{3}\mu\left(\frac{\partial u}{\partial x} + \frac{\partial v}{\partial y} + \frac{\partial w}{\partial z}\right)\right) \\ &\quad + \frac{\partial}{\partial x}\left(\mu\left(\frac{\partial u}{\partial z} + \frac{\partial w}{\partial x}\right)\right) + \frac{\partial}{\partial y}\left(\mu\left(\frac{\partial v}{\partial z} + \frac{\partial w}{\partial y}\right)\right)\end{aligned} \tag{A.25}$$

Where the acceleration of a differential mass element is defined as:

$$\frac{Du_i}{Dt} = \frac{\partial u_i}{\partial t} + u\frac{\partial u_i}{\partial x} + v\frac{\partial u_i}{\partial y} + w\frac{\partial u_i}{\partial z} \tag{A.26}$$

Figure 3.1 depicts an idealized geometry of a fluid film bearing. The major characteristic of a lubricant film and which allows a major simplification of its analysis, is that the film thickness h is very small when compared to its length l_0 and width b_0. Thus, the pressure gradient in the radial direction is considered to be constant. The bearing comprises of an inner rotating cylinder (journal or shaft) of radius R_J and an outer cylinder (bearing) of radius $R_b(> R_j)$. The two cylinders are closely spaced and the annular gap between the two cylinders is filled with some lubricant. The radial clearance between the stationary and rotating parts is $C = (R_b - R_j)$. The cartesian reference of frame (x, y, z) for the journal bearing is also defined in Figure 3.1. The rotating shaft has an angular velocity of Ω with respect to the inertial reference of frame $(\bar{x}, \bar{y})$; the bearing center is located at $\bar{x}, \bar{y} = 0$. The widthwise coordinate is defined by z, with $y = \theta R$ being the circumferential coordinate. The velocity components are defined as $u_i = (u, v, w)$. Equations A.23 - A.25 can be expressed in non-dimensioanal form introducing the following dimensionless parameters:

$$\begin{aligned}&X = \frac{x}{h_0} \quad Y = \frac{y}{l_0} \quad Z = \frac{z}{b_0} \quad T = \frac{t}{t_0} \quad U = \frac{u}{u_0} \\ &V = \frac{v}{v_0} \quad W = \frac{w}{w_0} \quad \rho^* = \frac{\rho}{\rho_0} \quad \mu^* = \frac{\mu}{\mu_0} \quad P = \frac{h_0^2 p}{\mu_0 u_0 l}\end{aligned} \tag{A.27}$$

Additionally, the Reynolds number is introduced. It is the ratio between inertial and viscous forces. It is normally defined as:

$$Re = \frac{\rho_0 u_0 h_0^2}{\mu_0} \tag{A.28}$$

However in fluid film lubrication the viscous term dominates, thus a modified version of the Reynolds number is used:

$$Re_x = \frac{\rho_0 u_0 h_0}{\mu_0} \quad Re_y = \frac{\rho_0 v_0 h_0^2}{\mu_0 l_0} \quad Re_z = \frac{\rho_0 w_0 h_0^2}{\mu_0 b_0} \tag{A.29}$$

The squeeze number is also defined as:

$$\sigma_s = \frac{\rho_0 h_0^2}{\mu_0 t_0} \tag{A.30}$$

Substituting eq. A.27, A.29 and A.30 in the second of the Navier-Stokes equations, A.24 yields:

$$\begin{aligned}\sigma_s \frac{\partial V}{\partial T} + Re_x U \frac{\partial V}{\partial X} + Re_y V \frac{\partial V}{\partial Y} + Re_z W \frac{\partial V}{\partial Z} = g \frac{l_0}{v_0^2} Re_x - \frac{1}{\rho^*} \frac{\partial P}{\partial Y} + \frac{1}{\rho^*} \frac{\partial}{\partial X} \left(\mu^* \frac{\partial V}{\partial X} \right) \\ - \frac{2}{3} \left(\frac{h_0}{l_0} \right)^2 \frac{1}{\rho^*} \frac{\partial}{\partial Y} \left[\mu^* \left(\frac{u_0}{v_0} \frac{l_0}{h_0} \frac{\partial U}{\partial X} + \frac{\partial V}{\partial Y} + \frac{w_0}{v_0} \frac{l_0}{b_0} \frac{\partial W}{\partial Z} \right) \right] \\ + \frac{1}{\rho^*} \left(\frac{h_0}{b_0} \right)^2 \frac{\partial}{\partial Z} \left[\mu^* \left(\frac{\partial V}{\partial Z} + \frac{w_0}{v_0} \frac{b_0}{l_0} \frac{\partial W}{\partial Y} \right) \right] \\ + \frac{2}{\rho^*} \left(\frac{h_0}{l_0} \right)^2 \frac{\partial}{\partial Y} \left(\mu^* \frac{\partial V}{\partial Y} \right) + \frac{1}{\rho^*} \frac{\partial}{\partial X} \left(\mu^* \frac{u_0}{v_0} \frac{h_0}{l_0} \frac{\partial U}{\partial Y} \right)\end{aligned} \tag{A.31}$$

Neglecting the terms of order $(h_0/l_0)^2$ and $(h_0/b_0)^2$ can be further simplified. Moreover in journal bearings gravity forces are negligible compared to the viscous terms and - for non extreme conditions - the inertia forces too. Thus eq. A.24 reduces to:

$$\frac{\partial P}{\partial Y} = \frac{\partial}{\partial X} \left(\mu^* \frac{\partial V}{\partial X} \right) \tag{A.32}$$

Similarly, the third Navier-Stokes equation A.25:

$$\frac{\partial P}{\partial Z} = \frac{\partial}{\partial X} \left(\mu^* \frac{\partial W}{\partial X} \right) \tag{A.33}$$

As for the first Navier-Stokes equation A.23, since the gradient in the radial direction is assumed to be negligible, it simply reduces to:

$$\frac{\partial P}{\partial X} = 0 \tag{A.34}$$

Going back to the dimensional form, eq. A.32 and A.33 are written as:

$$\frac{\partial p}{\partial y} = \frac{\partial}{\partial x} \left(\mu \frac{\partial v}{\partial x} \right) \tag{A.35}$$

$$\frac{\partial p}{\partial z} = \frac{\partial}{\partial x}\left(\mu \frac{\partial w}{\partial x}\right) \tag{A.36}$$

The velocity field can be calculated integrating twice eq. A.35 and A.36. The first integration gives the expressions for the velocity gradients. A further assumption is introduced at this step, as the fluid viscosity across the film is considered as the average value along $x-$ coordinate:

$$\frac{\partial v}{\partial x} = \frac{x}{\mu}\frac{\partial p}{\partial y} + \frac{A_1}{\mu} \tag{A.37}$$

$$\frac{\partial w}{\partial x} = \frac{x}{\mu}\frac{\partial p}{\partial z} + \frac{B_1}{\mu} \tag{A.38}$$

The velocity components are obtained from A.37 and A.38 upon integration:

$$v = \frac{x^2}{2\mu}\frac{\partial p}{\partial y} + A_1\frac{x}{\mu} + A_2 \tag{A.39}$$

$$w = \frac{x^2}{2\mu}\frac{\partial p}{\partial z} + B_1\frac{x}{\mu} + B_2 \tag{A.40}$$

As for the integration constants A_1, A_2, B_1 and B_2, these can be resolved imposing a no-slip between fluid and interface surfaces as boundary conditions:

$$x = 0, \quad v = v_j, \quad w = w_j \tag{A.41}$$

$$x = h, \quad v = v_b, \quad w = w_b \tag{A.42}$$

where the subscript j and b refer to the journal and bearing respectively. Substituting eq. A.41 and A.42 into A.39 and A.40, one obtains:

$$v = -x\frac{h-x}{2\mu}\frac{\partial p}{\partial y} + v_j\frac{h-x}{h} + v_b\frac{x}{h} \tag{A.43}$$

$$w = -x\frac{h-x}{2\mu}\frac{\partial p}{\partial z} + w_j\frac{h-x}{h} + w_b\frac{x}{h} \tag{A.44}$$

The Reynolds equations are then obtained introducing the velocity field components into the continuity equation A.5. It is however convenient to express this equation in integral form:

$$\int_0^h \left(\frac{\partial \rho}{\partial t} + \frac{\partial}{\partial x}(\rho u) + \frac{\partial}{\partial y}(\rho v) + \frac{\partial}{\partial z}(\rho w)\right) dx = 0 \tag{A.45}$$

Assuming that the the density ρ across the film is considered as the average value along $x-$ coordinate and integrating by parts, eq. A.45 becomes:

$$h\frac{\partial h}{\partial t} - \rho v_b \frac{\partial h}{\partial y} + \frac{\partial}{\partial y}\left(\rho \int_0^h v dx\right) - \rho w_b \frac{\partial h}{\partial z} + \frac{\partial}{\partial z}\left(\rho \int_0^h w dx\right) + \rho(u_b - u_j) = 0 \tag{A.46}$$

in which expression it is possible to insert eq. A.43 and A.48, which in integral form are defined as:

$$\int_0^h v dx = \frac{1}{2}(v_b + v_j)h - \frac{h^3}{12\mu}\frac{\partial p}{\partial y} \tag{A.47}$$

$$\int_0^h w dx = \frac{1}{2}(w_b + w_j)h - \frac{h^3}{12\mu}\frac{\partial p}{\partial z} \tag{A.48}$$

Physically these integrals represent the flow rate per unit width of the bearing.

Finally the Reynolds equation is obtained from eq. A.46 as:

$$\begin{aligned} &\frac{\partial}{\partial y}\left(\rho \frac{h^3}{12\mu}\frac{\partial p}{\partial y}\right) + \frac{\partial}{\partial z}\left(\rho \frac{h^3}{12\mu}\frac{\partial p}{\partial z}\right) = \\ &\frac{1}{2}\frac{\partial}{\partial y}\left[(v_b + v_j)\rho h\right] + \frac{1}{2}\frac{\partial}{\partial z}\left[(w_b + w_j)\rho h\right] + \rho\left(u_b - u_j - v_b\frac{\partial h}{\partial y} - w_b\frac{\partial h}{\partial z}\right) + h\frac{\partial \rho}{\partial t} \end{aligned} \tag{A.49}$$

where each group of terms represents:

- $\frac{\partial}{\partial x_i}\left(\rho \frac{h^3}{12\mu}\frac{\partial p}{\partial x_i}\right)$ is the family of Poiseuille terms, which represent the net flow rate due to pressure gradients in the lubricated area
- $\frac{1}{2}\frac{\partial}{\partial x_i}(u_b + u_j)_i \rho h$ the Couette terms are the net flow rates due to the surfaces motions
- $\rho\left(u_b - u_j - v_b\frac{\partial h}{\partial y} - w_b\frac{\partial h}{\partial z}\right)$ the squeeze terms are the net flow rate due to normal $\rho(u_b - u_j)$ and transational $-(\rho u_a)_i \frac{\partial h}{\partial x_i}$ squeezing movements
- $h\frac{\partial \rho}{\partial t}$ the local expansion term, which is the net flow rate due to density change

A standard reduced form of the Reynolds equation presented in A.49 can be obtained assuming:

$$\rho\left(u_b - u_j - v_b\frac{\partial h}{\partial y} - w_b\frac{\partial h}{\partial z}\right) + h\frac{\partial \rho}{\partial t} = \frac{\partial(\rho h)}{\partial t} \tag{A.50}$$

or, upon expansion of the derivative term on the right hand side:

$$\rho\left(u_b - u_j - v_b\frac{\partial h}{\partial y} - w_b\frac{\partial h}{\partial z}\right) + h\frac{\partial \rho}{\partial t} = h\frac{\partial \rho}{\partial t} + \rho\frac{\partial h}{\partial t} \tag{A.51}$$

thus:

$$u_b - u_j - v_b\frac{\partial h}{\partial y} - w_b\frac{\partial h}{\partial z} = \frac{\partial h}{\partial t} \tag{A.52}$$

must hold. Substituting:

$$(u_b - u_j) = \frac{Dh}{Dt} \quad v_b = \frac{\partial y}{\partial t} \quad w_b = \frac{\partial z}{\partial t} \tag{A.53}$$

into A.52:

$$\frac{Dh}{Dt} = \frac{\partial y}{\partial t}\frac{\partial h}{\partial y} + \frac{\partial z}{\partial t}\frac{\partial h}{\partial z} + \frac{\partial h}{\partial t} \tag{A.54}$$

which is equivalent to:

$$Dh = \frac{\partial h}{\partial y}dy + \frac{\partial h}{\partial z}dz + \frac{\partial h}{\partial t}dt \tag{A.55}$$

which is the formal expression of the total derivative of $h = h(y, z, t)$. Therefore the assumption made in A.50 is proven to be correct, and the reduced form of the Reynolds equation can be written as:

$$\frac{\partial}{\partial y}\left(\rho \frac{h^3}{12\mu}\frac{\partial p}{\partial y}\right) + \frac{\partial}{\partial z}\left(\rho \frac{h^3}{12\mu}\frac{\partial p}{\partial z}\right) = \frac{1}{2}\frac{\partial}{\partial y}\left[(v_b + v_j)\rho h\right] + \frac{1}{2}\frac{\partial}{\partial z}\left[(w_b + w_j)\rho h\right] + \frac{\partial(\rho h)}{\partial t} \tag{A.56}$$

For a typical journal bearing it is realistic to assume that the journal does not move in the axial direction, $w_j = 0$ and that the bearing housing is still, v_b, $w_b = 0$. Equation A.56 is then rewritten as:

$$\frac{\partial}{\partial y}\left(\rho \frac{h^3}{\mu}\frac{\partial p}{\partial y}\right) + \frac{\partial}{\partial z}\left(\rho \frac{h^3}{\mu}\frac{\partial p}{\partial z}\right) = 6v_j\frac{\partial \rho h}{\partial y} + 12\frac{\partial(\rho h)}{\partial t} \tag{A.57}$$

Appendix B

Mathematical modeling of a flexible rotor-bearing system

Flexible shaft

As the shaft under analysis is slender, meaning that the longitudinal span is considerable with respect to its cross-section, it is likely to exhibit some degree of flexibility. When modeling involves a flexible shaft, a continuum, or put in mathematical terms, a field problem, it is convenient to model it by the finite element method. When using FEM one has to be aware that it is not just a simplification of the physical problem, but a two level approximation. Firstly the continuum is approximated by a set of finite elements, and secondly the choice of shape or form functions also gives rise to yet an approximation.

Beam element formulation

The structure is divided into a finite number of elements, where each element is connected to each neighbor by common nodes defined by multiple degrees of freedom. A coupled system of equations is formulated considering the translational and angular displacement of each node and their mutual interaction. The system is analyzed in a finite set of degrees of freedom, which are the rotations and translations in both the XY and ZX planes as shown in Figure B.1. This gives the 8 degrees of freedom (dof) per element as given in equation B.1.

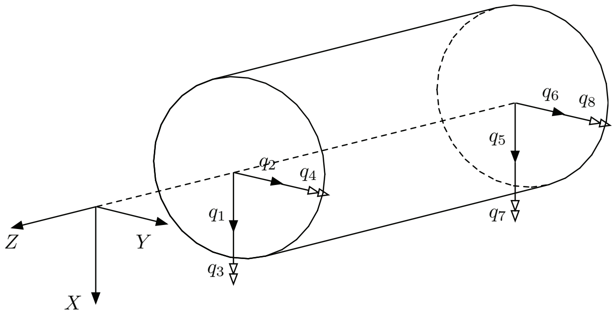

Figure B.1: A single shaft element showing the coordinate numbering.

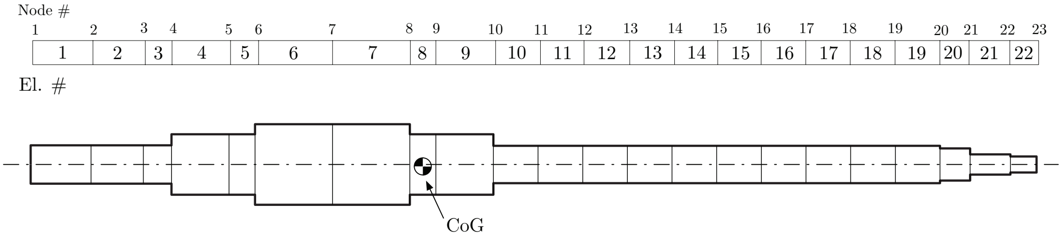

Figure B.2: Discretization of the shaft, including element and node numbering.

The axial forces along the Z axis are neglected, as the rotational speed around is set as a constant, Ω. This means, that the rotation around the Z axis only contributes as a kinematic variable, thus implying that the rotation Ω can be incorporated into the equation of motions as a parameter, therefore reducing the number of dofs by one. Moreover, axial displacements are also disregarded.

Each element has then 8 degrees of freedom, which can be arranged in vector form as $\mathbf{u} = [\ \mathbf{u}_1\ \mathbf{u}_2\ ]^T$, where $\mathbf{u}_i$ corresponds to the degrees of freedom in a particular node. This notation yields the degrees of freedom arranged as given in Figure B.1:

$$\mathbf{u} = [\ q_1\ q_2\ q_3\ q_4\ q_5\ q_6\ q_7\ q_8\ ]^T \quad = \quad [\ v_1\ w_1\ \beta_1\ \Gamma_1\ v_2\ w_2\ \beta_2\ \Gamma_2\ ]^T \tag{B.1}$$

Since the shaft and disc are rotating, it is convenient to consider the energy of the system rather than using a force-balance method. This is done by applying Lagrange's equation:

$$\frac{\partial}{\partial t}\left(\frac{\partial E_{kin}}{\partial \dot{q}_i}\right) - \left(\frac{\partial E_{kin}}{\partial q_i}\right) + \left(\frac{\partial E_{pot}}{\partial q_i}\right) = \mathcal{F}_i \qquad i = 1, 2, \cdots, n \tag{B.2}$$

where E_{kin} and E_{pot} are the kinetic and potential energy, q_i is a set of generalized coordinates, uniquely defining the state of the system at time t, F_i is the sum of generalized forces and $(\dot{})$ denotes differentiation with respect to time.

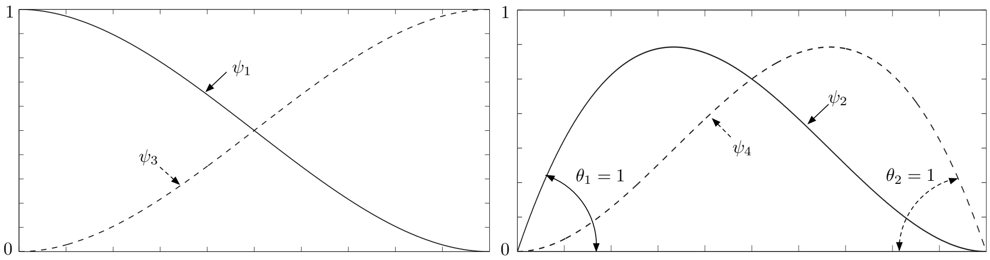

Figure B.3: Graphical visualization of the form functions.

Linear Beam Theory

Under the assumption of small translations and rotations, for each plane and for each element, one can write four form functions representing the beam deformations, see Figure B.3. These linear displacement can be described by the 3^{rd} order polynomial shape-function:

$$\begin{aligned}\psi(s) &= A + Bs + Cs^2 + Ds^3 \\ \frac{\partial \psi}{\partial s} &= \theta(s) = B + 2Cs + 3Ds^2\end{aligned} \tag{B.3}$$

where ψ is the linear displacement at a specific point s, $s \in [\ 0\ ;\ L\ ]$ and its derivative the angular displacement, θ.

The coefficients A, B, C, D can be determined by applying the appropriate boundary conditions; by applying a unit displacement for each degree of freedom at a time, while keeping the remaining fixed to zero, the corresponding shape can be found. It is worth noting that for each plane in Figure B.1 the four motions consists of one translation per node (two in total) and one rotation per node (two in total), as illustrated in Figure B.3. These element formulation can be determined individually for each plane of the system, since no direct coupling is present.

As for the derivation of the form functions, for each element one can write four displacement functions ψ_i, and four rotation functions θ_i, where $i = 1, 2, 3, 4$.

For the linear displacements in the $XY-$ plane, one obtains:

$$V(s,t) = \psi_1(s) \cdot q_1(t) + \psi_2(s) \cdot q_4(t) + \psi_3(s) \cdot q_5(t) + \psi_4(s) \cdot q_8(t) \tag{B.4}$$

where q_i is given in equation B.1. In a similar fashion, the rotations are found by taking the deriviative of $V(s,t)$.

$$\Gamma(s,t) = \frac{\partial V(s,t)}{\partial s} = \theta_1(s) \cdot q_1(t) + \theta_2(s) \cdot q_3(t) + \theta_3(s) \cdot q_5(t) + \theta_4(s) \cdot q_8(t) \tag{B.5}$$

Similarly, for the $XZ-$ plane:

$$\begin{aligned} W(s,t) &= \psi_1(s) \cdot q_2(t) - \psi_2(s) \cdot q_3(t) + \psi_3(s) \cdot q_6(t) - \psi_4(s) \cdot q_7(t) \\ \beta(s,t) &= -\frac{\partial W(s,t)}{\partial s} = -\theta_1(s) \cdot q_2(t) + \theta_2(s) \cdot q_3(t) - \theta_3(s) \cdot q_6(t) + \theta_4(s) \cdot q_7(t) \end{aligned} \tag{B.6}$$

Rewriting in matrix form the linear and angular deformations of the flexible shaft in both planes:

$$\begin{bmatrix} V(s,t) \\ W(s,t) \end{bmatrix} = \mathbf{\Psi}(s)\mathbf{q}^e(t) \tag{B.7}$$

$$\begin{bmatrix} \beta(s,t) \\ \Gamma(s,t) \end{bmatrix} = \mathbf{\Theta}(s)\mathbf{q}^e(t) \tag{B.8}$$

where:

$$\mathbf{\Psi}(s) = \begin{bmatrix} \psi_1(s) & 0 & 0 & \psi_2(s) & \psi_3(s) & 0 & 0 & \psi_4(s) \\ 0 & \psi_1(s) & -\psi_2(s) & 0 & 0 & \psi_3(s) & -\psi_4(s) & 0 \end{bmatrix} \tag{B.9}$$

$$\mathbf{\Theta}(s) = \begin{bmatrix} 0 & -\theta_1(s) & \theta_2(s) & 0 & 0 & -\theta_3(s) & \theta_4(s) & 0 \\ \theta_1(s) & 0 & 0 & \theta_2(s) & \theta_3(s) & 0 & 0 & \theta_4(s) \end{bmatrix} \tag{B.10}$$

$$\mathbf{q}^e = \begin{bmatrix} q_1(t) & q_2(t) & q_3(t) & q_4(t) & q_5(t) & q_6(t) & q_7(t) & q_8(t) \end{bmatrix}^T \tag{B.11}$$

Energy formulation

With the displacements expressions obtained in eq. (B.9) and (B.10), one can write the expressions for the energy terms in the Lagrange's equation B.2.

The potential energy related to the bending motion of an element of infinitesimal length:

$$\begin{aligned} \mathrm{d}E_{pot} &= \frac{1}{2} \begin{bmatrix} V'' \\ W'' \end{bmatrix}^T \begin{bmatrix} EI & 0 \\ 0 & EI \end{bmatrix} \begin{bmatrix} V'' \\ W'' \end{bmatrix} \\ &= \frac{1}{2} EI \cdot \mathbf{q}^{eT} \cdot \mathbf{\Psi}''^T \cdot \mathbf{\Psi}'' \cdot \mathbf{q}^e ds \end{aligned} \tag{B.12}$$

where E is the young's modulus, I is the area moment of inertia, $V'' = \frac{\partial^2}{\partial s^2} V(s,t)$ and $W'' = \frac{\partial^2}{\partial s^2} W(s,t)$.

The potential energy of one element can be then found by integrating over the shaft length l, yielding:

$$E^e_{pot} = \frac{1}{2} \mathbf{q}^{eT} \cdot \mathbf{K}^e_B \cdot \mathbf{q}^e \tag{B.13}$$

where:

$$\mathbf{K}_B^e = \int_0^l EI \cdot \mathbf{\Psi}''^T \cdot \mathbf{\Psi}'' \, ds \tag{B.14}$$

Evaluating the integral in B.14 gives:

$$\mathbf{K}_B^e = \frac{EI}{l^3} \begin{bmatrix} 12 & & & & & & & \\ 0 & 12 & & & & & & \\ 0 & -6l & 4l^2 & & & & & \\ 6l & 0 & 0 & 4l^2 & & & & \\ -12 & 0 & 0 & -6l & 12 & & & \\ 0 & -12 & 6l & 0 & 0 & 12 & & \\ 0 & -6l & 2l^2 & 0 & 0 & 6l & 4l^2 & \\ 6l & 0 & 0 & 2l^2 & -6l & 0 & 0 & 4l^2 \end{bmatrix} \qquad \mathbf{K}_B^e = (\mathbf{K}_B^e)^T \tag{B.15}$$

In a similar fashion, expressions for the kinetic energy of the system can be derived. The kinetic energy is a sum of different contributions. The first term denotes the kinetic energy from translational motion. The second term is kinetic energy from the spin of the rotor. The third term takes into consideration the energy from tilting motion of the beam section. The last term arises when applying the transformation matrices, and it describes the gyroscopic coupling due to changes in angular momentum.

$$\begin{aligned} \mathrm{d}E_{kin}^e = & \underbrace{\frac{1}{2}\begin{bmatrix} \dot{V} \\ \dot{W} \end{bmatrix}^T \begin{bmatrix} \mu & 0 \\ 0 & \mu \end{bmatrix} \begin{bmatrix} \dot{V} \\ \dot{W} \end{bmatrix}}_{linear\ displacements} + \underbrace{\frac{1}{2}\dot{\phi}^2 \cdot I_p ds}_{spin} + \\ & \underbrace{\frac{1}{2}\begin{bmatrix} \dot{\beta} \\ \dot{\Gamma} \end{bmatrix}^T \begin{bmatrix} I_d & 0 \\ 0 & I_d \end{bmatrix} \begin{bmatrix} \dot{\beta} \\ \dot{\Gamma} \end{bmatrix}}_{in-plane\ rotations} - \underbrace{\dot{\phi}\dot{\Gamma}\beta I_p ds}_{variation\ of\ angular\ momentum} \end{aligned} \tag{B.16}$$

$$\begin{aligned} &= \frac{1}{2}\mu \cdot \dot{\mathbf{q}}^{eT} \cdot \mathbf{\Phi}^T \cdot \mathbf{\Phi} \cdot \dot{\mathbf{q}}^e \, ds \; + \; \frac{1}{2}\dot{\phi}^2 \cdot I_p \, ds \; + \\ &+ \frac{1}{2} I_d \cdot \dot{\mathbf{q}}^{eT} \cdot \mathbf{\Theta}^T \cdot \mathbf{\Theta} \cdot \dot{\mathbf{q}}^e \, ds \; - \; \dot{\phi} I_p \cdot \dot{\mathbf{q}}^{eT} \cdot \mathbf{\Theta}_\Gamma^T \cdot \mathbf{\Theta}_\beta \cdot \mathbf{q}^e \, ds \end{aligned}$$

where $\mu = \rho\pi r^2$ is the distributed mass per unit length, I_p is the mass moment of inertia due to the shaft elements spinning motion around its axis, I_d is the mass moment of inertia related to tilting motion (the rotor is assumed to be axis-symmetric), $\mathbf{\Theta}_{\boldsymbol{\beta}}$ and $\mathbf{\Theta}_{\mathbf{\Gamma}}$ refers respectively to the upper and lower row of eq. B.10. Integrating over the shaft element length provides the three following integrals to be solved and evaluated

$$\begin{aligned} &\mathbf{M}_T^e = \int_0^l \mu \cdot \mathbf{\Phi}^T \cdot \mathbf{\Phi} \, ds \\ &\mathbf{M}_R^e = \int_0^l I_d \cdot \mathbf{\Theta}^T \cdot \mathbf{\Theta} \, ds \\ &\mathbf{G}^e = \mathbf{N}^e - \mathbf{N}^{eT} \; ; \quad \mathbf{N}^e = \int_0^l I_p \cdot \mathbf{\Theta}_\Gamma^T \cdot \mathbf{\Theta}_\beta \, ds \end{aligned} \tag{B.17}$$

where $\mathbf{M}_T^e$ is the mass matrix related to the linear motion, $\mathbf{M}_R^e$ is the mass matrix related to the angular motion, $\mathbf{G}^e$, the gyroscopic matrix. Evaluating these expressions over the element lengths yields the follwing three matrices:

$$\mathbf{M}_T^e = \frac{\mu l}{420}\left[\begin{array}{cccccccc} 156 & & & & & & & \\ 0 & 156 & & & & & & \\ 0 & -22l & 4l^2 & & & & & \\ 22l & 0 & 0 & 4l^2 & & & & \\ 54 & 0 & 0 & 13l & 156 & & & \\ 0 & 54 & -13l & 0 & 0 & 156 & & \\ 0 & 13l & -3l^2 & 0 & 0 & 22l & 4l^2 & \\ -13l & 0 & 0 & -3l^2 & -22l & 0 & 0 & 4l^2 \end{array}\right] \qquad \mathbf{M}_T^e = \left(\mathbf{M}_T^e\right)^T \tag{B.18}$$

$$\mathbf{M}_R^e = \frac{\mu r^2}{120l}\left[\begin{array}{cccccccc} 36 & & & & & & & \\ 0 & 36 & & & & & & \\ 0 & -3l & 4l^2 & & & & & \\ 3l & 0 & 0 & 4l^2 & & & & \\ -36 & 0 & 0 & -3l & 36 & & & \\ 0 & -36 & 3l & 0 & 0 & 36 & & \\ 0 & -3l & -l^2 & 0 & 0 & 3l & 4l^2 & \\ 3l & 0 & 0 & -l^2 & -3l & 0 & 0 & 4l^2 \end{array}\right] \qquad \mathbf{M}_R^e = \left(\mathbf{M}_R^e\right)^T \tag{B.19}$$

$$\mathbf{G}^e = \frac{2\mu r^2}{120l}\left[\begin{array}{cccccccc} 0 & & & & & & & \\ 36 & 0 & & & & & & \\ -3l & 0 & 0 & & & & & \\ 0 & -3l & 4l^2 & 0 & & & & \\ 0 & 36 & -3l & 0 & 0 & & & \\ -36 & 0 & 0 & -3l & 36 & 0 & & \\ -3l & 0 & 0 & l^2 & 3l & 0 & 0 & \\ 0 & -3l & -l^2 & 0 & 0 & 3l & 4l^2 & 0 \end{array}\right] \qquad \mathbf{G}^e = -\left(\mathbf{G}^e\right)^T \tag{B.20}$$

Note that all matrices in are symmetric, except $\mathbf{G}^e$ which is skew symmetric.

In order to assemble each element matrices into a global model for the shaft, each individual elements contribution is added to the degrees of freedom on which it influences. Graphically the local matrices can be considered 'overlapped' to formulate the global matrices, see Figure B.4.The global contribution is then:

$$\underbrace{\left(\mathbf{M}_T^S + \mathbf{M}_R^S\right)}_{\mathbf{M}^S}\ddot{\mathbf{q}} + \mathbf{D}^S\dot{\mathbf{q}} + \mathbf{K}^S\mathbf{q} = \mathbf{Q}^S \tag{B.21}$$

where $\mathbf{D}^S = -\Omega\mathbf{G}^S$ and $\mathbf{K}^S = \mathbf{K}_B^S$

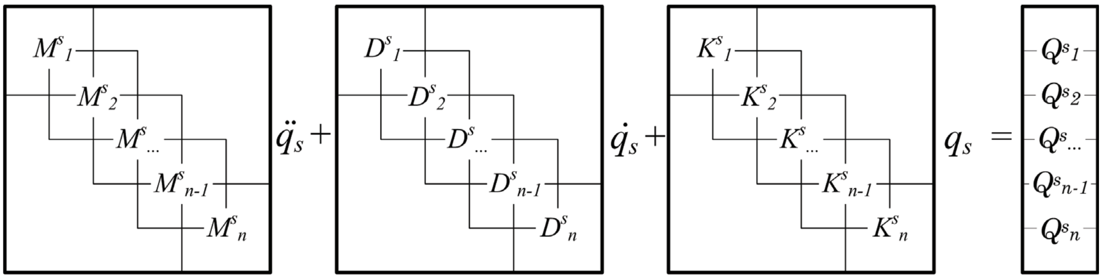

Figure B.4: Visualization of the matrices structure of the global shaft FE model.

Modelling the disc

Discs can generally be considered as rigid bodies. Similarly to the previous case, the equation of motion is obtained by solving the Lagrange's equation; to do so on has to define expressions for the potential and kinetic energy. Assuming the disc to be rigid, no potential energy due to deformation is stored, $E_{pot} = 0$. As for the kinetic energy, it will be generally dependent on both translational and angular motions. In order to define it then, displacement and velocity vectors both for translational and rotational movements need to be defined.

Concerning the translational motion one can observe how the momentum only depends on the mass, and not the mass distribution. The kinetic energy component is then written as:

$$E_{kin}^{translation} = \frac{1}{2}\dot{\mathbf{q}}^{T\,D}\mathbf{M}^{D}\dot{\mathbf{q}}^{D} \quad = \quad \frac{1}{2}\begin{bmatrix} \dot{V} \\ \dot{W} \end{bmatrix}^{T}\begin{bmatrix} m & 0 \\ 0 & m \end{bmatrix}\begin{bmatrix} \dot{V} \\ \dot{W} \end{bmatrix} \tag{B.22}$$

Where, analogously to shaft case, the axial degree of freedom is neglected.

As for the angular motion, unlike for the translatory one described above, one notices that the rotational inertia $\boldsymbol{I}$ is only constant in a reference frame where the mass distribution is constant. It is good practice to state the equation of motion in a reference of frame with constant inertia; this leads to the definition of three reference frames, $B1$, $B2$ and $B3$. They are defined as illustrated in Figure B.5.

Now the generalized variables that describe the rotational motion of the disc can be expressed as:

$$\mathbf{\Gamma}_{I} = \begin{bmatrix} 0 \\ 0 \\ \gamma \end{bmatrix}, \quad \boldsymbol{\beta}_{B1} = \begin{bmatrix} 0 \\ \beta \\ 0 \end{bmatrix}, \quad \mathbf{\Phi}_{B2} = \begin{bmatrix} \Phi \\ 0 \\ 0 \end{bmatrix} \tag{B.23}$$

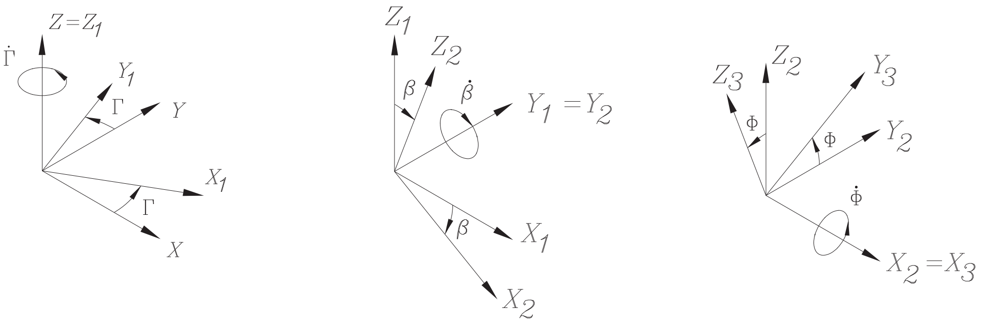

Figure B.5: Graphical illustration of rotations between reference of frames.

The expression for the angular velocity vector in the reference of frame with constant inertia B_3 is then obtained by using transformation matrices as:

$$\boldsymbol{\omega}_{B3} = \boldsymbol{T}_\Phi \boldsymbol{T}_\beta \boldsymbol{T}_\Gamma \dot{\boldsymbol{\Gamma}}_I + \boldsymbol{T}_\Phi \boldsymbol{T}_\beta \dot{\boldsymbol{\beta}}_{B1} + \boldsymbol{T}_\Phi \dot{\Phi}_{B2} \tag{B.24}$$

Where $\boldsymbol{\omega}_{B3}$ refers to the angular velocity components of $\mathbf{q}^D$, e.g. $\boldsymbol{\omega}_{B3} = \dot{\mathbf{q}}^D$. Now the rotational kinetic energy can be expressed as

$$E_c^{rotation} = \frac{1}{2}\boldsymbol{\omega}_{B3}^T \boldsymbol{I} \boldsymbol{\omega}_{B3} \quad = \quad \frac{1}{2}\begin{bmatrix} \dot{\Phi} \\ \dot{\beta} \\ \dot{\Gamma} \end{bmatrix}^T \begin{bmatrix} I_p & 0 & 0 \\ 0 & I_d & 0 \\ 0 & 0 & I_d \end{bmatrix} \begin{bmatrix} \dot{\Phi} \\ \dot{\beta} \\ \dot{\Gamma} \end{bmatrix} \tag{B.25}$$

Where I_p and I_d are the polar and transversal moment of inertia. The total potential and kinetic energy of the disc are then summarized as:

$$\begin{aligned} E_{pot} &= 0 \\ E_{kin} &= \frac{1}{2}\dot{\mathbf{q}}^{T\,D}\mathbf{M}^D\dot{\mathbf{q}}^D + \frac{1}{2}\boldsymbol{\omega}_{B3}^T \boldsymbol{I} \boldsymbol{\omega}_{B3} \end{aligned} \tag{B.26}$$

Now Lagrange's equations B.2 can be used together with the generalized coordinates $\mathbf{q}^D = [V^D, W^D, \Gamma^D, \beta^D]^T$, yielding:

$$\mathbf{M}^D \ddot{\mathbf{q}}^D - \Omega \mathbf{G}^D \dot{\mathbf{q}}^D = \mathbf{f}^D \tag{B.27}$$

Notice the absence of a stiffness component, since the disc is rigid. The mass, gyroscopic and force matrices are giving by

$$\mathbf{M}^D = \begin{bmatrix} m & 0 & 0 & 0 \\ 0 & m & 0 & 0 \\ 0 & 0 & I_d & 0 \\ 0 & 0 & 0 & I_d \end{bmatrix}, \quad \mathbf{G}^D = \begin{bmatrix} 0 & 0 & 0 & 0 \\ 0 & 0 & 0 & 0 \\ 0 & 0 & 0 & I_p \\ 0 & 0 & -I_p & 0 \end{bmatrix}, \quad \mathbf{f}^D = \begin{bmatrix} f_V \\ f_W \\ f_\Gamma \\ f_\beta \end{bmatrix}$$

One should be also aware that the external loading components f_V and f_W are forces while f_Γ and f_β represent moments. Similarly to the shaft model, the gyroscopic matrix $\mathbf{G}^D$ is skew symmetric; moreover it is noticed that only the angular coordinates are coupled.

Inserting the discs in the global model is straightforward; for any disc, its dofs coincide to the dofs of the shaft element at the given location where the bearing is placed, $\mathbf{q}_i^D = [V_i, W_i, \Gamma_i, \beta_i]^T$, where $_i$ denotes a specific node on the shaft.

Appendix C

Correcting the unbalance

Preliminary tests revealed a high level of unbalance in the system. Many causes can be listed as contributing to an unbalance condition, including material causes such as uneven density, porosity, voids. Fabrication problems may also have occurred, such as eccentric machining and poor assembly.

The mechanical system mainly comprises two bodies: flexible shaft and rigid disc. It follows then, that residual unbalance is located on either components. One of the most important design and manufacturing features of the shaft were concerning its balancing, due to the projected high rotational speed operation. Preliminary low speed measurements showed a noticeable unbalance, mainly due to imprecisions in the milling of the mounting rails for the disc and magnetic bearing rotor rings, see the visible grooves on Figure C.1. Such imprecisions proved to be difficult to address and in fact could not be suppressed completely.

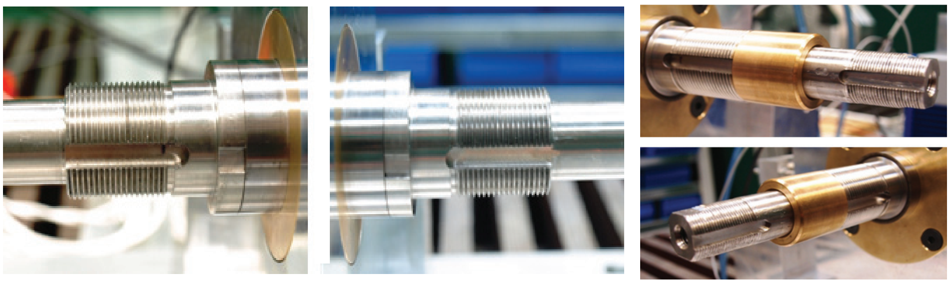

Figure C.1: Grooves locations.

For the disc on the other hand, it was possible to obtain high manufacturing precision. If the phase angle between resultant unbalance forces of shaft and disc is 0°, the response is the largest, as the unbalances are tuned and the superposition of effects applies. Ideally then, the two unbalance contributions should be completely detuned, in anti-phase (180°) with respect to each other. Practically the first balancing is then performed by turning the disc in relation to the shaft, as it is shown in Figure C.2.

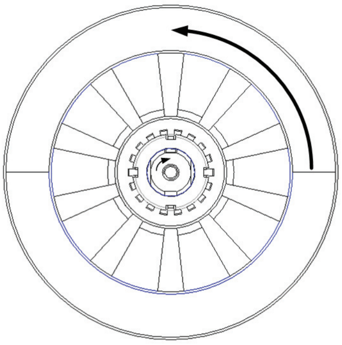

Figure C.2: Balancing the system: detuning disc and shaft unbalances.

The unbalance response (in this case evaluate as the maximum amplitude of the orbits) can be evaluated for different angular intervals along the circumference; it is then possible to identify the tuned unbalances position (0°, Figure C.3a) where the response is the largest, partially tuned (90°, Figure C.3b) and misuned (180°, Figure C.3c) where the response is the smallest. The adjusted unbalance for this case is 10e-5 kg.m.

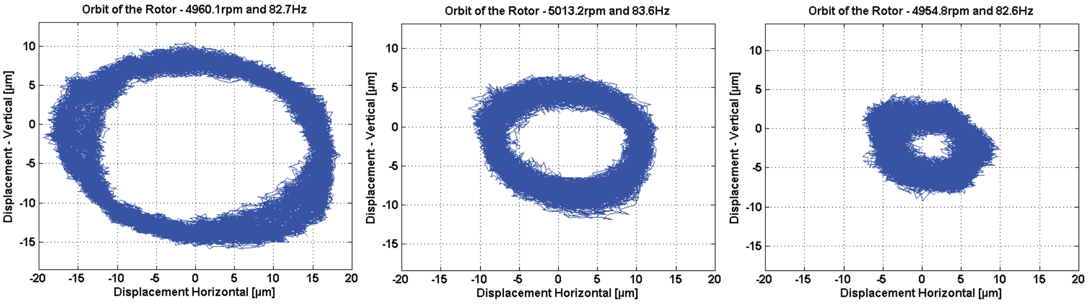

(a) 0°. **(b)** 90°. **(c)** 180°.

Figure C.3: Examples of detuning unbalance effect on orbits at $\Omega \simeq 5000$ rpm.

Appendix D

Least Squares Complex Exponential method (LSCE)

A N-DOF system transfer function from a generic i^{th} to jth node can be written as:

$$H_{ij}(s) = \sum_{r=1}^{N} \left[\frac{A_{ij}}{s - s_r} + \frac{A_{ij}^*}{s - s_r^*} \right] \tag{D.1}$$

For $A_{ij} = A_{ij}^*$ and $s_r = s_r^*$, it can be rewritten as:

$$H_{ij}(s) = \sum_{r=1}^{2N} \frac{A_{ij}}{s - s_r} \tag{D.2}$$

By applying the inverse Laplace transform to the transfer function, the IRF of the system i written as:

$$h_{ij}(t) = \sum_{r=1}^{2N} A_{ij} e^{s_r t} \tag{D.3}$$

Assuming that the IRF given in eq. (D.3) is sampled at a constant frequency ($1/k\Delta$, $k = 0, 1, ..., 2N$), one obtains a series of equally spaced sampled IRF data:

$$h(k\Delta) = \sum_{r=1}^{2N} A_{ij} z_r^k \quad ; \quad z_r^k = e^{s_r k\Delta} \tag{D.4}$$

Note that although the roots s_r and resifues A_{ij} of eq. (D.4) are complex, the imaginary parts disappear due to complex conjugates multiplication. Thus, the samples $h(k\Delta)$ are real-valued. Thus, the roots s_r and therefore z_r are solutions of a polynomial with only real coefficients (Prony's equation):

$$\beta_0 + \beta_1 z_r + \beta_2 z_r^2 + ... + \beta_{2N-1} z_r^{2N-1} + \beta 2N z_r^{2N} = 0 \tag{D.5}$$

Firstly, the coefficients β_k can be estimated by the sampled IRF data. By multiplying each equality of Eq. D.4 with the corresponding coefficient, and summing them together, one obtains:

$$\sum_{k=0}^{2N} \beta_k h_k = \sum_{k=0}^{2N} \beta_k \sum_{r=1}^{2N} A_{ij} z_r^k \tag{D.6}$$

or, equivalentlly:

$$\sum_{k=0}^{2N} \beta_k h_k = \sum_{r=1}^{2N} A_{ij} \sum_{r=1}^{2N} \beta_k z_r^k \tag{D.7}$$

For each solution of eq. (D.5), the right hand side of eq. (D.7) is zero; this yields a relationship which solution allows the determination of the polynomial coefficients:

$$\sum_{k=0}^{2N} \beta_k h_k = 0 \tag{D.8}$$

and:

$$\beta_0 h_0 + \beta_1 h_1 + \beta_2 h_2 + ... + \beta_{2N-1} h_{2N-1} = -\beta_{2N} h_{2N} \tag{D.9}$$

Letting $-\beta 2N = 1$ and taking a set of $2N$ samples of IRF, one obtains one linear equation for each β_i coefficients. Taking $2N$ sets, one obtains a linear system of $2N$ linear equations, such as:

$$\begin{bmatrix} h_0 & h_1 & h_2 & \cdots & h_{2N-1} \\ h_1 & h_2 & h_3 & \cdots & h_{2N} \\ \vdots & \vdots & \vdots & \ddots & \vdots \\ h_{2N-1} & h_{2N} & h_{2N+1} & \cdots & 0 \end{bmatrix} \begin{Bmatrix} \beta_0 \\ \beta_1 \\ \vdots \\ \beta_{2N-1} \end{Bmatrix} = \begin{bmatrix} h_{2N} \\ h_{2N+1} \\ \vdots \\ \beta_{2N-1} \end{bmatrix} \tag{D.10}$$

Note that in order to correclty setup eq. (D.10) it is required that the IRF data samples are evenly spaced and arranged sequentially. However, the number of rows can be increased for a least square solution.

Once the coefficients β are obtained by matrix inversion of eq. (D.10), they can be inserted in Prony's eq. (D.5), yielding the roots z_r. Moreover, the relation between such roots and the system eigenvalues s_r is given by Eq. D.4. Since the relation between eigenvalues, natural frequencies and damping ratio is known as:

$$s_r = -\zeta_r \omega_r \pm j\sqrt{1-\zeta^2}\omega_r \tag{D.11}$$

the expressions for the natural frequencies and damping ratios can be written as:

$$\omega_r = \frac{1}{\Delta}\sqrt{\ln z_r \ln z_r^*} \tag{D.12}$$

and:

$$\zeta_r = \frac{-\ln(z_r z_r^*)}{2\omega_r \Delta} \tag{D.13}$$

Appendix E

J1: Static, Dynamic, and Thermal Properties of Compressible Fluid Film Journal Bearings

Tribology Transactions, 54: 282-299, 2011
Copyright © Society of Tribologists and Lubrication Engineers
ISSN: 1040-2004 print / 1547-397X online
DOI: 10.1080/10402004.2010.538490

Static, Dynamic, and Thermal Properties of Compressible Fluid Film Journal Bearings

BO TERP PAULSEN, STEFANO MOROSI, and ILMAR F. SANTOS
Department of Mechanical Engineering, DTU
Technical University of Denmark
Nils Koppels Allé, 2800 Kgs.
Lyngby, Denmark

Modern turbo-machinery applications, high-speed machine tools, and laboratory equipment require ever-growing rotational speeds and high degree of precision and reliability. Gas journal bearings are often employed because they meet the demands of high-speed performance, in a clean environment, and work great efficiency. A great deal of literature has concentrated on the analysis and prediction of the static and dynamic performance of gas bearings, assuming isothermal conditions. The present contribution presents a detailed mathematical modeling for nonisothermal lubrication of a compressible fluid film journal bearing, in order to identify when this type of analysis should be of concern. Load capacity, stiffness, and damping coefficients are determined by the solution of the standard Reynolds equation coupled to the energy equation. Numerical investigations show how bearing geometry, rotational speed and load influence the bearing performance. Comparisons between isothermal and thermohydrodynamic models and discrepancies are quantified for three different types of bearing geometries.

KEY WORDS

Fluid Film Bearings; Compressible Reynolds Equation; Thermohydrodynamic Lubrication

INTRODUCTION

Compressible fluid film bearings, either in journal, thrust, aerostatic variants, or their closely related compliant foil bearings, have found their way into several industrial applications since the beginning of the 1960s. Among them, the most prominent include gyros, precision machine tools, hard disks, auxiliary power units, and more recently micro turbomachinery. It can therefore be considered a highly valued mature technology that possesses characteristics of cleanliness, high-speed operation capability, and construction and maintenance ease. Among the main advantages relative to more traditional oil lubrication is the ability of this type of bearing to operate at rotational speeds that far exceed the limits imposed by traditional lubrication. This is mainly due to the fact that the lubricant, typically air, is characterized by much lower values of viscosity; thus—for equivalent operational conditions—viscous friction forces are largely reduced. Because of such considerations, thermal effects in the gas lubrication literature have historically not been addressed. This choice has generally been justified by the fact that gas lubrication happens in near-isothermal regimes, because the viscous heat generation is small compared to the dissipation capacity of the bearing itself (Czolczynski *(1)*; Powell *(2)*). For most practical situations, the flow will be nearly isothermal because of the relatively high conductivity of the bearing material, and the assumptions are most definitely reasonable for typical operational ranges. However, the drive to meet the modern-day, ever-growing need for extremely high rotational speeds and/or heavy loading makes the inclusion of a thermohydrodynamic analysis of relevant importance.

Manuscript received July 15, 2010
Manuscript accepted November 3, 2010
Review led by Gregory Kostrzewsky

Literature Review on Gas Journal Bearings with Thermal Aspects

Studies on gas/air-lubrication saw fast development in the 1950s, when analytical approximations of the load-carrying capacity of full journals bearings were presented by Katto and Soda *(3)*. They assumed an infinitely long bearing and used the isothermal hypotheses, following earlier experimental observations and studies dating back to the beginning of the century. These results were compared with experimental findings by Ford, et al. *(4)*. The general trend of their data indicated an underestimation by the theoretical predictions. To check the validity of the isothermal assumption, they compared the variation of load-carrying capacity using gases with different specific heat ratios. They attributed the discrepancies to side leakages and not thermal effects. Ausman treated the film thickness as a small deviation from a uniform clearance and found analytical solutions of the side leakage problem of both the journal bearing Ausman *(5)* and stepped sector thrust bearings Ausman *(6)*. The potential significance of the thermal wedge effect, was first noted in the work of Hughes and Osterle *(7)*. They reasoned that the operating characteristics of gas bearings should fall somewhere between the isothermal and adiabatic limits, depending on the conductivity of the bearing

NOMENCLATURE

A = Ambient
atm = Atmospheric
b = Bearing
C = Radial bearing clearance (m)
c = Specific heat (J/kg · K)
$\mathbf{D}$ = Damping matrix (N · s/m)
D = Diameter (m)
e = Eccentricity ratio
e' = Eccentricities (m)
h = Clearance (m)
h' = Enthalpy (J)
i = Index $j \in \mathbb{R}$
j = Index $j \in \mathbb{R}$
$\mathbf{K}$ = Stiffness matrix (N/m)
k = Thermal conductivity (W/m · K)
L = Width of bearing (m)
N = Number of grid points
p = Pressure (Pa)
Pe = Peclet number ($Pe = \frac{vB}{k/(\rho c)}$)
q = Heat transfer through bearing housing in the z direction (W/m^2)
$\tilde{R}$ = Universal gas constant (J/K · mol)
R = Radius (m)
s = Shaft
iso = Isothermal
T = Temperature 1°
t = Time (s)
THD = Thermohydrodynamic
U = Surface velocity of shaft (m/s)
u = Fluid velocity in x direction (m/s)
v = Fluid velocity in y direction (m/s)
W = Weight of shaft (N)
w = Fluid velocity in z direction (m/s)
x = Circumferential coordinate (m)
y = Axial coordinate (m)
z = Radial coordinate (m)
Λ = Bearing number $\Lambda = \frac{6\mu U R_b}{p_A h_0^2}$
μ = Viscosity (N · s/m^2)
ρ = Density (kg/m^3)
Φ = Viscous dissipation (W/m^2)
ϕ = Attitude angle (°)
Ω = Rotational speed (rad/s or rpm)

material and degree of thermal insulation. They suggested that at very high-speed operation the thermal wedge effect may augment the load-supporting pressure in addition to geometrical wedge effects. Whitley and Betts *(8)* conducted experiments on a long bearing and yielded results deviating up to 24% from the Katto-Soda theory. While keeping faith with the isothermal conditions of the film, they found that side leakage losses only accounted for up to half of the discrepancies, leaving the remainder unexplained. While refining the infinitely long bearing theory, Elrod and Burgdorfer *(9)* showed analytically that in nonextreme conditions the internal temperature rise of the film can be neglected. Thus, as numerical studies of gas bearings became popular (e.g., Castelli and Pirvics *(10)*), the isothermal hypothesis has been largely accepted.

In incompressible lubrication the thermal issue acquired an ever-growing prominence, yielding the thermohydrodynamic (THD) branch of fluid film lubrication theory. With THD analysis one formally refers to the solution of the Reynolds equation in which the viscosity field is updated by coupling the solution of the energy conservation equation and the use of a suitable formula for temperature-dependence of viscosity. In 1966, Dowson and March *(11)* presented the first comprehensive paper considering compatible solutions of the Reynolds, energy, and heat conduction equations for two-dimensional conditions, as well as taking into account experimental observations presented earlier (Dowson, et al. *(12)*). This milestone work opened the field to a prolific literature, with the most significant contributions being included in the work of Pinkus *(13)*.

The subject of thermal aspects in gas lubrication remained rather unexplored until recently, in the context of research on compliant foil bearings; Salehi and Heshmat *(14)* were the first to include an analytical thermal analysis of foil bearings. Their model was based on the Couette approximation, as proposed by Pinkus *(13)*, in which heat dissipation is calculated without allowance for pressure gradients. This method substantially simplifies the numerics as it uncouples the energy and Reynolds equations. Good agreement with experimental data was found. The same model was utilized a year later by Salehi, et al. *(15)*, who published a more comprehensive study for steady-state operation as well as start up and coast-down regimes. They concluded that for speeds up to 30,000 rpm and 1.5 kN, the Couette approximation provided a reasonable tool for predicting temperatures, with overprediction estimated at 8–19% compared to the experimental values. Radil and Zeszotek *(16)* published an experimental study showing both load and rotational speed to cause heat generation in foil bearings, the latter being responsible for a more significant role. A comprehensive THD analysis of applied foil bearings was presented by Peng and Khonsari *(17)* that treats a simplified 3D energy equation. Sim and Kim *(18)* studied compliant flexure pivot tilting pad bearings, treating the Reynolds and 3D energy equations simultaneously with boundary conditions found internally through global energy balance. The work also shows the effect of thermal and centrifugal expansions on the hollow rotor and the influence of heating on the linear dynamic coefficients of the tilting pad bearing. They concluded that the dynamic performance of the bearing improves at high temperature, due to reduced clearance and increased viscosity. Lee and Kim *(19)* further developed the model for foil gas bearings analysis; the heat balance involves top foils, bump foils, cooling air channels, and bearing sleeves, allowing for thermal expansion of top/bump foils and bearing sleeves. They observed that the maximum growth of the rotor was about 20 times that of the foil structure. Their analysis also examined the influence of cooling flow rates on the temperatures of the system, identifying the influential parameters. San Andrés and Kim *(20)* and Kim and San Andrés *(21)* presented a comprehensive thermal energy transport model, that included convection and conduction through the bearing surfaces. They quantified the effectiveness of foil cooling flows on the bearing temperatures, showing that experimental data were in remarkable agreement with theoretical predictions.

Scope of the Present Work

The purpose of this work is to scrutinize the theoretical foundation of gas lubrication regarding when the isothermal hypothesis may not be valid and what parameters may call for attention under these circumstances. The full energy equation will be used to formulate a modeling approach of compressible fluid film lubrication. The heat balance will include an allowance of net heat conduction across the bearing walls. Performance parameters—eccentricity and attitude angle for given steady-state load and dynamic perturbation coefficients—will be examined for significant departure from isothermal predictions. The method of finite difference will be employed for a grid-based numerical simulation of the governing equations.

This article presents a detailed analytical modeling of compressible fluid film journal bearings considering nonisothermal conditions, followed by numerical evaluation of three different bearing sleeve geometries. The static (steady-state) and dynamic performance parameters are found from a linear perturbation analysis (Lund *(22)*, *(23)*; Faria and San Andres *(24)*; Kim and San Andres *(25)*), where numerical results for the zeroth- and first-order fields are computed by a finite difference method. The thermodynamic analysis is based on the solution of the energy equation coupled to the Reynolds equation (Dowson and March *(11)*), upon the introduction of certain simplifications that are compatible with the condition of nearly parallel flows and with due consideration of the thermal transport properties of gases. The influence of the three different bearing geometries on the static and dynamic properties is qualitatively and quantitatively presented and discussed.

Because the isothermal hypothesis has been established to be valid for common application environments, computation of the incipience of nonisothermal effects necessarily calls for an extraordinary demand for high numerical precision, including the baseline case of the isothermal solution; grid-convergence will be carefully examined in both pressure and temperature computations.

MATHEMATICAL MODEL

Film Thickness

The general geometry and coordinate systems of the bearings under analysis are presented in Figs. 1a and 1b. Centrifugal and thermal expansion of the shaft and bearing sleeve, have been taken into consideration when calculating the fluid film thickness. The centrifugal growth of the solid shaft is obtained by assuming a cylindrical plane stress model and is given by:

$$s_{cg} = \frac{\rho_s R^3 \omega^2}{4E}(1-\nu) \qquad [1]$$

where ρ_s is the shaft density, E is Young's modulus, and ν is Poisson's ratio of the shaft. The thermal growth of the shaft and bearing sleeve is assumed linear and is given by:

$$s_{tg} = \alpha_s R (T_s - T_A) \qquad [2]$$

$$BS_{tg} = \alpha_{Bs} R (T_{Bs} - T_A) \qquad [3]$$

where α is the material linear coefficient of thermal expansion and the subscripts s and Bs refer to the shaft and bearing sleeve respectively. Note that, similar to the work of Lee and Kim *(19)*, this model assumes that both shaft and bearing sleeve are free to expand in the radial direction.

By introducing a standard formulation for the fluid film thickness where axial misalignments between shaft and bearing housing are neglected, the fluid film thickness can be expressed as

$$h = C - (s_{cg} + s_{tg} - Bs_{tg}) + e_Z \cos(\Theta) + e_X \sin(\Theta) \qquad [4]$$

where Θ is the circumferential coordinate, redefined taking into account the attitude angle as:

$$x = \Theta R, \quad \Theta = \theta + \psi \qquad [5]$$

and C is a function that describes the nominal radial clearance of the bearing. In the present work three different bearing geometries will be considered. Sketches of the different configurations and corresponding expressions for the clearance are presented in Fig. 2 and Table 1, respectively.

Pressure Distribution

The pressure distribution $p(x, y)$ in a gas-lubricated journal bearing is governed by the general form of the Reynolds

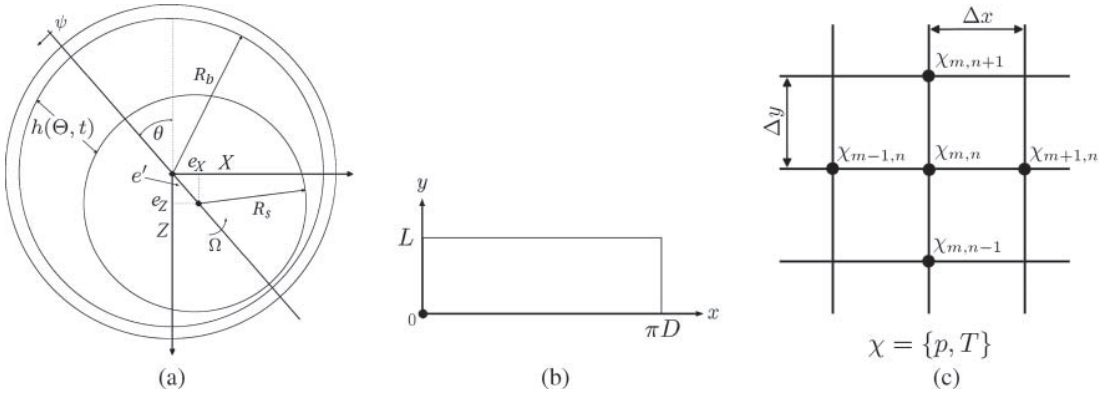

Fig. 1—Coordinate system and finite difference grid. (a) Bearing geometry and coordinate systems. (b) Bearing geometry and coordinate systems. (c) Finite difference grid.

TABLE 1—EXPRESSIONS FOR THE RADIAL CLEARANCE h_0 FOR DIFFERENT BEARING GEOMETRIES.

Geometry	C	Note
Cylindrical	$R_b - R_s$	
Ellipse	$\frac{ba}{\sqrt{a^2\sin^2(\phi)-b^2\sin^2(\phi)+b^2}} - R_s$	$\phi \in [0, 2\pi]$, $\{a, b\} :=$ major and minor axes respectively
Polygon	$R_p - R_s + cos(\phi)(R_s - R_p) + c$	$R_p :=$ Radius of one side, $\phi :=$ Angle covering one side, $c :=$ Clearance at center of side

equation:

$$\frac{\partial}{\partial x}\left(\frac{\rho h^3}{\mu}\frac{\partial p}{\partial x}\right) + \frac{\partial}{\partial y}\left(\frac{\rho h^3}{\mu}\frac{\partial p}{\partial y}\right) = 6U\frac{\partial}{\partial x}(\rho h) + 12\frac{\partial \rho h}{\partial t} \qquad [6]$$

where $(x, y) \in \{[0; 2\pi R], [0; L]\}$ are the circumferential and axial coordinates in the plane of the bearing. The ideal gas law establishes a relation between density and the other state variables as:

$$\rho = \frac{p\tilde{M}}{\tilde{R}T} \qquad [7]$$

where $\tilde{M}$ is the molar mass of the gas, $\tilde{R}$ is the universal gas constant and T is temperature. Implicit in the above statement is an assumption of the temperature, and hence the viscosity, being independent of z. Substituting Eq. [7] into [6] and simplifying the constant terms yields:

$$\frac{\partial}{\partial x}\left(\frac{p}{\mu T}h^3\frac{\partial p}{\partial x}\right) + \frac{\partial}{\partial y}\left(\frac{p}{\mu T}h^3\frac{\partial p}{\partial y}\right) = 6U\frac{\partial}{\partial x}\left(\frac{p}{T}h\right) + 12\frac{\partial}{\partial t}\left(\frac{p}{T}h\right) \qquad [8]$$

which is a non linear parabolic equation in p for a compressible, nonisothermal lubrication regime.

Perturbation Equations

Standard linear perturbation theory, where the perturbation is assumed small and harmonic, implies that higher order terms should be neglected; then the zeroth- and first-order lubrication equations are given by:

- Zeroth-order

$$\frac{\partial}{\partial x}\left(\frac{p_0}{\mu T}h_0^3\frac{\partial p_0}{\partial x}\right) + \frac{\partial}{\partial y}\left(\frac{p_0}{\mu T}h_0^3\frac{\partial p_0}{\partial y}\right) = 6U\frac{\partial}{\partial x}\left(\frac{p_0}{T}h_0\right) \qquad [9]$$

- First-order

$$\begin{aligned} X:\ & \frac{\partial}{\partial x}\left(\frac{p_0}{\mu T}h_0^3\frac{\partial p_X}{\partial x} + \frac{p_X}{\mu T}h_0^3\frac{\partial p_0}{\partial x}\right) \\ & + \frac{\partial}{\partial y}\left(\frac{p_0}{\mu T}h_0^3\frac{\partial p_X}{\partial y} + \frac{p_X}{\mu T}h_0^3\frac{\partial p_0}{\partial y}\right) - 6U\frac{\partial}{\partial x}\left(\frac{p_X}{T}h_0\right) \\ & - 12i\omega\left(h_0\frac{p_X}{T}\right) \\ = & -\frac{\partial}{\partial x}\left(3\frac{p_0}{\mu T}h_0^2\frac{\partial p_0}{\partial x}\cos\Theta\right) - \frac{\partial}{\partial y}\left(3\frac{p_0}{\mu T}h_0^2\frac{\partial p_0}{\partial y}\cos\Theta\right) \\ & + 6U\frac{\partial}{\partial x}\left(\frac{p_0}{T}\cos\Theta\right) + 12i\omega\left(\frac{p_0}{T}\cos\Theta\right) \qquad [10] \end{aligned}$$

$$\begin{aligned} Z:\ & \frac{\partial}{\partial x}\left(\frac{p_0}{\mu T}h_0^3\frac{\partial p_Z}{\partial x} + \frac{p_Z}{\mu T}h_0^3\frac{\partial p_0}{\partial x}\right) \\ & + \frac{\partial}{\partial y}\left(\frac{p_0}{\mu T}h_0^3\frac{\partial p_Z}{\partial y} + \frac{p_Z}{\mu T}h_0^3\frac{\partial p_0}{\partial y}\right) - 6U\frac{\partial}{\partial x}\left(\frac{p_Z}{T}h_0\right) \\ & - 12i\omega\left(h_0\frac{p_Z}{T}\right) \\ = & -\frac{\partial}{\partial x}\left(3\frac{p_0}{\mu T}h_0^2\frac{\partial p_0}{\partial x}\sin\Theta\right) - \frac{\partial}{\partial y}\left(3\frac{p_0}{\mu T}h_0^2\frac{\partial p_0}{\partial y}\sin\Theta\right) \\ & + 6U\frac{\partial}{\partial x}\left(\frac{p_0}{T}\sin\Theta\right) + 12i\omega\left(\frac{p_0}{T}\sin\Theta\right) \qquad [11] \end{aligned}$$

Notice that there is no allowance for perturbation dependency of μ and T in the first-order equations.

The pressure distribution in the bearing is continuous in the circumferential coordinate and equal to the atmospheric value at the bearing sides. The boundary conditions for the steady-state,

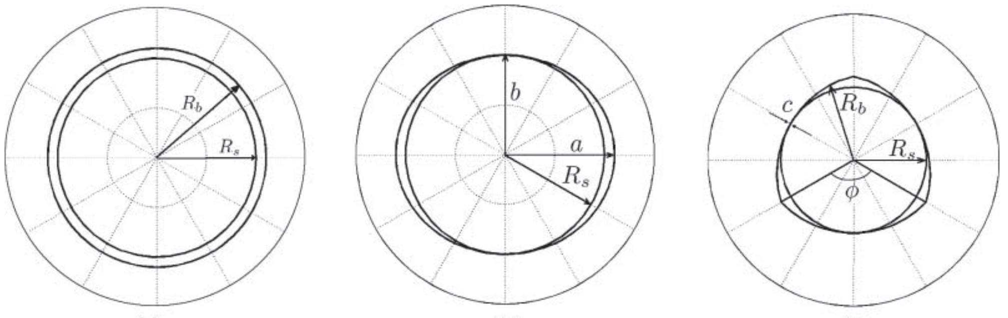

(a) (b) (c)

Fig. 2—Sketches of the different bearing geometries. (a) Sketch of a cylindrical bearing. (b) Sketch of elliptical bearing. (c) Sketch of polygonal bearing.

Eq. [9], and perturbation equations [10] and [11] are defined by:

$$p_0 : \begin{cases} p_0(x,0) = p_0(x,L) = p_{atm} \\ p_0(0,y) = p_0(2\pi R, y) \\ \dfrac{\partial p_0(0,y)}{\partial x} = \dfrac{\partial p_0(2\pi R, y)}{\partial x} \end{cases}$$
$$p_{X,Z} : \begin{cases} p_{X,Z}(x,0) = p_{X,Z}(x,L) = 0 \\ p_{X,Z}(0,y) = p_{X,Z}(2\pi R, y) \\ \dfrac{\partial p_{X,Z}(0,y)}{\partial x} = \dfrac{\partial p_{X,Z}(2\pi R, y)}{\partial x} \end{cases} \quad [12]$$

The Energy Equation

The temperature distribution of the gas film is determined by the solution of the energy equation. By combining the first law of thermodynamics and the continuity equation, the following expression appears:

$$\rho \frac{Dh'}{Dt} = \frac{Dp}{Dt} + div\,(k\nabla T) + \Phi \quad [13]$$

where h', ρ, and k are the enthalpy, density, and thermal conductivity of the fluid, respectively, and Φ is viscous dissipation. By the thermodynamic identity

$$\mathrm{d}h' = c\,\mathrm{d}T + (1 - \beta T)\frac{dp}{\rho} \quad [14]$$

Eq. [13] can be rewritten as:

$$\rho c \frac{DT}{Dt} = \beta T \frac{Dp}{Dt} + div\,(k\nabla T) + \Phi \quad [15]$$

where β and c are the coefficient of thermal expansion and the heat capacity, respectively. For an ideal gas, β is exactly equal to $\frac{1}{T}$. If only steady-state problems are considered and the fluid is assumed to obey the ideal gas law, the energy equation can then be reduced to:

$$\rho c\,(u \cdot \nabla T) - u \cdot \nabla p - div(k\nabla T) = \Phi \quad [16]$$

Upon imposing the approximation of $\frac{\partial T}{\partial z} = 0$, the energy equation should be replaced by the film-integral of Eq. [16], which governs the temperature in the fluid film.

$$\rho c \left(\Psi_x \frac{\partial T}{\partial x} + \Psi_y \frac{\partial T}{\partial y} \right) - \left[\frac{\partial}{\partial x}\left(k \frac{\partial T}{\partial x}\right) + \frac{\partial}{\partial y}\left(k\frac{\partial T}{\partial y}\right)\right] h$$
$$- \left(\Psi_x \frac{\partial p}{\partial x} + \Psi_y \frac{\partial p}{\partial y} \right) = S \quad [17]$$

where (Ψ_x, Ψ_y) are the convective fluxes, S is the heat source comprising the film-integrated viscous dissipation (Φ_{com}) and the net heat conduction through the wall–fluid interface (q).

$$S = \Phi_{com} + q \quad [18]$$

For near-parallel flow the viscous dissipation is given by

$$\Phi_{com} \equiv \int_h \Phi dz = \int_h \left(\tau_{ij} \frac{\partial u_i}{\partial x_j} \right) dz$$
$$\approx \frac{h^3}{12\mu} \left[\left(\frac{\partial p}{\partial x} \right)^2 + \left(\frac{\partial p}{\partial y} \right)^2 \right] + \frac{\mu U^2}{h} \quad [19]$$

This is an improvement over the formulation by Pinkus *(13)*, adding the contribution of the Poiseuille flow component to viscous heating.

In order to establish a mathematical expression of the net heat conduction through the fluid–wall interface, the following assumptions are made:

- It is assumed that the conduction through the bearing walls is dominant; therefore, heat conduction through the shaft, radiation, etc., are neglected. Regarding the adiabatic condition imposed on the shaft boundary, one should notice that in thermal steady-state conditions the net radial thermal conduction is zero; in practice, in the pressure convergent region temperature builds up and heat flows into the shaft, whereas the opposite takes place in the divergent part. Nevertheless, this assumption leads to an overestimation of the fluid temperatures, because axial thermal flows are neglected.
- Heat conduction in the bearing sleeve is assumed to obey the one-dimensional Fourier's law.

The heat transfer from the fluid film to the environment is assumed to occur by natural convection and conduction into the bearing through its layers. The one-dimensional energy flux through the bearing radial direction per unit area per unit time is

$$q = -k_{eq} \frac{\mathrm{d}T}{\mathrm{d}z} \quad [20]$$

where k_{eq} is an equivalent convection/conduction coefficient. In the present case the bearing inner sleeve and the outer case are modeled as bronze and aluminum rings with thicknesses of 30 and 50 mm, respectively. It can be calculated as:

$$\frac{1}{k_{eq}} = \frac{1}{h_{f-Br}} + \frac{R_{Br}^{in} \ln\left(\dfrac{R_{Br}^{out}}{R_{Br}^{in}}\right)}{k_{Br}} + \frac{R_{Br}^{in} \ln\left(\dfrac{R_{Al}^{out}}{R_{Al}^{in}}\right)}{k_{Al}} + \frac{R_{Br}^{in}}{R_{Al}^{out}} \frac{1}{h_{Al-\mathrm{inf}}} \quad [21]$$

where $k_{Br,Al}$ are the thermal conduction coefficients of bronze (60 W/m K) and aluminum (200 W/m K), and $h_{Al-\mathrm{inf}}$ is the natural heat convection coefficient from flat surfaces to a stagnant fluid (which for the temperature range under investigation can be assumed to be constant, at 8 W/m^2 K). The convection coefficient from the fluid film to the bearing sleeve, h_{f-Br}, is derived from the Nusselt number as in San Andrés and Kim *(20)*. The radii at the various locations are indicated by R_i^j, where the subscript $i = Br$, *Al* indicates either the bronze or aluminum layer and the superscript $j =$ in, out indicates either the inner or outer radius. Note that $R_{Al}^{in} = R_{Br}^{out}$.

As boundary condition for Eq. [20], it has been assumed that the temperature at the inner borders of the bearing is equal to the fluid temperature T, and the temperature outside the bearing is constant and equal to the ambient temperature T_A.

As boundary conditions for the fluid film, governed by Eq. [16], it has been assumed that the temperature in areas where the pressure is lower than ambient pressure is a mixing

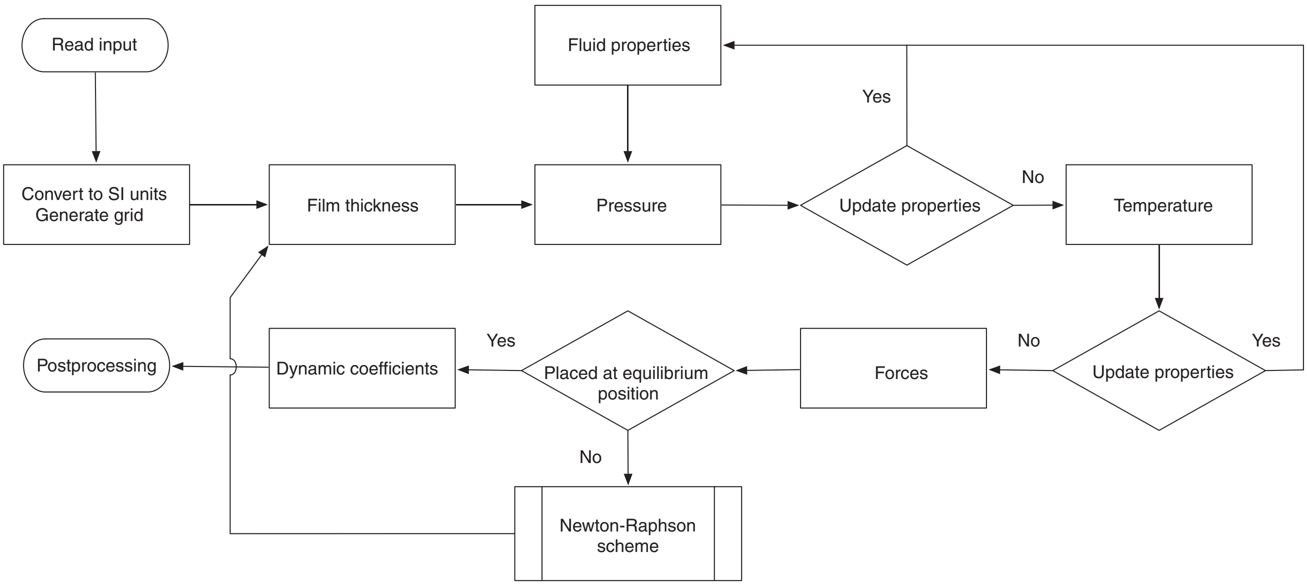

Fig. 3—General sketch of the solution procedure.

temperature T_{mix} between the fluid at ambient temperature entering from the bearing sides and the warmer recirculating air. According to the formulation presented in Peng and Khonsari *(17)* it can be approximated as:

$$T_{mix} = \frac{\dot{M}'T' + \dot{M}_A T_A}{\dot{M}' + \dot{M}_A} \qquad [22]$$

where $\dot{M}'$ and T' indicate the mass flux and temperature of the recirculating fluid and $\dot{M}_A$ is the mass flux of ambient fluid entering a control volume at the border of concern.

In areas where the pressure is higher than the ambient pressure, the temperature at the border is a fraction c between the temperature just inside the bearing sides and the ambient

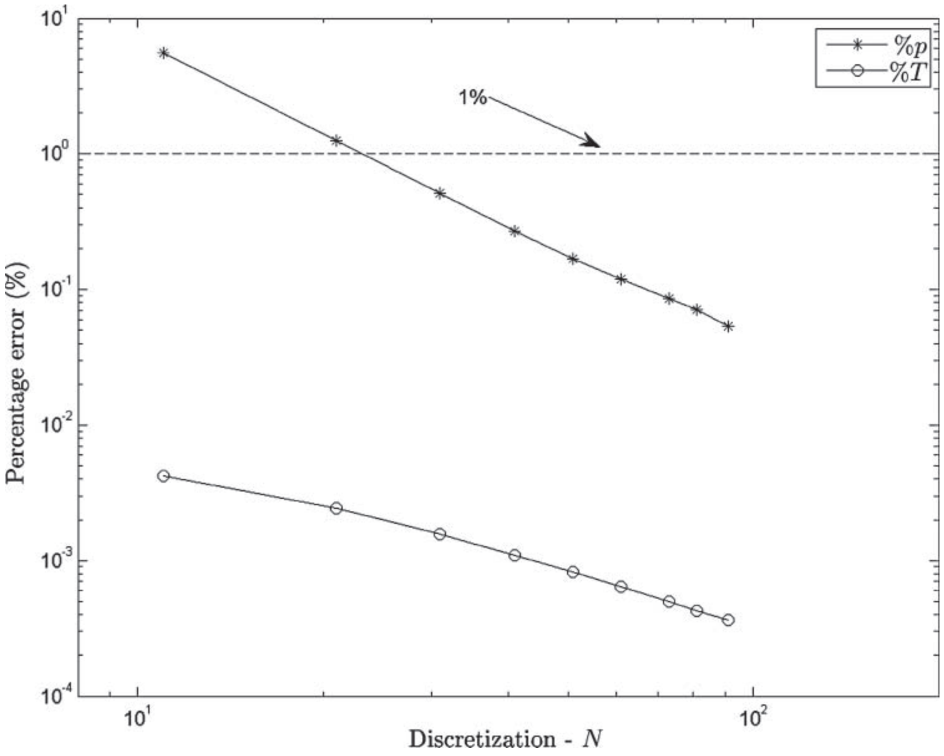

Fig. 4—Analysis of grid dependency on the compressible Reynolds and energy equations, respectively. The fine grid solution was obtained with *N* = 501.

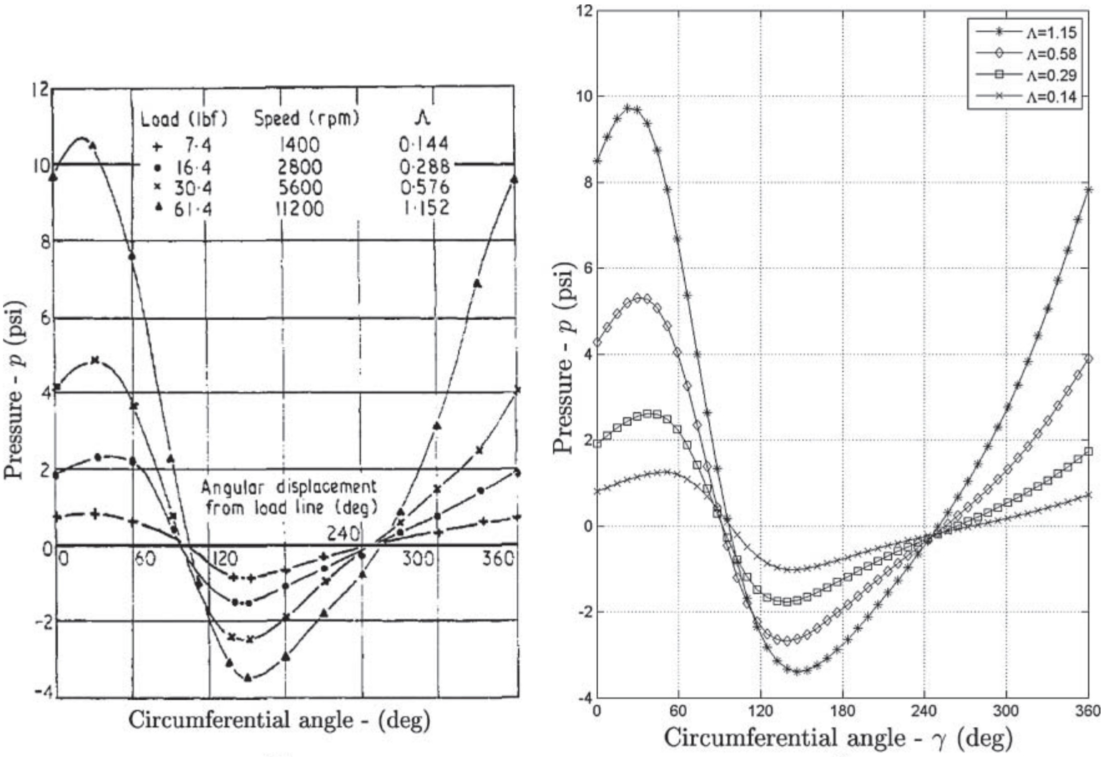

(a) (b)

Fig. 5—Comparison between experimental results from Powell *(2)* and numerical calculations. $L = 101.6$ mm, $D = 50.8$ mm, $C = 26.54$ μm. The numeric solution is obtained with $N = 40$ grid points. (a) Results from Powell *(2)*. (b) Numerical calculated pressure profiles.

temperature. This fraction is dependent on the Péclet number and $c = Pe/100$ if $Pe \le 100$; otherwise, $c = 1$. The boundary conditions for the compressible energy equation [16] can be then summarized as:

$$T : \begin{cases} T_{mix} \text{ for } (x, y) = \left(x\big|_{p \le p_A}, \{0, L\}\right) \\ T_A(1-c) + cT(x, y \pm \delta y) \text{ for } (x, y) = \left(x\big|_{p \ge p_A}, \{0, L\}\right) \\ T(0, y) = T(2\pi R, y) \\ \dfrac{\partial T(0, y)}{\partial x} = \dfrac{\partial T(2\pi R, y)}{\partial x} \end{cases} \qquad [23]$$

Numerical Procedure

Zeroth Order Equation

For given operation conditions $U = \Omega R$ and eccentricity, the nonlinear partial differential Eq. [9] is solved using as finite difference approximation on a discretized domain of dimension $m \times n$ in the x and y coordinates, respectively. All equations were solved on a uniform grid of $N \times N$ points as illustrated in Fig. 1c. The resulting algebraic system is also nonlinear in p_0; therefore, an iterative solution strategy is developed splitting the pressure terms in the Reynolds equation, Eq. [9], as:

$$\left[\frac{\partial}{\partial x}\left(\frac{p_0^\alpha}{\mu T} h^3 \frac{\partial}{\partial x}\right)\right] p_0^\beta + \left[\frac{\partial}{\partial y}\left(\frac{p_0^\alpha}{\mu T} h^3 \frac{\partial}{\partial y}\right)\right] p_0^\beta$$
$$= 6U\left(\frac{p_0^\alpha}{T}\frac{\partial h}{\partial x} - \frac{p_0^\alpha h}{T^2}\frac{\partial T}{\partial x}\right) + 6U\left(\frac{h}{T}\frac{\partial}{\partial x}\right) p_0^\beta \qquad [24]$$

Starting with an initial guess for p_0^α, the problem becomes linear in p_0^β and thus can be solved directly and is then used to update the guess for the next iteration. This is repeated until the difference between the solutions of two successive iterations is smaller than a set tolerance, which has been set to a value of 10^{-5}. An upwinded finite difference scheme has been adopted for the discretization of the compressible energy Eq. [16] to ensure numerical stability due to its parabolic character. When both the pressure and temperature distributions are known, the fluid properties are updated and the pressure and temperature are recalculated. This procedure continues until all properties converge, respecting the set tolerance. Once convergence is obtained, the zeroth-order pressure field is integrated over the bearing surface, which in turn imposes vertical and horizontal lubrication reaction forces:

$$F_X = \int_0^L \int_0^{2\pi} (p_0 - p_{atm}) \cos\Theta R d\Theta dy$$
$$F_Z = \int_0^L \int_0^{2\pi} (p_0 - p_{atm}) \sin\Theta R d\Theta dy \qquad [25]$$

First-Order Equations

The solution of the first-order perturbation Eqs. [10] and [11] for the perturbed pressures (p_X, p_Z) is straightforward, because these are linear partial differential equations. Given a zeroth-order field p_0 they are solved via a finite difference scheme and subsequently integrated over the bearing surface to determine

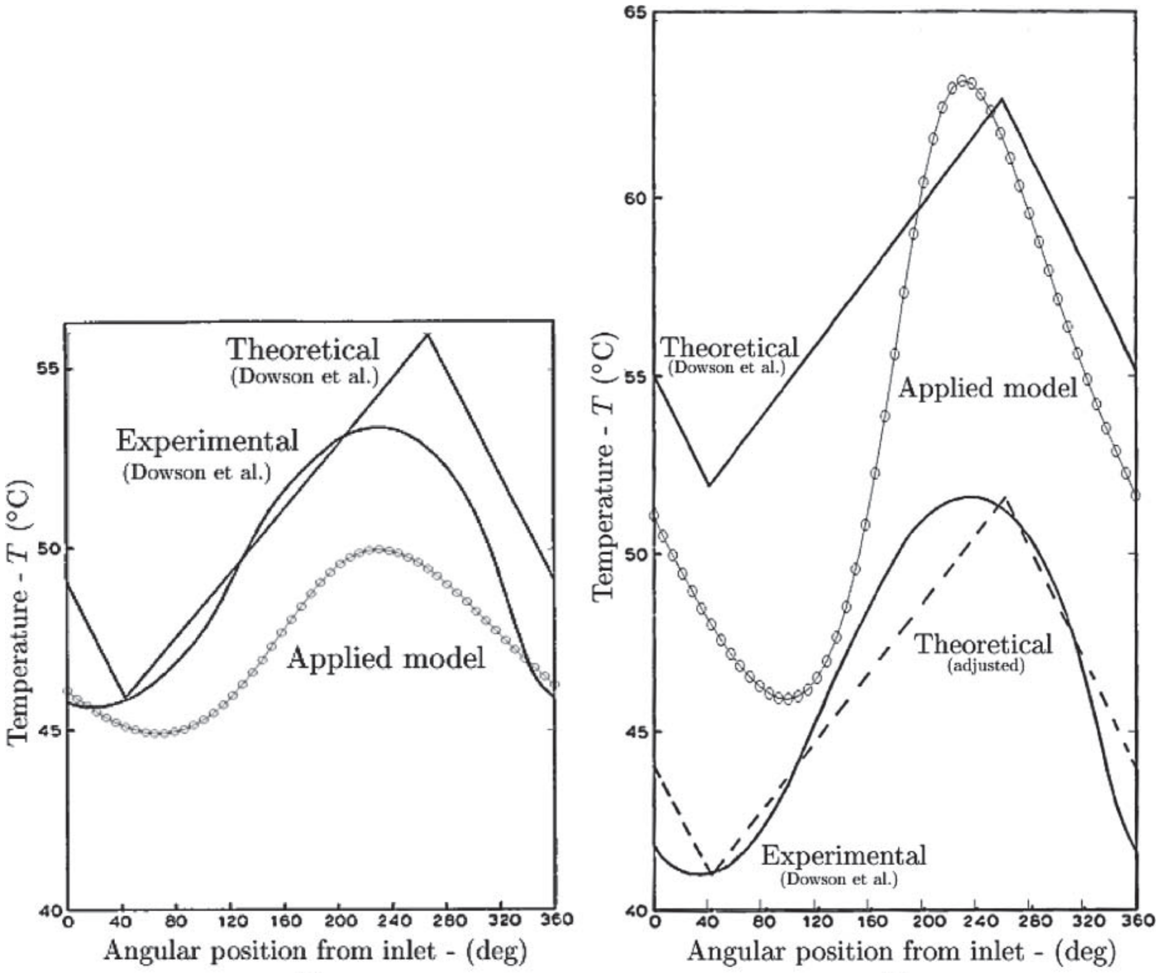

(a) (b)

Fig. 6—Comparison between numerical solution of the energy equation and results presented by Dowson, et al. *(11)*. Solid line with circles indicates the temperature profile calculated by the derived model. (a) Temperature distribution for eccentricity ratio of $e = 0.2$. (b) Temperature distribution for eccentricity ratio of $e = 0.5$.

the stiffness and damping coefficients:

$$\mathbf{K} + i\omega\mathbf{D} = \int_0^L \int_0^{2\pi} \begin{bmatrix} p_X \cos\Theta & p_X \sin\Theta \\ p_Z \cos\Theta & p_Z \sin\Theta \end{bmatrix} R d\Theta dy \qquad [26]$$

It is important to notice that the dynamic coefficients are dependent on the excitation frequency and that the model assumes small amplitude of perturbations. The steady-state position of the shaft is determined by a Newton-Raphson scheme where a force equilibrium in X and Z is considered. A full flowchart of the full THD-model is shown in Fig. 3, which is the flowchart of a full THD model. The first-order computation of dynamic perturbation coefficients does not involve the energy equation per se; all temperature-dependent quantities are designated to be those determined in the converged full-THD computation.

Grid Convergence

In order to determine a proper discretization of the domain, a grid convergence analysis has been performed. The parameter of concern is the relative deviation of a coarser solution compared to a fine one:

$$\xi = max\left(\frac{\varphi - \varphi_{fine}}{\varphi_{fine}}\right) \cdot 100 \qquad [27]$$

where $\varphi \in \{p, T\}$. The fine grid solution has been obtained with $N = 501$ grid points. The result of the analysis is shown in Fig. 4. It can be inferred that a discretization of $N = 40$ is sufficient to ensure that the discretization error of both the Reynolds and energy equation is less than 1%. Thus, unless otherwise stated, for computational speed reasons the coarser grid has been utilized for the numerical analysis.

NUMERICAL ANALYSIS AND DISCUSSION

Comparison with Published Results

Computed results according to the above described procedure are compared with the pressure profile data in Powell *(2)*, the temperature profile published by Dowson et al. *(12)* and the dynamic perturbation coefficients published by Arghir, et al. *(26)* respectively.

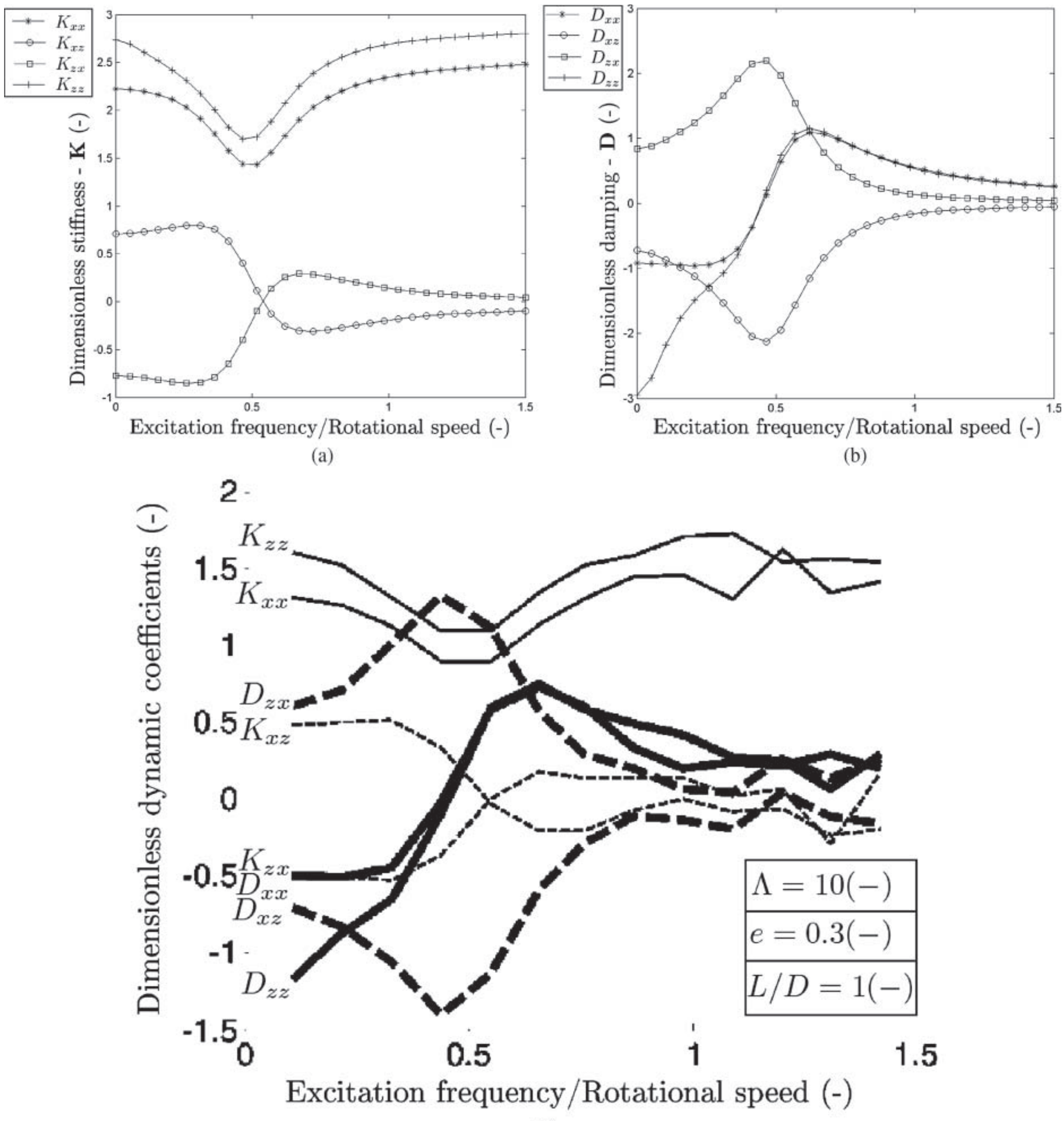

(a) (b)

(c)

Fig. 7—Comparison between calculated dimensionless dynamic coefficients and calculations presented by Arghir, et al. *(26)*. (a) Dimensionless stiffness for a cylindrical air bearing. $\Lambda = 10$, $e = 0.3$, and $L/D = 1$. (b) Dimensionless damping for a cylindrical air bearing. $\Lambda = 10$, $e = 0.3$, and $L/D = 1$. (c) Dimensionless damping and stiffness for a cylindrical air bearing calculated by Arghir, et al. *(26)*.

The solution of the compressible Reynolds equation has been validated against experimental results presented by Powell *(2)* shown in Fig. 5. The calculations are made with the full THD model and air as lubricant. From the figure, good agreement between the experimental results and the numerical calculations is seen, even though the maximum pressure for a bearing number of $\Lambda = 1.15$ is slightly underestimated. Because pressure solutions depend on the applied load rather than the temperature, the equilibrium position, which determines the pressure distribution, depends on the viscosity field and thus indirectly on temperature. The fact that the pressure solutions are equivalent thus reasonably suggests the validity of the model.

The solution of the energy equation has been validated against numerical solutions and experimental results presented by Dowson, et al. *(12)*. Firstly, it shall be noticed that the bearing geometry in the reference is discontinuous due to a single inlet slit. In addition, it has been assumed that the temperature variation in the radial direction could be neglected, which is only satisfied for limited bearing sizes. This assumptions is clearly violated by the bearing geometry applied in the article by Dowson, et al. *(12)*.

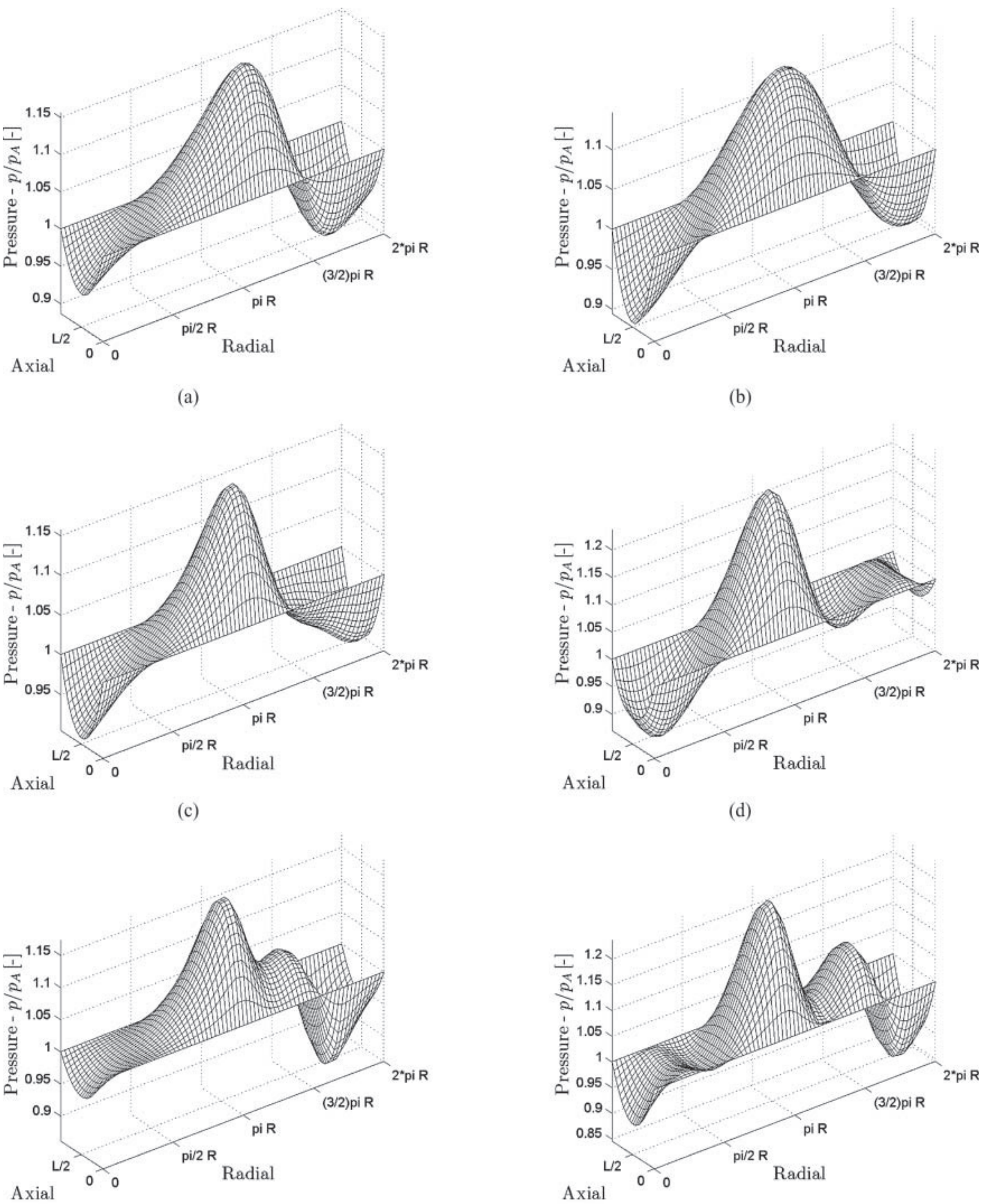

(a) (b) (c) (d) (e) (f)

Fig. 8—Pressure distribution in a cylindrical, elliptical and polygonal bearing, respectively. $W = 3$ kg; $h_0 = 25$ μm; $L = 40$ mm; $L/D = 1$. (a) Pressure distribution for a cylindrical bearing. $\Omega = 10{,}000$ rpm. (b) Pressure distribution for a cylindrical bearing. $\Omega = 30{,}000$ rpm. (c) Pressure distribution for an elliptical bearing. $\Omega = 10{,}000$ rpm. (d) Pressure distribution for an elliptical bearing. $\Omega = 30{,}000$ rpm. (e) Pressure distribution for a polygonal bearing. $\Omega = 10{,}000$ rpm. (f) Pressure distribution for a polygonal bearing. $\Omega = 30{,}000$ rpm.

By adopting the same bearing geometry and lubricant as used in the article by Dowson *(12)*, the comparison shown in Fig. 6 has been made.

Neither the theoretical model by Dowson, et al. *(12)* nor the applied model is capable of making a perfect compliance of the experimental results. However, many of the discrepancies between the experimental results and the applied model can be attribute to the violated assumption of limiting bearing size. It is expected that the applied model would provide a proper estimate of the temperature distribution if the assumption of limited bearing size is satisfied.

A comparison of computed dynamic perturbation coefficients is made against results presented by Arghir, et al. *(26)* as shown in Fig. 7; though a convincing qualitative agreement is observed,

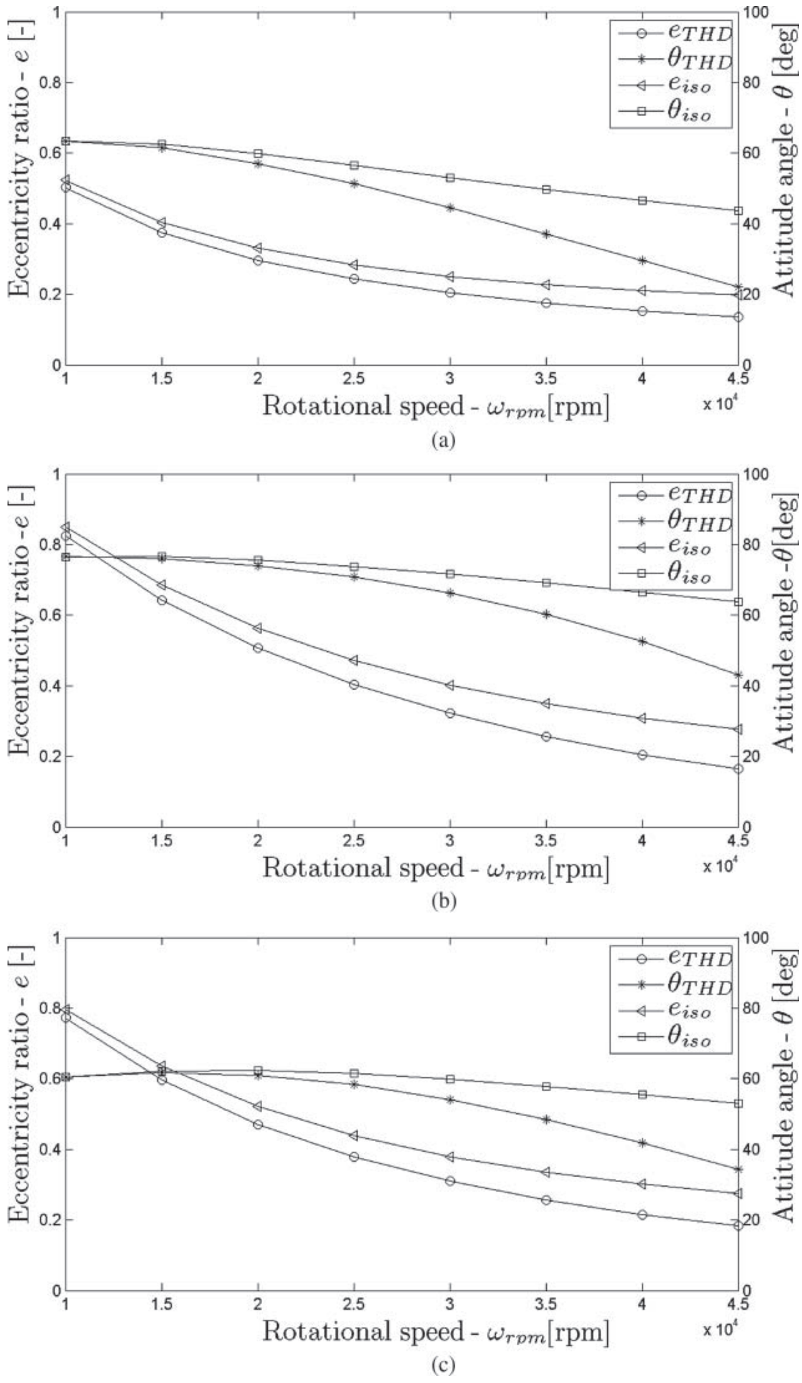

Fig. 9—Equilibrium position in a cylindrical, elliptical and polygonal bearing, respectively, as a function of the rotational speed. $W = 3$ kg; $L = 40$ mm; $L/D = 1$, $h_0 = 25$ μm. (a) Equilibrium position for a cylindrical bearing as a function of the rotational speed. (b) Equilibrium position for an elliptical bearing as a function of the rotational speed. (c) Equilibrium position for a polygonal bearing as a function of the rotational speed.

considerable quantitative disparity can be seen. There is a stark contrast between the smoothness of all curves in Figs. 7a and 7b to the jaggedness of those in Fig. 7c, especially in the range 1.0 to 1.5 of the abscissa. Because in the stability analysis of a rotor-bearing system determination of the neutral state of instability requires numerical root-finding of the characteristic determinant formed by the dynamic perturbation coefficients, a significant improvement in the numerical precision of the present scheme can be reasonably asserted.

Different Bearings Geometry

Throughout the numerical simulations, the bearing geometries are as indicated in Fig. 2 and with the dimensions stated in Table 2.

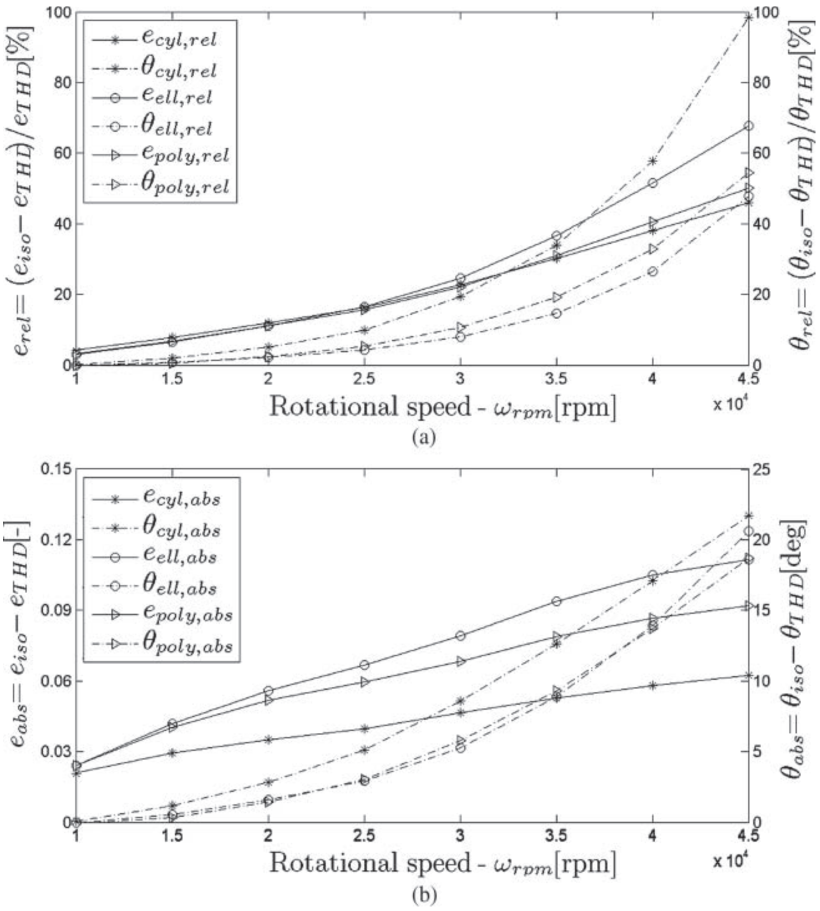

(a)

(b)

Fig. 10—Relative and absolute deviation between the isothermal and the THD model for the eccentricity ratios and attitude angles. $W = 3$ **kg;** $L = 40$ **mm;** $L/D = 1$; $h_0 = 25$ **μm. (a) Relative deviation between the isothermal and the THD model for the eccentricity ratio and attitude angles. (b)Absolute deviation between the isothermal and the THD model for the eccentricity ratio and attitude angle.**

Pressure Distribution

The two-dimensional pressure distributions for the three different bearing geometries presented in the proceeding section are shown in Fig. 8. Note that all pressure distributions are calculated for a static load in the vertical direction of $W = 3$ kg. Analysis of Figs. 8a and 8b, suggests that the maximum pressure for low bearing number solutions is higher than for higher bearing number solutions. This effect is due to the larger eccentricity ratio of the low bearing number solution. As the bearing number increasesm the peak of the pressure distribution starts to spread and the pressure is distributed over a larger area as the eccentricity decreases.

When pressure distributions for a rotational speed of $\Omega = 30k$ rpm are compared (see Figs. 8b, 8d, and 8f, it can be seen that the maximum pressure for the polygonal and elliptical bearings is significantly larger than in the cylindrical bearing case. Differences in the geometry, for which the weight is distributed over a relatively smaller area, are the cause of this behavior. The effect of the bearing geometry is most clearly seen by the two (respectively three peaks) for the elliptical and polygonal bearing.

TABLE 2—STANDARD BEARINGS GEOMETRY

Type	D (mm)	L/D	h_0 (μm)	p_A (Pa)	T_A (C)
Cylindrical	40	1	25	$1 \cdot 10^5$	20
Elliptic	40	1	25	$1 \cdot 10^5$	20
Polygonal (three-lobe bearing)	40	1	25	$1 \cdot 10^5$	20

Lubricant: Air.

Equilibrium Position

The equilibrium positions for the three different bearing geometries calculated with the THD and isothermal model are presented in Fig. 9. In the case of the elliptical and polygonal bearing, the eccentricity is normalized by the minimum nominal clearance, defined as the radius of the shaft subtracted from the minimum inner radius of the bearing housing.

Firstly, it can be seen that the eccentricity ratio for the cylindrical case is small compared to the elliptical and polygonal cases. This was expected due to the low pressure in the horizontal direction, which implies that the bearing would tend to move in that direction. Further, it is seen that both the eccentricity ratios and attitude angles predicted by the THD model are smaller than those predicted by the isothermal model. This is caused by an increase in the load-carrying capacity introduced by the thermal

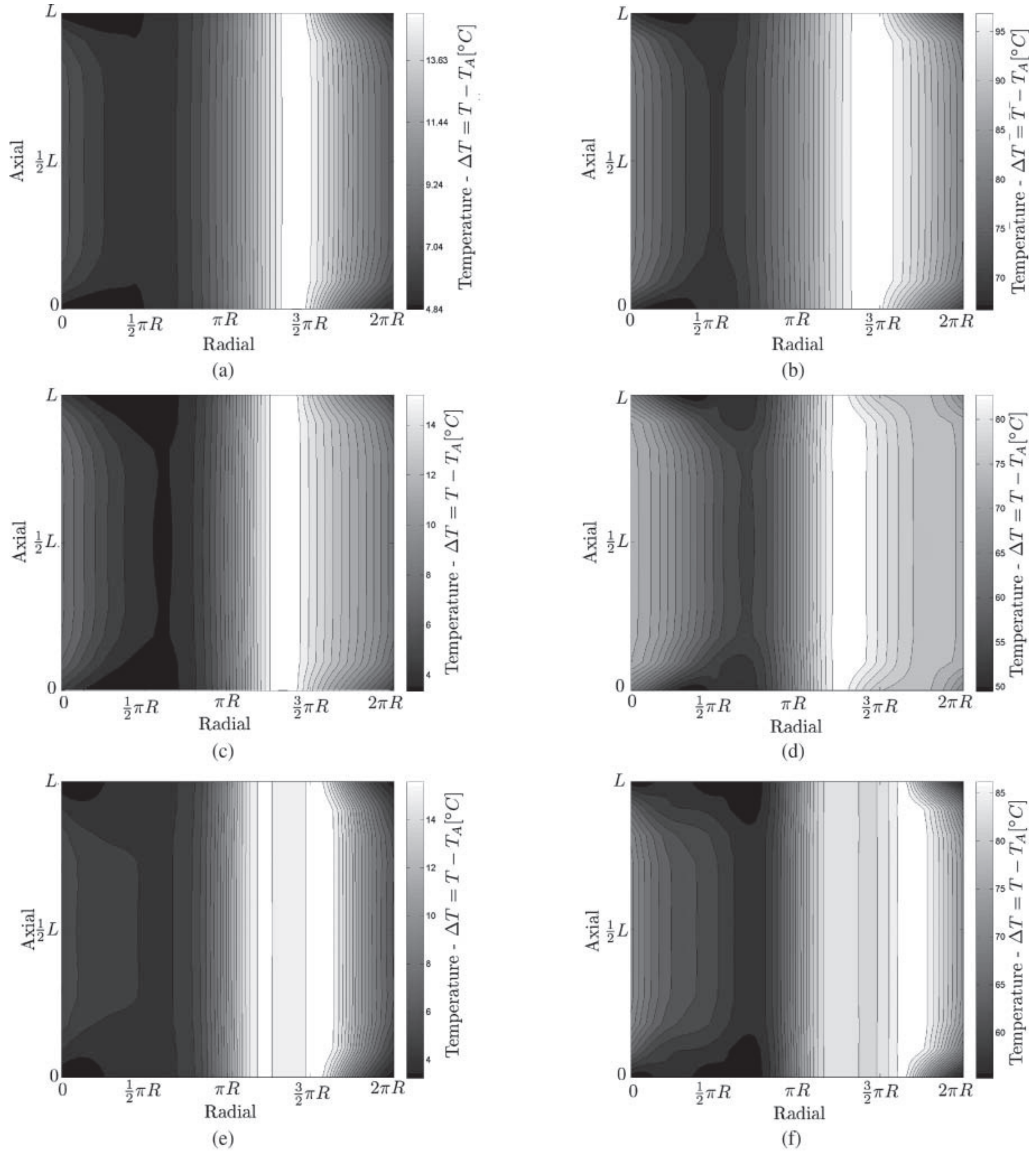

Fig. 11—Temperature distribution in a cylindrical, elliptical and polygonal bearing, respectively. $W = 3$ kg; $L = 40$ mm; $L/D = 1$; $h_0 = 25$ μm. (a) Temperature distribution for a cylindrical bearing. $\Omega = 10{,}000k$ rpm. (b) Temperature distribution for a cylindrical bearing. $\Omega = 30{,}000k$ rpm (c) Temperature distribution for an elliptical bearing. $\Omega = 10{,}000k$ rpm. (d) Temperature distribution for an elliptical bearing. $\Omega = 30{,}000k$ rpm. (e) Temperature distribution for a polygonal bearing. $\Omega = 10{,}000k$ rpm. (f) Temperature distribution for a polygonal bearing. $\Omega = 30{,}000k$ rpm.

wedge. It is also seen that the difference between the two curves increases with the rotational speed, which is naturally related to the increase in temperature, why the two models would starts to deviate.

The relative and absolute difference in the eccentricity ratios and attitude angles are presented in Figs. 10a and 10b, respectively. Firstly is can be seen that both the relative and absolute deviation between the isothermal and THD model increase with the rotational speed. Further, it can be seen that even though the relative difference between the isothermal and THD model grows rapidly, the absolute deviation of the eccentricity remains bounded.

Temperature Distribution

Examples of temperature distributions for the three different bearing geometries are shown in Fig. 11. Firstly, at low speeds the temperature variation is limited, although a gradient is still noticeable. In these conditions the assumption of the bearing operating in the isothermal regime can be assumed as satisfied. In general, the temperature variation in the axial direction *y* is small but

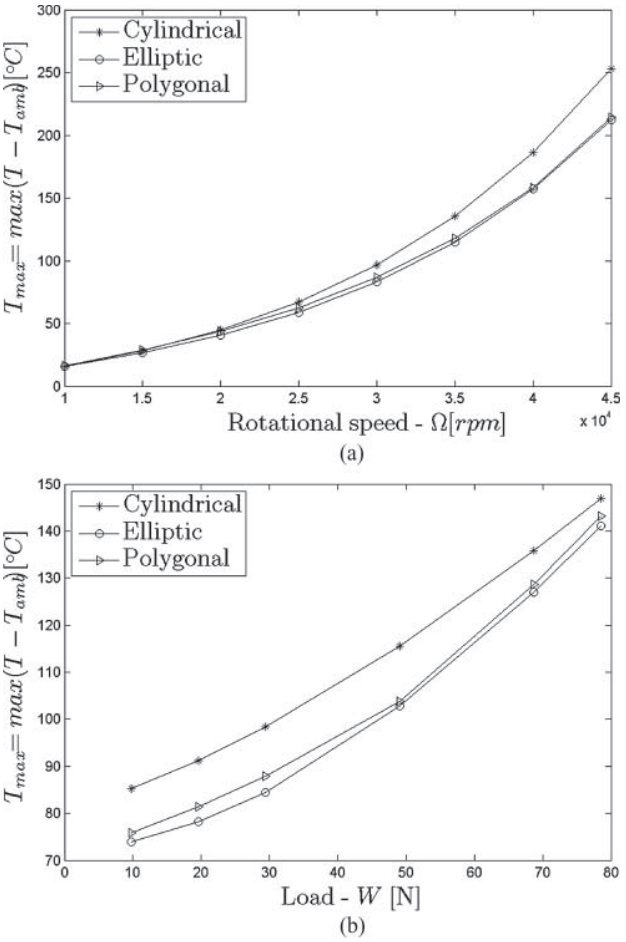

Fig. 12—Maximum temperature in a cylindrical, elliptical and polygonal bearing, respectively. $L = 40$ mm; $L/D = 1$; $h_0 = 25$ μm. (a) Maximum temperature as a function of the rotational speed. $W = 3$ kg. (b) Maximum temperature as a function of the load. $\Omega = 30{,}000$ rpm.

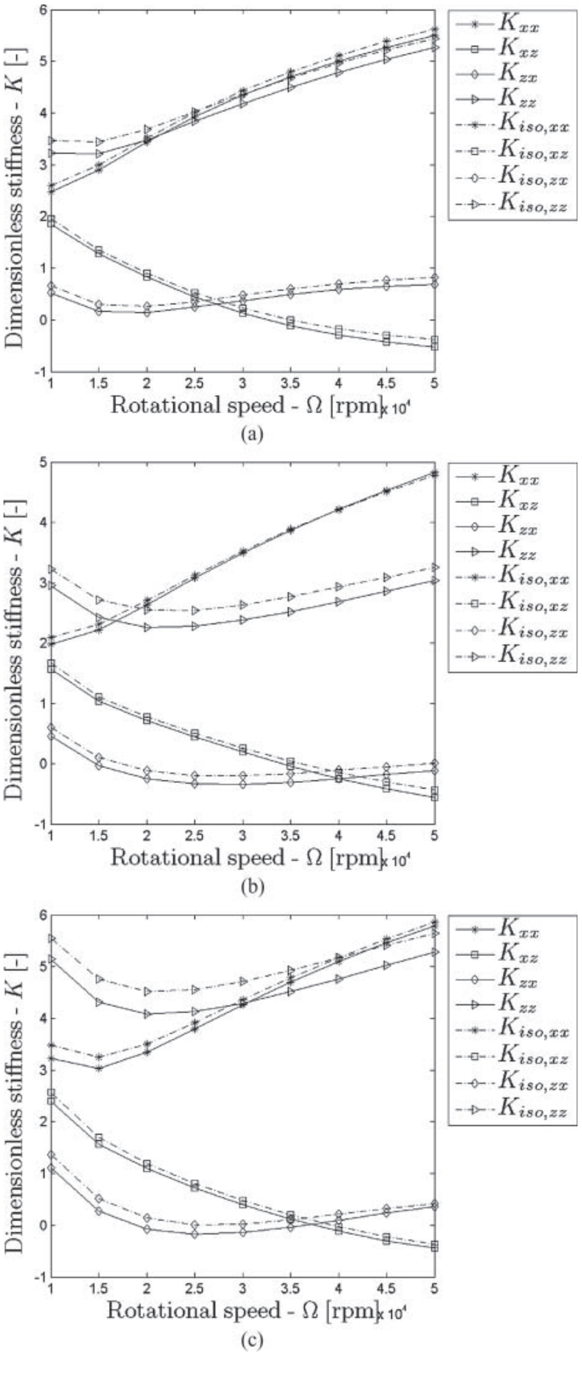

Fig. 13—Components of the stiffness matrix for a cylindrical, elliptical and polygonal bearing, respectively. Primes indicates coefficients calculated with an isothermal model. $W = 3$ kg; $h_0 = 25$ μm; $L = 40$ mm; $L/D = 1$. (a) Components of the stiffness matrix for a cylindrical bearing. Primes indicate coefficients calculated with an isothermal model. (b) Components of the stiffness matrix for an elliptical bearing. Primes indicate coefficients calculated with an isothermal model. (c) Components of the stiffness matrix for a polygonal bearing. Primes indicate coefficients calculated with an isothermal model.

significant in suction areas where the pressure is below ambient pressure and fresh air enters from the bearing sides. One could argue that solving for the temperature in the axial direction is not needed. On the other hand, the contribution of the axial pressure gradient of the viscous heating would be neglected. Moreover, from a numerical point of view, it is convenient to know the temperature on the same grid points as the pressure. Solving the energy equation on a two-dimensional grid also makes it easy to take the natural inflow of lubricant into consideration, because it can be introduced as a boundary condition. Looking at Eq. [19], the last term of the expression for the dissipation is proportional to the square of the velocity, and the first term is proportional to the gradient of the pressure squared. The effect of these terms can be seen in Fig. 11. From the pressure distribution of the cylindrical bearing, seen in Fig. 8a and 8b, one observes that the difference between the pressure gradient for high and low rotational speed, is small. The difference in temperature, seen in Fig. 11b, is not caused by a change in the pressure gradient but rather by the variation in rotational speed. The fact that the maximum temperatures are observed in areas where the film thickness is small is a combined effect of the gradient of the pressure distribution and the film thickness, which are large in the areas before and after the location of minimum film thickness. The drops in temperature in the circumferential direction, are due to the way in which

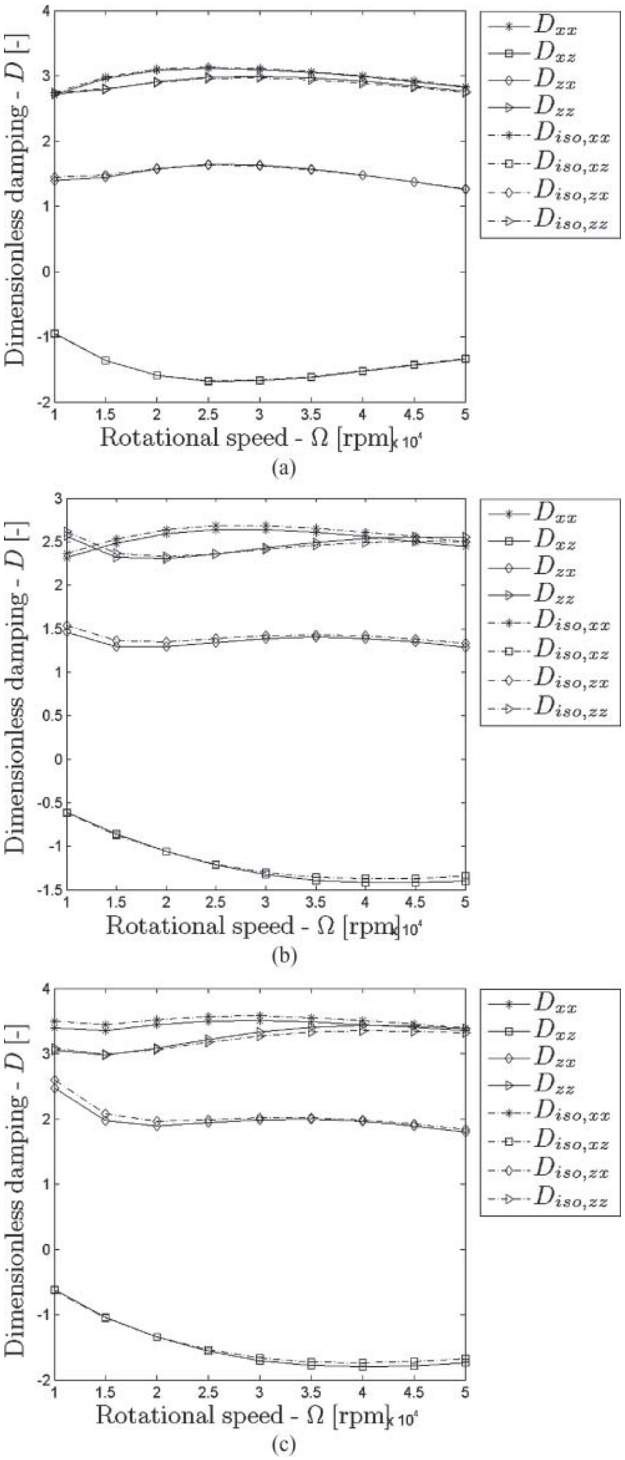

Fig. 14—Components of the damping matrix for a cylindrical, elliptical and polygonal bearing, respectively. Primes indicate coefficients calculated with an isothermal model. $W = 3$ kg; $h_0 = 25\ \mu$m; $L = 40$ mm; $L/D = 1$. (a) Components of the stiffness matrix for a cylindrical bearing. Primes indicate coefficients calculated with an isothermal model. (b) Components of the stiffness matrix for an elliptical bearing. Prime indicate coefficients calculated with an isothermal model. (c) Components of the stiffness matrix for a polygonal bearing. Primes indicate coefficients calculated with an isothermal model.

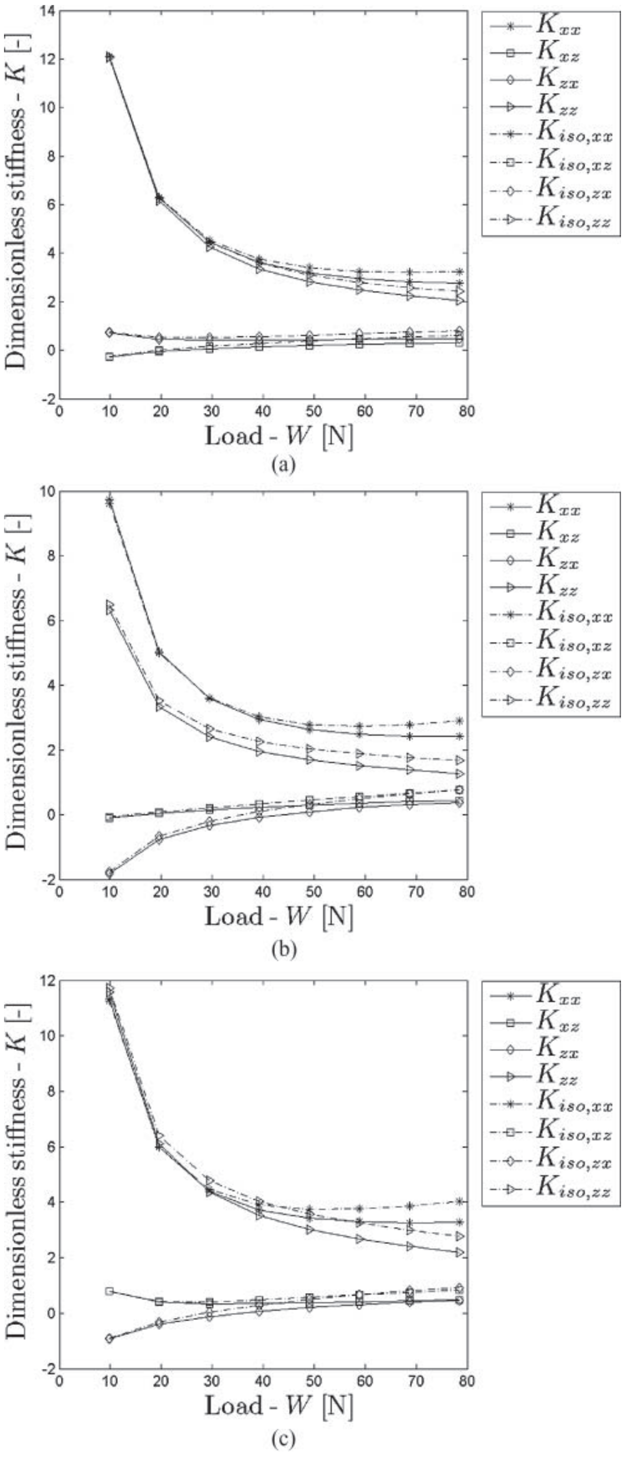

Fig. 15—Components of the damping matrix for a cylindrical, elliptical and polygonal bearing, respectively. Primes indicate coefficients calculated with an isothermal model. $\Omega = 30{,}000$ rpm; $h_0 = 25\ \mu$m; $L = 40$ mm; $L/D = 1$. (a) Components of the damping matrix for a cylindrical bearing. Primes indicate coefficients calculated with an isothermal model. (b) Components of the damping matrix for an elliptic bearing. Primes indicate coefficients calculated with an isothermal model. (c) Components of the damping matrix for a polygonal bearing. Primes indicate coefficients calculated with an isothermal model.

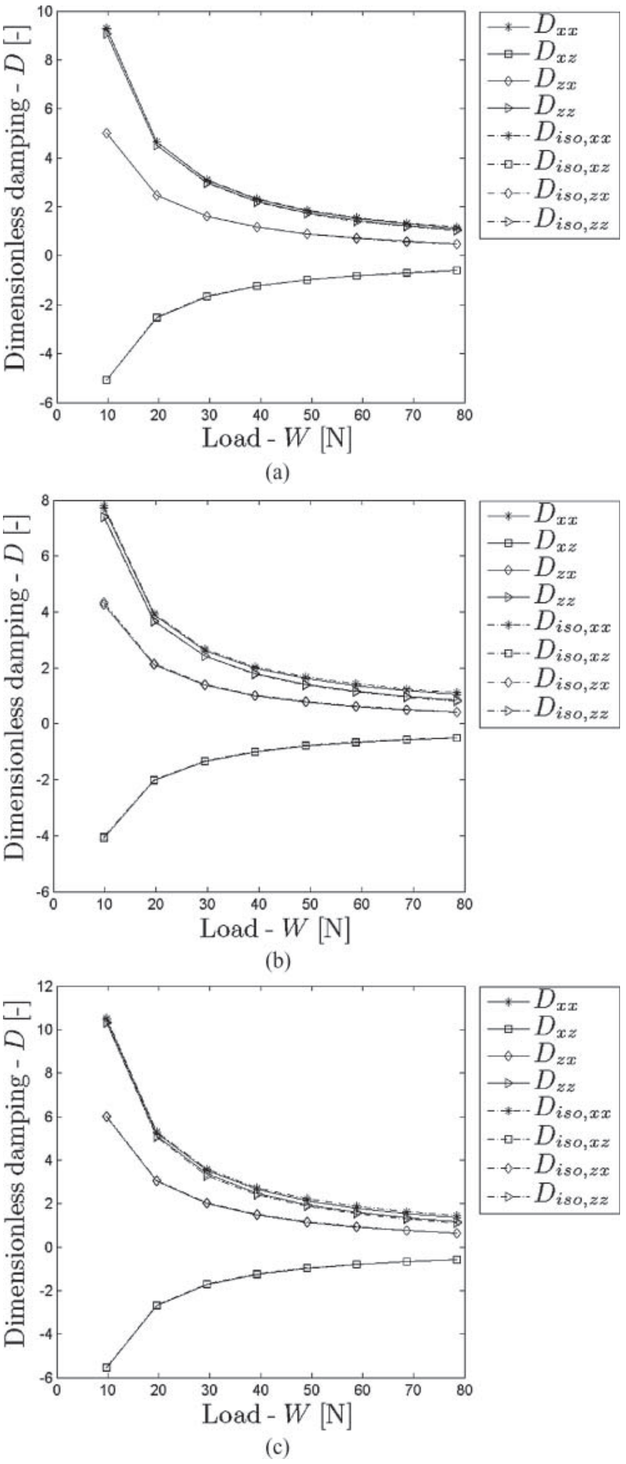

Fig. 16—Components of the damping matrix for a cylindrical, elliptical and polygonal bearing, respectively. Primes indicate coefficients calculated with an isothermal model. $\Omega = 30{,}000$ rpm; $h_0 = 25\ \mu$m; $L = 40$ mm; $L/D = 1$. (a) Components of the damping matrix for a cylindrical bearing. Primes indicates coefficients calculated with an isothermal model. (b) Components of the damping matrix for an elliptical bearing. Primes indicate coefficients calculated with an isothermal model. (c) Components of the damping matrix for a polygonal bearing. Primes indicate coefficients calculated with an isothermal model.

boundary conditions are imposed; in areas where the pressure is lower than ambient pressure, there will be a natural inflow of lubricant with a temperature of $T = T_{amb}$, which in turn cools down the fluid. For all three bearings the total circumferential temperature variation is $\simeq 10^\circ$C at 10,000 rpm and is $\simeq 30^\circ$C at 30,000 rpm. Figure 12 shows the influence of the rotational speed and the load on the maximum temperature for the three different bearing geometries. As seen from the figure, the maximum temperatures for the cylindrical bearing are larger compared to the elliptical and polygonal bearings. This is a result of the fact that the averaged film thickness, for the cylindrical bearing is smaller than for the elliptical and polygonal bearings.

The maximum film temperature as a function of increasing load at a constant rotational speed is presented in Fig. 12. The maximum temperature for the elliptical and polygonal bearings approaches the cylindrical as the load increases. Once the effect of the velocity is isolated, the temperature increase becomes related to the Poiseuille flow components. Though in heavier load conditions the fluid film thickness function approaches relatively similar values for the various bearing geometries—thus producing similar, single pressure peaks—at lighter loading the pressure gradients are generally different, exhibiting particular behaviors for each case.

Dynamic Coefficients

The dynamic coefficients were calculated for the three different bearing geometries. For comparison, the calculations were made with both the isothermal and THD models.

The dynamic coefficient as a function of the rotational speed is presented in Figs. 13 and 14.

Firstly, it can be seen that the deviation between the two models is generally small and constant in the entire domain. In general, the dynamic coefficients, which build the stiffness and damping matrices **K** and **D**, are used to obtain a linear representation of the aerodynamic force. Therefore, the integral of the aerodynamic pressure is the fundamental field to get such dynamic coefficients. The pressure distribution in a journal bearing is directly affected by both the temperature distribution and by the equilibrium position at which the dynamic coefficients are calculated, because these quantities enter directly into their mathematical expressions, Eqs. [9]–[11]. Moreover, viscosity increases driven by the heating of the air film indirectly affect the equilibrium position, because the aerodynamic forces also increase. As for the heat generation, one should consider that it is essentially driven by the two phenomena described in the previous section; Poiseuille terms are especially relevant at high loads or low rotational speeds and a Couette term dominates the energy equation at higher rotational speeds. Then, the deviation between isothermal and THD calculated dynamic coefficients is given by a combination of the shifting of the equilibrium position and the different mechanisms that drive the heat generation; at low speed the deviation must be mostly driven by temperature and viscosity gradients caused by the Poiseuille dissipation, because little deviation is observed in the eccentricity and attitude angles values (see Figs. 10a and 10b). At high speed, although the temperatures and viscosity fields are subjected to larger variations, the equilibrium position is shifted more toward the center of the bearing, where the pressure fields tend to assume asymptotic values.

The impact of the thermal effects on the general dynamic behavior of the different bearing geometries seems to be quite similar for the different bearings under analysis. The deviation between the direct coefficients of stiffness K_{XX} and K_{ZZ} appears different in the case of the elliptical and polygonal bearings, where larger discrepancies are observed in the Z direction. This behavior is consistent with the temperature fields presented in Fig. 11, where for these types of bearings high temperatures persist longer along the circumferential direction.

To further investigate the impact of the THD model on the dynamic coefficients, stiffness and damping were calculated as a function of the load for a constant rotational speed. The result of the analysis is shown in Figs. 15 and 16. As seen from Fig. 15, the deviation of the stiffness between the components increases as the load increases. This comes as no surprise: because the rotational speed is fixed in these cases, the only thing that varies is the increasing load. This determines a higher eccentric equilibrium, which in turn increases the Poiseuille dissipation, and the Couette term is kept constant.

Finally, it can be seen that the impact of the THD model on the components of the damping matrix, irrespective of the rotational speed or load, is small.

CONCLUSIONS

This article presents a detailed analytical model for the characterization of a compressible fluid film journal bearing under thermohydrodynamic lubrication. The solution couples the two-dimensional compressible Reynolds and energy equations, taking into consideration the variations of fluid properties as well as the thermal and centrifugal growth of the shaft and bearing sleeve. The static and dynamic performance under THD lubrication is compared for different sleeve geometries.

Despite incorporating a thermal conduction/convection dissipation model from the fluid film to the ambient air, heat fluxes along the axial and circumferential direction of the housing and the axial direction of the shaft are not included in the analysis, leading to a general overestimation of the temperature increase due to viscous effects. Further research is ongoing to determine in which conditions these contributions need to be taken into consideration. Moreover, the variation of clearance due to thermal growth of the shaft and bearing housing was addressed with a simplified model in which the two bodies are free to expand in the circumferential direction. Although this assumption can be considered as a physically correct-approximation for the rotating shaft, the same cannot be said for the housing, where thermal, induced stresses are expected to produce a nonuniform distortion along the circumferential direction due to the temperature gradient.

Numerical findings support the common literature assumption of the bearing being isothermal when operating in the low bearing number regime, regardless of the bearing geometry. Furthermore, it is observed that temperature variations in the axial direction are generally small.

The static properties calculated with the THD and isothermal models were compared. The eccentricity ratio for all geometries shows an increasing relative and absolute deviation between the isothermal and THD models. It was observed that larger eccentricity ratios were predicted by the isothermal model. This was expected, because the load, carrying capacity is dictated by the temperature changes in the lubricant viscosity. Similarly, deviations between the two models were observed for the attitude angle. This behavior is of special concern for the calculation of the dynamic coefficient, which is strongly dependent on the pressure solution. The unrestricted rise of temperature due to increasing operational speed or static loading to values that can be hundreds of degrees above ambient temperature also pose serious concerns regarding the thermal limits of the bearing materials when operating in extreme conditions.

On the other hand, it was observed that the difference between the dynamic coefficients calculated with isothermal and THD models were small and almost constant as a function of the rotational speed. This behavior was explained by assuming a combined effect involving the shifting of the equilibrium position and different thermal phenomena due to pressure gradients and journal velocity. These assumption were confirmed by observing increasing deviation of the dynamic coefficients with increasing loads.

It is therefore suggested that thermohydrodynamic effects in air-lubricated journal bearings should be considered in cases where the bearing is heavily loaded and static and dynamic properties or the temperature itself are of special concern.

REFERENCES

(1) Czolczynski, K. (1999), *Rotordynamics of Gas-Lubricated Journal Bearing Systems*, Springer: New York.

(2) Powell, J. W. (1970), "A Review of Progress in Gas Lubrication," *Review of Physics and Technology*, **1**(2), p 96.

(3) Katto, Y. and Soda, N. (1952), "Theory of Lubrication by Compressible Fluid with Special Reference to Air Bearing," *Proceedings of the Second Japan National Congress for Applied Mechanics*, Tokyo, pp 267-270.

(4) Ford, G. W. K., Harris, D. M., and Pantall, D. (1956), "Gas-Lubricated Bearings," *Machinery Market*, **182**(2924), pp 26-30.

(5) Ausman, J. (1957), "Finite Gas-Lubricated Journal Bearing," *The Institute of Mechanical Engineers, Proceedings of the Conference on Lubrication and Wear*, London, pp 39-45.

(6) Ausman, J. S. (1961), "An Approximate Analytical Solution for Self-Acting Gas Lubrication of Stepped Sector Thrust Bearings," *Tribology Transactions*, **4**(2), pp 304-313.

(7) Hughes, W. F. and Osterle, J. F. (1957), "On the Adiabatic Couette Flow of a Compressible Fluid," *Zeitschrift für angewandte Mathematik und Physik ZAMP*, **8**, pp 89-96.

(8) Whitley, S. and Betts, C. (1959), "Study of Gas-Lubricated, Hydrodynamic, Full Journal Bearings," *British Journal of Applied Physics*, **10**, pp 455-463.

(9) Elrod, H. G. and Burgdorfer, A. (1960) "Refinements of the theory of the Infinitely-Long, Self-Acting, Gas-Lubricated Journal Bearing," Proceedings of The International Symposium on Gas–Lubricated Bearing, pp. 93-118.

(10) Castelli, V. and Pirvics, J. (1968), "Review of Numerical Methods in Gas Bearing Film Analysis," *Journal of Lubrication Technology*, **90**, pp 777-792.

(11) Dowson, D. and March, C. H. (1966), "A Thermohydrodynamic Analysis of Journal Bearings," *Proceedings of the Institution of Mechanical Engineers*, **181**, pp. 117-126.

(12) Dowson, D., Hudson, J., Hunter, B., and March, C. (1966), "An Experimental Investigation of the Thermal Equilibrium of Steadily Loaded Journal Bearings," *Proceeding of the Institution of Mechanical Engineers*, **181**(32), pp 70-80.

Appendix F

J2: On the modelling of hybrid aerostatic-gas journal bearings

On the modelling of hybrid aerostatic-gas journal bearings

S Morosi* and **I F Santos**
Department of Mechanical Engineering, DTU – Technical University of Denmark, Lyngby, Denmark

The manuscript was received on 29 September 2010 and was accepted after revision for publication on 19 January 2011.

DOI: 10.1177/1350650111399845

Abstract: Gas journal bearings have been increasingly adopted in modern turbo-machinery applications as they meet the demands of operation at high rotational speeds, in clean environment, and with great efficiency. Due to the fact that gaseous lubricants, typically air, have much lower viscosity than more conventional oils, carrying capacity and dynamic characteristics of passive systems are generally poorer. In order to enhance these characteristics, one solution is used to combine the aerodynamic effect with the addition of external pressurization. This study presents a detailed mathematical model for hybrid lubrication of a compressible fluid-film journal bearing. Additional forces are generated by injecting pressurized air into the bearing gap through orifices located on the bearing walls. A modified form of the compressible Reynolds equation for active lubrication is derived. By solving this equation, stiffness and damping coefficients can be determined. A multibody dynamics model of a global system comprised of rotor and hybrid journal bearing is built in order to study the lateral dynamics of the system. Campbell diagrams and stability maps are presented, showing the main advantages and drawbacks of this special kind of hybrid fluid-film bearing.

Keywords: rotodynamics, Reynolds equations, fluid film bearings

1 INTRODUCTION

Gas lubrication has, in recent years, witnessed a marked development, with applications varying from microturbomachinery to high precision spindles. It is essentially a development of traditional fluid-film bearing theory. Despite sharing a common base principle for which a carrying load is developed as a result of viscous shear stress generation, the main difference is that compressibility effects need to be taken into consideration. Due to the fact that the lubricant, typically air, has a much lower viscosity than oil, gas bearings are characterized by lower carrying capacity, higher rotational speed, and lower film thickness. Reduced clearances necessitate a higher degree of surface finishing and treatment to minimize the risk of contact between surfaces and their damage.

As the load capacity and dynamic properties are proportional to the operational speed, aerodynamic gas bearings are generally characterized by poor start-up and shut-down properties [**1**, **2**]. These bearings present, however, several advantages. Friction forces are very limited; therefore, operation is possible at rotational speeds that exceed the maximum admissible for other types of bearings. Heat generation is also very low. Gas lubricants are generally very stable with respect to temperature; they cannot boil, freeze, or become flammable. Moreover, viscosity increases with increasing temperatures; thus, heating provides additional load-carrying capacity [**3**]. The absence of contaminants makes these bearings suitable for clean environments.

Aerostatic bearings are in specific cases used for high speed rotors, where stability becomes the most

---

*Corresponding author; Department of Mechanical Engineering, DTU – Technical University of Denmark, Nils Koppels Allé, 2800 Kgs. Lyngby, Denmark.
email: smo@mek.dtu.dk

important matter. This type of bearing shares many of the advantages of the aerodynamic bearing. In addition, it supports all of its designed load at zero speed. This effect results from its principal disadvantage: it requires an external pressure source to create the air film.

Regarding the dynamic coefficients of aerodynamic bearings, one should be aware that these are highly dependent on the rotational speed of the rotor. In general, they are characterized by relatively low damping. For this reason, it is very dangerous to cross the rotor-bending critical speeds. The coefficients of aerostatic bearings are, on the other hand, easier to identify and mainly dependent on the air injection pressure. Acting on this parameter, it is therefore possible to modify the dynamic characteristic for a given rotational speed.

The knowledge of gas film stiffness and damping is necessary for calculating the rotor stability limit. The stability limit must be determined with sufficient precision in advance; because, the rotor instability in reality ends immediately by catastrophic failure. The knowledge of gas film stiffness and damping is therefore essential condition for calculating the rotor stability limit.

The concept of hybrid aerostatic-gas journal bearing is introduced in order to (a) improve the start-up and shut-down properties; (b) offer a soft failure mechanism in case of pressure injection malfunctioning; (c) improve the dynamic characteristic of the bearing and therefore the stability margin of the system which employs it.

The main original contribution of the work is of theoretical nature. This article presents first a detailed analytical model of the hybrid aerostatic-gas journal bearing, introducing an original modified form of the Reynolds equation for active lubrication based on the incompressible version proposed by Santos *et al.* [**4**]. The static and dynamic performance of a cylindrical aerodynamic gas bearing is evaluated by means of a perturbation analysis [**5–7**], where expressions for the zeroth- and first-order field are obtained by a finite difference method. Second, a numerical analysis is presented, where the test bearing is part of a mechanical system comprising also of a flexible rotor and a rigid disc. Comparisons are shown between the bearing working in aerodynamic and hybrid aerostatic–aerodynamic modes.

2 MATHEMATICAL MODEL

The mechanical system under analysis is shown in Fig. 1. It consists of three main parts: rotor, disc, and bearings. The rotor is modelled as a flexible body with distributed mass.

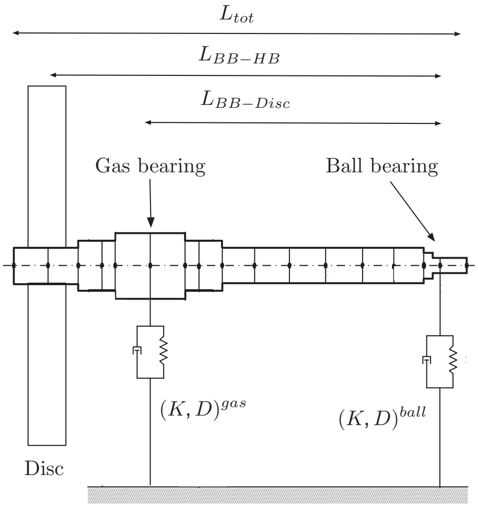

Fig. 1 Schematic view of the mechanical system

The disc is considered to be a rigid body. The bearings are modelled as (linear) forcing elements acting on the rotor. At one end, the rotor is supported by a ball bearing, the other being the hybrid bearing under investigation. Individual mathematical models of each component are developed and then assembled in a global system of equations describing the rotor-bearing system.

2.1 Free rotating elastic shaft

For the mathematical model of the elastic shaft, a finite element (FE) approach has been followed. This is a standard procedure, one may refer to references [**8**] or [**9**]. Only lateral dynamics are modelled, as axial and torsional movements are neglected, and the rotational speed is set as a constant Ω. Structural damping is also not considered. A local description of the element linear deformations is formulated based on Euler's beam theory. The potential and kinetic energy related to bending, linear, and angular motions are then formulated and inserted into the Lagrange's equation to obtain the equation of motion for the shaft

$$\underbrace{\left(M_T^e + M_R^e\right)}_{M^e} \ddot{q}^e + D^e \dot{q}^e + K_B^e q^e = F^e \tag{1}$$

where $\mathbf{D}^e = -\Omega \mathbf{G}^e$ is the gyroscopic matrix, M_T^e the element mass matrix considering the linear motion, and M_R^e the mass matrix considering angular motion, K_B^e the element stiffness matrix, $\mathbf{F}^e$ the generalized forces, and $\ddot{q}^e$, $\dot{q}^e$, and $\mathbf{q}^e$ the generalized acceleration, velocity, and displacement vectors, respectively.

2.2 Rigid disc

Unlike the rotor, the disc can be considered as a rigid body. To obtain its equation of motion, the Lagrange's equation is applied for which one needs to find the potential and kinetic energy. Because the disc is rigid, no potential energy due to deformation is stored, therefore $E_{pot} = 0$. The kinetic energy is expressed as function of four generalized coordinates, two translations of the centre of mass and two rotations of the plane of the disc perpendicular to the rotational axis. The equation of motion is determined

$$M^d \ddot{q}^d - \Omega G^d \dot{q}^d = Q^d \tag{2}$$

where the $\mathbf{M}^d$ and $\mathbf{G^d}$ are the mass and gyroscopic matrices, respectively, $\mathbf{Q}^d$ the force vector, and $\ddot{q}^d$ and $\dot{q}^d$ the generalized acceleration and velocity vectors, respectively.

2.3 Modelling the bearings

The dynamics of bearings depend on the bearing type, but can, in general, be interpreted by the following basic mechanical model, where the housing is considered as clamped and not moving, i.e. $M^b \ddot{q}^b = 0$

$$Q^b = -D^b \dot{q}^b - K^b q^b \tag{3}$$

where $\mathbf{Q}^b$ is the static force acting on the bearings from the weight of the shaft and disc.

2.3.1 Ball bearing

The coefficients of $\mathbf{D}^b$ and $\mathbf{K}^b$ can be obtained through different methods and theories for different bearings. For a ball bearing, only the direct stiffness coefficients are considered, whereas the cross-coupling effect as well as the damping can be neglected and set to zero. Typical values can be found in reference [**10**].

2.3.2 Hybrid aerostatic–gas journal bearing

The hybrid bearing under investigation consists of a traditional cylindrical journal bearing with circular orifices distributed along its surface (radial injection). In order to define the pressure profile in the bearing, a modified version of the general compressible form of the Reynolds equation is derived and proposed. Assuming an isoviscous, Newtonian, compressible fluid in a laminar regime, one can write the Navier–Stokes equations as

$$\begin{aligned} &\frac{\partial}{\partial x}\left[\mu \frac{\partial u}{\partial x}\right] = 0 \\ &\frac{\partial}{\partial x}\left[\mu \frac{\partial v}{\partial x}\right] = \frac{\partial p}{\partial y} \\ &\frac{\partial}{\partial x}\left[\mu \frac{\partial w}{\partial x}\right] = \frac{\partial p}{\partial z} \end{aligned} \tag{4}$$

where the coordinate system is defined as shown in Fig. 2. Note that the pressure is assumed to be constant across the film, and it solely considered the variation of tangential stresses upon the normal to the surface. The following boundary conditions are imposed

$$\begin{aligned} &u_b(0, y, z) = V_{\text{inj}} \quad u_j(h, y, z) = V \\ &v_b(0, y, z) = 0 \quad v_j(h, y, z) = U = \Omega R \\ &w_b(0, y, z) = 0 \quad w_j(h, y, z) = 0 \end{aligned} \tag{5}$$

Integrating twice equation (4) upon applying the boundary conditions above, one obtains

$$\begin{aligned} &u = \frac{x}{h} V + \left(\frac{h - x}{h}\right) V_{\text{inj}} \\ &v = -x\left(\frac{h - x}{2\mu}\right)\frac{\partial p}{\partial y} + \frac{x}{h} U \\ &w = -x\left(\frac{h - x}{2\mu}\right)\frac{\partial p}{\partial z} \end{aligned} \tag{6}$$

External radial injection. Regarding the external air injection, a velocity profile is defined in the domain comprised between the supply chamber and the bearing; see Fig. 3 for a schematic representation of the injection flow. Assuming fully developed laminar flow, an analytical expression is easily obtained by simplifying the N–S equations. Considering the injection ducts to be circular, it is conveniently expressed in cylindrical coordinates

$$V_{\text{inj}}(y, z, t) = -\frac{1}{4\mu}\left(\frac{\partial p}{\partial x}\right)\left[\frac{d_o^2}{4} - (y - y_i)^2 - (z - z_i)^2\right] \tag{7}$$

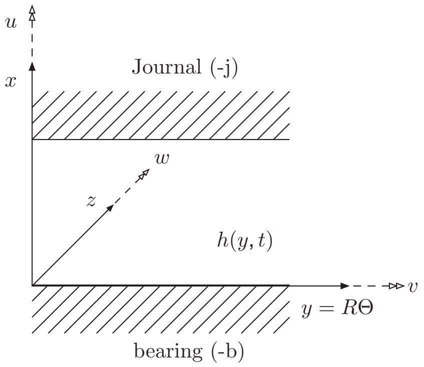

Fig. 2 System of coordinates

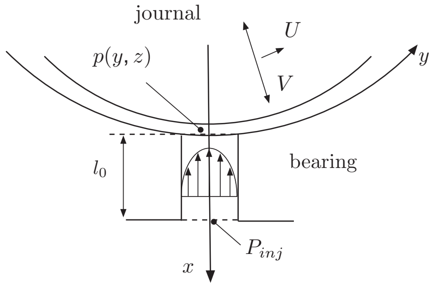

Fig. 3 Model of the injection flow

Equation (7) is known as Hagen–Poiseuille formula and formally applies to both incompressible and compressible fluids since it concerns only an infinitesimal length dx of the feeding pipe. Considering this dimension to be small, the change of density of the fluid within this distance can be neglected; this assumption allows a further simplification, by assuming the variation of injection pressure along the duct length (l_0, along the $-x$ direction) to be linear and proportional to the difference between supply and journal pressures

$$\frac{\partial p}{\partial x} = \frac{P_{\text{inj}} - p(y,z,t)}{l_0} \tag{8}$$

The injection velocity is zero outside the orifice region. Note that if the length of the injection feeding ducts is considerable, the flow density changes as the pressure changes, so that, although the mass flow rate is constant, the volumetric flow Q is not and the compressibility effect ought to be taken into consideration. Note that care should be taken when choosing the simulation parameters, in order to satisfy the laminar flow assumption ($\text{Re} = \rho Q d_o / \mu A_o < 2300$ [**11**]). In general, larger orifice diameters and higher flow velocities result in turbulent flow. As an example, a pressure difference of $\Delta p = 5\,atm$ and $d_o = 0.1$ mm result in $\text{Re} = 453$–therefore laminar flow–but increasing the size ten times would cause turbulence. Nevertheless, the assumption of laminar flow is taken as it provides a very simple mathematical model for the introduction of the injection terms, and it allows a direct numerical approach. In practice, if the flow is not laminar, the effect can be dealt with mathematically by modifying the parabolic form function of the injection term. Further CFD analysis investigating the matter and providing new form functions for transition and turbulent flow is currently underway [**12**].

Modified Reynold's equation. Introducing the velocity profiles of equation (6), upon the inclusion of equation (7), into the general form of the continuity equation

$$\int_0^h \left[\frac{\partial \rho}{\partial t} + \frac{\partial}{\partial x}(\rho u) + \frac{\partial}{\partial y}(\rho v) + \frac{\partial}{\partial z}(\rho w)\right] \mathrm{d}x = 0 \tag{9}$$

After the integration of equation (9), the velocity profiles become coupled, meaning that the lubricating film is continuous.

The pressure distribution p in a hybrid aerostatic–gas journal bearing working in near-isothermal conditions is governed by the modified general form of the Reynold's equation

$$\begin{aligned} &\frac{\partial}{\partial y}\left(ph^3 \frac{\partial p}{\partial y}\right) + \frac{\partial}{\partial z}\left(ph^3 \frac{\partial p}{\partial z}\right) - \frac{3}{l_0}\sum_{i=1}^{s} F_i p^2 \\ &\quad = 6\mu U \frac{\partial (ph)}{\partial y} + 12\mu \frac{\partial (ph)}{\partial t} - \frac{3}{l_0}\sum_{i=1}^{s} F_i P_{\text{inj}} p \end{aligned} \tag{10}$$

where $\mathcal{F}_i$ is a form function taking into account the injection flow profile and the position of the orifices

$$F_i(y,z) = \begin{cases} \dfrac{d_0^2}{4} - (y - y_i)^2 - (z - z_i)^2 \\ (y - y_i)^2 - (z - z_i)^2 \leqslant \dfrac{d_0^2}{4} \\ 0, (y - y_i)^2 - (z - z_i)^2 \geqslant \dfrac{d_0^2}{4} \end{cases} \tag{11}$$

Equation (10) is a non-linear parabolic equation for the pressure, where (y, z) are the circumferential and axial coordinates on the plane of the bearing. The boundary conditions for equation (10) impose that the pressure at the bearing sides equals the atmospheric pressure p_{atm} and the pressure is continuous and periodic in the circumferential direction.

Addressing the temperature issue, it should be noticed that in actuality, the operating characteristics for a slider bearing fall somewhere between the isothermal and adiabatic limits, depending on the conductivity of the bearing material and degree of insulation. For most practical situations, the flow will be nearly isothermal because of the relatively high conductivity of the bearing material [**3**].

Film thickness. The location of the minimum film thickness is defined by the attitude angle Φ (Fig. 4). The film thickness function $h = h(y, t)$ depends on the position of the centre of the shaft according to

$$h = C + e_X \cos\Theta + e_Y \sin\Theta \tag{12}$$

where $C = R_b - R_j$ is the radial clearance of the bearing and $\Theta = \theta + \Phi$.

Perturbation equations. Expressions for the static and dynamic pressure equations are derived with a perturbation method, as introduced by Lund and Thomsen [**13**]. The general motion of the rotor at frequency (ω) with small amplitude harmonic motion (Δe_X, Δe_Y) around an equilibrium position (e_{X_0}, e_{Y_0})

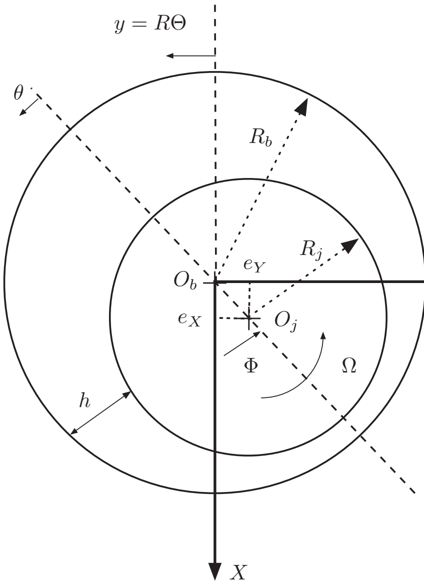

Fig. 4 Journal bearing schematic

leads to the following perturbation expression for the film thickness function and pressure field

$$h = C + e_{X_0}\cos\Theta + e_{Y_0}\sin\Theta + (\Delta e_X\cos\Theta + \Delta e_Y\sin\Theta)e^{i\omega t} \tag{13}$$

$$p = p_0 + \left(\Delta e_X p_X + \Delta e_Y p_Y\right)e^{i\omega t} \tag{14}$$

Equations (13) and (14) can be inserted into equation (10), yielding (neglecting higher order terms) the zeroth- and first- order lubrication equations

Zeroth order

$$\frac{\partial}{\partial y}\left(p_0 h_0^3\frac{\partial p_0}{\partial y}\right) + \frac{\partial}{\partial z}\left(p_0 h_0^3\frac{\partial p_0}{\partial z}\right) - \frac{3}{l_0}\sum_{i=1}^{s}F_i p_0^2 = 6\mu U\frac{\partial(p_0 h_0)}{\partial y} - \frac{3}{l_0}\sum_{i=1}^{s}F_i p_0 P_{\text{inj}} \tag{15}$$

First order

$$\begin{aligned} X : &\frac{\partial}{\partial y}\left(p_0 h_0^3\frac{\partial p_X}{\partial y} + p_X h_0^3\frac{\partial p_0}{\partial y}\right) \\ &+ \frac{\partial}{\partial z}\left(p_0 h_0^3\frac{\partial p_X}{\partial z} + p_X h_0^3\frac{\partial p_0}{\partial z}\right) - 6\mu U\frac{\partial}{\partial y}(p_X h_0) \\ &- 12\mu i\omega(h_0 p_X) - \frac{3}{l_0}\sum_{i=1}^{s}2F_i p_0 p_X \\ = &-\frac{\partial}{\partial y}\left(3p_0 h_0^2\frac{\partial p_0}{\partial y}\cos\Theta\right) - \frac{\partial}{\partial z}\left(3p_0 h_0^2\frac{\partial p_0}{\partial z}\cos\Theta\right) \\ &+ 6\mu U\frac{\partial}{\partial y}(p_0\cos\Theta) + 12\mu i\omega(p_0\cos\Theta) \\ &- \frac{3}{l_0}\sum_{i=1}^{s}F_i p_X P_{\text{inj}} \end{aligned} \tag{16}$$

$$\begin{aligned} Y : &\frac{\partial}{\partial y}\left(p_0 h_0^3\frac{\partial p_Y}{\partial y} + p_Y h_0^3\frac{\partial p_0}{\partial y}\right) \\ &+ \frac{\partial}{\partial z}\left(p_0 h_0^3\frac{\partial p_Y}{\partial z} + p_Y h_0^3\frac{\partial p_0}{\partial z}\right) - 6\mu U\frac{\partial}{\partial y}(p_Y h_0) \\ &- 12\mu i\omega(h_0 p_Y) - \frac{3}{l_0}\sum_{i=1}^{s}2F_i p_0 p_Y \\ &= -\frac{\partial}{\partial y}\left(3p_0 h_0^2\frac{\partial p_0}{\partial y}\sin\Theta\right) - \frac{\partial}{\partial z}\left(3p_0 h_0^2\frac{\partial p_0}{\partial z}\sin\Theta\right) \\ &+ 6\mu U\frac{\partial}{\partial y}(p_0\sin\Theta) + 12\mu i\omega(p_0\sin\Theta) \\ &- \frac{3}{l_0}\sum_{i=1}^{s}F_i p_Y P_{inj} \end{aligned} \tag{17}$$

Zeroth-order equation. For given operating conditions $U = \Omega R_j$ and eccentricity, the zeroth-order equation is a non-linear partial differential equation, which is solved using a finite difference approximation on a non-uniformly discretized domain of dimensions $m \times n$ in the y and z coordinates, respectively. The discretization is refined around the orifices. The resulting algebraic system is also non-linear in p_0; therefore, the solution is achieved by means of a recursive scheme. Once a solution is found, the zeroth-order pressure field is integrated over the bearing surface, which in turn imposes vertical and horizontal lubrication reaction forces

$$\begin{aligned} F_X^{\text{gas}} &= \int_0^L\int_0^{2\pi}(p_0 - p_{\text{atm}})\cos\Theta R d\Theta \mathrm{d}z \\ F_Y^{\text{gas}} &= \int_0^L\int_0^{2\pi}(p_0 - p_{\text{atm}})\sin\Theta R d\Theta \mathrm{d}z \end{aligned} \tag{18}$$

First order equations. The solution of the first-order perturbation equations for the perturbed pressures (p_X, p_Y) is straightforward, as these are linear PDEs. Given a zeroth order field p_0, they are solved *via* a finite difference scheme and subsequently integrated over the bearing surface to determine the stiffness and damping coefficients

$$K + i\omega D = \int_0^L\int_0^{2\pi}\begin{bmatrix} p_X\cos\Theta & p_X\sin\Theta \\ p_Y\cos\Theta & p_Y\sin\Theta \end{bmatrix} R d\Theta dz \tag{19}$$

It is important to notice that the dynamic coefficients are dependent on the excitation frequency and that the model assumes small amplitude of perturbations [**4**,**14**].

2.4 Assembly of the global matrices

To form the global equations of motion, the superposition principle can be used since the model is considered linear. The shaft discretization is coupled with the discs and bearings by means of placing nodes at the points where these are mounted on the shaft. The global equation of motion takes the form

$$M^g \ddot{q}^g + D^g \dot{q}^g + K^g q^g = Q^g \tag{20}$$

which is achieved by choosing the global damping matrix to be $D^g = -\Omega G^{e,d} + D^b_e$. To solve this system with regards to the natural frequencies and mode shapes, it is rearranged into a first-order system. This is done by introducing $z = [q^g, \dot{q}^g]$

$$\underbrace{\begin{bmatrix} M & 0 \\ 0 & M \end{bmatrix}}_{M_{\text{glob}}} \underbrace{\begin{bmatrix} \dot{q} \\ \ddot{q} \end{bmatrix}}_{\dot{z}} + \underbrace{\begin{bmatrix} K & G \\ -M & 0 \end{bmatrix}}_{K_{\text{glob}}} \underbrace{\begin{bmatrix} q \\ \dot{q} \end{bmatrix}}_{\dot{z}} = \underbrace{\begin{bmatrix} Q \\ 0 \end{bmatrix}}_{\tilde{Q}} \tag{21}$$

This can be rewritten in a simple matrix notation, from which it is possible to state a general eigenvalue problem

$$M_{\text{glob}} \dot{z} + K_{\text{glob}} z = \tilde{Q} \tag{22}$$

The state space system can be set up in a number of different ways, and here it has been set up to make the $\mathbf{M}_{\text{glob}}$ matrix diagonal banded.

3 NUMERICAL ANALYSIS AND DISCUSSION

For a given position of the journal (e_X, e_Y), the Reynolds equation can be solved for the pressure, which in turn imposes vertical and horizontal lubrication forces on the shaft equation (18). For the system to be in equilibrium, the total moment around the pivoting point (ball bearing) generated by bearing forces must equilibrate the one resulting from the total weight of the shaft-disc subsystem. This leads to a non-linear system of equations that can be solved by a Newton–Rhapson scheme with the Jacobian calculated *via* finite differences.

A summary of the mass and geometric properties of the various system components is given in Tables 1 and 2.

The pressure distribution at equilibrium position for the bearing operating in passive mode (without orifices, thus reducing the solution to an ordinary aerodynamic journal bearing) is obtained by solving equation(15). The results are presented in Fig. 5(a) and will be used as a benchmark for comparison with the bearing operating in hybrid mode. Note that, since no orifice has to be modelled, $\mathcal{F}_i(y, z) = 0$ over the whole domain; thus, a uniform discretization mesh is employed.

Table 1 Summary of bearing properties

Diameter, D	40 mm
Length, L	40 mm
Clearance, C	10 μ m
Viscosity, μ	18.36e-6 Pa s

3.1 Hybrid-bearing parameters configurations

In order to study the influence of different injection parameters on the dynamic performance of the bearing, different configurations have been analysed. The attention has been focused on the following.

1. *Injection pressure*: Values between P_{inj} 1 and 7 atm have been considered. Note that an injection pressure of 1 atm corresponds to a practical situation in which the injection system is malfunctioning and the pressure on the reservoir is at ambient value. At 7 atm, it is ensured that the injection pressure is above the aerodynamic one.
2. *Orifice diameter*: Values between d_0 0.1 and 1 mm have been considered. For a qualitative drawing, see Fig. 6(a).
3. *Number of orifices in the circumferential direction*: Between 4 and 8, equally spaced orifices are considered in this direction. Note that $y = 0$ corresponds to an orifice location in all cases (see Fig. 6(b)).
4. *Number of orifices in the axial direction*: 1 or 2 rows are considered. For single-row configuration, the orifices are located at the axial midplane of the bearing; for the double-row, the rows are equally spaced along the axis and located at $z = \frac{1}{3}L$ and $z = \frac{2}{3}L$ (Fig. 6(c)).

For the hybrid bearing case, a non-uniform grid is used, with gradual variations of step size meshing refining around the orifices areas. This is an important factor to take into consideration, as sudden changes of meshing can introduce significant numerical errors.

Figure 5(b) presents the pressure distribution in the bearing considering the air being injected through the orifices at atmospheric pressure, simulating the case of injection system failure. The configuration is of eight orifices in the circumferential direction on a single row in the axial direction. It is evident how the aerodynamic pressure is affected around

Table 2 Summary of shaft properties

L_{tot}	500 mm
L_{BB-HB}	317 mm
$L_{BB-Disc}$	430 mm
Density, ρ^e	7800 kg/m^3
El. modulus, E	1.8e11 Pa
Shaft mass, m^e	2.55 kg
Total mass, m^e_{tot}	3.53 kg
Disc mass, m_{Disc}	8 kg
Total mass, of rotor-bearing system	11.53 kg

orifice areas. Although the pressure sees a moderate increase in the divergent zone (sub ambient pressures), the convergent zone is characterized by a marked decrease, especially in the highest pressure area. As a result, the carrying capacity of the bearing is reduced.

When the injection pressure is increased to 5 atm (Fig. 5(c)), the mean and maximum pressure becomes higher and the forces on the journal increase accordingly, allowing a greater carrying capacity. Note that the number of orifices in the circumferential direction is in this case reduced to 4, whereas a single axial row is kept similarly to the previous case. The pressure increase is clearly driven by the radial air injection, with injection pressures well above those generated by the aerodynamic effect.

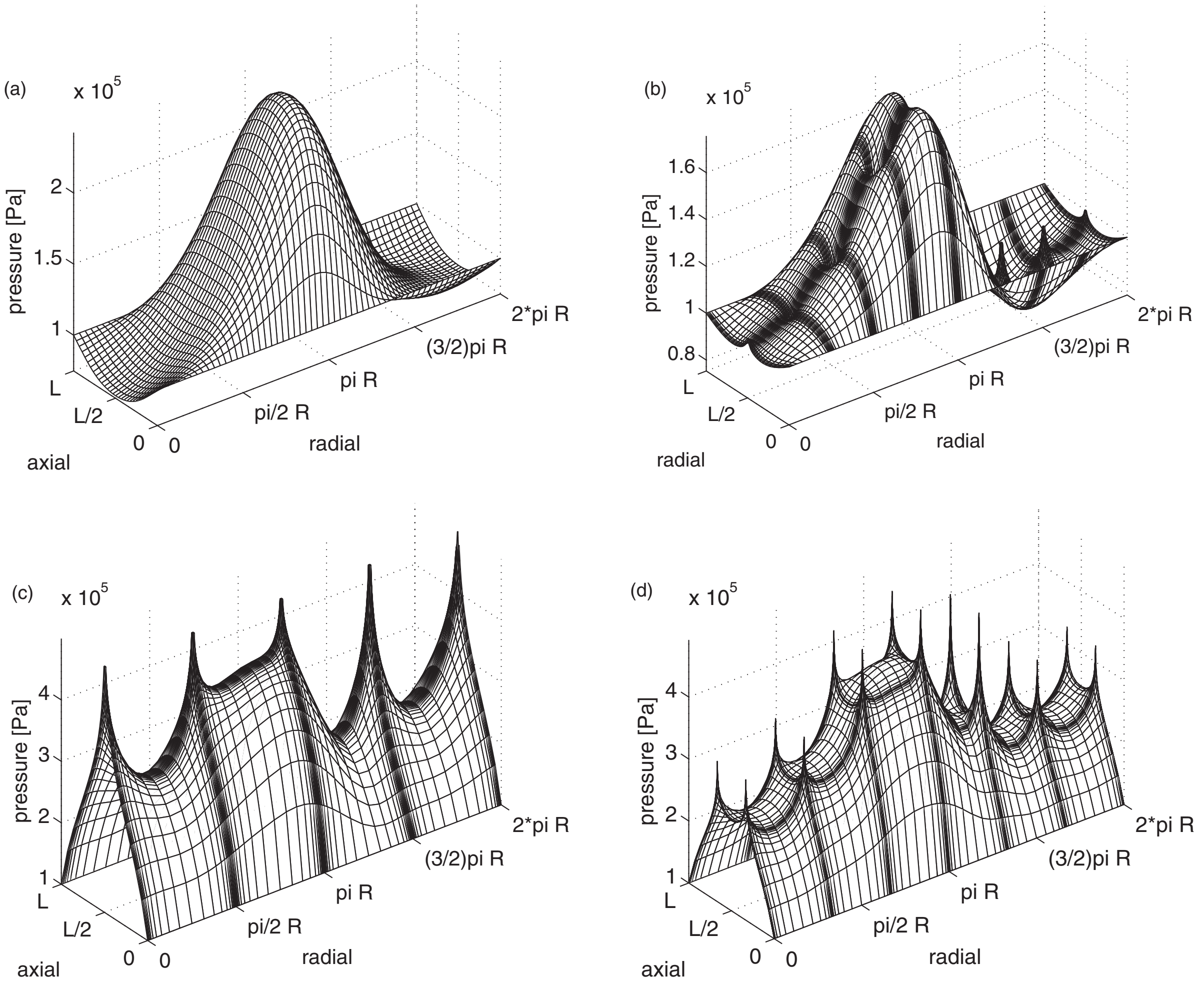

Fig. 5 Examples of pressure distributions for the aerodynamic and hybrid bearing. (a) Pressure distribution, aerodynamic bearing. Ω = 30 000 rpm. (b) Pressure distribution, hybrid bearing. Ω = 10 000 rpm. P_{inj}=1 atm. Configuration: 8x1 d_{OR}=1 mm. (c) Pressure distribution, hybrid bearing. Ω = 20 000 rpm. P_{inj}=5 atm. Configuration: 4x1d_{OR} = 1mm. (d) Pressure distribution, hybrid bearing. Ω=20 000 rpm. P_{inj}=5 atm. configuration: 6x2d_{OR} = 0.1 mm

Fig. 6 Hybrid-bearing parameters configurations. (a) Hybrid-bearing parameters: orifice diameter. (b) Hybrid-bearing parameters: orifices in circumferential direction. (c) Hybrid-bearing parameters: orifices in circumferential direction

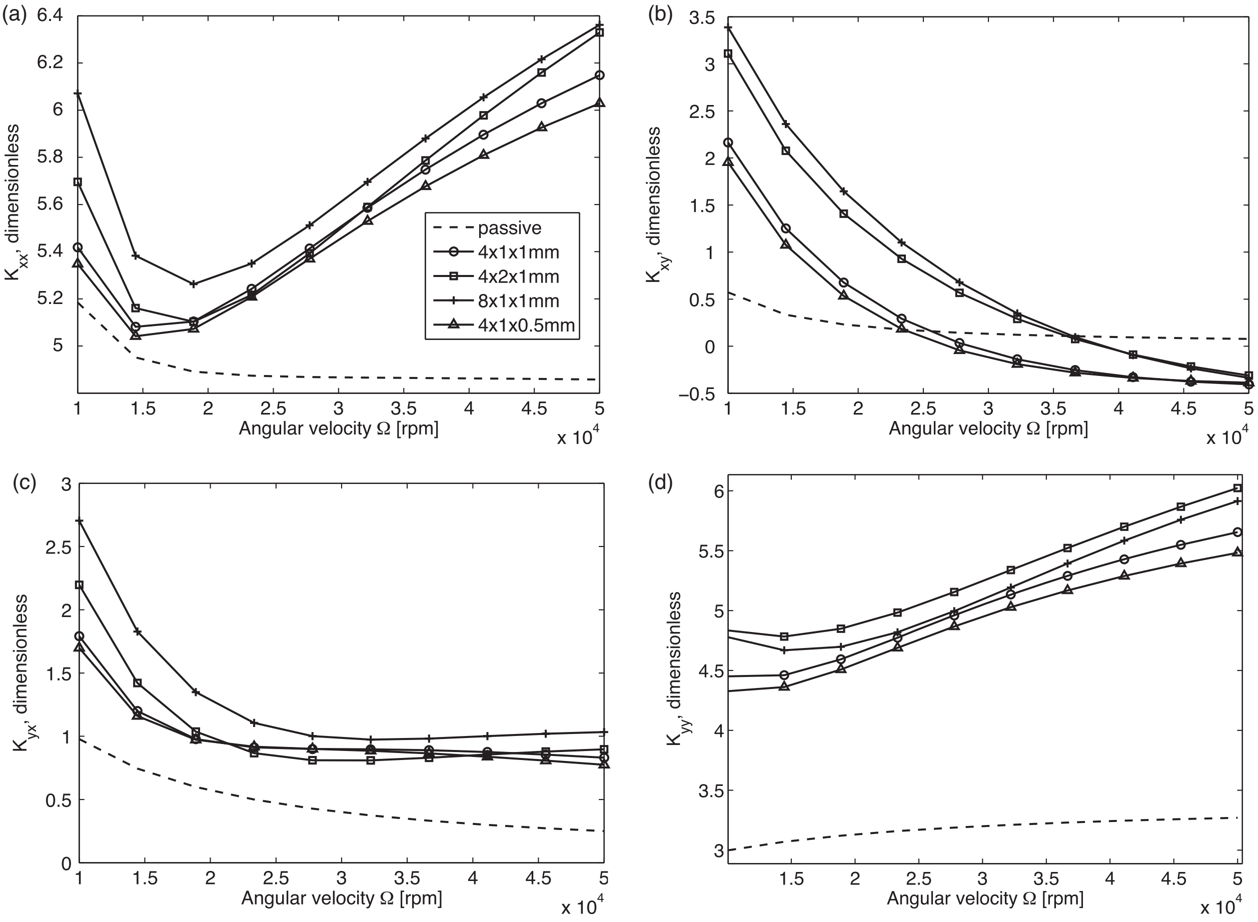

Fig. 7 Examples of stiffness coefficients for the aerodynamic and hybrid bearing. (a) Direct stiffness coefficient, K_{XX}. $P_{\text{inj}} = 5$ atm. (b) Cross-coupled stiffness coefficient, K_{XY}. $P_{\text{inj}} = 5$ atm. (c) Cross-coupled stiffness coefficient, K_{YX}. $P_{\text{inj}} = 5$ atm. (d) Direct stiffness coefficient, K_{YY}. $P_{\text{inj}} = 5$ atm

It is important to ensure that, for a given set of operational parameters, the injection pressure should be higher than the corresponding aerodynamic pressure in order to avoid back-flow, which would compromise the performance of the bearing. Figure 5(d) shows the pressure distribution for a double axial row of orifices, with a diameter decreased to $d_{OR} = 0.1$ mm. The injection pressure is the same as in the previous cases, at $P_{\text{inj}} = 5$ atm. Note, however, that only in the highest pressure zone, the injection pressure reaches the prescribed 5 atm, whereas is lower for the orifices located in the other positions. This behaviour is due to the decreased injected mass flow rate due to smaller orifice diameter, which in high radial clearance areas is not sufficient to keep the pressure at the P_{inj} value. At this point, it should be emphasized that the hybrid bearing is designed to offer contact-free support in static conditions and during start-up or shut-down. Acting on the injection pressure, it is possible to aerostatically lift the rotor, providing an injection pressure sufficiently high.

The dynamic characteristic of the rotating machine when the hybrid bearing is used can be considerably affected. These parameters may be directly used in different rotor-dynamics calculations like unbalance response, random vibrations response, critical speeds, and rotor stability [**15–18**].

3.2 Dynamic coefficients

In order to study the influence of the design parameters on the dynamic performance of the hybrid bearing, at first the dynamic coefficients–stiffness and damping–have been calculated and compared to the aerodynamic case. Figures 7 and 8 present examples of stiffness and damping coefficients as function of rotational speed, for different design parameters. As a benchmark, the aerodynamic (passive) dynamic

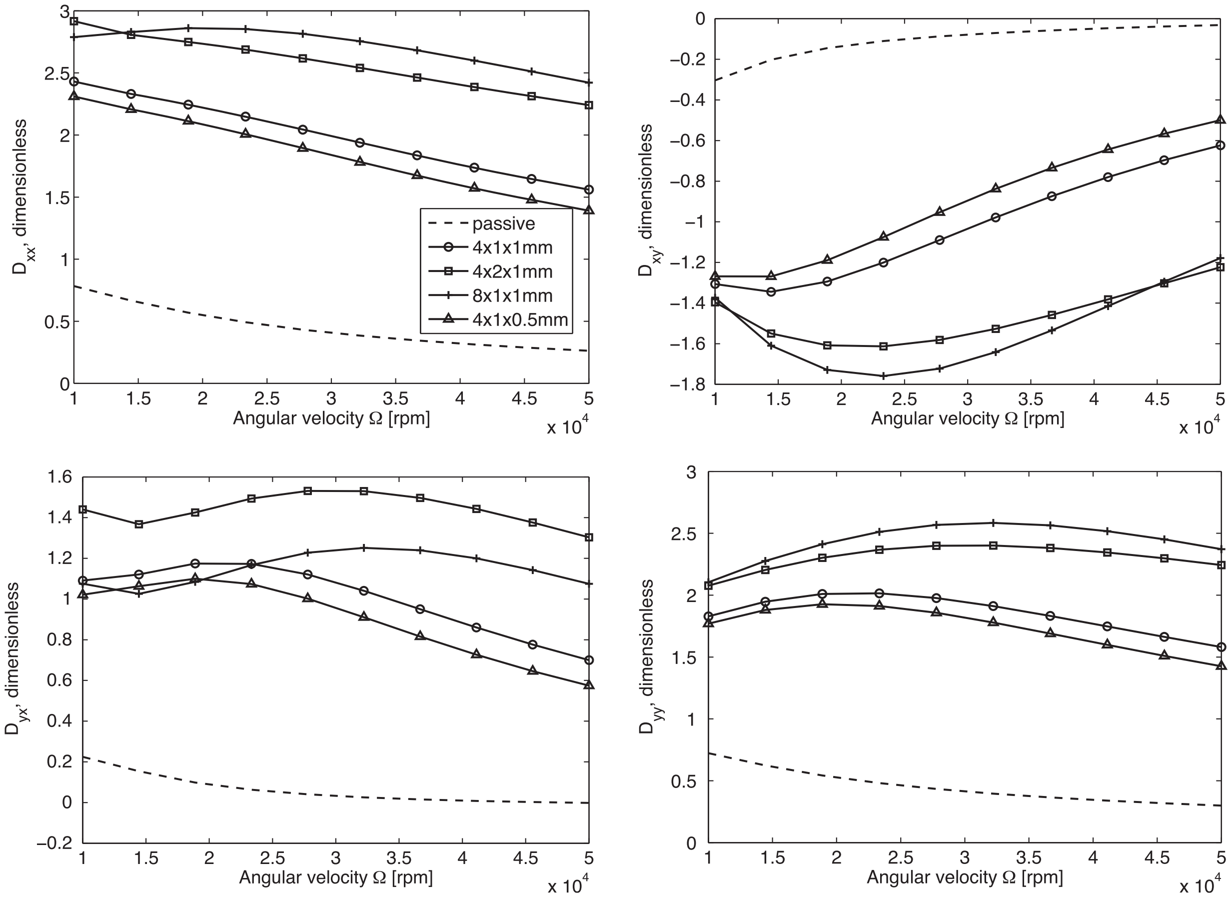

Fig. 8 Examples of damping coefficients for the aerodynamic and hybrid bearing. (a) Direct damping coefficient, D_{XX}. $P_{\text{inj}} = 5$ atm. (b) Cross-coupled damping coefficient, D_{XY}. $P_{\text{inj}} = 5$ atm. (c) Cross-coupled damping coefficient, D_{YX}. $P_{\text{inj}} = 5$ atm. (d) Direct damping coefficient, D_{YY}. $P_{\text{inj}} = 5$ atm

characteristic has been plotted. The following configurations have been analysed.

1. Marker ○ refers to a configuration of four orifices in the circumferential direction arranged in a single axial row. The orifice diameter is $d_{OR}=$ 1 mm.
2. Marker □ refers to a configuration of four orifices in the circumferential direction arranged in a double axial row. The orifice diameter is $d_{OR}=$ 1 mm.
3. Marker △ refers to a configuration of eight orifices in the circumferential direction arranged in a single axial row. The orifice diameter is $d_{OR}=$ 1 mm.
4. Marker + refers to a configuration of four orifices in the circumferential direction arranged in a single axial row. The orifice diameter is $d_{OR}=$ 0.5 mm.

The general behaviour of the direct stiffness coefficients is readily identifiable; an increase of their absolute values can be seen as the aerostatic terms are added. In particular, the configurations □ and + are those that yield the greatest contribution. This can be explained arguing that in these cases, the injection flow rate is higher. In general, higher direct stiffness terms give a positive contribution to the dynamic behaviour of the system. Looking at the cross-coupled stiffness terms, one observes a similar trend with respect to the injection parameters influence, but this time the coefficients tend to assume an asymmetric behaviour. One should consider that asymmetry in cross-coupled dynamic coefficients is generally undesirable. As for the damping coefficients, similar considerations can be made. Increasing direct coefficients are observed at higher injection flow rates. The cross-coupled coefficients exhibit a larger skew-symmetric behaviour.

3.3 Critical speeds and stability analysis

As a reference, the Campbell diagram relative to the rotor-bearing system in which the bearing operates in

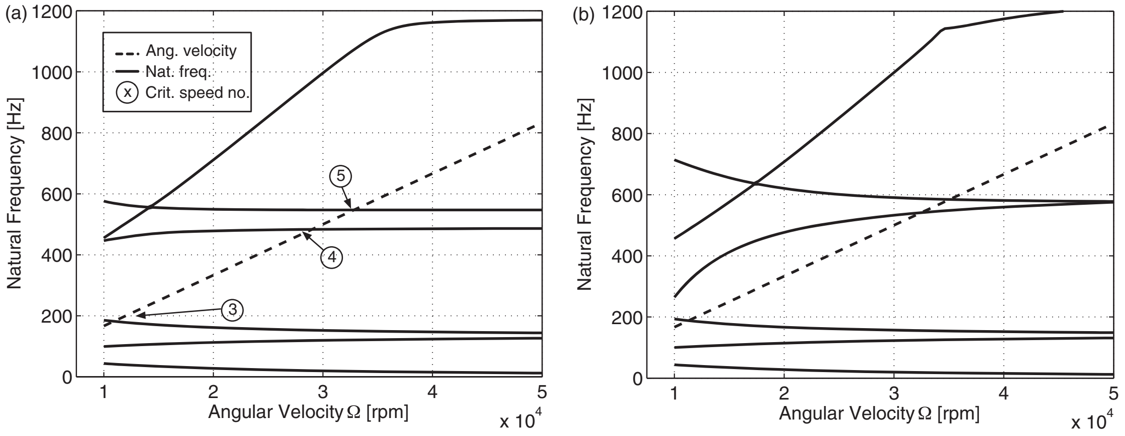

Fig. 9 Examples of Campbell diagrams for the aerodynamic and hybrid bearing. (a) Campbell diagram, passive mode. (b) Campbell diagram, hybrid mode P_{inj} = 5 atm. Configuration: 4x1, d_{OR} = 1 mm

passive mode (aerodynamic only) is presented in Fig. 9(a). In rotordynamics analysis, Campbell diagram plots are often used to characterize the response of the system as a function of the rotational speed [**19**]. In such systems, eigenfrequencies generally vary with speed due to gyroscopic effects and variable dynamic coefficients. The simulation shows the machine having an utile operational range between the third critical speed at 10 850 rpm and the fourth at 28 950 rpm. Note that the modal interaction appears as veering regions in which different natural frequencies come close to each other, but the corresponding modes keep their orthogonality. In practice no crossing occurs, but as they approach each other, they veer the other's frequency path. A direct comparison of the influence of the hybrid injection on the critical speeds of the system is directly made by observing Fig. 9(b). The configuration in this case is of four orifices in the circumferential direction arranged in a single row, with diameter $d_{OR} = 1$ mm. The injection pressure is $P_{\text{inj}} = 5$ atm. In general, the three lowest critical speeds appear to be rather unaffected, while the largest deviations are observed in those above. What is interesting to observe is that the useful operational range has now increased by about 10%, see also Fig. 10. In order to verify whether this behaviour can be consistently observed for other orifice configurations and for different injection pressure, further analysis has been performed, where values of the third, fourth and fifth critical speeds are analysed as function of the variation of various operational parameters. The results of such analysis are summarized in Fig. 10. Figure 10(a) analyses the influence of the injection pressure P_{inj}. The fixed parameters are the configurations of four orifices in circumferential direction–either single or double axial rows–and orifice diameter $d_{OR} = 1$ mm. Note that zero injection pressure corresponds to the bearing working in passive mode ($*$, $\bigcirc$, $+$; Fig. 9(a)). The third critical speed seems to be quite unaffected by the external injection and negligible differences are appreciated either for increasing injection pressures or number of axial rows of orifices. This suggests this frequency being a nodal mode for the bearing. The fifth critical speed sees a constant increment across the P_{inj} range, with the double row configuration with slightly higher values. What is interesting to observe, however, is the behaviour of the fourth critical speed, which, after an initial increase, approaches near stationary values for the single row configuration and decreases for the double row. This might be assumed as a somehow unexpected result, since the direct dynamic coefficients are higher for double row configurations; however, it is true that the cross-coupled ones also grow, accentuating the asymmetry of the stiffness matrix. That the cross-coupled coefficients are responsible of this behaviour, is confirmed by looking at Fig. 10(b), which is obtained by varying the number of orifice in circumferential direction and fixing the injection pressure and orifice diameter. What is interesting to read in this graphic is again the behaviour of the fourth critical speed, which decreases in both the single and double axial row configurations, when the number of orifices is increased. This decrease is consistent with the assumptions made, as looking at Figs 7 and 8, one observes that the eight orifice and double row configurations are the ones that show the worst possible configuration of the off-diagonal dynamic coefficients. Finally, the influence of orifice diameter is analysed while keeping the other

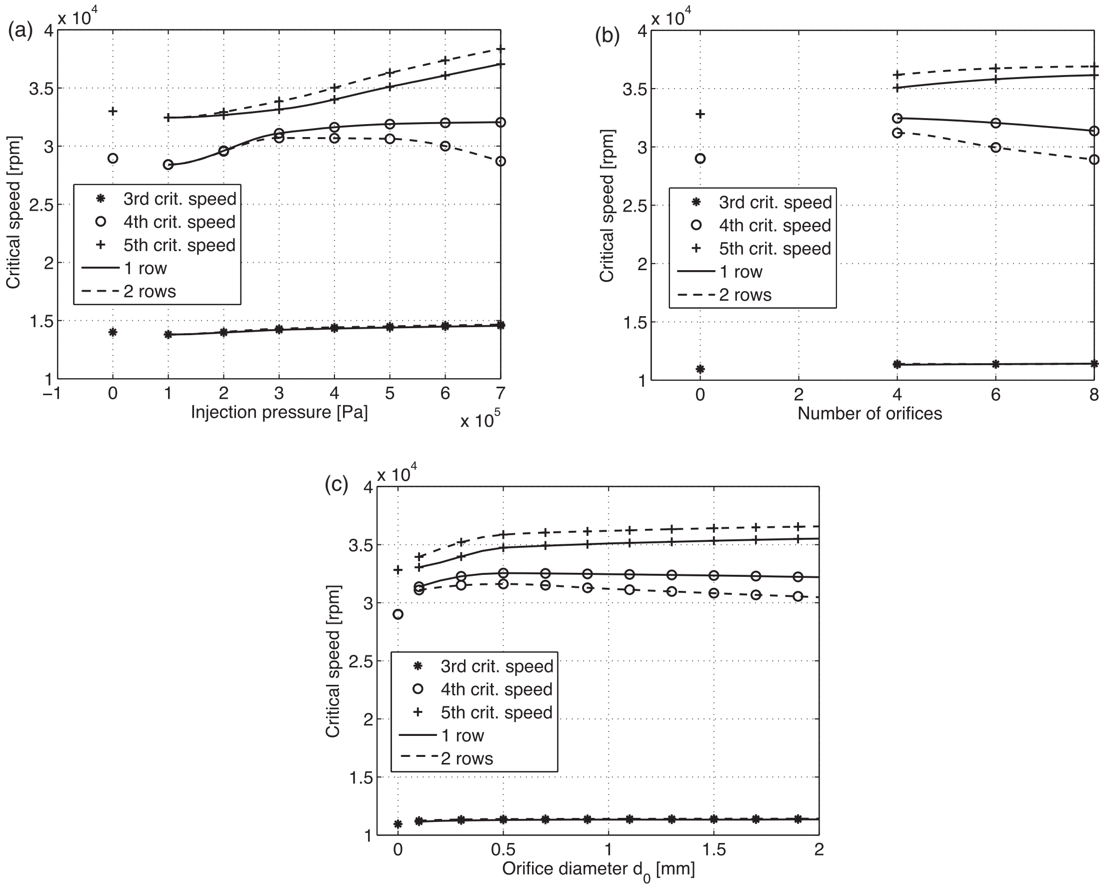

Fig. 10 Examples of operational range variations as function of various operational parameters. (a) Operational range, hybrid mode. Variable P_{inj}. Configuration: 4x1/2 rows, d_0 = 1 mm. (b) Operational range, hybrid mode. Variable number of orifices in radial direction, 1 and 2 axial rows, d_{OR} = 1 mm, P_{inj} = 5 atm. (c) Operational range, hybrid mode. Variable d_0. configuration: 4x1/2 rows, P_{inj} = 5 atm

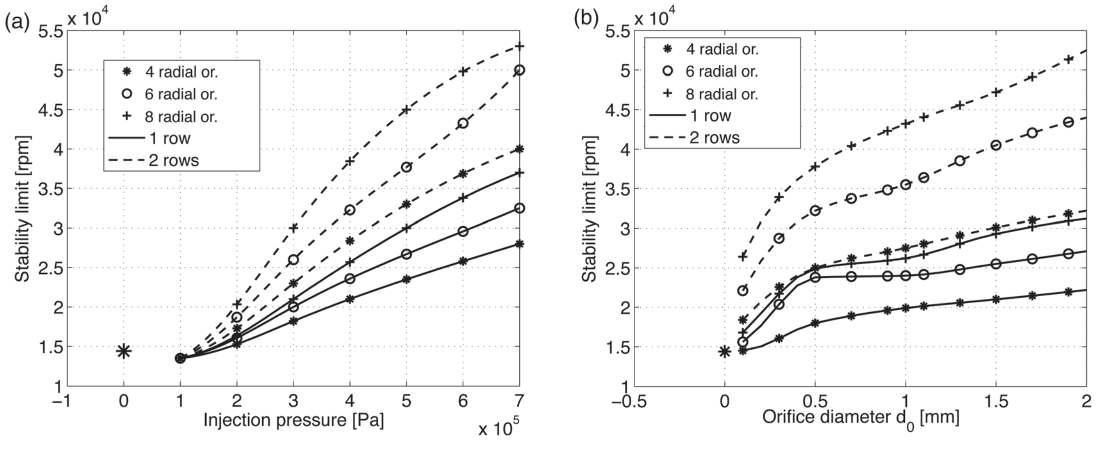

Fig. 11 Examples of stability limit variations as function of various operational parameters. (a) Stability limit, hybrid mode. Variable P_{inj}. configuration: 4/6/8x1/2 rows, d_0 = 1 mm. (b) Stability limit, hybrid mode. Variable d_0. congiguration 4/6/8x1/2 rows. P_{inj} = 5 atm

parameters constant (Fig. 10(c)). Again, the useful operational range between the third and fourth critical speeds is characterized by shrinking trend, as the orifice size is increased. Evident is also the influence of the number of orifices in the axial direction: the gap between the fourth and fifth critical speed is wider for the two row configuration; however, it does not widen much throughout the analysis domain.

The influence on the dynamic characteristic of the rotor-bearing system of the hybrid lubrication becomes even more evident when analysing the stability limit as function of the air injection parameters (see Fig. 11). The stability limit is hereby defined as the minimum rotational speed at which the real part of any of the eigenvalues of the system becomes positive. In Fig. 11(a), the analysis focuses on variable injection pressure with 4, 6, or 8 circumferential orifice configurations, either single or double row. Similarly to the critical speed analysis, zero injection pressure corresponds to the sole aerodynamic mode (∗). At lower injection pressure, one observes an initial decrease of the margin. This is probably due to the fact that in this injection pressure range, the aerodynamic pressure is lowered by the aerostatic contribution (which is lower; Fig. 5(b)). As the pressure is increased, a different general behaviour is however observed in comparison to the Campbell diagrams. Here, increasing the pressure results in an increment of the stability limit, no matter which particular parameter configuration is analysed. Also, increasing the number of orifice produces better results over the whole injection pressure range. Increasing the number of orifices either in circumferential or radial direction produces an improvement of the stability threshold. The influence of the orifice diameter is somehow different (Fig. 11(b)). Initially, the limit sees an increase, which is sharper for higher number of orifices in circumferential direction. Above $d_0 = 0.5\,\text{mm}$, the variation is less pronounced and a further increase of the orifice size does not translate into a significant improvement of the stability limit–particularly for the single axial row cases. From a stability limit point of view then, configurations with a double axial row seem to be preferable over the single row, whereas the opposite can be observed regarding critical speed analysis.

4 CONCLUSION

This article presents a detailed analytical model for the characterization of a hybrid aerostatic–gas journal bearing. The development of the compressible form of the modified Reynolds equation for hybrid lubrication is presented. Numerical simulations of different configurations of evenly distributed orifices on the bearing surface show how values of injection pressure can in some situations determine a reduction of the journal pressure and a decrease of the load-carrying capacity. When operating in hybrid aerostatic/aerodynamic mode, it is important to ensure that the aerostatic pressure is higher than the aerodynamic one. Enhancing the injection pressure contribution can also increase the lubrication forces during start-up and shut-down conditions and/or during normal operation. The external injection parameters can significantly influence the lateral dynamic response of the rotating machine. The variation of the critical speeds shows that it is possible to widen the operational speed range by increasing the aerostatic contribution. However, an optimum value of the injection pressure, orifice diameter, and orifice distribution can be identified as function of different parameters. By acting on these parameters, it is also possible to enhance the stability limit of the machine. In light of these considerations, one can optimize the performance of the machine for the design operation parameters, but it may be also possible to design a hybrid bearing which offers acceptable dynamic characteristics if the injection mechanism fails (soft failure design).

ACKNOWLEDGEMENT

The authors would like to thank Lloyds Register ODS for the financial support of the project.

REFERENCES

1 **Hamrock, B. J.** *Fundamentals in fluid film lubrication*, 1994 (McGraw-Hill, New york).
2 **Constantinescu, N. V.** *Sliding bearings ('Lagare cu alunecare',* editura technica, translated from the Romanian), 1985 (Allerton Press).
3 **Hughes, W. F.** and **Osterle, J. F.** On the adiabatic Couette flow of a compressible fluid. *Zeitschrift für Angewandte Mathematik und Physik (ZAMP)*, 1957, **8**(2), 89–96.
4 **Santos, I. F., Scalabrin, A.,** and **Nicoletti, R.** Ein beitrag zur aktiven schmierungstheorie. In *Scwingungen in rotierenden maschinen* (Eds R. Irretier, H. Nordmann, and H. Springer), 2001, vol. 5, pp. 21–30 (Viewing Verlag, Braunschweig).
5 **Lund, J. W.** and **Thomsen, K. K.** Calculation method and data for the dynamic coefficients of oil-lubricated journal bearings. In *Topics in fluid film bearing and rotor bearing system design and optimization*, 1978, pp. 1–28 (ASME).
6 **San Andres, L.** and **Faria, M. T. C.** On the numerical modeling of high-speed hydrodynamic gas bearings. *J. Tribol, Trans. ASME*, 2000, **122**, 124–130.

7 **San Andres, L.** and **Kim, T. H.** Heavily loaded gas foil bearings: a model anchored to test data. *J. Eng. Gas Turbines Pwr*, 2008, **130**, 012504–1-012504-8.

8 **Cook, R. D., Malkus, D. S., Plesha, M. E.,** and **Witt, R. J.** *Concepts and applications of finite element analysis*, fourth edition, 2002 (John Wiley and Sons, New York).

9 **Nelson, H. D.** and **McVaugh, J. M.** The Dynamics of rotor-bearing systems using finite elements. *J. Eng. Industry, Trans. ASME*, 1976, **98**(2), 593–600.

10 **Brandlein, J., Eschmann, P.,** and **Hasbargen, L.** *Die Walzlagerpraxis,* 2002 (Vereinigte Fachverlage GmbH, Mainz).

11 **Fox, R. W.** and **McDonald, A. T.** *Introduction to fluid mechanics*, fourth edition, 1994 (Wiley).

12 **Horvat, S., Morosi, S., Braun, M. J.,** and **Santos, I. F.** *characterization and modeling of fluid injection profiles with focus on active fluid film lubrication*, 2010, internal report (Technical University of Denmark – The Univeristy of Akron).

13 **Lund, J. W.** and **Thomsen, K. K.** A Calculation method and data for the dynamic coefficients of oil-lubricated journal bearings. In *Topics in fluid film bearing and rotor bearing system design and optimization*, 1978, pp. 1–28 (ASME Publication, USA).

14 **Arghir, M., Le Lez, S.,** and **Frene, J.** Finite volume solution of the compressible reynolds equation: linear and non-linear analysis of gas bearings. *Proc. IMechE, Part J: J. Engineering Tribology*, 2006, **220**, 617–627.

15 **Lund, J. W.** and **Orcutt, F. K.** Calculations and experiments on the unbalance response of a flexible rotor. *J. Eng for Industry, Trans. ASME, Series B*, 1967, **89**(4), 785–796.

16 **Lund, J. W.** Calculation of stiffness and damping properties of gas bearings. *J. Lubrication Technology, Trans. ASME, Series F*, 1968, 793–803.

17 **Lund, J. W.** Stability and damped critical speeds of a flexible rotor in fluid-film bearings. *J. Engineering for Industry, Trans. ASME, Series B*, 1974, **96**(2), 509–517.

18 **Lund, J. W.** Linear transient response of a flexible rotor supported in gas-lubricated bearings. *J. Lubrication Technol., Trans. ASME, Series F*, 1976, **98**(1), 57–65.

19 **Campbell, W.** *Protection of steam turbine disk wheels from axial vibration*, 1924, pp. 31–160 (ASME).

Appendix G

J3: Active lubrication applied to radial gas journal bearings. Part I: modeling

Tribology International ▮ (▮▮▮▮) ▮▮▮–▮▮▮

Contents lists available at SciVerse ScienceDirect

Tribology International

journal homepage: www.elsevier.com/locate/triboint

Active lubrication applied to radial gas journal bearings. Part 1: Modeling

Stefano Morosi *, Ilmar F. Santos

Department of Mechanical Engineering, DTU—Technical University of Denmark, Nils Koppels Allé, 2800 Kgs. Lyngby, Denmark

ARTICLE INFO

Article history:
Received 10 May 2011
Received in revised form
4 August 2011
Accepted 9 August 2011

Keywords:
Fluid film bearings
Mechatronic system
Active lubrication
Active vibration control

ABSTRACT

Active bearings represent a mechatronic answer to the growing industrial need to high performance turbomachinery. The present contribution aims at demonstrate the feasibility of applying active lubrication to gas journal bearings. The principle of operation is to generate active forces by regulating radial injection of lubricant through the means of piezoelectric actuators mounted on the back of the bearing sleeves. A feedback law is used to couple the dynamic of a simplified rotor-bearing system with the pneumatic and dynamic characteristics of a piezoelectric actuated valve system. Selected examples show the considerable performance advantages of such new kind of bearing.

1. Introduction

Current research on rotating machinery is driven by an ever-growing demand for higher performance and greater availability. On the one hand, modern industrial needs, for example the API 617 specification, to push the performance boundaries to faster speed, lighter components, more efficiency. Increasing availability, on the other hand, means enhancing the flexibility of the machine to adapt to different operation conditions and environments, eliminate or minimize service intervals, extend their useful life. Such extreme needs demand not only very accurate design, optimization and manufacturing, but also continuous monitoring and control of vibration levels. Recent years have seen an increasing number of researchers to explore innovative and non-traditional solutions to address such needs and the relative arising issues. Passive solutions, such as squeeze film [1,2] and seal dampers [3], have been investigated as well as active ones. The use of "active" mechatronic elements, combining transducers, actuators and control systems, can serve multiple purposes, from calibration and self-diagnostic tasks, to the reductions of vibration levels, minimizing the effect of system unbalances and smoothening the operation during those critical operational phases, such as the crossing of critical speeds or when starting-up and coasting-down.

Several active elements have been proposed, many characterized by unique solution and working principles. Smart fluids have been successfully used in conjunction with dampers, like electro-rheological and magneto-rheological squeeze film dampers [4,7] and disk-type dampers [6,7]. However, active bearings – in different forms and configurations – have been by far the most investigated subject. On the one hand, active magnetic bearings [8] can be nowadays considered as an established technology, finding industrial applications in electric power generation, petroleum refining, machine tool operation and natural gas pipelines. On the other hand, active lubrication represents a more novel branch of research. Nevertheless, several authors have turned their attention to active lubrication problems, from variable impedance journal bearings [9] to electronically controlled radial oil injection into the bearing gap [10].

The first hydrodynamic journal bearing equipped with controllable radial oil injection was proposed almost two decades ago [11]. This kind of bearing operates by acting directly on the fluid film by radially injecting lubricant through orifices distributed on the bearing surface. Servovalves are used to modify the injection pressures, which in turn makes it possible to significantly influence the hydrodynamic forces [10].

Along with traditional oil lubrication, increasing demand for high speed application has renewed attention to gas bearings technology. Passive aerostatic and aerodynamic gas lubrication has been widely used in a variety of applications, ranging from high speed spindles to micro- and meso-scale turbomachinery. Aerostatic bearings have the advantage of offering excellent stiffness and start-up performance, however they suffer from inherent tendency to onset instability, known as pneumatic hammer. Aerodynamic bearings offer excellent high speed, limited friction, clean environment and low heat generation characteristic, but also a limited load carrying capacity and poor dynamic performance, particularly prone to the onset of subsynchronous

---

* Corresponding author.
E-mail addresses: smo@mek.dtu.dk (S. Morosi), ifs@mek.dtu.dk (I.F. Santos).

0301-679X/$ - see front matter © 2011 Elsevier Ltd. All rights reserved.
doi:10.1016/j.triboint.2011.08.007

Please cite this article as: Morosi S, Santos IF. Active lubrication applied to radial gas journal bearings. Part 1: Modeling. Tribol Int (2011), doi:10.1016/j.triboint.2011.08.007

whirling motions. Hybrid configurations aim at combining the advantages of either technologies, however they also inherit their instability related drawbacks.

In order to improve their performance, a number of solutions have been proposed. Among other, much research has been devoted to compliant foil bearings [12–14]. As they offer some improvements compared to conventional rigid sleeve bearings, with improved static and dynamic properties, they are objective of current research supported by many manufacturers. However, issues associated with high costs and lack of reliable analytical designing tools have for now limited their diffusion. Another solution is represented by tilting pad gas bearings. Their main advantage concerns the dynamic properties, as they lack of cross-coupling stiffness and damping coefficients which generally result in improved rotordynamic stability [15]. However, pivot wear and especially manufacturing tolerance stack-up are their drawback. A design improvement proposed to overcome such issues is represented by flexure pivot gas journal bearings [16,17], but the small bearing clearance in tilting pad gas bearings is still a technical challenge to overcome for their wide applications [18].

The first active gas journal bearing was introduced by Horikawa and Shimokohbe [19]. In their prototype four pads provide a contact free support to a rotating shaft. These pads are connected to the bearing housing through elastic hinges, in which space piezoelectric actuators are also fitted. Thus, measurements of the radial position of the shaft are sent to a control system which acts by sending a control signal to the actuators, which effectively work by modifying the fluid film thickness profile.

Mizumoto et al. [20] propose an active inherent restrictor design which can be retrofitted in conventional aerostatic bearings. The system is comprised of a set of piezoelectric actuators with through holes coupled to capacitance displacement sensors. The control system simply takes the measured input and a control feedback signal is calculated using a PI algorithm, which produces beneficial effects on static stiffness and vibration levels.

Qiu et al. [21] describe a tilting pad gas journal bearing, where each pad is supported by a pivot with an embedded piezoelectric actuator, which is used to adjust the radial clearance between shaft and pad. Experimental work is carried out to perform active control of the self-excited vibrations of a rotor-bearing system, making use of a PID controller. It is shown that – provided that the controller gains are accurately tuned – subsynchronous vibrations can be effectively suppressed, however synchronous vibration could not be addressed.

A hybrid flexure pivot gas bearing with controllable supply pressure is investigated by San Andres and Ryu [22]. Stemming from previous work on flexure pivot bearings, in which they demonstrate how external pressurization induces an increase in stiffness and decrease of damping coefficients, they develop a regulated supply pressure system with the aim of minimizing a rotor-bearing system response while passing its critical speeds. Their strategy is to employ electro-pneumatic air regulators combined with open and closed loop control rules in order to modify the supply pressure level in relation with the rotational speed of the machine. Theoretical and experimental coast down tests are in good agreement, and so in most situation the effectiveness of suppressing vibration levels.

Mizumoto et al. [23] propose a high speed aerodynamic bearing where the wedge angle on the aerodynamic bearing surface is controlled by piezoelectric actuators in order to generate aerodynamic damping force. Experimental findings show how the spindle vibrations at high rotational speed are suppressed.

The present contribution lays the theoretical and numerical background for the modeling of a compressible fluid journal bearing with active radial injection. In principle, the injection of air can be used to actively modify the pressure profile over the bearing, which in turn changes the thickness of the fluid film, thus creating an active force on the rotor that can be used to suppress vibrations of the rotor-bearing system. A modified form of the compressible Reynolds equation for hybrid gas journal bearings is proposed, coupled with the dynamic model of a piezoelectric injection system. One may argue about the necessity of the inclusion of piezoelectric controller dynamics; while piezoactuators are generally characterized by fast response times, such analysis makes sense when considering the high speeds that characterizes gas bearing operation. A proportional–differential feedback law is established in order to minimize the vibration response of the system. The performance of the active bearing is investigated with several numerical examples based on simplified rotordynamic disc-bearing system.

While adding cost and complexity with respect to a conventional aerodynamic or aerostatic bearing, the marked increase in performance of this type of active bearing constitutes an interesting alternative for applications where either (a) absolute performance either in terms of maximum allowable speed and/or strict vibration level tolerance is of primary concern or (b) long-term production increase due to the enhanced performance can offset the initial investment for the control system. In this respect it should be noted that in recent years average prices for piezoelectric actuators and their electronic have seen a marked decline, making such costs less substantial.

2. Mathematical model

A mathematical model is developed in order to obtain an accurate description of the prototype active gas journal bearing shown in Fig. 1. The design comprises essentially of a rigid sleeve gas journal bearing, in which four orifices are drilled. These are positioned in the axial mid-plane and equally spaced in the circumferential direction, each pair aligned with the vertical and horizontal directions. On the back of the sleeve four piezoelectric actuator are placed in order to open and close the connection between the pressure supply line and the gap between journal and sleeve. Details of the operation is presented in the following sections.

The mathematical description of the bearing is organized in several modules. A fluid dynamic section, where an expression for

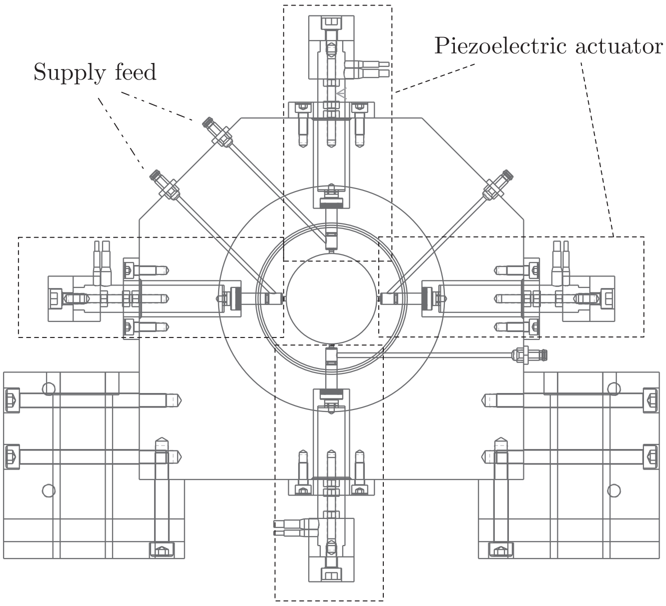

Fig. 1. Prototype active gas journal bearing.

Please cite this article as: Morosi S, Santos IF. Active lubrication applied to radial gas journal bearings. Part 1: Modeling. Tribol Int (2011), doi:10.1016/j.triboint.2011.08.007

the Reynolds equation modified for hybrid injection is derived, is followed by the description of the injectors dynamic. The latter consists of the thorough modeling of the piezoelectric, pneumatic and mechanical subsystems. The last part describes the control law, which provides the mathematical link between the different modules.

2.1. Modeling of the hybrid journal bearing

A hybrid form of the Reynolds equation can be derived upon introducing a simple modification to the standard reduction of the Navier–Stokes equations, as shown also in [10]. Note that this formulation has an advantage over the classical method of including aerostatic contributions [25], as mass conservation is implicitly respected without the need of iterating for mass flow balancing. There are, however, some limiting assumptions. Most prominently, it is assumed that the radial injection flow is laminar and fully developed; moreover the injection ducts are also considered to be short.

The derivation of a hybrid modified from of the Reynold's equation is as follows. Assuming an isoviscous, Newtonian, compressible fluid in a laminar regime, one can write the Navier–Stokes equations as

$$\frac{\partial}{\partial x}\left[\mu\frac{\partial u}{\partial x}\right]=0$$

$$\frac{\partial}{\partial x}\left[\mu\frac{\partial v}{\partial x}\right]=\frac{\partial p}{\partial y}$$

$$\frac{\partial}{\partial x}\left[\mu\frac{\partial w}{\partial x}\right]=\frac{\partial p}{\partial z} \tag{1}$$

where x is the across-film coordinate, y the circumferential, z the axial, as presented in Fig. 2. Note that the pressure is assumed to be constant across the film, and it solely considered the variation of tangential stresses upon the normal to the surface. The following boundary conditions are imposed:

$$u_b(0,y,z)=V_{inj},\quad u_j(h,y,z)=V$$

$$v_b(0,y,z)=0,\quad v_j(h,y,z)=U$$

$$w_b(0,y,z)=0,\quad w_j(h,y,z)=0 \tag{2}$$

Integrating twice Eq. (1) upon applying the boundary conditions above, one obtains

$$u=\frac{x}{h}V+\left(\frac{h-x}{h}\right)V_{inj}$$

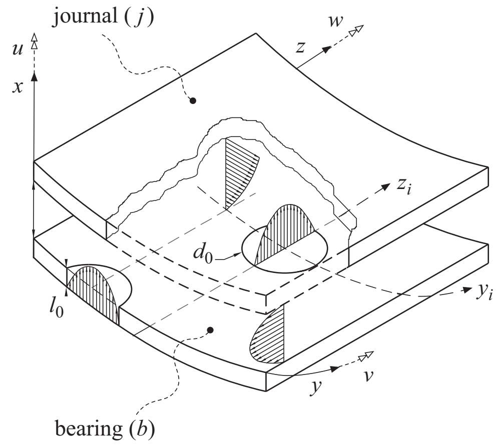

Fig. 2. Coordinate system schematic.

$$v=-x\left(\frac{h-x}{2\mu}\right)\frac{\partial p}{\partial y}+\frac{x}{h}U$$

$$w=-x\left(\frac{h-x}{2\mu}\right)\frac{\partial p}{\partial z} \tag{3}$$

External radial injection: Regarding the external air injection, a velocity profile is defined in the domain comprised between the supply chamber and the bearing. A schematic view can be seen in Fig. 3. A simplified analytical expression is easily obtained by simplifying the N–S equations, expressed in cylindrical coordinates [28]

$$V_{inj}(y,z,t)=-\frac{1}{4\mu}\left(\frac{\partial p}{\partial x}\right)\left[\frac{d_o^2}{4}-(y-y_i)^2-(z-z_i)^2\right] \tag{4}$$

Eq. (4) is known as Hagen–Poeiseuille formula and despite formally it applies to incompressible fluids, if one considers only an infinitesimal length dx of the feeding pipe, the change of density of the fluid within this distance can be neglected. This assumption allows a further simplification, by assuming the variation of injection pressure along the duct length (l_0, along the $-x$ direction) to be linear and proportional to the difference between supply and journal pressures:

$$\frac{\partial p}{\partial x}=\frac{P_{inj}-p(y,z,t)}{l_0} \tag{5}$$

The injection velocity is zero outside the orifice region. Note that if length of the injection feeding ducts is appreciable, the flow density changes as the pressure changes, so that although the mass flow rate is constant, the volumetric flow is not and the compressibility effect ought to be taken in consideration. Moreover, it should be noted that such formulation is in general valid for steady conditions; however, in case of high injection frequencies, the rapid opening and closing of the orifice might render necessary the inclusion of fluid inertia effects.

Modified Reynolds equation: Introducing the velocity profiles of Eq. (3), upon the inclusion of Eq. (4), into the general form of the continuity equation

$$\int_0^h\left[\frac{\partial\rho}{\partial t}+\frac{\partial}{\partial x}(\rho u)+\frac{\partial}{\partial y}(\rho v)+\frac{\partial}{\partial z}(\rho w)\right]dx=0 \tag{6}$$

After the integration of Eq. (6) the velocity profiles become coupled, meaning that the lubrication film is continuous.

In the case of a compressible lubricant obeying the ideal gas law, the pressure distribution p in near-isothermal conditions is governed by the modified general form of the Reynolds equation:

$$\frac{\partial}{\partial y}\left(ph^3\frac{\partial p}{\partial y}\right)+\frac{\partial}{\partial z}\left(ph^3\frac{\partial p}{\partial z}\right)=6\mu U\frac{\partial(ph)}{\partial y}+12\mu\frac{\partial(ph)}{\partial t}+12pV_{inj} \tag{7}$$

Note that the extra term $12pV_{inj}$ is only to be included in orifice areas, whereas it is zero elsewhere. Substituting the expression presented in Eq. (4) and introducing an auxiliary function $\mathcal{F}_i$ which describes the velocity profile while taking into account the

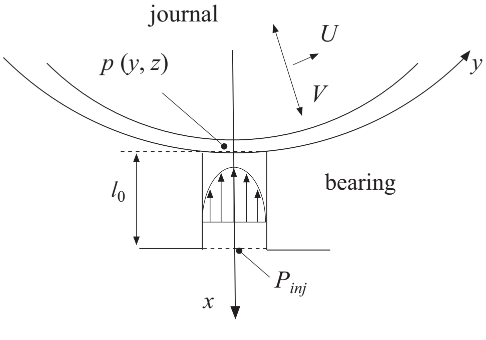

Fig. 3. Model of the injection flow.

Please cite this article as: Morosi S, Santos IF. Active lubrication applied to radial gas journal bearings. Part 1: Modeling. Tribol Int (2011), doi:10.1016/j.triboint.2011.08.007

position of the orifices:

$$V_{inj}(y,z,t) = -\frac{1}{4\mu l_0}(P_{inj}-p)\cdot\mathcal{F}_i(y,z) \qquad (8)$$

$$\mathcal{F}_i(y,z) = \begin{cases} \frac{d_0^2}{4} - (y-y_i)^2 - (z-z_i)^2, & (y-y_i)^2 - (z-z_i)^2 \le \frac{d_0^2}{4} \\ 0, & (y-y_i)^2 - (z-z_i)^2 \ge \frac{d_0^2}{4} \end{cases} \qquad (9)$$

Note that the form function $\mathcal{F}_i$ is used to describe the parabolic velocity profile in the orifice region, whereas is zero elsewhere.

Film thickness: The location of the minimum film thickness is defined by the attitude angle Φ, see Fig. 4. The film thickness function $h = h(y,t)$ depends on the position of the center of the shaft according to

$$h = C + e_X\cos\Theta + e_Y\sin\Theta \qquad (10)$$

where $C = R_b - R_j$ is the radial clearance of the bearing and $\Theta = \theta + \Phi$.

The pressure distribution in the bearing is continuous in the circumferential coordinate and equal to the atmospheric value at the bearing sides. The boundary conditions for the steady state, Eq. (7) states that the pressure is equal to the ambient one at the axial sides and continuous in the circumferential direction. They are defined as

$$\begin{cases} p(x,0) = p(x,L) = p_{atm} \\ p(0,y) = p(2\pi R,y) \\ \frac{\partial p(0,y)}{\partial x} = \frac{\partial p(2\pi R,y)}{\partial x} \end{cases} \qquad (11)$$

Fluid film forces: Vertical and horizontal lubrication reaction forces can be found by integrating pressure field solution over the bearing surface:

$$F_X^{fluid} = \int_0^L \int_0^{2\pi} (p-p_{atm})\cos\Theta R\, d\Theta\, dz$$

$$F_Y^{fluid} = \int_0^L \int_0^{2\pi} (p-p_{atm})\sin\Theta R\, d\Theta\, dz \qquad (12)$$

Equilibrium position: For a given position of the journal (e_X, e_Y), the Reynolds equation can be solved for the pressure, which in turn imposes vertical and horizontal lubrication forces on the shaft, see Eq. (12). For a bearing to be in equilibrium the lubrication forces must equilibrate a given load – in this case the weight of the rotor, $W = mg$ – acting on the vertical direction, see Fig. 5

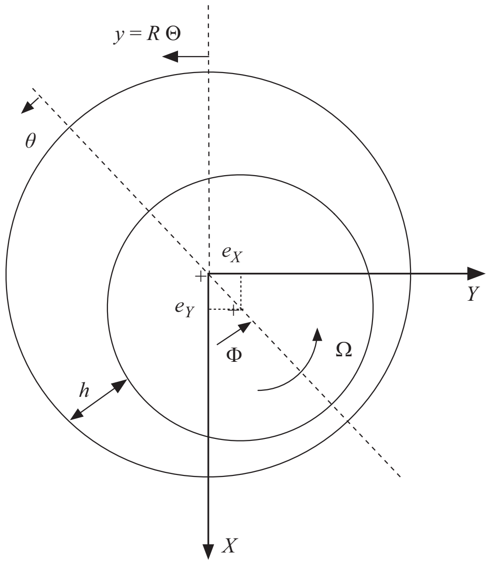

Fig. 4. Journal bearing schematic.

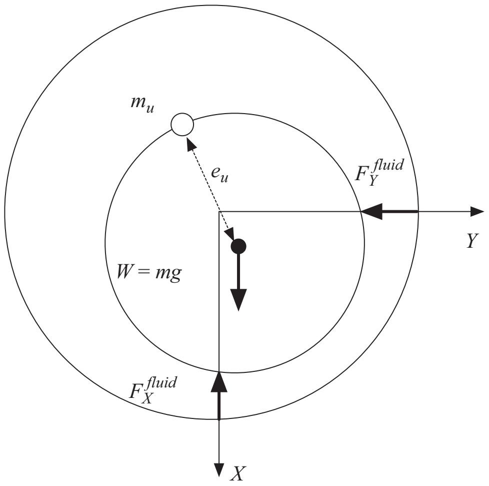

Fig. 5. Physical representation of the forces acting on the rotor.

$$\begin{cases} W + F_X^{fluid}(e_X, e_Y) = 0 \\ F_Y^{fluid}(e_X, e_Y) = 0 \end{cases} \qquad (13)$$

Note that for the steady state case, the time-dependent term in Eq. (7) vanishes, i.e. $12\mu\partial(ph)/\partial t = 0$.

Dynamic analysis: The equation of motion of the rotating system is expressed by

$$\mathbf{M}\ddot{\mathbf{q}}(t) + \mathbf{D}\dot{\mathbf{q}}(t) + \mathbf{K}\mathbf{q}(t) = \mathbf{F}^{ext}(t) + \mathbf{F}^{fluid}(t) \qquad (14)$$

where **M**, **D** and **K** are the mass, damping and stiffness matrices of the rotor, $\mathbf{q}(t) = [e_X\ e_Y]^T$ the displacement vector. $\mathbf{F}^{ext}(t)$ is the vector of externally applied forces, which accounts for gravity and eventual unbalance, and $\mathbf{F}^{fluid}(t)$ the vector of (nonlinear) dynamic reaction forces of the bearing, defined by Eq. (12). It should be remarked that to keep a very simple mathematical description of the rotodynamic system, the rotor is assumed to be rigid, thus **D** and **K** can be neglected, so one can rewrite Eq. (14) in matrix form as

$$\begin{bmatrix} m & 0 \\ 0 & m \end{bmatrix} \begin{Bmatrix} \ddot{e}_X \\ \ddot{e}_Y \end{Bmatrix} = \begin{Bmatrix} mg + m_u e_u \Omega^2 \cos(\Omega t) \\ m_u e_u \Omega^2 \sin(\Omega t) \end{Bmatrix} + \begin{Bmatrix} F_X^{fluid}(e_X, \dot{e}_X, e_Y, \dot{e}_Y) \\ F_Y^{fluid}(e_X, \dot{e}_X, e_Y, \dot{e}_Y) \end{Bmatrix} \qquad (15)$$

2.2. Piezoelectric injection system

The air injection is physically performed by the means of piezoactuators. Piezoceramic actuators have been subjects of increasing research in the last two decades; a comprehensive comparative study was performed by Ulbrich [29], underlying the advantages of such components. In general, piezoelectric actuators are characterized by a more compact design and faster response when compared to other types of actuators [30–32]. A schematic view of the piezoelectric air injection system is presented in Fig. 6. In this system, the air injection is regulated by the activation of the piezoelectric stack. When a voltage signal is sent to this stack, the attached injection pin can be moved vertically, allowing or blocking the passage of air from the supply reservoir at P_{sup} to the injection chamber at P_{inj} and subsequently to the journal bearing at P_{JB}. Belleville washers are positioned between the injection pin and its casing to aid the backwards

Please cite this article as: Morosi S, Santos IF. Active lubrication applied to radial gas journal bearings. Part 1: Modeling. Tribol Int (2011), doi:10.1016/j.triboint.2011.08.007

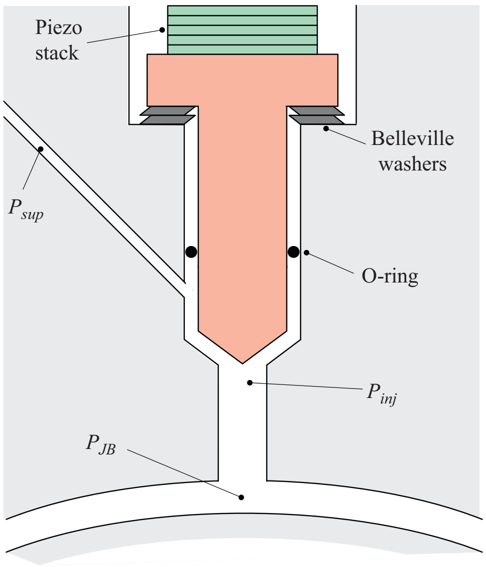

Fig. 6. Schematic view of the piezoelectric air injection system.

stroke of the pin. O-rings are also conveniently placed in order to minimize the loss of air toward the piezoactuator. The main governing equations for the electrical, mechanical and pneumatic subsystems are presented next. Although four actuators are employed, these can operate independently from each other. The following mathematical description refers to either of them.

2.2.1. *Modeling of the piezoelectric stack*

Material strain and electrical charge density displacement of a piezoelectric stack are affected both by the mechanical stress and electrical field the material is subjected to. The ANSI-IEEE 176 Standard on Piezoelectricity [33] declares the linear constitutive law for piezoelectrical materials. Considering a stack consisting of several layers of piezoelectric material, from the constitutive law the resultant piezoelectric force F_{piezo} and electric charge Q_{piezo} can be derived as

$$F_{piezo} = -k_{piezo} y(t) + k_{piezo} c_{piezo} N_{stack} u(t) \tag{16}$$

$$Q_{piezo} = -k_{piezo} c_{piezo} y(t) + \varepsilon_{piezo} N_{stack} E_{piezo}^{-1} u(t) \tag{17}$$

where k_{piezo} is the elastic stiffness of the piezoelectric stack, $y(t)$ the total displacement, c_{piezo} the piezoelectric coupling coefficient, $u(t)$ the feeding voltage, ε_{piezo} the dielectric permittivity of the material, E_{piezo} its elastic modulus and N_{stack} the number of layers of piezoelectric material that constitute the piezoactuator stack. It should be noted that this model does not include the effect of hysteresis nonlinearities, which would limit the performance of the actuator (both static and dynamic). Depending on whether such effects are relevant for each individual system, one could compensate it using one of several strategies developed in recent years; a review can be found in [34]. As a practical note, several piezoelectric motion control unit on the market are equipped with closed loop hysteresis feedback compensation, where a near linear response between $u(t)$ and $y(t)$ can be obtained, as noted in [35] (Fig. 7).

2.2.2. *Modeling of the mechanical subsystem*

In order to model the main mechanical components of the piezoelectric injection system, a simplified model is proposed, see Fig. 8. It consists of a basic 1 degree of freedom system, which dynamic behavior is described by

$$m_{pin} \ddot{y}(t) = F_{piezo} - k_{mech} y(t) - d_{mech} \dot{y}(t) \tag{18}$$

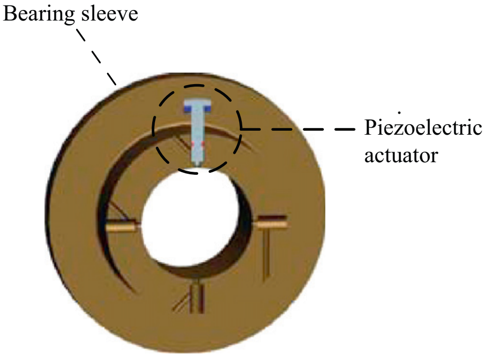

Fig. 7. 3D view of the piezoelectric injection system inside the bearing sleeve.

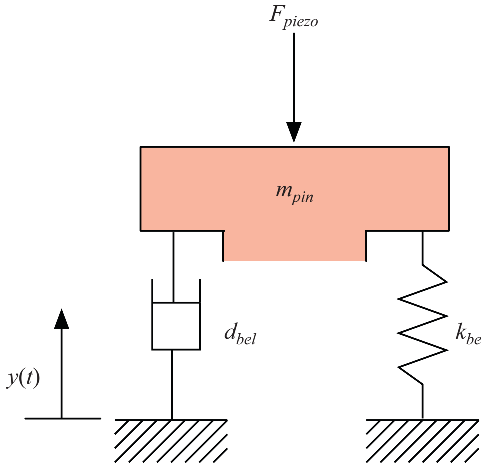

Fig. 8. Schematic view of the piezoactuator mechanical subsystem.

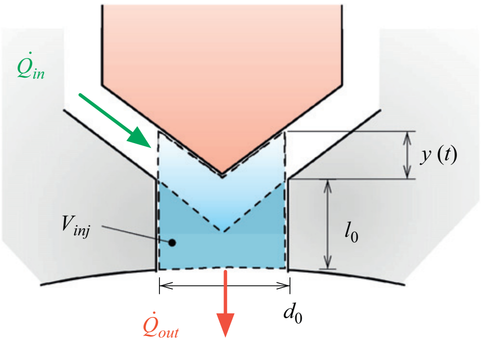

Fig. 9. Schematic view of the piezoactuator pneumatic subsystem.

where m_{pin} is the mass of the injector pin plus that of the piezoelectric stack, k_{mec} is the stiffness of the Belleville washers and d_{mech} is the combined equivalent viscous friction coefficient of the Belleville springs and O-rings. Note that the stiffness of the O-ring is not included in this analysis, as its magnitude is negligible for the configuration under consideration, where its contribution would be in parallel with the larger one due to the Belleville washers.

2.2.3. *Modeling of the pneumatic subsystem*

The pneumatic subsystem, see Fig. 9, is considered as a container of unknown pressure and volume V_{inj}, with cross sectional area greater than the inlet and outlets ducts. From the

Please cite this article as: Morosi S, Santos IF. Active lubrication applied to radial gas journal bearings. Part 1: Modeling. Tribol Int (2011), doi:10.1016/j.triboint.2011.08.007

definition of mass conservation

$$\frac{dm}{dt} = \rho(-\dot{Q}_{in} + \dot{Q}_{out}) \tag{19}$$

where $\dot{Q}_{in}$ and $\dot{Q}_{out}$ are the in- and outlet volumetric flow rates, respectively. If inertia is neglected and only the elasticity effect is taken into account, it can be assumed that the control volume has uniform pressure. Compressibility of the fluid needs also to be accounted for; the pressure change within a control volume of the pneumatic subsystem can be expressed by substituting the definition of the (isothermal) bulk modulus of elasticity. Equation (19) can then be modified, expressing the variation of pressure as

$$\frac{dP}{dt} = \frac{\beta}{V_{inj}}\left(\frac{dV_{inj}}{dt} - \dot{Q}_{in} + \dot{Q}_{out}\right) \tag{20}$$

where β is the bulk modulus of elasticity and the term dV_{inj}/dt takes into account the variation of volume due to the motion of the injector pin. The intake and outtake volumetric flows can be derived by the Bernoulli's law, modified by introducing an expansion factor to account for the compressibility of gases [36]. Their expressions are also function of the speed of the flow (sub/supersonic). For subsonic flows

$$\dot{Q} = c_D A(y(t))\sqrt{2RT\left(\frac{k}{k-1}\right)\left[\left(\frac{P_{dwn}}{P_{up}}\right)^{2/k} - \left(\frac{P_{dwn}}{P_{up}}\right)^{(k+1)/k}\right]} \tag{21}$$

For supersonic (chocked) flows

$$\dot{Q} = c_D A(y(t))\sqrt{kRT\left(\frac{2}{k+1}\right)^{(k+1)/(k-1)}} \tag{22}$$

Where c_D is the discharge coefficient, $A(y(t))$ is the area of the orifice, R is the specific gas constant for air, T is the absolute upstream temperature of the gas, k is specific heat ratio ($c_p/\ c_v$), P_i are the downstream and upstream pressures, respectively. Note that the last two quantities interchange their places whether the flow is directed form the supply tank toward the journal bearing or vice versa (backflow). As for the volume change due to the motion of mechanical parts, it holds that

$$V_{inj} = \pi\frac{d_0^2}{4}[l_0 + y(t)] \implies \frac{dV_{inj}}{dt} = \pi\frac{d_0^2}{4}\dot{y}(t) \tag{23}$$

2.2.4. *State space representation of global mathematical model of the injection system*

For each piezoelectric injector system, the mechanical and pneumatic subsystem are coupled. All the equations that describe the mathematical model of each piezo-actuated injector can be rewritten in state space form as

$$\dot{\mathbf{y}}(t) = f(t, \mathbf{y}(t), \mathbf{u}(t)) \tag{24}$$

where $\mathbf{y} = [y\ \dot{y}\ P_{inj}]^T$. In state space representation then

$$\begin{bmatrix} \dot{y} \\ \ddot{y} \\ \dot{P}_{inj} \end{bmatrix} \Leftrightarrow \begin{bmatrix} \dot{x}_1 \\ \dot{x}_2 \\ \dot{x}_3 \end{bmatrix} = \begin{bmatrix} x_2 \\ \frac{(k_{piezo}x_1 + k_{piezo}c_{piezo}N_{stack}u - k_{mech}x_1 - d_{mech}x_2)}{m_{pin}} \\ \frac{\beta}{V_{inj}(x_3)}\left(\dot{V}_{inj}(x_1) - \dot{Q}_{in}(x_1, x_3) + \dot{Q}_{out}(x_3, P_{JB})\right) \end{bmatrix} \tag{25}$$

Note that each piezoelectric subsystem is linearly independent with respect to each other, but coupling arises through the journal pressure P_{JB}.

2.3. *Modeling of the control system*

Once the mathematical model for the hybrid bearing and piezo-actuated injection system is formulated, the next step is to develop the control system. It is assumed that the instantaneous position and velocity of the journal are measured by sensors mounted on the bearing. First, the objective of the controller needs to be defined. In order to minimize the response of the system subjected to some kind of excitation, one could for instance increase the stiffness or damping coefficients. With this objective in mind, it is then necessary to establish a feedback control law in order to construct the signal to send to the piezoactuators as function of the information received by the sensors. General input signals can be defined as a combination of displacement and velocity, for either the vertical (X) or horizontal (Y) coordinates as

$$\mathbf{u}(t) = \mathbf{G}^k\mathbf{q}(t) + \mathbf{G}^d\dot{\mathbf{q}}(t) \Rightarrow \begin{array}{l} u_X = G_X^k e_X + G_X^d \dot{e}_X \\ u_Y = G_Y^k e_Y + G_Y^d \dot{e}_Y \end{array} \tag{26}$$

where $G_{X,Y}^{k,d}$ are the gains of the control system. The superscripts k,d refer respectively to the proportional or derivative gain. Depending on the goal of the control system, the gain coefficients should be calculated and optimized with the help of the developed model.

Despite not included in the present modeling, one should be aware that under certain operation conditions and parameters, an active controlled system could be interested by lag or lead times, which could result in poor performance or even instability. Delays often arise mechanical systems (in the present case for example due to the dynamic of the actuator), as well as in measurement and computation (for example due to filtering or coarse sampling frequencies).

3. Numerical solution

3.1. *Static equilibrium*

The necessary steps in order to determine the equilibrium position of the rotor-bearing system are as follows:

1. Determine an analytical expression for the film thickness function, Eq. (10), depending on the instantaneous position of the rotor, e_{X_0}, e_{Y_0}.
2. Solve the nonlinear partial differential equation (7) (in its steady state form) via a recursive method. For given operating conditions $U = \Omega R_j$ and eccentricity, the steady state equation is a nonlinear partial differential equation, in which each iteration is obtained using a finite difference approximation on a non-uniformly discretized domain of dimensions $m \times n$ in the y and z coordinate, respectively. The discretization is refined around the orifices. Boundary conditions are as indicated in Eq. (11).
3. Numerically integrate (Simpson's rule) the zeroth-order pressure distribution to obtain the fluid forces (Eq. (12)).
4. Calculate the static equilibrium point of the rotor-bearing system. The resulting algebraic system of Eq. (13) is implicit with respect to the unknown equilibrium position, therefore the solution is achieved by the means of a Newton–Raphson scheme. Steps 1–3 are then repeated in an iterative scheme until the equilibrium is reached.

3.2. *Dynamic response*

In principle, dynamic analysis of the rotor-bearing system operating with active lubrication could be performed bypassing the dynamic of the piezoelectric injection system described in Section 2.2, under the assumption that the injection pressures P_{inj} are known as a function of time. As it has been shown, see Eq. (25), these pressures depend on the actuators dynamics and the gain coefficients of the feedback law. For calculating the

Please cite this article as: Morosi S, Santos IF. Active lubrication applied to radial gas journal bearings. Part 1: Modeling. Tribol Int (2011), doi:10.1016/j.triboint.2011.08.007

dynamic response it is then necessary to take into account Eqs. (24) and (26), which provide the coupling between rotor-bearing system and piezoactuators. The numerical procedure is essentially similar to that described in the previous section for the equilibrium position. In this case, starting from a calculated equilibrium position, the dynamic solution in time domain is obtained by numerically integrate the dynamic equations of the rotor-bearing system, injector dynamic and feedback law. A simple Runge–Kutta scheme has been implemented for this purpose. In practice, the following equations are solved at each time step:

1. The equation of motion of the rotor-bearing system:

$$\ddot{\mathbf{q}}(t) = \mathbf{M}^{-1}\mathbf{F}^{ext}(t) + \mathbf{M}^{-1}\mathbf{F}^{fluid}(t) \tag{27}$$

2. The dynamic nonlinear fluid film forces:

$$\mathbf{F}^{fluid}(t) = \int\int_A (p - p_{atm})dA \tag{28}$$

Note that in the dynamic case, in order to obtain the correct pressure profile, Eq. (7) must be solved taking into account the transient term, which is implicitly integrated as

$$12\frac{\partial(ph)}{\partial t} = 12\left[\frac{(p_t - p_{t-1})h_t}{\Delta t} + \frac{\partial h}{\partial t}p_t\right] \tag{29}$$

Where $\frac{\partial h}{\partial t}$ is the squeeze component, which can be obtained by analytical differentiation of Eq. (10)

3. The injector dynamic set

$$\dot{\mathbf{y}}(t) = f(t, \mathbf{y}(t), \mathbf{u}(t)) \tag{30}$$

4. The feedback law

$$\mathbf{u}(t) = \mathbf{G}^k\mathbf{q}(t) + \mathbf{G}^d\dot{\mathbf{q}}(t) \tag{31}$$

which provides the essential coupling between the rotor-bearing system degrees of freedom, $\mathbf{q}(t)$, and the injector ones $\mathbf{y}(t)$, through the input signal $\mathbf{u}(t)$.

4. Results and discussion

Selected numerical examples are presented for the journal bearing operating in passive and active mode. An overview of the simulations parameters is presented in Table 1. The passive mode refers to regular hybrid aerostatic/aerodynamic operation, with the piezoelectric actuators fixed in the open position. In the active mode the actuators receive the feedback control signal as an input, regulating the closing and opening of the valves. As an example with obvious practical purposes, the goal of the PD controller is set to minimize the vibration amplitude of the system.

In general, when the system is excited by an unbalance or subjected to a shock it will start oscillate around its equilibrium with a certain amplitude and at frequencies depending on the excitation and the system itself. In order minimize the response, one strategy is to direct the active forces against these movements around the equilibrium. The term active forces here refers to the portion of aerostatic force contribution that can be adjusted by regulating the movement of the piezoactuators. In practice the following solution has been adopted: according to a given displacement and velocity of the rotor, the piezoactuators are selectively open or closed in order to generate a resultant force in the appropriate direction, see Fig. 10. In this case, one should note that by closing one of the piezovalve, its net contribution to the active force is “negative”, as its aerostatic component is suppressed. Moreover, the piezoactuators aligned on the horizontal ($-X$) direction are fed back with the horizontal displacement and velocity components (e_X, $\dot{e}_X$) and similarly for the vertical direction.

Table 1
General simulations parameters.

Bearing length	$L = 40$ mm
Bearing length	$D = 40$ mm
Nominal clearance	$C = 25$ μm
Supply pressure	$P_{sup} = 5$ atm
Orifice diameter	$d_0 = 1$ mm
Feeding duct length	$l_0 = 10$ mm
Rotor disc mass	$m = 5$ kg
Unbalance mass	$m_u = 0.0025$ kg
Unbalance eccentricity	$e_u = D/2$
Piezoactuator pin mass	$m_{pin} = 0.05$ kg
Belleville spring stiffness	$k_{mech} = 5e6$ N/m
Piezoactuator equivalent damping	$d_{mech} = 2e3$ N/m s
Piezoelectric element stiffness	$k_{piezo} = 3e7$ N/m
Piezoelectric coupling coefficient	$c_{piezo} = 65e-8$ C/N
No. of piezoelectric elements in stack	$N_{stack} = 100$
Air dynamic viscosity	$\mu = 18.27e-6$ Pa s
Air temperature	$T = 293$ K
Gas constant of air	$R = 287$ J/kg K
Specific heat ratio	$k = 1.4$
Proportional gains	$G_X^k = G_Y^k = 1e5$ V/m
Derivative gains	$G_X^d = G_Y^d = 1e3$ Vs/m
Time step	$\Delta t = 1e-7$ s

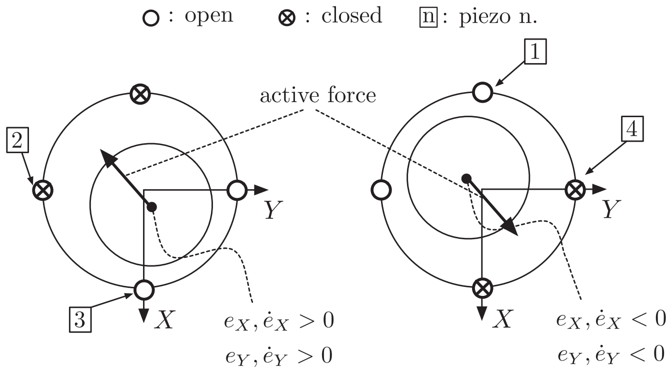

Fig. 10. Schematic view of the control strategy adopted.

A first test is performed at a rotational speed of 12,000 rpm. Starting from the equilibrium position of the passive system for this operation parameters, the equation of motion is integrated and after ensuring that the transient has decayed, the controller is turned on. Fig. 11 presents the time history of the rotor vertical displacement compared to the displacement of the piezoactuator 3. Prior to the controller switch on, the rotor appears to have a periodic behavior, which is typical linear synchronous response to unbalance excitation. Note the vibration amplitude is limited to less than 10% of the radial clearance and the equilibrium position is taken as a reference value. As the controller is switched on, the response is significantly altered. Most importantly, it is noticed that after an initial settling time the steady vibrations of the active system are noticeably reduced compared to the passive case. Secondly, it is possible to observe another, higher, frequency component overlapped to the fundamental one. The situation becomes more clear when analyzing the harmonic content of the passive and active signals as a function of the normalized frequency (with respect to the rotational one), see Fig. 12. While it is confirmed the ability of the controller to efficiently reduce the synchronous vibration component, it becomes evident how the system responds to another, higher one. This frequency is in fact a new characteristic of the mechatronic system composed by the rotor-bearing and piezoelectric injection system; its value is a

Please cite this article as: Morosi S, Santos IF. Active lubrication applied to radial gas journal bearings. Part 1: Modeling. Tribol Int (2011), doi:10.1016/j.triboint.2011.08.007

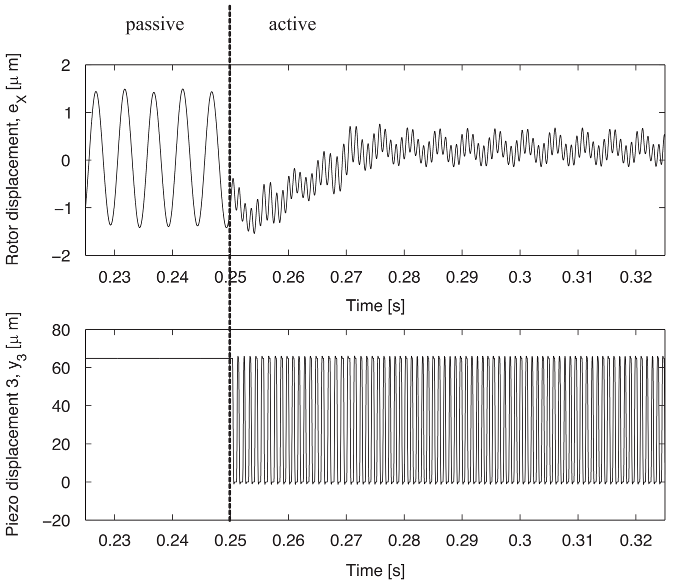

Fig. 11. Rotor and piezoactuator displacement responses around the equilibrium, passive and active mode, $\Omega = 12,000$ rpm.

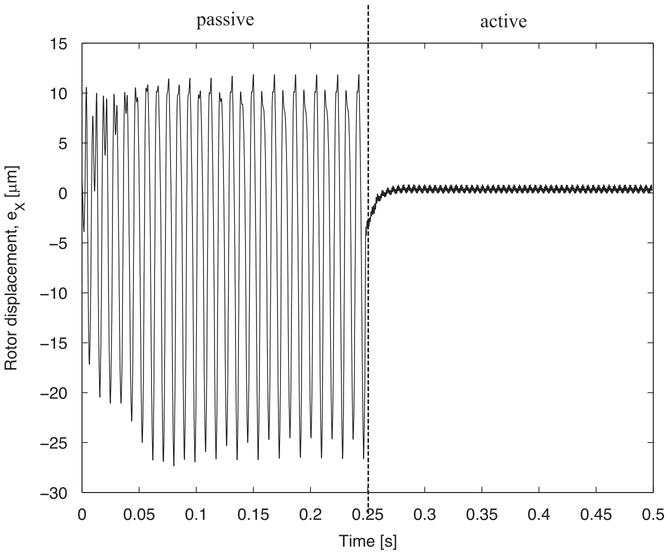

Fig. 13. Rotor and piezoactuator displacement responses around the equilibrium, passive and active mode, $\Omega = 13,000$ rpm.

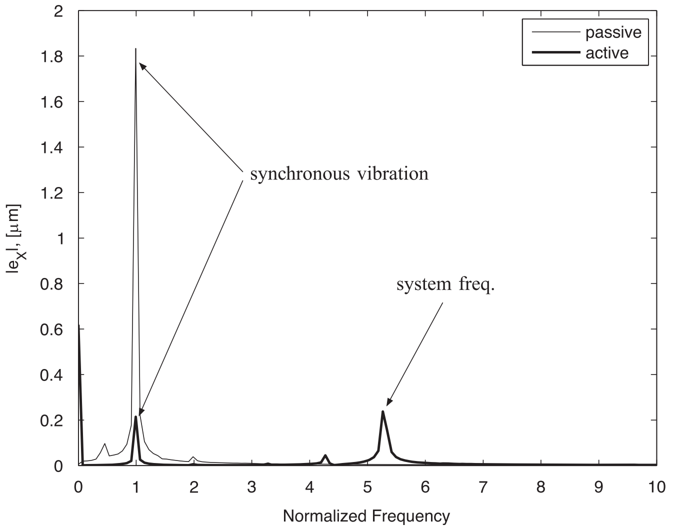

Fig. 12. Single-sided power spectra of rotor displacement responses, passive and active mode, $\Omega = 12,000$ rpm.

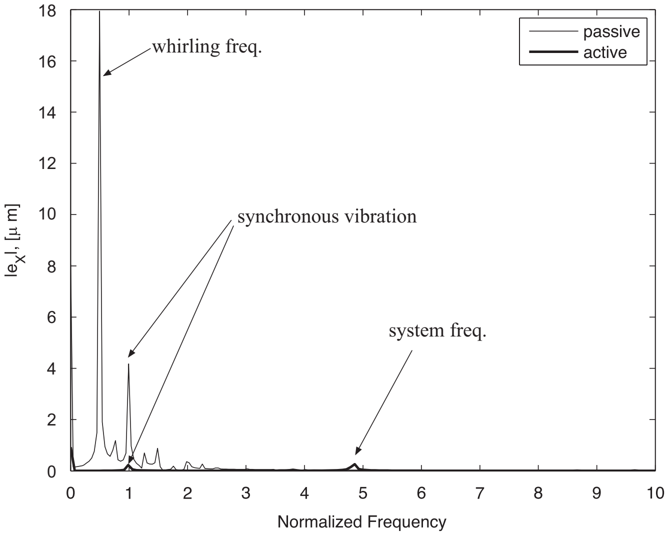

Fig. 14. Single-sided power spectra of rotor displacement responses, passive and active mode, $\Omega = 13,000$ rpm.

function of the physical and operational parameters of rotor-bearing system, the characteristics of the piezoelectric actuators and the mechanical subsystem they are mounted within and, most importantly, the controller gains.

As the speed is increased to 13,000 rpm, the passive system response sees a marked change. Starting from the equilibrium position, the vibrations show an unstable behavior which lead to a growth to much larger amplitudes, spanning much of the bearing nominal clearance (Fig. 13). The corresponding frequency spectrum analysis, Fig. 14, reveals the nature of this motion, which, besides the synchronous response due to the unbalance, is dominated by a subharmonic, half-period component: the half-speed whirl. This feature is characteristic of rigid sleeve, gas lubricated journal bearings and it is perhaps the primary factor that limits their performance and usefulness [37], as the journal is characterized by extremely large motion amplitudes, spanning as much as the whole clearance. However, when the controller is turned on, the vibration level is dramatically reduced and, the half-frequency whirl motion suppressed and the steady state motion assumes similar qualitative and quantitative characteristics to those described earlier for the 12,000 rpm case, with a higher system frequency superimposed to a limited synchronous component. Note that although for both of the cases examined the vibrations response with active lubrication settles to similar steady state values, the performance compared to the passive mode appears sensibly different from case to case, due to the largely different passive system response.

For a final example of the qualities of the active lubrication in addressing the unbalance response of the system, the speed is further increased to 18,000 rpm, well above the whirling threshold. For the passive operation, at this speed the sub-synchronous motion amplitude is not contained within the bearing clearance anymore, but large enough to cause touch-down between rotor and bearing. With the controller on, however, the vibrations are kept to limited values, see Fig. 15, while the whirling motion is eliminated, see Fig. 16, and only low-energy synchronous and system frequencies are retained.

Please cite this article as: Morosi S, Santos IF. Active lubrication applied to radial gas journal bearings. Part 1: Modeling. Tribol Int (2011), doi:10.1016/j.triboint.2011.08.007

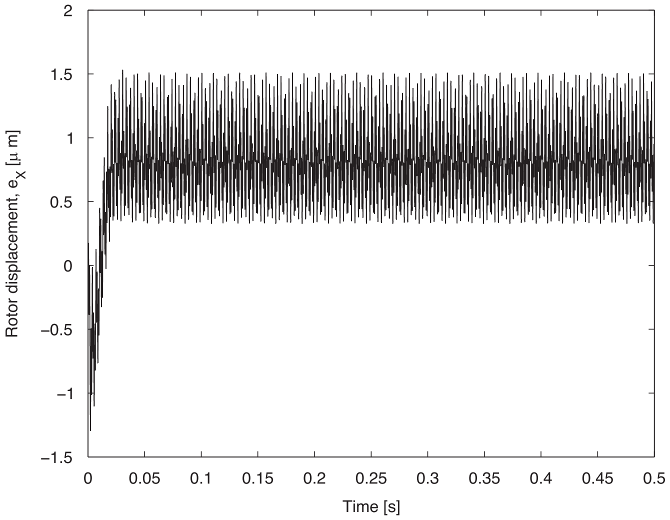

Fig. 15. Rotor and piezoactuator displacement responses around the equilibrium, active mode, $\Omega = 18,000$ rpm.

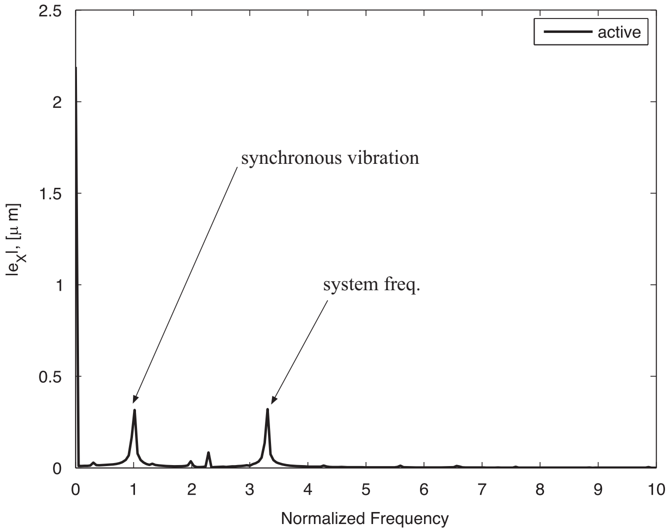

Fig. 16. Single-sided power spectra of rotor displacement responses, active mode, $\Omega = 18,000$ rpm.

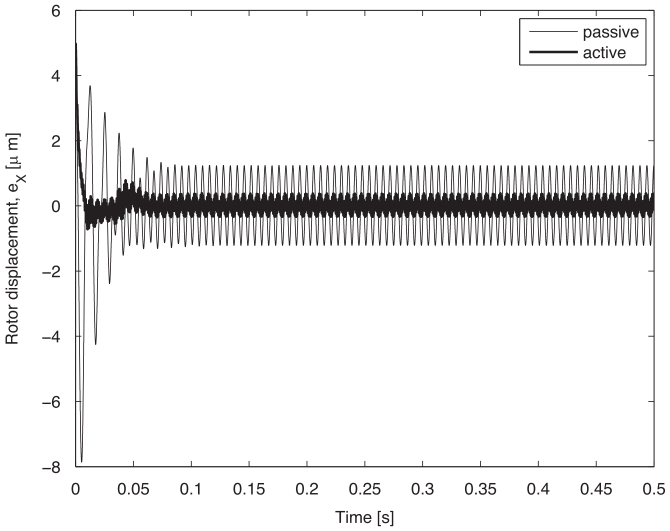

Fig. 17. Rotor displacement responses around the equilibrium, passive active mode, $e_X|_{t=0} = 5$ μm; $\Omega = 10,000$ rpm.

Typical industrial rotating machinery environments may induce sudden shocks which result in sudden large amplitude responses. Therefore it is utmost favorable that the rotating system is well damped and able to quickly reduce or possibly limit such vibrations. Fig. 17 compares passive and active unbalance responses when an initial condition of displacement is applied to the rotor, $e_X|_{t=0} = 5$ μm. While the passive system shows a typical logarithmic decrement of the transient vibrations, remarkably the active system is able to suppress the largest – and most dangerous – amplitudes faster and more efficiently.

The above examples compare operation either with the control system either switched on or off. One however could imagine a working situation in which active lubrication is only applied when a shock is detected.

5. Conclusions and future aspects

This paper lays the theoretical basis for applying active control to gas lubricated journal bearings. The principle of operation is to generate active forces by regulating radial injection of lubricant through the means of piezoelectric actuators mounted on the back of the bearing sleeves. The developed mathematical model couples the rotor-bearing system dynamics with the mechanical and fluid dynamics of the actuators through a simple proportional-derivative feedback law.

Numerical examples show how this new kind of bearing offers considerable advantages compared to conventionally lubricated bearings, not only showing a significative reduction of the synchronous vibration components, but also effectively addressing the half-frequency whirling motion, thus in fact extending the range of applicability of gas lubricated bearings. Moreover, it is shown how this type of active bearing also offers improved transient response characteristics, which translated in a better ability to respond to sudden shocks and excitations the system may be subjected to.

Implementing active lubrication adds however a considerable number of parameters and variables to the system under analysis. The performance of a good control system lies most importantly on a good choice of control gains, which in general are different depending on the goal of the controller. Future numerical and experimental efforts are directed at confirming the theoretical findings and identifying the optimum tuning of the active system.

References

[1] San Andres L, Lubell D. Imbalance response of a test rotor supported on squeeze film dampers. ASME Transactions, Journal of Engineering for Gas Turbines and Power 1998;120(2):397–404.

[2] Pietra LD, Adiletta G. The squeeze film damper over four decades of investigations. part i: characteristics and operating features. Shock and Vibration Digest 2002;34:3–27.

[3] Vance JM, Li J. Test results of a new damper seal for vibration reduction in turbomachinery. ASME Transactions, Journal of Engineering for Gas Turbines and Power 1996;118(4):843–6.

[4] Jung CS, Choi SB. Analysis of a short squeeze film damper operating with electrorheological fluids. STLE Tribology Transactions 1995;38(4):857–62.

[6] Vance JM, Ying D, Nikolajsen J. LActively controlled bearing dampers for aircraft engine applications. ASME Transactions, Journal of Engineering for Gas Turbines and Power 2000;122(3):466–72.

[7] Zhu C, Robb DA, Ewins DJ. On-Off control of rotor vibration by a disk-type magneto-rheological fluid damper. In: Proceeding of the 9th international symposium on transport phenomena and dynamics of rotating machinery, Honolulu, Hawaii, 10–14, 1–7 February 2002.

[8] Schweitzer G, Traxler A, Bleuler H. Active magnetic bearings—basics properties and applications of active bearings. Berlin, Heidelberg, New York: Springer Verlag; 1994.

[9] Goodwin MJ, Boroomand T, Hooke CJ. Variable impedance hydrodynamic journal bearings for controlling flexible rotor vibrations. In: 12th Biennial ASME conference on vibration and noise, Montreal, Canada, 17–21 September 1989; 261–267.

Please cite this article as: Morosi S, Santos IF. Active lubrication applied to radial gas journal bearings. Part 1: Modeling. Tribol Int (2011), doi:10.1016/j.triboint.2011.08.007

[10] Santos IF, Russo FH. Tilting-Pad journal bearings with electronic radial oil injection. ASME Transactions, Journal of Tribology 1998;120(3):583–94.

[11] Santos IF. Design and evaluation of twotypes of activetilting pad journal bearings. In: Burrows CR, Keogh PS, editors. The active control of vibration. London, England: Mechanical Engineering Publications Limited; 1994. p. 79–87. ISBN 0-85298-916-4.

[12] Agrawal GL. Foil Air/Gas Bearing Technology—An Overview. Publication 97-GT-347 (American Society of Mechanical Engineers); 1998.

[13] DellaCorte C, Valco MJ. Load capacity estimation of foil air journal bearings for oil-free turbomachinery applications. Tribology Transactions 2000;43(4): 795–801.

[14] Kim TH, San Andrés L. Heavily loaded gas foil bearings: a model anchored to test data. Journal of Engineering for Gas Turbines and Power 1998;130(1): 012504.

[15] Childs DW. Turbomachinery rotordynamics: phenomena, modeling, and analysis. New York: Wiley-Interscience; 1993.

[16] San Andrés L. Hybrid flexure pivot-tilting pad gas bearings: analysis and experimental validation. Journal of Tribology 2006;128(3):55.

[17] Sim K, Kim D. Design of flexure pivot tilting pads gas bearings for high-speed oil-free micro turbomachinery. ASME Journal of Tribology 2007;129(1):112–9.

[18] Sim K, Kim D. Thermohydrodynamic analysis of compliant flexure pivot tilting pad gas bearings. Journal of Engineering for Gas Turbines and Power 2008;130(3):032502.

[19] Horikawa O, Kaiji S, Shimokohobe A. An active air journal bearing. Nanotechnology 1992;3:84–90.

[20] Mizumoto H, Arii S, Kami Y, Goto K, Yamamoto T, Kawamoto M. Active inherent restrictor for air bearing spindles. Precision Engineering 1996;19(2–3):141–7.

[21] Qiu J, Tani J, Kwon T. Control of self-excited vibration of a rotor system with active gas bearings. ASME Journal of Vibration and Acoustics 2003;125: 328–34.

[22] San Andrés L, Ryu K. Hybrid gas bearings with controlled supply pressure to eliminate rotor vibrations while crossing system critical speeds. Journal of Engineering for Gas Turbines and Power 2008;130(6):062505.

[23] Mizumoto H, Arii S, Yabuta Y, Tazoe Y. Vibration control of a high-speed air-bearing spindle using an active aerodynamic bearing. In: Proceedings of 2010 international conference on control, automation and systems (ICCAS 2010); pp. 2261–2264.

[25] Hamrock BJ. Fundamentals in fluid film lubrication. McGraw-Hill; 1994.

[28] Morosi S, Santos IF. On the modelling of hybrid aerostatic—gas journal bearings. Journal of Engineering Tribology. In: Proceedings of the institution of mechanical engineers vol. 225, Part J: Journal of Engineering Tribology NordTrib Special Issue, 2011, vol. 7.

[29] Ulbrich H. Comparison of different actuators concepts for applications in rotating machinery. International Journal of Rotating Machinery 1994;1(1): 61–71.

[30] Near C. Piezoelectric actuator technology. Proceedings of the SPIE—The International Society for Optical Engineering 1996;2717:246–58.

[31] Prechtl EF, Hall SR. Design of a high efficiency, large stroke, electromechanical actuator. Smart Materials and Structures 1999;8(1):13–30.

[32] Taylor CJ, Washington GN. A comprehensive piezoceramic actuator review. Procedings fo SPIE—The International Society for Optical Engineering 2002;4701:443–54.

[33] ANSI/IEE Standard on Piezolectricity. Technical Report Std 176–1987. IEEE Ultrasonics, Ferroeletrics and Frequency Control Society, New York, 1987.

[34] Devasia S, Eleftheriou E, Moheimani S. A survey of control issues in nanopositioning. IEEE Transactions on Control Systems Technology 2007;15(5): 802–23.

[35] Cade I, Necip Sahinkaya M, Burrows CR, Keogh PS. On the design of an active auxiliary bearing for rotor/magnetic bearing systems. In: Proceedings of the 11th international symposium on magnetic bearings, Nara, Japan, 26–29 August 2011, pp. 144–151.

[36] Fox RW, McDonald AT. Introduction to fluid mechanics.fourth ed. New York: John Wiley & Sons Inc; 1994.

[37] Ausman JS. Linearized pH stability theory for translatory half-speed whirl of long self-acting gas-lubricated journal bearings. ASME Journal of Basic Engineering 1963;83:619.

Please cite this article as: Morosi S, Santos IF. Active lubrication applied to radial gas journal bearings. Part 1: Modeling. Tribol Int (2011), doi:10.1016/j.triboint.2011.08.007

Bibliography

[1] Agrawal, G L. (1998), Foil Air/Gas Bearing Technology — An Overview, Publication 97-GT-347 American Society of Mechanical Engineers.
8

[2] ANSI/IEE Standard on Piezolectricity. Tech. Rep. Std 176-1987, IEEE Ultrasonics, Ferroeletrics and Frequency Control Society, New York. 58

[3] Arghir,M Le Lez, S, and Frene, J (2006), Finite-volume solution of the compressible Reynolds equation. Proceedings of the Institution of Mechanical Engineers, Part J: Journal of Engineering Tribology, vol. 220, pp. 617–627. ix, 80, 83

[4] Ausman, J, (1957), Finite Gas-Lubricated Journal Bearing. The Institute of Mechanical Engineers, Proceedings of the Conference on Lubrication and Wear, pp. 39–45.
6

[5] Ausman, J. S, (1961), An Approximate Analytical Solution for Self-Acting Gas Lubrication of Stepped Sector Thrust Bearings. Tribology Transactions, vol. 4, no. 2, pp. 304– 313.
6

[6] Ausman, J S (1963), Linearized pH stability theory for translatory half-speed whirl of long self-acting gas-lubricated journal bearings, ASME J. Basic Engineering; 83, pp 619-619
98

[7] Azzerboni, B and Cardelli, E (1993). Magnetic field evaluation for disk conductors, IEEE Trans. Magn. 29(6): 2419–2421.
10

[8] Baatz, M. and Hyrenbach, M, (1991), Method of Calculating the Magnetic Flux Density and Forces in Contact-Free Magnetic Bearings, ETEP Vol. 1, No 4, 195-199.
x, 10, 14, 101, 103, 106

[9] Backers, F T (1961), A Magnetic Journal Bearing, Philips Tech. Rev., 22, pp. 232-238.
10

[10] Boden K, Fremerey J.K (1992), Industrial Realization of the "System KFA-Jülich" Permanent Magnet Bearing Lines. Proceedings of MAG ?92, Alexandria, Virginia, July 29-31.
10

[11] Brown, D L, Allemang, R J, Zimmerman, R and Mergeay, M, (1979). Parameter estimation techniques for modal analysis. SAE Technical Paper 790221.
143

[12] Cade, I, Necip Sahinkaya, M, Burrows, C R, and Keogh, P S (2011), On the Design of an Active Auxiliary Bearing for Rotor/Magnetic Bearing Systems. Proceedings of the 11th International Symposium on Magnetic Bearings, Nara, Japan, August 26-29, 144-151. 58

[13] Castelli, V and Pirvics, J, (1968), Review of Numerical Methods in Gas Bearing Film Analysis. Journal of Lubrication Technology, vol. 90, pp. 777–792.
6

[14] Childs, D W (1993), Turbomachinery Rotordynamics: Phenomena, Modeling, and Analysis. Wiley-Interscience, New York.
8

[15] Constantinescu V (1985), Sliding Bearings, Allerton Press. Translated from the Rumanian, Lagare cu Alunecare, Editura Technica.

[16] Czolczynski, K, (1999), Rotordynamics of Gas-Lubricated Journal Bearing Systems. Springer.
3

[17] Delamare J, Rullikre E, Yonnet J P (1995), Classification and Synthesis of Permanent Magnet Bearing Configurations. IEEE Transactions on Magnetics, 31(6): 4190-4192.
9

[18] DellaCorte, C and Valco, M J (2000) Load Capacity Estimation of Foil Air Journal Bearings for Oil-Free Turbomachinery Applications. Tribology Transactions 2000; 43(4), 795-801.
8

[19] Devasia, S, Eleftheriou E and Moheimani, S (2007), A survey of control issues in nanopositioning, IEEE Trans. Control Syst. Technol., vol. 15, no. 5, pp. 802–823. 58

[20] Dewell, D L and Mitchell, L D, (1984), Detection of a misaligned disk coupling using spectrum analysis. ASME Trans. J. Vibration, Acoustics, Stress and Reliability Design. 106, 9-16.
140

[21] Dimofte, F (1991), Fast methods to numerically integrate the Reynolds equation for gas fluid films. Proceedings of STLE-ASME Joint Tribology Conference, St. Louis, MO, 13-16 Oct.
viii, 79, 81

[22] Dowson, D and March, C H (1966), A thermohydrodynamic analysis of journal bearings. Proceedings of the Institution of Mechanical Engineers, vol. 181, pt 3.
6, 13

[23] Dowson, D, Hudson, J, Hunter, B, and March, C (1966). An experimental investigation of the thermal equilibrium of steadily loaded journal bearings. Proc. Inst. Mech. Eng, vol. 181, no. 32, pp. 70–80.
6

[24] Earnshaw, S (1842), On the nature of molecular forces which Regulate the Constitution of the Luminiferous Ether. Trans. Cambridge Philisophical Society, vo1.7, part.1, pp 97-112.
4, 101

[25] Elert, G (2010) The Physics Hypertextbook-Viscosity. Physics.info. Retrieved 2010-09-14.
40

[26] Elrod, H G and Burgdorfer, A (1960) Refinements Of The Theory Of The Infinetly-Long, Self -Acting, Gas-Lubricated Journal Bearing.
6

[27] Faria, M T C and San Andrés, L (2000), On the Numerical Modeling of High-Speed Hydrodynamic Gas Bearings. Journal of Tribology, vol. 122, no. 1, p. 124.
13

[28] Filatov, A and Maslen, E (2001), Passive magnetic bearing for flywheel energy storage systems. IEEE Trans. Magn. 37(6): 3913–3924.
5

[29] Fox, R W and McDonald, A T (1994), Introduction to Fluid Mechanics. Fourth Edition, John Wiley & Sons, Inc, New York, 1994.
59

[30] Ford, G W K, Harris, D M, and Pantall, D (1956), Gas-lubricated bearings. Machinery Market, vol. 182, no. 2924, pp. 26–30.
6

[31] Fremerey, J K M. Kolk (1999), A 500-Wh power flywheel on permanent magnet bearings, Proceedings of the 5th International Symposium on Magnetic Suspension Technology, 1-3. 12, Santa Barbara, CA
10

[32] Gash, R and Lang, M, (2000), LEVITRON - rein permanentmagnetische Lagerung eines Rotors. ZAMM - Zeitschrift fur Angewendete Mathematik und Mechanik, 80(2), pp.137-144 (in German).
102

[33] Gilbert, R G (1955), Magnetic suspension, US Patent 2,946,930, 1955.
10

[34] Goodwin M J, Boroomand T, Hooke C J (1989) Variable Impedance Hydrodynamic Journal Bearings for Controlling Flexible Rotor Vibrations. 12th Biennial ASME Conference on Vibration and Noise, Montreal, Canada, Sept 17-21; 261-267
8

[35] Hamrock, B J (1994), Fundamentals in Fluid Film Lubrication. McGraw-Hill, New York.
44

[36] Holman, J P (1990), Heat Transfer. McGraw-Hill, New York.
55

[37] Horikawa, O, Kaiji, S, and Shimokohobe, A (1992), An active air journal bearing. Nanotechnology, 3, 84-90.
8

[38] Hughes, W F and Osterle, J F (1957), On the adiabatic Couette flow of a compressible fluid. Zeitschrift für angewandte Mathematik und Physik ZAMP, vol. 8, pp. 89– 96.
6

[39] Heshmat H, Ming-Chen H, Walton II J F (2000). On the Performance of Hybrid Foil-Magnetic Bearings. ASME Trans, Journal of Engineering for Gas Turbines and Power; 122(1): 73-81.
5

[40] Holmes, F. T. and Beams, J. W. (1937). Frictional torque of an axial magnetic suspension, Nature 140: 30–31.

[41] Hussien, A A, Yamada, S, Iwahara, M, Okada, T and Ohji, T (2005). Application of the repulsive-type magnetic bearing for manufacturing micromass measurement balance equipment, IEEE Trans. Magn. 41(10): 3802–3804.
5

[42] Jung, C S and Choi, S B (1995), Analysis of a Short Squeeze Film Damper Operating with Electrorheological Fluids. STLE Tribology Trans. 1995; 38(4), pp.857-862.
8

[43] Kadoya, K, Matsunaga, N and Nagashima, A (1985). Viscosity and Thermal Conductivity of Dry Air in Gaseous Phase, J. Phys. Chem. Ref. Data, Vol.14, No 4.
40

[44] Katto, Y and Soda, N, (1952), Theory of lubrication by compressible fluid with special reference to air bearing. Proceedings of the Second Japan National Congress for Applied Mechanics, pp. 267–270.
5

[45] Kim, T H and San Andrés, L (2008), Heavily Loaded Gas Foil Bearings: A Model Anchored to Test Data, Journal of Engineering for Gas Turbines and Power, vol. 130, no. 1, p. 012504.
8, 13

[46] Kim, T H and San Andrés, L (2010), Thermohydrodynamic Model Predictions and Performance Measurements of Bump-Type Foil Bearing for Oil-Free Turboshaft Engines in

Rotorcraft Propulsion Systems. Journal of Tribology, vol. 132, no. 1, p. 011701.
7

[47] Krodkiewski J M, Sun, L (1998), Modeling of Multi-Bearing Rotor System Incorporating an Active Journal Bearing. Journal of Sound and Vibration. 210(1): 215-229.

[48] Lang, M and Fremerey, J K (2001), Optimization of Permanent-Magnet Bearings. 6th International Symposium on Magnetic Suspension Technology, Turin.
10

[49] Lang, M (2002), Fast calculation method for the forces and stiffnesses of permanent-magnet bearings. 8th International Symposium on Magnetic Bearing pp. 533–537.
10

[50] Lee S Q and Gweon, D G (2000), A new 3-DOF Z-tilts micropositioning system using electromagnetic actuators and air bearings, Precision Engineering, Volume 24, Issue 1, January, 24-31.
5

[51] Lee, D and Kim, D (2010), Thermohydrodynamic Analyses of Bump Air Foil Bearings With Detailed Thermal Model of Foil Structures and Rotor. Journal of Tribology, vol. 132, no. 2, p. 021704.
7, 48

[52] Lemarquand, V and Lemarquand, V. (2010). Passive Permanent Magnet Bearing for Rotating Shaft : Analytical Calculation, Magnetic Bearings, Theory and Applications, Bostjan Polajzer (Ed.), ISBN: 978-953-307-148-0.
10

[53] Liu, Z S, Zhang, G H and Xu, H J (2009), Performance Analysis of Rotating Externally Pressurized Air Bearings. Proceedings of the Institution of Mechanical Engineers, Part J: Journal of Engineering Tribology. 223(4), 653–663. viii, 79, 81, 82

[54] Lo, C Y, Wang, C C and Lee, Y H (2005). Performance Analysis of High Speed Spindle Aerostatic Bearings. Tribology International, 38(1), 5-14.
79

[55] Lund, J W (1967), A theoretical analysis of whirl instability and pneumatic hammer for a rigid rotor in pressurized gas journal bearings, Journal of Lubrication Technology, 89(2), 145-167.
63, 140

[56] Lund, J W (1968), Calculation of stiffness and damping properties of gas bearings, Journal of Lubrication Technology, 90, 793-803.

[57] Lund, J W (1968), Calculation of stiffness and damping properties of gas bearings, ASME Journal of Lubrication Technology, vol. 90, no. (1968), pp. 793–803.
13, 42, 116

[58] Lund, J W (1975), Linear Transient Response of a Flexible Rotor Supported in Gas-Lubricated Bearings. American Society of Mechanical Engineers and American Society of Lubrication Engineers, Joint Lubrication Conference, Miami Beach, Fla, January.
13

[59] Mayer, D and Vesley, V (2003), Solution Of Contact-Free Passive Magnetic Bearing. J. of Electrical Engineering, Vol.54, No 11-12, 293-297.
14, 101, 107

[60] Mizumoto, H, Arii, S, Kami, Y, Goto, K, Yamamoto, T and Kawamoto, M (1996), Active Inherent Restrictor for Air Bearing Spindles. Precision Engineering, 19(2-3), 141–147.
8

[61] Mizumoto, H, Arii, S, Yabuta, Y, Tazoe, Y (2010), Vibration Control of a High-Speed Air-Bearing Spindle Using an Active Aerodynamic Bearing. Proceedings of 2010 International Conference on Control, Automation and Systems (ICCAS 2010); 2261-2264.
9

[62] Meeks, C (1974), Magnetic bearings, optimum design and applications. First workshop on RE-Co permanent magnets, Dayton.
9

[63] Morosi S and Santos I F (2011), On The Modelling Of Hybrid Aerostatic - Gas Journal Bearings, Journal of Engineering Tribology, Proceedings of the Institution of Mechanical Engineers Vol. 225, Part J: Journal of Engineering Tribology NordTrib Special Issue, Vol

7.
45

[64] Near, C (1996), Piezoelectric Actuator Technology. Proceedings of the SPIE - The International Society for Optical Engineering 2717; 246-258.
57

[65] Nelson, H D and McVaugh, J M (1976), The dynamics of rotor-bearing systems using finite elements. Journa of Engineering for Industry, 593-600.
119

[66] Othmer, D F, Josefowitz, S, (1946), Correlating Viscosities of Gases with,Temperature and Pressure, Ind. Eng. Chem., 1946, 38 (1), pp 111–116.
40

[67] Osborne, D, San Andres, L (2006), Experimental Response of Simple Gas Hybrid Bearings for Oil-Free Turbomachinery. Journal of Engineering for Gas Turbines and Power, 128(3), 626-633.
142, 147

[68] Palazzolo, A B, Lin, R R, Alexander, R M, Kascak, A F, and Montague, G (1991), Test and Theory for Piezoelectric Actuator – Active Vibration Control of Rotating Machinery. ASME Trans., Journal of Vibration and Acoustics; 113(2), pp.167-175.
8

[69] Peng, Z-C and Khonsari, M M, (2006), A Thermohydrodynamic Analysis of Foil Journal Bearings. Journal of Tribology, vol. 128, no. 3, p. 534.
7, 52, 55, 88

[70] Pietra, L D and Adiletta, G (2002) The Squeeze Film Damper over Four Decades of Investigations. Part I: Characteristics and Operating Features. Shock and Vibration Digest; 34(1), pp.3-27.
4

[71] Pinkus, O (1990), Thermal aspects of fluid film tribology.
6, 7

[72] Powell, J W, (1970), A review of progress in gas lubrication. Review of Physics and Technology, vol. 1, no. 2, p. 96.
viii, 3, 78, 80

[73] Prechtl, E F and Hall, S R (1999), Design of a High Efficiency, Large Stroke, Electromechanical Actuator. Smart Materials and Structures; 8 (1), 13-30.

[74] Qiu, J, Tani, J, and Kwon, T (2003), Control of Self-Excited Vibration of a Rotor System With Active Gas Bearings. ASME J. Vibr. Acoust.; 125, pp. 328–334.
9

[75] Radil, K and Zeszotek, M, (2004), An Experimental Investigation into the Temperature Profile of a Compliant Foil Air Bearing. Tribology Transactions, vol. 47, no. 4, pp. 470–479.
7

[76] Raimondi, A A (1961), A Numerical Solution for the Gas Lubricated Full Journal Bearing of Finite Length. ASLE Transactions, Volume 4, Issue 1, 131-155.
79

[77] Ro, S-K, Kim, S, Kwak, Y and Park, C H (2008), Development of magnetically preloaded air bearings for a linear slide: Active compensation of three degrees of freedom motion errors, Rev. Sci. Instrum. 79, 036104.
5

[78] Salehi, M and Heshmat, H (2000), On the Fluid Flow and Thermal Analysis of a Compliant Surface Foil Bearing and Seal. Tribology Transactions, vol. 43, no. 2, pp. 318–324.
6

[79] Salehi, M, Swanson, E, and Heshmat, H (2001), Thermal Features of Compliant Foil Bearings - Theory and Experiments. Journal of Tribology, vol. 123, no. 3, p. 566.
7

[80] San Andrés, L and Lubell, D, (1998), Imbalance Response of a Test Rotor Supported on Squeeze Film Dampers. ASME Trans., Journal of Engineering for Gas Turbines and Power; 120(2), pp.397-404.
4

[81] San Andrés, L (2006), Hybrid Flexure Pivot-Tilting Pad Gas Bearings: Analysis and Experimental Validation. Journal of Tribology; 128(3), 55.
8

[82] San Andrés, L, Rubio, D and Kim, T H (2007), Rotordynamic Performance Of A Rotor Supported On Bump Type Foil Gas Bearings: Experiments and Predictions. Journal of Gas Turbines and Power; 129(3), p.850. 141

[83] San Andrés, L and Kim, T H (2007), Forced Nonlinear Response of Gas Foil Bearing Supported Rotors. Tribology International; no. 41, p. 704. 141

[84] San Andrés, L, and Ryu, K (2008), Hybrid Gas Bearings With Controlled Supply Pressure to Eliminate Rotor Vibrations While Crossing System Critical Speeds. Journal of Engineering for Gas Turbines and Power; 130(6), 062505.
9

[85] San Andrés, L and Kim, T H, (2010), Thermohydrodynamic Analysis of Bump Type Gas Foil Bearings: A Model Anchored to Test Data. Journal of Engineering for Gas Turbines and Power, vol. 132, p. 042504.
7, 55

[86] Santos I F (1994), Design and Evaluation of TwoTypes of ActiveTilting Pad Journal Bearings. The Active Control of Vibration, edited by Burrows CR and Keogh PS, Mechanical Engineering Publications Limited, London, England: 79-87; ISBN 0-85298-916-4.
8

[87] Santos I F (1995) Strategien fur die Erhohung der Dämpfungsreserve von kippsegmentgelagerten Rotorsystemen" (trans: Strategies for Increasing the Damping Properties of Rotating Systems supported by Tilting-Pad Bearings) , Schwingungen in rotierenden Maschinen. Edited by Irretier H, Nordmann R,Springer H, Vieweg Verlag, Braunschweig, Germany, 3: 3-12, 1995; ISBN 3-528-06655-5.

[88] Santos, I F and Russo, F H (1998) Tilting-Pad Journal Bearings with Electronic Radial Oil Injection. ASME Trans., Journal of Tribology; 120(3), pp.583-594.
8, 44

[89] Santos, I F, Scalabrin A and Nicoletti R (2001), Ein Beitrag Zur Aktiven Schmierungstheorie. Scwingungen in Rotierenden Maschinen; Vol 5, 21-30. In German.

[90] Schwartz, B J, Richardson, M H (1999), Experimental modal analysis, CSI Reliability Week, Orlando, FL October.
143

[91] Schweitzer, G, Traxler, A and Bleuler, H (1994), Active Magnetic Bearings - Basics, Properties and Applications of Active Bearings. Springer Verlag, Berlin, Heidelberg, New York.
8

[92] Sekhar, A S and Prabhu, B S, (1995), Effects of coupling misalignment on Vibrations of rotating machinery. J. Sound Vibration. 185 (4), 655-671.
139

[93] Sim, K and Kim, D (2007), Design of Flexure Pivot Tilting Pads Gas Bearings for High-Speed Oil-Free Micro Turbomachinery. ASME J. Tribol. 2007; 129(1), pp. 112–119.
8

[94] Sim, K and Kim, D (2008), Thermohydrodynamic Analysis of Compliant Flexure Pivot Tilting Pad Gas Bearings. Journal of Engineering for Gas Turbines and Power, vol. 130, no. 3, p. 032502.
7, 8

[95] Simon, M D, Heflinger, L O and Ridgway, S L (1997), Spin stabilized magnetic levitation. American Journal of Physics 65(4), 286-292.
102

[96] Tang P, Palazzolo A, Kascak A, Montague G, Li W (1995), Combined Piezoelectric-Hydraulic Actuator Based Active Vibration Control for Rotordynamic System. ASME Trans, Journal of Vibration and Acoustics; 117(3): 285-293.
8

[97] Taylor, C J and Washington, G N (2002), A Comprehensive Piezoceramic Actuator Review. Procedings fo SPIE - The International Society for Optical Engineering 4701; 443-454.
57

[98] Ulbrich H, Althaus J (1989), Actuator Design for Rotor Control. 12th Biennial ASME Conference on Vibration and Noise, Montreal, Canada; 17-21.
8

[99] Ulbrich H (1994), Comparison of Different Actuators Concepts for Applications in Rotating Machinery. International Journal of Rotating Machinery 1994; 1 (1), 61-71.
57

[100] Vance, J M and Li, J (1996), Test Results of a New Damper Seal for Vibration Reduction in Turbomachinery. ASME Trans., Journal of Engineering for Gas Turbines and Power; 118(4), pp.843-846.
4

[101] Vance, J M, Ying, D and Nikolajsen, J (2000), Actively Controlled Bearing Dampers for Aircraft Engine Applications. ASME Trans., Journal of Engineering for Gas Turbines and Power; 122(3), pp.466-472.
8

[102] Wauman, T, Peirs, J, Reynaerts, D and Al-Bender, F, (2011). On the dynamic stability of high-speed gas bearings: stability study and experimental validation. Proc of SCAD 2011.
148

[103] Wendt, J F (1992), Computational Fluid Dynamics, New York, Springer-Verlag. 69

[104] Whitley, S and Betts, C (1959), Study of gas-lubricated, hydrodynamic, full journal bearings. British Journal of Applied Physics, vol. 10, pp. 455–463.
6

[105] Yonnet, J P (1978), Passive magnetic bearings with permanent magnets. IEEE Trans. Magn. 14(5): 803–805.
9, 10

[106] Yonnet, J P, Lemarquand, G, Hemmerlin, S, and Olvierrulliere, E (1991), ‘Stacked Structures of Passive Magnetic Bearings. J. Appl. Phys., 70(10), pp. 6633-6635.
10

[107] Zhu, C, Robb, D A and Ewins, D J (2002), A Magneto-Rheological Fluid Squeeze Film Damper for Rotor Vibration Control. Proceeding of SPIE's 9th Annual International Symposium on Smart Structures and Materials 2002; I, pp.516-522.
8

[108] Zhu, C, Robb, D A and Ewins, D J (2002) On-Off Control of Rotor Vibration by a Disk-Type Magneto-Rheological Fluid Damper. Proceeding of the 9th International Symposium on Transport Phenomena and Dynamics of Rotating Machinery, Honolulu, Hawaii, pp.1-7.
8

DTU Mechanical Engineering
Section of Solid Mechanics
Technical University of Denmark

Nils Koppels Allé, Bld. 404
DK- 2800 Kgs. Lyngby
Denmark
Phone (+45) 45 25 42 50
Fax (+45) 45 93 14 75
www.mek.dtu.dk
SBN: 978-87-90416-67-6

DCAMM
Danish Center for Applied Mathematics and Mechanics

Nils Koppels Allé, Bld. 404
DK-2800 Kgs. Lyngby
Denmark
Phone (+45) 4525 4250
Fax (+45) 4593 1475
www.dcamm.dk
ISSN: 0903-1685